Mathematical modelling of cell growth in tissue engineering bioreactors

Lloyd A.C. Chapman
Lady Margaret Hall
University of Oxford

A thesis submitted for the degree of
Doctor of Philosophy

Hilary 2015

To my parents, brother and Marinella for all their love and unending support.

Acknowledgements

Firstly I would like to thank three friends without whom I would not have been here to write this thesis: Charlie, Natalie and James. I am eternally grateful for their support in the times in my life when I needed it most.

I would like to thank my supervisors, Sarah Waters, Helen Byrne, Jonathan Whiteley and Becky Shipley, for all their help, patience and guidance over the last three and a half years. Their knowledge and support, both academic and non-academic, has been invaluable.

I owe a big thank you to all those involved in teaching and running the Life Sciences Interface Doctoral Training Centre (LSI DTC), at which I have been a student since 2010. The DTC taught courses during the first year of my DPhil were really enjoyable and opened my eyes to the wonder of biology, and my fellow DTC students have been great companions throughout my DPhil. I am very grateful to the Engineering and Physical Sciences Research Council for funding my research through the DTC. I would also like to thank my college, Lady Margaret Hall, for providing me with great tutors as an undergraduate, for engaging with and supporting my research, and for supporting the college boat club.

I have had the privilege of being part of both the Oxford Centre for Industrial and Applied Maths in the Mathematical Institute and the Computational Biology Group in the Department of Computer Science during my DPhil, and thank everyone in both groups for their help and for providing so much intellectual stimulation over such a broad range of research. In particular, I would like to thank my office mates Mo and Natalie for many helpful discussions on fluid mechanics and mixture theory, and all the support staff for providing me with great facilities to do my research.

There are many friends without whom my DPhil would certainly not have been as much fun as it has been and to whom I am very grateful: my good friend Joe, my housemates from 12 Harcourt Terrace: Loz, Petra, Fird, Clement, Richard, Jon and James; those from 1 Leopold Street: Andrea and Sam; and those from 57 Norreys Avenue: Bav, Beth, Jeremy and Sam. I owe huge thanks to my parents for their endless support and for encouraging me to follow my interests, and to my brother for always giving me good advice and being a great older brother. Finally, I would like to thank my girlfriend, Marinella, for her incredible support and encouragement in all aspects of my life.

Mathematical modelling of cell growth in tissue engineering bioreactors

Lloyd A.C. Chapman
Lady Margaret Hall, University of Oxford
A thesis submitted for the degree of *Doctor of Philosophy*

Hilary Term 2015

Expanding cell populations extracted from patients or animals is essential to the process of tissue engineering and is commonly performed in laboratory incubation devices known as bioreactors. Bioreactors provide a means of controlling the chemical and mechanical environment experienced by cells to ensure growth of a functional population. However, maximising this growth requires detailed knowledge of how cell proliferation is affected by bioreactor operating conditions, such as the flow rate of culture medium into the bioreactor, and by the initial cell seeding distribution in the bioreactor. Mathematical modelling can provide insight into the effects of these factors on cell expansion by describing the chemical and physical processes that affect growth and how they interact over different length- and time-scales.

In this thesis we develop models to investigate how cell expansion in bioreactors is affected by fluid flow, solute transport and cell seeding. For this purpose, a perfused single-fibre hollow fibre bioreactor is used as a model system. We start by developing a model of the growth of a homogeneous cell layer on the outer surface of the hollow fibre in response to local nutrient and waste product concentrations and fluid shear stress. We use the model to simulate the cell layer growth with different flow configurations and operating conditions for cell types with different nutrient demands and responses to fluid shear stress. We then develop a 2D continuum model to investigate the influence of oxygen delivery, fluid shear stress and cell seeding on cell aggregate growth along the outer surface of the fibre. Using the model we predict operating conditions and initial aggregate distributions that maximise the rate of growth to confluence over the fibre surface for different cell types.

A potential limitation of these models is that they do not explicitly consider individual cell interaction, movement and growth. To address this, we conclude the thesis by assessing the suitability of a hybrid framework for modelling bioreactor cell aggregate growth, with a discrete cell model coupled to a continuum nutrient transport model. We consider a simple set-up with a 1D cell aggregate growing along the base of a 2D nutrient bath. Motivated by trying to reduce the high computational cost of simulating large numbers of cells with a cell-based model, and to assess the validity of our previous continuum description of cell aggregate growth, we derive a continuum approximation of the discrete model in the large cell number limit and determine whether it agrees with the discrete model via numerical simulations.

Contents

List of acronyms

AHM adaptive hybrid model

BAL bioartificial liver device

BSA bovine serum albumin

CA cellular automata

CFD computational fluid dynamics

CHM composite hybrid model

DNA deoxyribonucleic acid

ECM extra-cellular matrix

ECS extra-capillary space

FE finite element

FEM finite element method

HFB hollow fibre bioreactor

MSC mesenchymal stem cell

ODE ordinary differential equation

PDE partial differential equation

PLGA poly(lactide-co-glycolide)

PVA poly(vinyl alcohol)

Chapter 1

Introduction

Tissue engineering combines knowledge of biology, chemical engineering and material science to develop biological substitutes to maintain and repair damaged tissues and organs. Currently, most replacements for tissue and organs that are lost, damaged or have become defective through trauma, disease or ageing take the form of donor transplants or artificial implants. However, there is a chronic shortage of donor tissue available: in the UK alone there are over 10,000 people who need a transplant and of these three die every day waiting to receive one [185]. Even when a donor transplant is available there are often additional complications. The donor tissue may not match the tissue of the patient sufficiently well to be useable, or once implanted may suffer immune rejection (see [262] for statistics on transplant rejection in the US). Even if the transplant is not rejected the recipient generally has to take strong immunosuppressant drugs for the rest of their life. In some cases it may be possible to harvest tissue from another part of the patient's body to make the repair, *e.g.* for bone grafts [8] and vein transplants [79]. However, the harvested tissue often does not fully restore the functionality of the tissue into which it is implanted, and the tissue functionality in the harvested region is reduced. There is also the pain and discomfort associated with the tissue removal and the risk of post-operative infection [8]. There are similar complications with using artificial materials, *e.g.* the limited lifespan of hip and knee replacements [210] and risk of infection with artificial patches for repairing blood vessels [128]. Clearly, therefore, there is a significant need for alternative sources of cells and tissue for grafts. Tissue engineering has the potential to meet this need provided cells and tissues can be grown at sufficiently large scale for clinical application (*i.e.* to cell populations of $\sim 10^8$ and tissue grafts of the order of centimetres or tens of centimetres [233]). A major advantage of tissue engineering is that grafts can be grown from a patient's own cells (autologous cells), which removes the need for testing donor and recipient compatibility prior to transplantation and overcomes the problem of immune rejection [244].

Successes and challenges in tissue engineering

A number of different types of cells and tissue have already been successfully engineered and used clinically, including skin substitutes [98] and cartilage cells for knee cartilage repair [21]. Perhaps the most notable success has been in engineered tracheae transplants, with the first ever transplant (using a decellularised donor windpipe seeded with the patient's own stem cells) having been carried out by Macchiarini *et al.* [160]. Other engineered tissues and organs that are undergoing clinical trials include bladders [12], corneas, blood vessels and bronchial tubes [123]. Despite these successes, many challenges remain to be overcome, including improving understanding of how different cell types respond to their external environment and developing ways to engineer larger tissues [166]. The latter requires determining how to enhance nutrient supply to, and waste product removal from, growing tissues, since the size and type of tissues that can currently be engineered is limited by the diffusion distance of nutrients and waste products in tissue. While thin tissues (up to a few hundred micrometers in depth) and avascular tissues, such as those described above, can be adequately supplied with nutrients by diffusion, larger tissues or those with higher metabolic demands become nutrient-depleted without alternative transport mechanisms [165]. Hence there is a need for further research into vascularising engineered tissue and scaling up laboratory experiments for clinical use.

In vivo and *in vitro* tissue engineering

Tissue engineering methods can be viewed as either *in vivo* or *in vitro*. Although both types normally entail expanding a cell population and then seeding it onto a porous scaffold (to form a cell-scaffold construct), in the *in vivo* method the construct is implanted directly into the body, whereas in the *in vitro* method it is incubated in a bioreactor external to the body prior to implantation. The main purpose of the scaffold is to provide a structure to which the cells can attach, on which they can grow and through which essential nutrients can be transported, although some scaffolds also provide physical and chemical cues to influence the growth of the cell population (*e.g.* guidance channels for neural cells in nerve regeneration [276] and chemical and topographical patterning of the scaffold surface for bone, muscle and skin cell culture [153]). Scaffolds made from biodegradable polymers will degrade and be replaced by new tissue once implanted into the body, potentially enabling the complete regeneration of the damaged tissue [98]. A potential advantage of *in vitro* tissue engineering is that culturing the cell-scaffold construct in a bioreactor allows the nutrient, temperature and pH environment of the cells to be controlled to ensure the growth of a functional cell population.

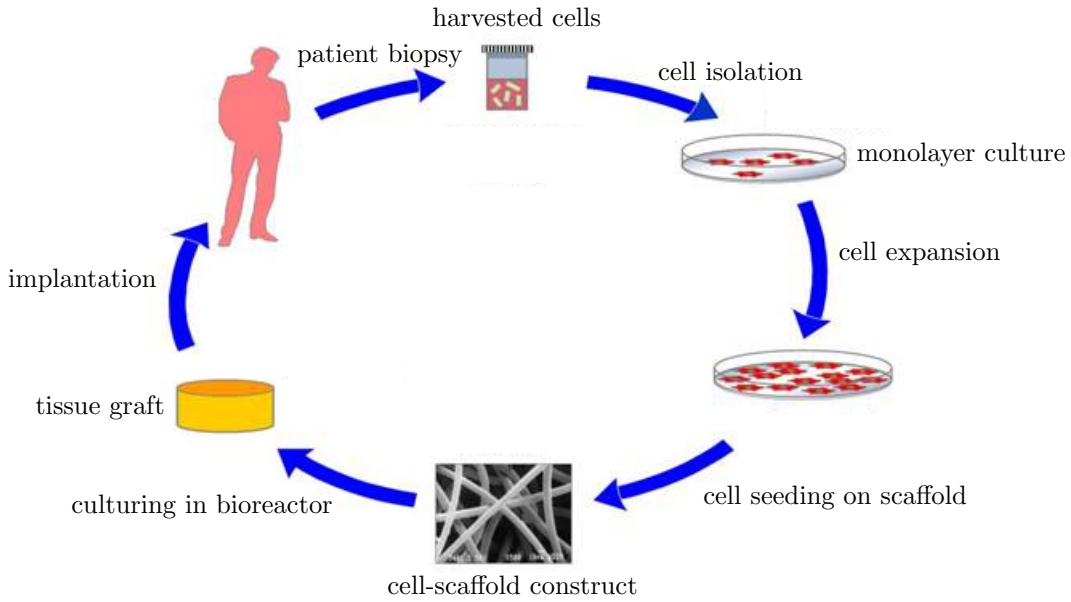

Figure 1.1: Summary of the *in vitro* tissue engineering process. Adapted from [1].

In this thesis we focus on *in vitro* tissue engineering, the process of which is summarised in Figure 1.1, and in particular the use of bioreactors for expanding cell populations. Bioreactors nevertheless have a number of other uses in tissue engineering and medicine that include promoting stem cell differentiation, investigating normal and pathological tissue development, testing drug delivery and action on tumour cells [98], and as potential external organ support devices [168].

Motivation for mathematical modelling

Historically, advances in tissue culture in bioreactors have relied on many expensive and time-consuming experiments. However, since tissue growth is a complex multiscale phenomenon, consisting of many coupled biophysical and biochemical processes occurring over a wide range of length- and time-scales, it is very difficult to unpick the effects of the processes involved solely by experimental investigation. Mathematical modelling and computer simulation can offer significant assistance in understanding the processes underlying tissue growth and thus enable major improvements in bioreactor design and operation. Mathematical models also permit rapid and cost-efficient exploration of different experimental scenarios, and can provide detailed spatial and temporal information, *e.g.* on nutrient distributions in bioreactors, that is difficult to obtain via experiments.

In this thesis we develop mathematical models to investigate the influence of fluid flow, nutrient and waste metabolite transport, and cell seeding on cell population growth in bioreactors. For this purpose we focus on a particular bioreactor system: the single-fibre

hollow fibre bioreactor (HFB) as used by Dr M. Ellis' group at the Centre for Regenerative Medicine at the University of Bath. This bioreactor provides a model system for investigating the effect of the above factors on cell population expansion, as it enables cells to be cultured in different flow and seeding configurations. The models we develop yield predictions of optimal operating and seeding conditions for cell population expansion in the single-fibre HFB, but also provide insight into potential means of improving cell culture in similar bioreactor systems.

Chapter outline

In §1.1, we describe the biological processes that underpin tissue engineering, discussing the different cell types that are used to grow new tissue, the processes by which cells respond to their external environment, and the different types of bioreactor used to culture cells (including a full description of the HFB system we consider). Following this, we describe the different types of mathematical models that have been used to represent tissue growth in tissue engineering bioreactors in §1.2, and those specifically applied to HFBs, to provide background to the models we consider. In §1.3 we give an outline of the thesis and discuss the motivation and aims for each of the models that we develop. To conclude, we discuss the novel contributions of our work in §1.4.

1.1 Biological background

1.1.1 Cell types

As described above, *in vitro* tissue engineering involves seeding a cell population onto a scaffold and culturing the resulting construct in a bioreactor. A large array of different cell types can be used [244] and there are various different sources from which the cells can be harvested. They can be *autologous*, *i.e.* taken directly from the patient via a biopsy; *allogeneic*, *i.e.* taken from a human donor or embryo; or *xenogeneic*, *i.e.* from a different species. Although autologous cells are preferable to allogeneic or xenogeneic cells in terms of avoiding immune rejection, they may be difficult to harvest in large quantities [52] or, for some cell types such as nerve cells, to harvest at all [244]. The function required of the cells, in combination with their availability and biocompatibility, is often a key determining factor in the choice of cell source. Thus porcine hepatocytes are used for bioartificial liver devices because they are more widely available than human hepatocytes and are able to maintain liver-specific functions *in vitro* [7].

A further distinction that can be made in the types of cells used is between stem cells and differentiated cells (mature, tissue-specific cells). Stem cells generally proliferate at high

rates and are able to differentiate into many cell types, so theoretically make ideal candidates for engineering different tissues [98, 244]. However, it can be difficult to control their proliferation and differentiation, even with specific growth factors and specially designed scaffolds [75, 148, 244]. Differentiated cells, on the other hand, proliferate more slowly and can be difficult to expand sufficiently. Some approaches use a combination of stem cells and differentiated cells or cells at different stages of differentiation to achieve the desired cell behaviour [98].

Stem cells can be isolated both from embryos and adult tissue. Although embryonic stem cells are pluripotent, *i.e.* can differentiate into any cell type in the adult body, their use is associated with many ethical issues [138]. Hence, much research has been aimed at isolating and identifying multipotent adult stem cells, or so called mesenchymal stem cells (MSCs) [257]. These cells are most commonly found in bone marrow, but can also be obtained less invasively from other tissues, including amniotic fluid, placenta, umbilical cord tissue and blood, adipose tissue and dental pulp [103, 112].

1.1.2 Chemosensitivity and mechanotransduction

The external chemical and mechanical environment of cells in a bioreactor affects numerous cell processes including migration, growth, proliferation, differentiation and death. This thesis focusses on the effects of nutrient and waste product concentrations and fluid shear stress on cell growth, proliferation and death.

There are numerous examples of the effects of nutrient concentration on the proliferation of different cell types, *e.g.* the effects of oxygen concentration on the proliferation of fibroblasts [20, 125, 183], endothelial cells [219] and MSCs [146, 269]; and those of glucose concentration on pancreatic beta cells [249] and mesangial cells (smooth muscle cells around blood vessels in the kidneys) [275]. Cells have minimum requirements for glucose and oxygen in order to be able to perform oxidative phosphorylation to produce adenosine triphosphate, the 'molecular unit of intracellular energy'. Insufficient oxygen (hypoxia) and glucose can lead to cell death via apoptosis (programmed cell death) or necrosis (premature cell death due to internal cell damage). During cell growth and proliferation the metabolic demands of cells increase significantly, as a considerable amount of energy is required to double the cell's contents. Recent research has shown close links between the cell signalling pathways that control cell metabolism and proliferation, and suggested that proliferating cells may undergo a shift in metabolism towards that of cancer cells, with increases in the uptake of key nutrients such as glucose [157, 266]. For many cell types, increased extracellular oxygen leads to an increase in cell proliferation [125, 183, 269], as does increased extracellular glucose [249], but for some stem cells proliferation is greater under low oxygen

concentrations [20, 146]. In the models that we develop, we will assume that the rates of cell proliferation and growth increase with nutrient concentration (at least over some intermediate range of concentrations), and use simple functional forms to facilitate investigation of the effects of changes in the nutrient concentration.

Mechanotransduction is the process by which cells convert mechanical stimuli (such as shear or compression) into intracellular chemical activity and a coordinated cellular response [113], which can include alignment, growth, differentiation and proliferation [121, 179]. In our models we will investigate the influence of fluid shear stress on cell proliferation and death. Exposure to excess fluid shear stresses results in cell death for many cell types, as observed for cardiomyocytes [215] and hepatocytes [47], but shear stress can also stimulate proliferation, *e.g.* for osteoblasts [121] and chondrocytes [162]. Furthermore, exposure to fluid shear stress during cell culture has beneficial effects for various cell types [165], including increased extra-cellular matrix (ECM) deposition by osteoblasts [14] and enhanced protein synthesis by chondrocytes [57], which improve the mechanical strength of engineered bone and cartilage respectively. We will incorporate shear-induced cell death and shear-stimulated cell proliferation into our models using simple relationships between the cell death/proliferation rate and the fluid shear stress.

1.1.3 Cell seeding

As mentioned above, cell seeding is the process by which cells are incorporated into or onto the scaffold prior to being cultured in a bioreactor. Different seeding methods give different initial densities and spatial distributions of cells within the scaffold, which in turn affect the development of the tissue and therefore the physical and chemical properties of the final construct. Seeding cells into 3D scaffolds at high densities has been shown to improve the structural integrity of cartilaginous tissue constructs [83], increase bone mineralisation [110], and enhance the structure and function of constructs grown from cardiac cells [29]. Conversely, low density and non-uniform seeding has produced inferior tissue constructs in the case of cartilage regeneration [82].

There are two main cell seeding strategies: surface seeding, in which cells are put onto an exposed surface of the scaffold, and bulk seeding, in which the cells are distributed throughout the scaffold. Surface seeding is normally achieved via static loading of the cells onto the scaffold surface using a micropipette. This is the most commonly used seeding method despite evidence that it can lead to tissue constructs with non-uniform cell distributions [110, 124, 152]. The spatial heterogeneity in the final cell distributions obtained with this method is mainly due to cells remaining near the scaffold surface where the nutrient concentration is high and preventing the nutrient reaching the scaffold centre. Bulk

seeding is often performed by agitating a cell suspension surrounding the scaffold to encourage the convection of cells into the scaffold or by directly perfusing the scaffold with the cell suspension, and has been reported to give constructs with a higher density and more uniform distribution of cells [110, 124, 152]. Although these general relationships between the density and distribution of seeded cells and the properties of the final construct have been identified, optimal seeding strategies are highly dependent on the specific bioreactor set-up (*e.g.* the scaffold architecture, fluid dynamics and nutrient transport) and cell type. In many cases, further experimental and theoretical investigations are required to determine the influence of the seeding strategy on the growth of the seeded cell population.

1.1.4 Types of bioreactor

Bioreactors can be divided into two types: those that use static culture and those that use dynamic culture. In static culture, cells are simply placed in culture medium rich in the nutrients and growth factors that they need to grow and divide, and the culture medium is periodically replaced to avoid the build up of toxic waste products. Dynamic culture, meanwhile, uses fluid flow to enhance transport of the nutrient-rich culture medium to the growing tissue. Typical static culture systems, used mainly to culture cell monolayers, include the petri dish and T-flask. Whilst they are easy to use, their major drawback is that nutrient delivery to, and waste product removal from, the cells occur via diffusion alone, which limits the size of cell culture that can be grown.

A variety of different dynamic bioreactors exist, all designed with the aim of closely mimicking the *in vivo* environments in which specific cell types grow. In addition to providing improved nutrient delivery, they also enable exposure of the cells to controlled levels of fluid shear stress, which can have numerous benefits as described above. The most basic examples of dynamic bioreactors are shake flasks and spinner flasks (Figures 1.2(a) and 1.2(b) respectively), in which the cell-scaffold construct is submerged or suspended in culture medium and the medium is mixed, by agitation of the whole flask or the motion of a magnetically-driven stirrer. Issues with shake and spinner flasks include unpredictability of the flow and their limited potential for growing large cell populations. Spinner flasks also have the disadvantage that turbulent eddies created by the stirrer increase the shear stress on the cells, potentially leading to cell damage [165].

Another type of dynamic bioreactor is the rotating wall vessel bioreactor (Figure 1.2(c)), in which cell-scaffold constructs are maintained in a state of free-fall through the culture medium by the rotation of the vessel about its longitudinal axis. Rotating wall vessel bioreactors provide more uniform flow and lower shear stresses than shake and spinner

flasks, and thus better culture conditions for several cell types [165], but the rotation rate has to be varied as the construct grows to keep it in free fall [166].

In direct perfusion bioreactors (Figure 1.2(d)), culture medium is pumped directly through the cell-scaffold construct, significantly enhancing mass transport to the scaffold interior. Direct perfusion bioreactors have been shown to improve cell survival, growth and function in comparison with static methods and other dynamic bioreactors for a variety of cell types [165]. Nevertheless, in choosing the flow rate through the scaffold, care must be taken to avoid exposing the cells to damaging levels of shear stress. Other bioreactor types include dynamic force bioreactors, in which mechanical forces are applied to the cell-scaffold construct to mimic forces experienced in the body, such as compression in cartilage and bone (Figure 1.2(e)); and fixed-bed and fluidised-bed bioreactors, in which cells are immobilised in macroporous carriers and packed or suspended respectively in a column perfused with culture medium (Figure 1.2(f)).

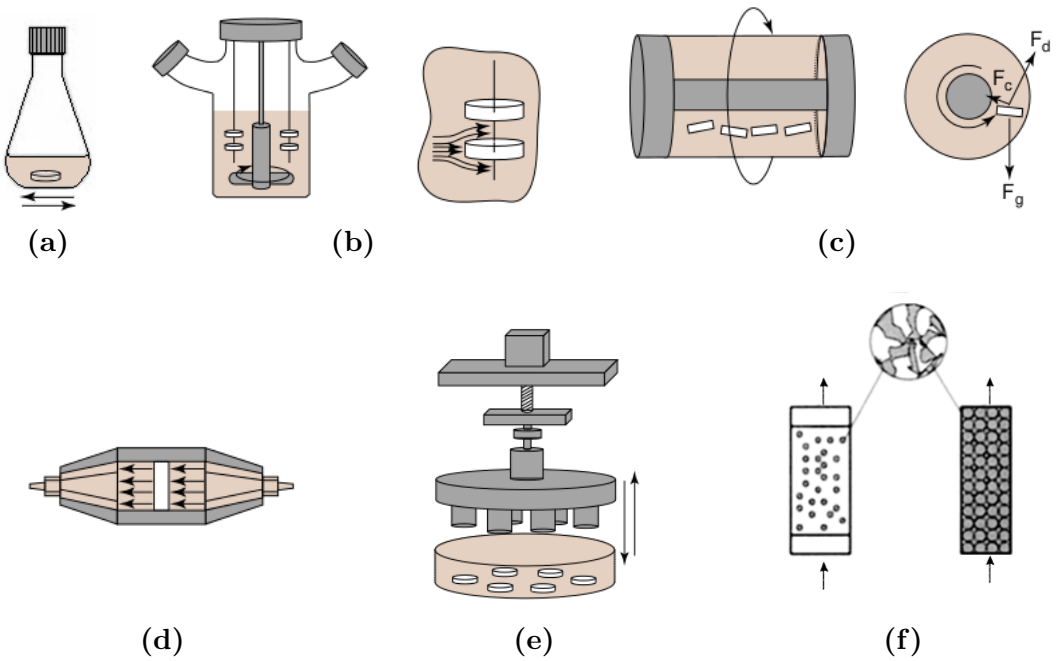

Figure 1.2: Different types of bioreactor. (a) Shake flask, (b) spinner flask (c) rotating wall vessel, (d) direction perfusion, (e) dynamic compression, and (f) fluidised-bed (left) and fixed-bed (right). Arrows show direction of motion and/or fluid flow. Cell-scaffold constructs shown in white, culture medium in light brown in (a)-(e); inset sketch in (f) shows porous structure of carriers into which cells are seeded. Adapted from [165, 210].

Hollow fibre bioreactors

The bioreactor that we consider in this thesis is a particular type of HFB. HFBs have been used for various tissue engineering applications, including mammalian cell expansion (see [278] for a review) and bioartificial liver devices [7, 168]. A number of different cell types have been cultured in HFBs, including lymphocytes [93, 94], hepatocytes [187] and osteoblasts [70]. In many respects, HFBs are similar to direct perfusion bioreactors. They consist of a glass module containing a single hollow fibre or a bundle of multiple aligned fibres (Figures 1.3(a) and 1.3(b)). Each fibre has a central lumen surrounded by a porous wall (or membrane) (Figure 1.4), that separates it from the space around the fibres, known as the extra-capillary space (ECS). In the typical mode of operation, cells are seeded in the ECS and nutrient-rich culture medium is pumped through the fibre lumen(s), but the cells can also be seeded in the lumen(s) and the culture medium pumped through the ECS [278]. Combinations of flow and cells inside and outside the fibres can also be used [278]. The fibre is designed so that the pores in the membrane are large enough to allow nutrients, waste products, proteins and growth factors to pass from the lumen to the ECS and vice versa, but sufficiently small that cells are unable to move into the membrane. With the flow separated from the cells by the membrane, cells are protected from high fluid shear stresses. This enables relatively high flow rates, which promote mass transport across the membrane, to be used without damaging the cells. HFBs also show much greater promise for expanding cell populations to the numbers necessary for clinical applications than other bioreactor types, due to the large surface area (relative to the bioreactor volume) for cell seeding and proliferation provided by the fibres [278]. For example, as many cells can be cultured in a 0.5 l HFB as in a 1000 l standard culture flask [69, 278]. A further benefit of HFBs for clinical applications is that the fibres mimic capillaries *in vitro* by guiding nutrient delivery to the cells, and so have the potential to direct the formation of new blood vessels when implanted into the body [70]. Furthermore, if the fibres are made from a biodegradable and biocompatible polymer, they will degrade following implantation as new tissue grows, until eventually just the new tissue will be left [70].

Despite these advantages, there is still a considerable amount of work required to develop HFBs for clinical use, both in terms of improving understanding of their operation and scaling them up. In particular, better understanding of the combined effects of cell seeding, operating conditions, and bioreactor design on flow, nutrient transport and cell population growth in HFBs is needed. To achieve a desired end cell yield or distribution, precise control over the nutrient, waste product, and fluid shear stress environment of the cells is required. Since the factors affecting this environment interact in a complex way, we choose to focus

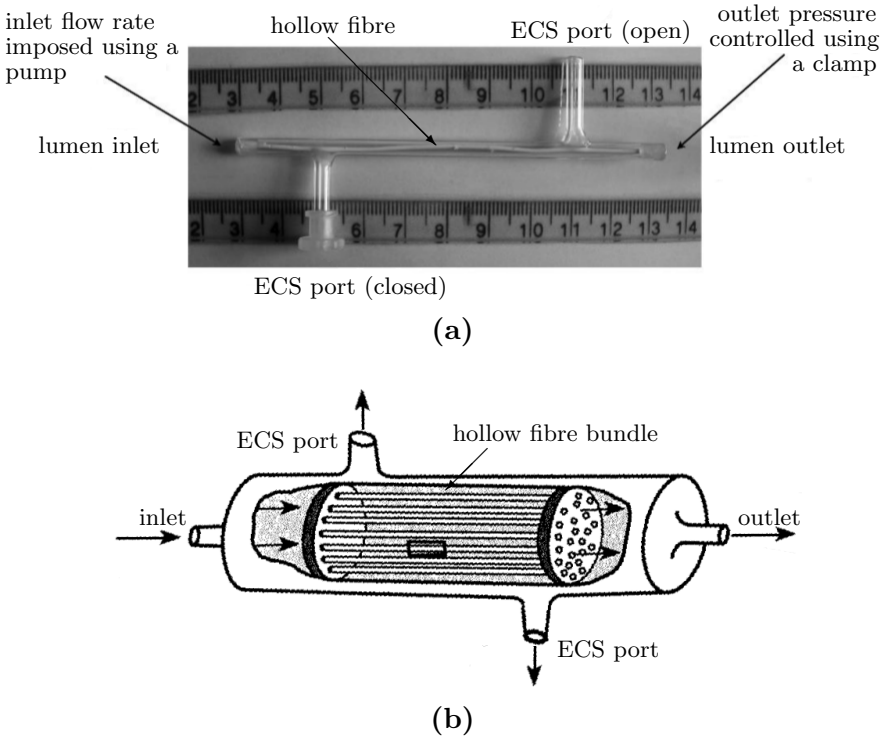

Figure 1.3: (a) Photograph of the single-fibre HFB module considered in this thesis (adapted from [231]). (b) Schematic of a HFB containing a bundle of hollow fibres (adapted from [186]). ECS = extra-capillary space. Arrows in (b) show the direction of fluid flow when fluid is pumped into the bioreactor at the lumen inlet.

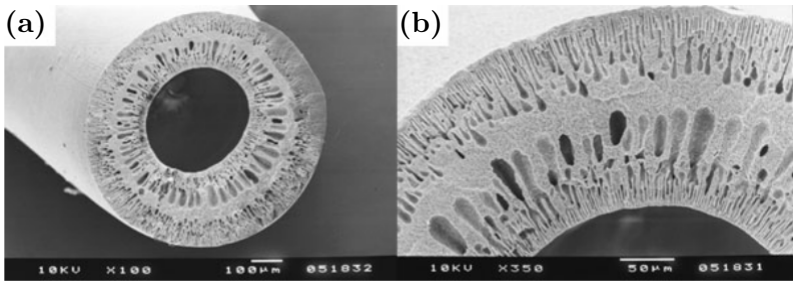

Figure 1.4: (a) Cross-section of a poly(lactide-co-glycolide) (PLGA) hollow fibre. (b) Close-up of the membrane showing the pore structure. From [70].

on a relatively simple laboratory-scale HFB set-up with the aim of gaining deeper insight into the factors influencing growth.

The HFB we consider is shown in Figure 1.3(a). It consists of a single porous hollow fibre housed in a cylindrical glass module. The bioreactor has two ECS ports, one at either end, on opposite sides of the module. Cells are typically seeded either by injecting an inoculum of cells into the ECS ports and rotating the bioreactor (on a drum rotating at 6.6 rpm for 6 hrs) so that the cells settle onto the outer surface of the fibre [70], or injecting a suspension of the cells in collagen gel through the ECS ports and leaving the gel to set

[281]. The former approach leads to the formation of aggregates of cells on the fibre surface and is used for cell population expansion experiments [278]. In the latter approach the cell-seeded gel typically occupies the entire ECS and the set-up is used to culture 3D constructs. Different flow configurations are possible, with neither, one or both of the ECS ports open and the culture medium either driven through the lumen or the ECS ports (or both) by a pump at a prescribed flow rate. For flow driven through the lumen, culture medium passes through the fibre walls to the cells, which absorb nutrients and growth factors from the medium and produce waste products. If one or both of the ECS ports are open, some of the culture medium (the *retentate*) exits the bioreactor via the lumen outlet and some (the *permeate*) via the ECS ports, and a pressure is applied at the lumen outlet to control the ratio of the two. A large number of the bioreactor design and operating parameters can be varied, including the bioreactor length, the membrane depth and permeability, the inlet flow rates, the inlet solute concentrations, and the cell seeding distribution.

Experiments are currently being carried out by Dr M. Ellis' group at the Centre for Regenerative Medicine at the University of Bath to investigate the use of this system for engineering bone, cardiac and liver tissue. Their prior research involved characterising the properties of, and testing cell attachment and culture on, hollow fibre membranes made from biodegradable poly(lactide-co-glycolide) (PLGA) [70, 71, 174, 178]. One outcome of this research was that fabricating the membranes with a mix of PLGA and poly(vinyl alcohol) (PVA), as opposed to just PLGA (which is hydrophobic), improved the hydrophilicity and porosity of the membrane and removed the need for special wetting agents [174]. The research also showed that, given the right culture conditions and culture period, cells seeded onto the surface of the fibre proliferate over the surface until they reach confluence [70, 175].

It is known from experiments with HFBs containing multiple fibres [59, 155, 251, 281] that once cells have reached confluence over the fibre surface, given suitable culture conditions they can proliferate outwards into the ECS to establish a layer multiple cells deep. However, uneven cell distributions over the fibre surface following culture (Figure 1.5), and poor cell yields compared to those achieved with tissue culture plastic in a T-flask have been observed [70]. Another issue associated with the single-fibre HFB is the difficulty of obtaining detailed spatial information about the nutrient, fluid shear stress and cell distributions in the bioreactor. Whilst the inlet and outlet flow rates and nutrient concentrations can be measured, it is difficult to mount flow and nutrient sensors inside the bioreactor due to its small size. Monitoring the evolution of the cell distribution in the bioreactor is also not straightforward, requiring the use of sophisticated imaging techniques [27, 105, 273]. These issues motivate our development of theoretical models of fluid and mass transport and cell proliferation in the single-fibre HFB.

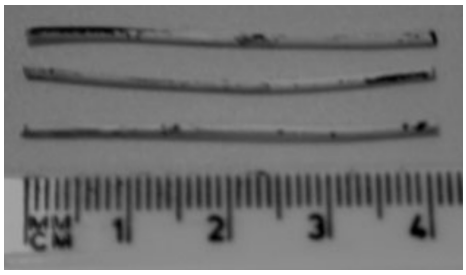

Figure 1.5: Uneven distribution of pZIP osteogenic cells cultured on a PLGA hollow fibre in a HFB for seven days. Dark patches are methylene-blue-stained cells. Top section is from the outlet end of the fibre, middle section from the middle of the fibre and bottom section from the inlet end, with the flow going from right to left. From [70].

1.2 Mathematical modelling

As mentioned above, mathematical modelling of tissue engineering systems can lead to significant improvements in their design and operation. Different types of mathematical models, namely continuum, discrete and hybrid discrete-continuum models, can be used to describe tissue growth in bioreactors. Continuum models of tissue construct growth treat the cells, scaffold and culture medium as continua [49, 85, 192, 204, 229], while discrete models treat the cells (and sometimes also the scaffold and nutrients) as discrete entities [38, 90]. Hybrid models use a combination of discrete and continuum models for the tissue construct components and culture medium [39, 42, 283]. For a given bioreactor set-up, how appropriate it is to use each type of model varies according to the properties of the cell-scaffold construct and how these change in space and time. Continuum models have the advantage over discrete models that they can generally be expressed in terms of partial differential equation (PDE) systems that can be investigated analytically and/or numerically. However, they are only valid when the properties of the construct vary smoothly on a length scale much larger than that of a cell and for cell densities that are large enough to justify treatment as a continuum variable. This is often not the case during the initial growth phase of the tissue construct since the cell density in the scaffold is frequently low [29, 110, 124]. In such situations, a discrete cell-based model may be more suitable. Another potential drawback of continuum models is that subcellular and cellular processes are represented via macroscale constitutive terms rather than being described explicitly as in cell-based models. Thus it is difficult to establish how the behaviour of individual cells or groups of cells affects tissue growth using a continuum model, unless it is derived by spatially averaging a cell-based model.

Although cell-based models are often more appropriate for the initial stages of growth and can provide valuable insight into the effect of cell-level behaviour on the development

of the tissue construct, at a certain stage of cell proliferation—once the number of cells has become large ($\sim 10^6$)—it becomes computationally challenging to track all the cells in the construct [127]. At this point it may be appropriate to revert to a continuum tissue growth model, provided that the number of cells is large and the tissue properties are sufficiently homogeneous. However, switching between discrete and continuum descriptions requires knowledge of how to relate cell-level parameters to continuum ones and conditions determining when it is valid to use a continuum description [60, 127, 193].

In the rest of this section we review the literature on continuum, discrete and hybrid models of tissue growth in tissue engineering (for further reviews see [193, 228]), before describing the models that have been applied specifically to HFBs.

1.2.1 Continuum modelling

To date, most models of tissue growth in bioreactors have been continuum models. Such models can be broadly categorised as follows:

1. models of nutrient-limited tissue growth in *static culture systems*; and
2. models of *dynamic culture systems*, in which cells are either considered to be point sources/sinks in the nutrient/waste product fields and occupy no volume, or to occupy a finite volume and interact chemically and mechanically with the culture medium and scaffold.

Below we review examples of each type of model and discuss the insights they have yielded.

Models of static culture

The transport and consumption of nutrient and its effect on tissue growth in static culture have been described for the most part by 1D and 2D continuum models [66, 85–87, 150, 189]. In these models, nutrient diffusion and uptake have been described via reaction-diffusion equations, with different forms used for the nutrient consumption term (corresponding to different uptake kinetics [86, 189] and inclusion of dependence on the cell density [66, 150]). Cell proliferation has been modelled in a number of different ways. Galban and Locke [85], for example, modelled proliferation implicitly using a moving boundary approach, taking the boundary separating a region of scaffold occupied by cells from a void region to move at a rate proportional to the local concentration of a growth-rate-limiting nutrient. Based on the timescale for cell proliferation being much longer than that for nutrient diffusion in the scaffold, quasi-steady state assumptions were employed to simplify the reaction-diffusion equations governing the nutrient distribution. Linear uptake kinetics were used for the nutrient consumption in the cell region. The aim of this study was to explain

the experiments of Freed *et al.* [80, 81], in which the proliferation rate of chondrocytes seeded in highly porous polymer scaffolds and immersed in culture medium decreased with increasing scaffold thickness. Galban and Locke used their model to compare surface seeding with seeding in the centre of the scaffold by considering the two limiting cases of cells growing inwards from the scaffold periphery and growing outwards from the middle of the scaffold towards the source of nutrients. Although numerical simulations gave better agreement with Freed *et al.*'s results with the centre-seeding mode, the predictions of the model were generally inconsistent with the experimental findings, with good agreement only being obtained for scaffolds of intermediate thickness. In later work [86, 87], Galban and Locke assumed that tissue growth could occur at any position within the construct by treating the cells and culture medium as two distinct phases, and taking the cell volume fraction to increase with the local nutrient concentration. Incorporating heterogeneity in the cell population in this way significantly improved the agreement between their simulations and Freed *et al.*'s data. However, Galban and Locke's model ignored cell migration, which has been observed for primary chondrocytes on certain scaffolds [33, 100], and contact inhibition of growth (inhibition of cell division due to cell contact).

Dunn *et al.* [66] extended an earlier model for the growth of a cartilaginous tissue construct [150] to include contact inhibition by using a logistic growth law for the cell density, with a growth rate proportional to the nutrient concentration. Their model agreed closely with experiments which showed that the increase in cell density in a uniformly seeded scaffold after culture was restricted to a narrow region near the fluid-scaffold interface. Meanwhile Chung *et al.* [40] developed a two-phase model similar to that of Galban and Locke but with cell migration modelled as a diffusion-like process. Chung *et al.* observed that the inclusion of cell migration resulted in a higher overall growth rate and cell distributions that were generally more uniform, and that uniform cell seeding increased the density and uniformity of the final cell distribution by reducing competition for nutrients.

Models of dynamic culture

As discussed in §1.1.4, dynamic culture systems enhance nutrient and waste product transport to the cell-scaffold construct in the bioreactor using advection of the culture medium, and enable controlled application of fluid shear stress to the cells. Several computational models have been developed to simulate dynamic bioreactors [19, 43, 44, 139, 140, 216], perhaps most notably in the realm of computational fluid dynamics (CFD). Such models generally consider the full bioreactor and scaffold geometry and solve the Navier-Stokes equations for the fluid flow and reaction-advection-diffusion equations for nutrient transport. However the influence of cell proliferation on the flow and nutrient transport is often

neglected [193]. While they offer a high degree of spatial and temporal detail on fluid and nutrient distributions, such models generally incur a high computational cost. Here, therefore, we concentrate on approaches in which analytical techniques have been used to first simplify the governing equations so that they can be solved analytically or with less computationally intensive numerical methods. For reviews of computational models, we refer the reader to [114, 193, 228].

A prime example of the analytical reduction that can be achieved is the model of tissue construct growth in a rotating bioreactor developed by Cummings and Waters [49]. The authors simplified governing equations for fluid flow, nutrient transport and construct growth by exploiting the large aspect ratio of the bioreactor (its small depth relative to its radius) and the large separation in the timescales for the flow, nutrient transport and growth. This allowed the problem to be solved in separate stages: first the flow around the tissue construct was determined, then the motion of the construct in the bioreactor due to the flow, then the nutrient distribution around the construct, and finally the growth rate of the tissue construct. Nutrient was assumed to be supplied at a constant rate at the circular boundary of the bioreactor, transported through the bioreactor by a combination of advection and diffusion, and absorbed at the boundary of the tissue construct at a rate proportional to its concentration. Flow far from and near to rigid-body rotation was found to generate periodic construct orbits and orbits in which the construct drifted towards the edge of the bioreactor respectively. These flow regimes and construct trajectories were later validated experimentally [50]. A key finding of the modelling was that nutrient depletion zones which form around the construct when it remains in a state of free fall are removed when the construct trajectory is time-dependent. These findings are typical of the insight into improving bioreactor design and operation that asymptotically reduced models can provide.

Further examples of asymptotically reduced models include [271] and [272]. In [271], Waters *et al.* developed a single-phase model to explain differences observed in the morphology of suspended tissue constructs grown in different types of rotating bioreactor. As in [49], they exploited the small (or large) aspect ratios of the bioreactors to simplify the governing equations for the fluid flow. However, the effects of cell growth and proliferation were neglected. Whittaker *et al.* [272], meanwhile, investigated the effects of inserting porous hollow fibres into a cylindrical porous scaffold of the same material and porosity on the flow and nutrient transport in the scaffold. Fluid was pumped into the scaffold via an inlet pipe and/or the fibres, and allowed to leave the scaffold either via a specific outlet pipe or across the entire curved outer surface of the scaffold. Flow in the scaffold was modelled

using Darcy's Law, with point source and sink terms in the mass conservation equation representing the inlet and outlet and line sources representing the fibres. Lubrication theory was used to simplify the equations for the flow in the fibres, and the flow problem in the scaffold reduced to a Poisson problem for the fluid pressure and solved numerically. The flow solutions were then used to determine the shear stress, nutrient and waste product distributions in the bioreactor. The set-up with the curved surface of the scaffold as a distributed outlet was found to yield the most uniform flow distribution, but also the highest shear stresses.

Whilst these kinds of studies of dynamic culture systems can help to identify optimum bioreactor design and operating conditions for a given cell type, they typically focus on the timescales associated with transport processes and ignore the effect that cell population growth has on the fluid flow and scaffold permeability.

Multiphase modelling

A tissue construct in a bioreactor may comprise many different interacting constituents, including cells of different types, ECM, a scaffold and interstitial fluid. Multiphase modelling or mixture theory, in which each of the different constituents is treated as a separate phase, with its own time- and space-dependent volume fraction, offers a natural framework for investigating interactions between the different phases. The phases are treated as continua that occupy the same region of space, and interactions are described via mass and momentum transfer between the phases. Many different constitutive equations for the interphase forces can be used, and one of the main challenges is establishing the right constitutive assumptions to make [167].

Multiphase models have been widely used to investigate the effect of fluid flow and nutrient transport on tissue construct growth in dynamic culture systems. For example, Coletti *et al.* [46] and Causin and Sacco [31] considered how cell proliferation affects fluid and nutrient transport (through changes in scaffold porosity) and vice versa in perfusion bioreactors. In these models, the scaffold was treated as a rigid porous solid and the cells were assumed to be immobile. Fluid flow through the scaffold was modelled by the Brinkman equations, with the permeability of the scaffold taken to depend on the cell density (and hence on the cell proliferation). A reaction-advection-diffusion equation, with Michaelis-Menten uptake kinetics, described the evolution of the nutrient concentration, and nutrient-dependent cell proliferation was modelled using a Contois equation. Simulations of both models showed significant reductions in nutrient delivery to parts of the scaffold where the pore fraction decreased due to cell proliferation.

Chung *et al.* [41] incorporated cell migration into a similar model of fluid and nutrient transport and cell proliferation in a perfusion bioreactor using a linear diffusion term to describe movement of the cellular phase. Numerical simulations of the model showed that perfusion increased cell proliferation and spatial uniformity of the cell population. Shakeel *et al.* [229] extended this approach by describing density-dependent cell spreading via non-linear diffusion in their model of cell proliferation in a perfusion bioreactor. They assumed that cell proliferation and nutrient uptake in the scaffold depended on both the local nutrient concentration and fluid shear stress. They adapted a functional form proposed by O'Dea *et al.* [192] to describe elevated proliferation at intermediate shear stress levels, and used a similar function to describe an associated increase in nutrient uptake over the same shear stress range. Like Coletti *et al.* and Causin and Sacco, they included feedback from cell proliferation on the scaffold permeability, by modelling the decrease in scaffold porosity as cells proliferated and filled the scaffold voids. They investigated the influence of the scaffold porosity and initial seeding distribution on the final tissue construct composition, and found that adding high-porosity channels spanning the scaffold aided nutrient delivery to cells deep within the construct.

In the aforementioned studies, momentum transfer between phases was simplified by using the Darcy or Brinkman equations for the fluid flow. A more detailed consideration of the interphase interactions was given by Lemon *et al.* [145]. Their approach allowed for an arbitrary number of fluid phases and a solid phase for the porous scaffold and/or ECM, and provided general forms for the interphase interaction terms based on constitutive assumptions. They focussed on the case in which there are two fluid phases (one inviscid for the culture medium, the other viscous for the cells) and the scaffold is a rigid inert structure. The model was used to study proliferation, migration and aggregation in a population of motile cells seeded in an artificial scaffold. The cells formed aggregates or spread out until uniformly distributed throughout the scaffold depending on the relative strengths of the cell-cell and cell-scaffold drag forces. In a later paper [144], Lemon *et al.* extended the model to include a reaction-advection-diffusion equation for a generic nutrient and coupled this to cell proliferation to assess the impact of nutrient depletion on tissue growth. The patterns of growth associated with surface and bulk seeding were compared and analytical solutions were derived for the limits of high and low cell-scaffold drag. The effect of spatial variation in the scaffold porosity was also considered. With higher porosity near the scaffold edge there was more growth there than in the scaffold centre, due to the greater volume of free space available for the cells to grow into and depletion of the nutrient in the culture medium advected to the scaffold centre. O'Dea *et al.* [192, 195] used the same multiphase formulation to study the response of a perfused tissue construct to different mechanical

stimuli. The cell density, hydrostatic pressure and fluid shear stress on the cells were all shown to have a significant effect on the final construct composition.

Although multiphase modelling permits investigation of the interactions between different constituents of the tissue construct, it does not explicitly account for cell-cell and cell-environment interactions at the scale of individual cells. Instead, constitutive laws describe the effect of such cell-scale interactions on the macroscale. In order to explicitly describe cellular processes such as migration, proliferation, apoptosis and adhesion, it is necessary to use a discrete cell-based model. In the next section we review the two main types of cell-based models—on-lattice and off-lattice models—and discuss their advantages and disadvantages, and their use in modelling tissue growth.

1.2.2 Discrete modelling

On-lattice models

In on-lattice cell-based models, cells occupy sites in a regular fixed (square or hexagonal in 2D, cubic in 3D) lattice and have a predefined cell-cell interaction neighbourhood (the set of cells with which they interact). Square-lattice cellular automata (CA), the canonical type of on-lattice model, use the principle of mutual exclusion in space, *i.e.* that each grid site can be occupied by at most one cell. The interaction neighbourhood of each cell is typically defined as the four cells with which it shares an edge (the von Neumann neighbourhood), or the eight cells with which it shares an edge or a corner (the Moore neighbourhood). Cells move between lattice sites either according to deterministic rules, *e.g.* linking migration speed and direction to nutrient concentration, or as a random walk or a directed random walk, *e.g.* due to chemotaxis (movement up a nutrient concentration gradient) or haptotaxis (movement over the scaffold up a gradient of cellular adhesion sites). Cell division and death can be treated as stochastic processes and/or linked to detailed subcellular models of signalling pathways. In the field of cancer modelling, square-lattice CA have been used to simulate avascular [62, 73, 120, 286] and vascular tumour growth [197, 242], tumour cell invasion [10, 287], and tumour interactions with various environmental factors, such as nutrients and growth factors and ECM [15, 72, 89].

Cellular automata have also been used in the context of tissue engineering. Cheng *et al.* [38], for instance, used a 3D cubic-lattice CA model to investigate the effect of the competing processes of migration and contact inhibition on tissue growth. The scaffold was taken to be a uniform grid that allowed free movement of cells in all directions, and each cell was assumed to execute a persistent random walk until it collided with another cell or its division time (as measured by a division counter) elapsed. Once a cell's division counter reached zero, if at least one of the neighbouring sites was available the cell was split into two

daughter cells, one of which was left in the current site and the other of which was placed randomly in one of the available neighbouring sites. In simulations of the CA, Cheng *et al.* found that cell migration compensated for the limiting effect of contact inhibition on tissue growth, but to differing extents for different seeding distributions. For surface-seeded cells the tissue growth rate increased continually with increasing cell motility, whereas for bulk seeded cells the improvement in the growth rate plateaued at large migration speeds. However, the study neglected the effects of nutrient availability on cell proliferation and migration.

One issue with CA is that the rules governing cell movement, division and death can be difficult to relate directly to corresponding biological mechanisms. Cell growth and proliferation are particularly difficult to capture as each cell in the lattice has a fixed volume and shape, and when a cell divides a new cell of equal volume is instantaneously produced. In reality, a cell steadily increases in size until its volume has approximately doubled, at which point it divides in a finite time to produce two cells of equal volume.

Many of the issues associated with CA can be avoided by using a cellular Potts (or Glazier-Graner-Hogeweg) model [95], in which each cell occupies multiple square (or cubic, in 3D) lattice sites. Deformation in cell shape and cell-cell interactions are modelled by sampling lattice updates and using a global energy function, known as a Hamiltonian, to calculate the probability of accepting updates. Although the definition of the Hamiltonian allows a number of effects including cell-cell and cell-substrate adhesion to be described, it is unclear whether growing tissue should be modelled as energy conserving at the cellular level [180]. Cellular Potts models have been used to simulate various forms of tissue growth including angiogenesis and tumour invasion [218, 236, 258].

Off-lattice models

Off-lattice cell-based models provide a more realistic framework for modelling tissue growth than on-lattice models, as the cells are not required to occupy sites in a regular grid. There are two main types of off-lattice models: cell-centre models and cell-vertex models. In cell-centre models, the locations of the cells are determined by their centres, which move in response to the net forces exerted on them by neighbouring cells and any substrate to which they are attached. In cell-vertex models, the cells are modelled as polygons, whose size and shape evolve due to movement of their vertices. This movement is typically governed by deterministic equations of motion.

Cell-centre models require definitions of cell-connectivity (*i.e.* which cells are in contact with each other) and the cell-cell interaction force (the force between two neighbouring cells). In 2D, cell-connectivity is usually determined either by the overlapping spheres

method, in which two cells interact if their centres are within a certain distance, or a Voronoi tessellation method, in which neighbours are determined through a Delaunay triangulation of the domain with the cell centres as nodes. The cell-cell interaction force depends on the positions of the cell-centres and can take a variety of different forms, from a simple linear spring force to more complex nonlinear expressions that include cell-cell and cell-substrate adhesion [200]. Cell proliferation can be incorporated in spring-based cell-centre models by, for instance, making the cells divide after a prescribed time and placing the daughter cell close to the mother cell in a randomly chosen direction [263]. Cell growth is modelled implicitly in this way by the relaxation of the springs connecting the mother and daughter cell from compression after the division event [181].

In cell-vertex models the equations of motion for the vertices are typically derived by balancing the viscous drag on the vertices from the surrounding medium with the gradient of a free energy function, which is assumed to exert a force on each vertex [77, 196]. Contributions from cell-deformation, membrane surface tension and cell adhesion can be included in the free energy to ensure that the cells attain their target area and shape and conserve their membrane length. Cell division can be implemented by splitting cells in two along their short axis at the end of the cell cycle, halving the target area of the daughter cells and allowing it to gradually increase to its original value [196].

Geris *et al.* [90] used an overlapping spheres cell-centre model to investigate cell aggregate behaviour for bone tissue engineering applications. Their model incorporated cell-cell and cell-environment interactions such as adhesion, repulsion and drag. Oxygen, glucose, lactate and a growth factor and inhibitor were represented in the model as clusters of diffusing particles, which could be absorbed by cells. A subcellular model for cell metabolism including the essential reactions of glycolysis and the Krebs cycle and an explicit model for the cell cycle were included. Cell growth and proliferation were governed by the availability of different metabolites, the space free for division and the cellular mechanical stress. Various types of cell death—necrosis, apoptosis and anoikis (programmed cell death due to detachment from surrounding ECM)—were implemented in the model according to the stress levels and the levels of nutrients, waste products and growth factors in the culture medium. The difference in the growth of the aggregate under normoxic and hypoxic conditions was compared, and necrosis in the aggregate centre observed in low oxygen conditions.

Although cell-based models allow investigation of the effect of cellular processes on tissue development, as mentioned earlier simulations of cell-based models with large numbers of cells generally have a far greater computational cost than the numerical solution of continuum PDE models. Off-lattice models are particularly computationally intensive due to the difficulty of handling the information on the cell-connectivity.

1.2.3 Hybrid modelling

Various definitions of hybrid modelling exist in the literature [9, 154, 270], but all hybrid models of tissue growth combine some form of discrete and continuum descriptions in a single model. We follow [60] and separate hybrid models into composite hybrid models (CHMs), in which cell-based models are coupled to continuum fields for chemicals and mechanics; and adaptive hybrid models (AHMs), in which discrete and continuum descriptions of the tissue are used in different regions of space and at different times. In the following, we focus on CHMs, but note that adaptive hybrid models have been used to model avascular and vascular tumour growth [84, 127, 154, 245, 274].

CHMs can be subdivided according to the type of cell-based model they use: on-lattice or off-lattice models. Cellular automata are often used in CHMs, since a refined version of the underlying grid for the cell locations can be used as the lattice for discretising the continuum chemical and mechanical fields. The rules governing the movement and proliferation of cells are also relatively straightforward to implement on a regular lattice. However, a major disadvantage of hybrid cellular automata is that the discretisation of the tissue into a regular lattice of cells can introduce artifacts in the simulations [180]. For instance, the distribution of cells will be skewed differently depending on whether von Neumann or Moore interaction neighbourhoods are chosen [180]. It is also difficult to represent cell division accurately within the constraints of a fixed lattice, as in standard CA.

Hybrid CA models have been used extensively to model tumour growth [4, 5, 62, 91, 118, 239]. Early models coupled CA with reaction-diffusion equations for nutrients such as oxygen and glucose [118, 239], while more recent models have incorporated blood flow and vascular remodelling [170, 197] and descriptions of subcellular processes like cell cycle progression and protein expression [4, 236]. The application of CHMs to tissue engineering has been more limited, but there are some notable examples. Cheng *et al.* [39] used a CHM to study how tissue growth in a 3D scaffold in a spinner flask bioreactor is affected by nutrient transport. Their model consisted of a CA describing cell migration and proliferation coupled to an advection-diffusion equation for the nutrient concentration, with Michaelis-Menten uptake kinetics in lattice sites occupied by cells and zero uptake in unoccupied sites. The division rate and migration speed of each cell were assumed to increase with the nutrient concentration at the lattice site of the cell. Cheng *et al.* used their model to assess the influence of the initial seeding distribution, cell migration speed and scaffold size on the rate and pattern of tissue growth. Their results suggested that tissue growth is enhanced if the initial seeding distribution is uniform and that increased cell migration speed can compensate for contact inhibition to a greater extent for surface-seeded cells than for bulk-seeded cells. Chung *et al.* [42] developed a similar CHM to investigate the effect of nutrient

limitations on the growth of a cartilaginous tissue construct. They argued that increased cell migration speed enhanced tissue growth for bulk-seeded cells only in the initial stages, as at slow migration speeds local aggregation of cells allowed continued nutrient delivery to the scaffold centre, while at high migration speeds nutrient delivery was blocked by cells moving to the scaffold periphery and proliferating there.

CHMs have also been employed to study the effect of scaffold material properties and fluid flow on the development of a tissue construct. Zahedmanesh and Lally [283] modelled vascular smooth muscle cells growing in a perfused tubular scaffold using an overlapping spheres cell-centre model and a poro-elastic finite element model for the pore fluid velocity and cyclic strain fields. The division time of the cells was defined to be an increasing function of the strain and a decreasing function of the fluid velocity in each element. To account for remodelling due to tissue growth, the geometry and boundary conditions for the poro-elastic component were updated at each time step. The results demonstrated that low scaffold compliance contributes to growth of cells into the lumen of the blood vessel construct, but pulsatile flow reduces ingrowth and promotes collagen synthesis.

Composite hybrid models allow detailed modelling of dynamics at the cell-scale to be coupled to the macroscale chemical and mechanical environment. However, the use of a cell-based model for the whole cell population means that CHMs are often computationally expensive for large cell numbers. Adaptive hybrid models represent a potential solution to this problem, by allowing the discrete and continuum representations of the tissue to be chosen dynamically and adaptively (*e.g.* according to the local cell density or proliferation rate). Nevertheless, there are several issues that must be addressed to implement an AHM. In particular, it is necessary to know how to relate parameters at the cell-level to those at the tissue-level in order to couple the discrete and continuum descriptions, and conditions are needed to determine when and where it is valid to use each description. One approach that could resolve these issues, and the computational cost of simulating CHMs, is to rigorously derive continuum approximations of cell-based models that can be used in place of the cell-based models under certain conditions. We now review the approaches taken in the literature to do this that are relevant to the work in Chapter 4 of this thesis.

1.2.4 Deriving continuum approximations of cell-based models

A number of authors have derived continuum approximations of either deterministic [18, 78, 181] or stochastic [6, 64, 158, 238, 259] cell-based models in 1D and 2D (see [78] for a review). Whilst the approach taken and the continuum model obtained have depended on the particular discrete model used, a common feature of the continuum approximations is that they can be expressed in terms of nonlinear diffusion equations for the cell number

density. Here we focus on the work of Murray *et al.* [181] and Fozard *et al.* [78] on deriving continuum limits of 1D deterministic cell-based models.

Murray *et al.* [181] considered a 1D off-lattice cell-centre model with a line of cells connected by linear springs (Figure 1.6(a)). By balancing the drag forces on the cells from the surrounding medium with the cell interaction forces and taking the continuum limit of the discrete model equations for a large number of cells, they derived a nonlinear diffusion equation for the cell density. They modelled cell proliferation in the discrete model by dividing cells symmetrically in two once they reached a certain age, and showed that cell proliferation could be included in the continuum model via an appropriate source term in the nonlinear diffusion equation. Simulations of the continuum model and discrete model with 700 cells showed excellent agreement in the cell density distribution and the authors demonstrated that, in the limit of incompressible cells, cell velocity is directly related to cell production as is commonly assumed in continuum modelling of tumour growth. In a later paper [182], Murray *et al.* considered nonlinear cell interaction force laws and showed that they give rise to different nonlinear diffusion coefficients in the cell density diffusion equation.

Fozard *et al.* [78] investigated how the behaviour of a 1D cell-vertex model (Figure 1.6(b)) of adherent epithelial cells can be approximated by a continuum model in the limit of a large number of cells. The cells were taken to have viscoelastic properties and experience drag from the underlying substrate. Differential-algebraic equations for the motion of the cells were derived from energy considerations using a Hamiltonian formulation, and cell growth modelled via a linear increase in the cell resting lengths with time. Cell proliferation, however, was not included in the model. A continuum approximation of the discrete system was obtained for cell parameters varying slowly in space by replacing the finite differences in the governing equations with derivatives. A continuum approximation was also derived for the case of heterogeneous spatially-periodic cell parameters, *i.e.* parameters that vary substantially between adjacent cells, via homogenisation. For a total cell number N, the errors in the continuum approximations were $\mathcal{O}(1/N^2)$ and $\mathcal{O}(1/N)$ for the cases of slowly-varying and spatially-periodic parameters respectively, suggesting that the continuum approximation could be used for slowly-varying parameters for relatively modest values of N. Fozard *et al.* used the model to study the expansion of a cell aggregate due to cell growth, and its behaviour in the limits of slow growth and long time. Numerical solutions for discrete and continuum cell pressures and vertex velocities were in close agreement for $N = 20$ for uniform cell parameters, and reasonable agreement for N as low as 8 for heterogeneous parameters. Fozard *et al.* were also able to provide a mechanistic

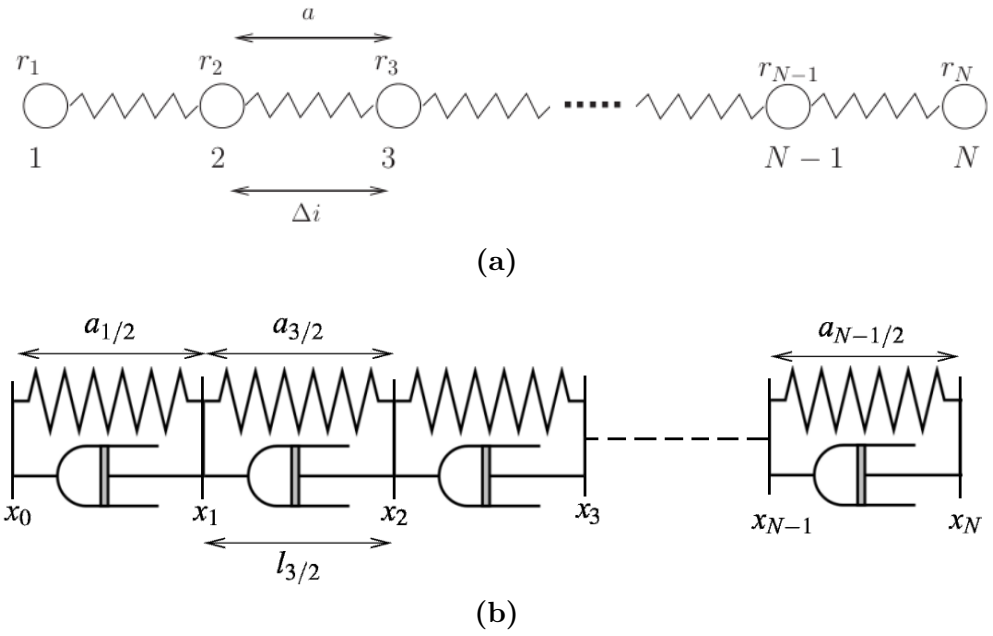

Figure 1.6: Schematics of (a) Murray *et al.*'s 1D linear spring cell-centre model (adapted from [181]) and (b) Fozard *et al.*'s 1D viscoelastic cell-vertex model [78]. In (a) r_i $(i = 1, \ldots, N)$ denote the positions of the cell centres with labelling indices i, Δi denotes the distance between cells along the indexing coordinate, and a denotes the resting length of the springs. The system is in equilibrium since $\Delta i = a$. In (b) x_n $(n = 0, \ldots, N)$ denote the positions of the cell vertices, $l_{n+1/2}$ the cell lengths, and $a_{n+1/2}$ the resting cell lengths. Each cell is represented by a linear spring and dashpot connected in parallel. Again, the system is shown in equilibrium with $l_{n+1/2} = a_{n+1/2}$.

explanation for the acceleration of the leading edge observed in wound healing assays with the model.

Further details of Murray *et al.*'s and Fozard *et al.*'s models and their approaches to deriving continuum approximations are given in Chapter 4 and Appendix E.

1.2.5 Hollow fibre bioreactor modelling

Models of fluid and nutrient transport

Numerous theoretical studies of fluid and solute transport in HFBs have been carried out with the aim of improving their design and operation for cell culture [231]. Typically these studies have focussed on the timescales associated with fluid and solute transport rather than the longer timescale associated with cell proliferation. As such, they have neglected the effects of cell proliferation on the flow and solute transport in the bioreactor. Solute transport has generally been studied by overlaying mass transport models on models for the fluid transport through a representative subunit of the bioreactor known as the Krogh cylinder [22]. Each Krogh cylinder consists of a single fibre surrounded by a uniform annulus

of ECS that contains a homogeneous distribution of cells, and the annuli of neighbouring Krogh cylinders are assumed to be touching. There are several issues with this approach, including that it ignores the interstitial spaces between the Krogh cylinders, any non-uniform spacing of the fibres in the bundle and probable coupling between the flows in adjacent fibres [22]. Most studies have described the fluid and mass transport in the fibre lumen using the Stokes equations and advection-diffusion equations respectively, but have ignored convective effects in the membrane and ECS and assumed that the mass transport in these regions is diffusion-dominated. This is representative of the single-fibre set-up with the ECS ports closed.

Oxygen is generally considered to be the rate-limiting nutrient for growth of the cell population [231, 246] and its transport and consumption has been the most widely modelled [55, 201, 204, 208, 226, 234, 248], though glucose [3, 54, 280] and protein transport [133, 134, 235] have also been considered. In contrast, the transport of lactate, a waste product of cell metabolism that is toxic to cells at high concentrations, has only recently been modelled [231]. For cells seeded in gel throughout the ECS, nutrient uptake has been described via a reaction term in the ECS mass transport equation, which has followed zeroth-order, first order or full nonlinear Michaelis-Menten kinetics depending on the nutrient demands of the cells. Where the uptake kinetics have been approximated as zeroth- or first-order, analytical approaches have been employed to solve the nutrient transport equations [116, 126, 208, 234]. Where full nonlinear uptake kinetics have been used, the transport equations have been solved numerically, with finite difference [206] or finite element [54–56, 247, 248, 280] schemes. Below we review in more detail the different models of fluid and mass transport and cell population growth in HFBs that have been developed.

The work in Chapter 2 of this thesis builds largely upon the studies of fluid and solute transport in HFBs of Shipley and co-workers [231, 233, 234]. In [233], the authors developed a model for fluid transport in a single-fibre HFB with no cells in the ECS, using Navier-Stokes equations to describe the flow in the lumen and ECS, and Darcy's Law for the flow through the membrane. Exploiting the small aspect ratio of the bioreactor, the authors used lubrication theory to simplify the governing equations and derive expressions for the retentate and permeate flow rates in terms of the lumen inlet flow rate, lumen radius, fibre length, and membrane thickness and permeability. By comparing these with experimental measurements of the retentate and permeate masses over time, they determined a value for the membrane permeability. This enabled the derivation of an operating equation for specifying the permeate to lumen inlet flow rate ratio by varying the inlet flow rate and retentate pressure (and fibre geometrical parameters if necessary). Next, in [234], a Krogh cylinder model for the oxygen transport through the bioreactor with Poiseuille flow in

the lumen was developed. Oxygen uptake by the cells was described via zeroth-order or Michaelis-Menten kinetics, according to the validity of approximating the uptake as constant for the cell type in question, and the transport equations solved analytically or numerically respectively. The model was used to define operating equations for determining the inlet flow rate, lumen length and ECS depth necessary to maintain the oxygen concentration above a cell-specific minimum. In [231], Shipley and Waters modelled the fluid flow, and oxygen and lactate transport in the bioreactor with cells seeded in gel throughout the ECS. They considered the ECS ports to be either closed or open, and described the flow and mass transport in the membrane and cell-packed ECS using Darcy's Law and reaction-advection-diffusion equations respectively. They used the model to define conditions on the bioreactor geometry (the lumen length and ECS depth) and operating parameters (the inlet flow rate, outlet pressure and cell seeding density) that would ensure sufficient oxygen delivery and lactate removal with the ports either open or closed. In this way, they were able to demonstrate that opening the ECS ports to enhance the radial flow, and therefore the oxygen and lactate transport, through the ECS enabled a much larger cell population to be cultured within the bioreactor. Growth of the cell population and its effect on the ECS permeability were, however, not considered.

Krogh cylinder models have also been used to inform the design and operation of HFBs as bioartificial liver devices (BALs) [55, 56, 104, 106, 201, 247, 248] and for engineering 3D bone tissue [3, 280]. Davidson *et al.* [55] used a Krogh cylinder model of oxygen transport in a BAL to determine the range in the number of fibres that can be used to culture a hepatocyte population of a certain size without the cells being exposed to hypoxic conditions. The dependence of the range on different parameters, such as the lumen radius, fibre length, flow rate, cell number and membrane thickness, was investigated, and narrower lumens, shorter fibres, higher flow rates and thinner membranes found to give larger operating regions for non-hypoxic culture of the hepatocyte population. In a later paper [56], Davidson *et al.* extended their investigation to consider other parameters, such as the inlet oxygen concentration and oxygen uptake rate, and determined the operating conditions necessary to replicate the zones of different oxygen concentration found in the liver *in vivo* (a phenomenon known as liver zonation).

Ye *et al.* [280] modelled glucose and oxygen transport in a multi-fibre HFB used for engineering 3D bone tissue with cells seeded throughout the entire ECS. They observed that at high cell densities glucose depletion was more significant than oxygen depletion for short fibre lengths (3 cm), but that oxygen depletion was more significant for longer fibres. They also demonstrated that increasing the thickness of the cellular matrix led to a greater radial drop in the glucose and oxygen concentrations, and that higher lumen flow

rates helped to sustain greater glucose and oxygen concentrations throughout the cellular matrix. Abdullah *et al.* [3] built on this work by comparing the suitability of the multi-fibre HFB for growing bone tissue with that of two other bioreactors: a suspended tube bioreactor and a confined perfusion bioreactor. Glucose was assumed to be the limiting nutrient for cell viability and the governing equations for the flow and glucose transport were solved using the finite element method. Using the glucose concentration profiles within the different bioreactors as proxies for cell viability, the HFB was found to offer the best conditions (*i.e.* highest glucose concentrations) for culturing cells at the high densities required for bone tissue.

In a recent study by De Napoli *et al.* [58], a Krogh cylinder model of glucose and oxygen transport in a multi-fibre HFB with a cell-seeded ECS and closed ECS ports was used to perform a detailed numerical investigation of the effect of various operating conditions and design parameters on the nutrient environment of the cells. Charts were obtained showing the non-hypoxic ECS regions and regions receiving sufficient glucose as a function of the main dimensionless parameter groupings affecting the flow and solute transport. Parameter variations that increased the magnitude of recirculating flows were found to significantly enhance cell oxygenation and glucose availability. The study was designed to help tissue engineers optimise cell culture in the bioreactor, either for specific therapeutic applications or to recreate physiological nutrient conditions *in vitro*.

Multiscale and multiphase models

Other modelling approaches have been employed to describe cell culture in HFBs. Das [54], for example, adopted a multiscale approach to modelling bone cell culture in the multi-fibre HFB to take account of the processes affecting nutrient transport from the cellular scale to the bioreactor scale. A computational framework was developed in which individual cells in the ECS and their nutrient uptake were modelled, and the framework used to determine the effects of the inlet glucose concentration, inlet fluid velocity, and cell size and density on the glucose concentration profiles in the bioreactor. The multiscale approach was also compared with the standard Krogh cylinder model and found to predict different glucose concentration profiles—with transport limitations occurring both radially and axially as opposed to just radially.

Recently, multiphase models of fluid flow, nutrient transport and cell proliferation in the single-fibre HFB have been developed by Pearson *et al.* [204, 205], building on the work of Lemon *et al.* [145] and O'Dea *et al.* [192] described above. In [204], a 2D model of the HFB with cells seeded in collagen gel throughout the ECS was developed, and a multiphase description used to track the dynamics of each phase (the cells, culture medium and collagen

scaffold), and the solute concentration, in the ECS. The small aspect ratio of the bioreactor was exploited to reduce the governing equations to a much simpler system that was then solved numerically. Different case studies corresponding to different experimental scenarios and cell types were considered, including nutrient-driven cell proliferation, chemotaxis and a prescribed ECS flow opposing that in the lumen. For each case, the influence of the inlet flow rate on the cell yield and distribution was determined, and optimal flow rates for achieving a spatially uniform cell population predicted. The model was also used to determine whether a sufficient nutrient supply was maintained for the entire cell population. A variety of different steady state cell distributions were predicted, with both upstream and downstream bunching of the cells in the ECS, but in nearly all cases it was possible to choose a flow rate such that the cell distribution was highly uniform and the cells received sufficient nutrient. Furthermore, the maximum cell yield was found to correlate well with the minimum spatial variation in the cell distribution, suggesting that uniform cell populations can be achieved without compromising cell yield. In [205], the authors considered a different experimental set-up with a cell layer of constant depth filling part of the ECS and culture medium pumped into the bioreactor through the upstream ECS port as well as the lumen inlet. They modelled the cell layer as a three-phase mixture of cells, culture medium and scaffold as before, with cell proliferation captured via a source term in the cell mass conservation equation. The effects of altering the flow rate into the ECS port and the cell layer depth on the cell yield for different forms of shear-stress-dependent growth (either enhanced or limited by increasing shear stress) were investigated. The authors found that thinner cell layers could withstand higher flow rates before the cell yield was compromised, since cells in thinner layers experienced lower shear stresses for a given flow rate. As far as we are aware, this is the only study other than our own to consider the effect of shear stress on cell proliferation in the single-fibre HFB.

Mohebbi-Kalhori *et al.* [177] used a sophisticated CFD approach to solve a multiphase model of fluid flow and oxygen and glucose transport in a HFB containing a hexagonal array of 200 hollow fibres around which bone marrow cells were seeded in a gel matrix. Cell proliferation and migration were modelled respectively via a nutrient-dependent source term and linear diffusion term in the ECS cell mass conservation equation. The influence of a number of key parameters on long-term tissue growth, including the inter-fibre spacing (usually neglected in Krogh cylinder models as described above), membrane thickness and bioreactor length, were studied. The inter-fibre spacing was found to have little effect on the mean cell volume fraction in the short term, but greater fibre spacings resulted in much larger cell volume fractions in the long term. In agreement with the work of Ye *et al.* [280], decreasing the membrane thickness and fibre length allowed higher nutrient levels to be

sustained, enhancing the growth of the cell population. Predictions of the mean cell volume fraction and oxygen concentration were validated against experimental measurements from Ye *et al.'s* [281] study of rat bone marrow cell growth in a HFB and found to be in close agreement.

Despite the insights into optimising HFB cell culture provided by the models described above, further research is required to elucidate the interactions of the cell distribution, fluid flow and solute transport, and their effects on cell proliferation. In particular, none of the above studies have investigated the influence of the initial seeding distribution on the growth of the cell population in the ECS. Whilst opening the ECS ports and increasing the lumen inlet flow rate and outlet pressure have been found to enhance solute transport through the single-fibre HFB, the potentially adverse effects on cell survival of the resulting higher ECS fluid shear stresses have not been accounted for. These issues motivate the development of the models in this thesis, which we outline below.

1.3 Thesis outline

In this thesis we develop models of fluid flow, solute transport and cell population expansion in the single-fibre HFB shown in Figure 1.3(a) and test the suitability of a discrete-to-continuum modelling framework for describing nutrient-dependent cell aggregate growth in the HFB. Since the focus of our work is on cell population expansion, we consider cells being seeded onto the surface of the fibre rather than embedded in gel throughout the ECS. Each of the models we develop considers the effects of cell growth and proliferation on the overall population expansion at a different spatial scale, from the population scale to the cell scale. Each model is thus appropriate to a different stage of cell population expansion. Although the models we formulate for solute transport in the HFB are applicable to a generic nutrient or waste product, we focus on oxygen and lactate as potentially growth-rate-limiting solutes. Since the experimental data needed to validate our models is not yet available, we have instead focussed on determining the range of growth behaviour possible under different flow configurations, operating conditions and initial cell distributions, and for different cell types.

In Chapter 2, we develop an axisymmetric 3D model for the growth of the cell layer formed in the HFB by cells proliferating into the ECS after reaching confluence over the fibre surface. The net rate of cell proliferation, and therefore of growth (or recession) of the cell layer, is assumed to depend on the local oxygen and lactate concentrations and fluid shear stress on the cells. The model is used to predict the effects of varying the lumen inlet flow rate and the pressure imposed at the lumen outlet on the growth of the cell layer for different cell types. We also compare two flow configurations—one in which both ECS ports

are open and one in which both are closed—and investigate the impact of the uniformity of the initial cell layer on the growth. We are thus able to predict the flow configuration and parameters that maximise the cell yield in a given time frame.

In Chapter 3, we consider the initial stages of cell culture in the HFB, shortly after cell seeding and attachment, when the cells are attached to the outer surface of the fibre in aggregates. We consider a different flow configuration from Chapter 2, with the upstream ECS port closed and the downstream port open, and model the flow, oxygen transport and cell aggregate growth in a 2D cross-section of the bioreactor. The growth rate of the aggregates is assumed to depend on the local oxygen concentration and fluid shear stress on the cells due to the ECS flow. We use the model to investigate how the lumen inlet flow rate and outlet pressure affect the growth of the aggregates, and to predict optimal conditions for growth of the aggregates to confluence over the fibre surface. We also investigate the potential combined effects of the cell seeding and flow conditions on the rate of cell aggregate growth by simulating the growth for different initial aggregate distributions and lumen outlet pressures.

To test whether the discrete-to-continuum framework of Fozard *et al.* described in §1.2.4 could be used to model cell aggregate growth in the HFB, we develop a hybrid discrete-continuum model of nutrient-dependent cell aggregate growth using this framework in Chapter 4. To facilitate our investigation we consider a simple static culture set-up with a single aggregate of cells (modelled via linear springs) growing along the base of a nutrient bath. Equations for the diffusion of the nutrient and its uptake by the cells are coupled to the discrete cell model, and a continuum approximation of this model derived in the limit of a large number of cells. The discrete cell model allows greater biomechanical detail to be incorporated into the cell aggregate growth than in the model of Chapter 3—the growth is assumed to depend both on the local nutrient concentration and the degree of extension/compression of the cells. The aim of deriving the continuum limit is to determine if the discrete cell model coupled to the nutrient transport can be closely approximated by a continuum description that is more straightforward to analyse and less computationally expensive to solve for large cell numbers. It also enables us to assess the validity of the continuum description for the cell aggregate growth rate used in Chapter 3. We test the agreement between the discrete cell model and continuum approximation by comparing simulations of the cell aggregate growth with each model over a range of parameter values and initial cell distributions. We also compare our model to those of Murray *et al.* and Fozard *et al.*, and show the equivalence of their approaches to deriving the continuum limit of the discrete model. We conclude this chapter by discussing the further work that is needed to use the discrete-to-continuum framework to model cell aggregate growth in the HFB.

In Chapter 5 we summarise the key results of the thesis and discuss ideas for future work that would extend the models developed in Chapters 2–4.

1.4 Novel contributions

As described in §1.2.5, the majority of previous modelling studies of cell culture in HFBs have not considered cell population growth or its effect on fluid flow and nutrient distribution in the bioreactor. In addition, only one previous study has considered the effect of fluid shear stress on cell proliferation in the single-fibre HFB [205]. The approaches used to model cell population expansion in the single-fibre HFB in Chapters 2 and 3 are novel in these respects. The model in Chapter 3 is also the first theoretical study of the influence of cell seeding distribution on cell population expansion in HFBs. This work has been published in *PLoS ONE* [34]. The work in Chapter 4 extends the study of Fozard *et al.* [78] by coupling their discrete-to-continuum framework to a continuum model for external nutrient transport, and demonstrating that close agreement is maintained between the continuum approximation and the discrete model. In addition, we are the first to show the equivalence of Fozard *et al.*'s and Murray *et al.*'s approaches to deriving the continuum limit of discrete 1D cell models.

Chapter 2

Cell layer growth in the hollow fibre bioreactor

2.1 Introduction

In this chapter, we develop a model of cell layer growth in a single-fibre HFB by extending the model of Shipley and Waters [231] described in Chapter 1. Rather than assuming that the ECS is completely filled with cells as in [231], we consider a different set-up in which the cells form a distinct layer on the outer surface of the fibre and culture medium is able to flow freely through the rest of the ECS (see Figure 2.1). The cell layer is assumed to grow outwards into the ECS (or recede towards the fibre surface) as a result of net cell proliferation (or death), depending on the oxygen and lactate concentrations and the fluid shear stress experienced by the cells. Instead of considering the timescale of transport processes as in [231], we consider the longer timescale of cell proliferation. The model we present is therefore more relevant to cell expansion experiments.

We consider two different flow configurations as in [231], with the ECS ports either open or closed. In both cases, culture medium is pumped into the bioreactor at the lumen inlet at a prescribed flow rate. With the ECS ports open, the flow through the membrane is controlled by the pressure imposed at the lumen outlet. We consider the same order of magnitude of flow rates as Shipley and Waters, for which the fluid and solute transport are quasi-steady on the timescale of cell proliferation and there is a balance between the axial advection and radial diffusion of the solutes with the ECS ports open.

Opening the ECS ports increases the radial flow through the bioreactor, which can be further enhanced by increasing the lumen inlet flow rate and outlet pressure. This increases oxygen delivery to, and lactate removal from, the cells, which has a positive effect on the growth of the cell layer. However, the greater radial flow also exposes the cells to higher shear stress, which can lead to cell death and detachment of cells from the layer. For any given cell type, it is therefore necessary to determine whether opening the ECS ports will

improve growth, and if so what inlet flow rate and outlet pressure will maximise growth (enable the cell layer to grow to the maximum possible depth) over a long culture period (here taken to be 60 days). Hence we use the model to determine the effect of opening the ECS ports and varying the inlet flow rate and outlet pressure on the cell layer growth for different cell types (using cell-type-specific data taken from the literature).

2.1.1 Chapter outline

The overall purpose of this chapter is to investigate how optimal operating conditions (*i.e.* flow configuration and flow parameters) for expanding cell layers in the single-fibre HFB vary for cell types with different oxygen requirements and shear stress tolerances. For most of this chapter we discuss the case when the ECS ports are open, and summarise the key differences in the flow, solute transport and growth when the ECS ports are closed in §2.9. We begin by describing the model set-up in §2.2 and giving the governing equations for the fluid flow, oxygen and lactate transport and cell layer growth in §2.3. In §2.4 we nondimensionalise the governing equations and then use lubrication theory to simplify them. Details of the parameter values used in the model are given in §2.5 followed by a description of how the reduced model is solved in §2.6. In §2.7, we compare the flow profiles and oxygen and lactate distributions in the bioreactor for cell layers of uniform and non-uniform depths. Results of numerical simulations for different cell types are compared in §2.8, including results for the variation in growth with the lumen inlet flow rate and outlet pressure. In §2.10 we summarise our key findings and conclude by discussing possible extensions to the model. The work in this chapter provides new insight into optimising HFB culture conditions for a dynamic cell population, by accounting, unlike most existing models, for changes in the fluid and oxygen transport in the bioreactor with cell proliferation. It also highlights the potential effects of shear stress on the growth of the cell population in the HFB, which nearly all HFB models to-date have neglected.

2.2 Model set-up

Figure 2.1(a) shows a schematic of the single-fibre HFB with a cell layer surrounding the fibre. It is assumed that cells originally seeded on the outer surface of the fibre have proliferated to confluence over the surface and then outwards from the surface, so that the cell layer is several cells deep at the point from which we model the growth.

We assume that the lumen is cylindrical with radius R_l and that the fibre, cell layer and ECS are all annular in cross-section, with outer radii R_m, R_c and R_e respectively. For simplicity, we view the flow and solute distributions as symmetric about the lumen axis. We can therefore describe the system using axisymmetric cylindrical polar coordinates (r, z)

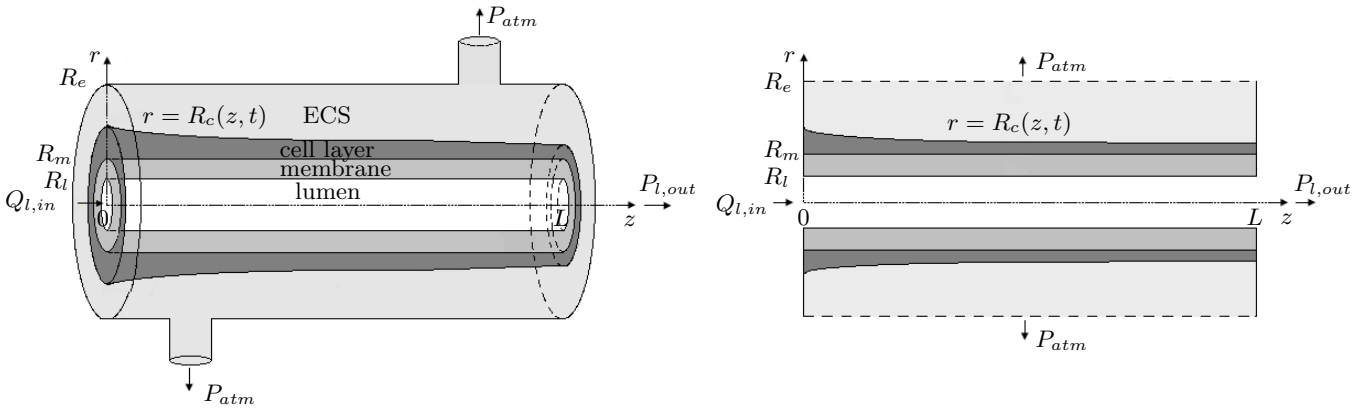

Figure 2.1: (a) Schematic of the single-fibre HFB module with a cell layer on the outer surface of the fibre and open ECS ports. (b) 2D cross-section of the model set-up showing the distributed ECS port. Arrows show the direction of fluid flow into the lumen and out of the lumen outlet and ECS port(s). Notation as described in main text.

(*i.e.* neglect any azimuthal-dependence), where r is the radial distance from the lumen axis and z is the distance along the lumen axis from the inlet at $z = 0$ to the outlet at $z = L$ (Figure 2.1(b)). The corresponding unit vectors in the r- and z-directions are denoted by $\mathbf{e}_r$ and $\mathbf{e}_z$. The radial position of the outer surface of the cell layer is assumed to vary with axial position and time, so that $R_c = R_c(z,t)$. Typically $L \approx 10\,\text{cm}$, $R_l \approx 100$–$200\,\mu\text{m}$, $(R_m - R_l) \approx 200$–$400\,\mu\text{m}$ and $R_e \approx 1\,\text{mm}$. The aspect ratio of the fibre lumen, ϵ, is therefore very small

$$\epsilon = \frac{R_l}{L} \approx 2 \times 10^{-3} \ll 1, \tag{2.1}$$

as are those of the membrane, cell layer and ECS.

We denote the flow rate at which culture medium is pumped into the lumen inlet by $Q_{l,in}$ and the pressure imposed at the lumen outlet by $P_{l,out}$. We treat the outer wall of the ECS as a distributed port following Shipley *et al.* [231, 233] (see [202] for a consideration of the effect of the positions of the ECS ports on the fluid flow and solute transport). With the port open, fluid leaving the port is at atmospheric pressure, P_{atm}, and the ratio of the amounts of fluid passing through the ECS and down the fibre lumen is controlled by $P_{l,out}$. With the port closed there is no flow or flux of solute out of the ECS outer boundary.

Oxygen enters the system at constant concentration C_{in} via the culture medium pumped into the lumen inlet, is transported through the bioreactor by a combination of advection and diffusion, and is consumed by the cells in the cell layer. Lactate is produced by the

cells in the cell layer as a by-product of respiration and transported out of the system by advection and diffusion. While high oxygen levels promote proliferation, lactate is toxic to cells, and so causes cell death, above a certain concentration.

Cell proliferation and death are assumed to be localised to the outer surface of the cell layer due respectively to contact inhibition (which is appropriate for the cell types we consider, see §2.3.3) and higher oxygen and lower lactate levels in the bulk of the cell layer. The rates of proliferation and death are assumed to depend on the oxygen and lactate concentrations and interstitial fluid shear stress at the outer surface. Hence we model the growth of the cell layer by prescribing the rate of evolution of its outer surface $r = R_c(z,t)$ as a function of the local oxygen and lactate concentrations and shear stress. As the cell layer grows or recedes, the flow, oxygen uptake and lactate production change, and this in turn affects the growth.

2.3 Governing equations

2.3.1 Fluid transport

We denote the fluid velocity and pressure by $\mathbf{u}$ and p, and the lumen, membrane, cell layer and ECS with subscripts l, m, c and e. We assume that the culture medium is an incompressible Newtonian fluid of constant viscosity. In the lumen and ECS, viscous forces in the fluid dominate inertial forces since the aspect ratio of each region is very small (see §2.5.1), and the flow can be assumed to be quasi-steady on the timescale of cell layer growth since this is much longer than the timescale for advection (see §2.5.3). Hence the flow can be modelled as steady incompressible Stokes flow

$$\boldsymbol{\nabla}\cdot\mathbf{u}_i = 0, \quad \mu\nabla^2\mathbf{u}_i = \boldsymbol{\nabla}p_i \quad \text{for} \;\; i = l, e, \tag{2.2}$$

where μ is the dynamic fluid viscosity.

Following several other authors [2, 22, 231, 280], we model the membrane and cell layer as rigid porous media and describe the fluid flow through them using the incompressible Darcy flow equations

$$\boldsymbol{\nabla}\cdot(\phi_i\mathbf{u}_i) = 0, \quad \phi_i\mathbf{u}_i = -\frac{k_i}{\mu}\boldsymbol{\nabla}p_i, \quad i = m, c,\,[1] \tag{2.3}$$

where ϕ_i $(i = m, c)$ are the membrane and cell layer porosities (assumed constant), $\mathbf{u}_i$ and p_i $(i = m, c)$ are the interstitial fluid velocities and pressures (averaged over the fluid fraction), and k_i $(i = m, c)$ are the permeabilities of the membrane and cell layer. Although

[1] We note that we could equivalently have written Darcy's Law as $\mathbf{u}_i = -\frac{k_i'}{\mu}\boldsymbol{\nabla}p_i$ $(i = m, c)$ with $k_i' = k_i/\phi_i$, since we have assumed the porosities ϕ_i are constant, but we have written it in this way so that it is explicit that $\mathbf{u}_i$ are the averaged interstitial velocities and not the Darcy fluxes.

it is standard to use Darcy's Law to model flow in a cell-packed ECS or Krogh cylinder, relatively few experimental studies have sought to verify the validity of this model [104, 105]. Given that the cells are small relative to the dimensions of the layer (cell diameter $\approx 10\,\mu\text{m}$ compared to the typical cell layer depth $\approx 100\,\mu\text{m}$ and length $\approx 10\,\text{cm}$) and there are approximately $10^4 - 10^6$ cells packed into a typical cell layer, we assume that it is reasonable to treat the cell layer as a porous medium.

The fluid stress tensors in the different regions, $\boldsymbol{\sigma}_i$ $(i = l, m, c, e)$, corresponding to equations (2.2) and (2.3) are given by

$$\boldsymbol{\sigma}_i = -p_i\mathbf{I} + \mu(\boldsymbol{\nabla}\mathbf{u}_i + (\boldsymbol{\nabla}\mathbf{u}_i)^T) \quad \text{for } i = l, e, \quad \boldsymbol{\sigma}_i = -p_i\mathbf{I} \quad \text{for } i = m, c. \tag{2.4}$$

At the lumen-membrane and membrane-cell layer interfaces we prescribe continuity of normal fluid velocity and normal stress. Following previous studies [204, 205, 231], we assume that all of the lumen fluid stress is taken up by the fluid in the membrane, and then by the fluid in the cell layer (noting that other constitutive relations could be considered, see [145] for a full discussion). Hence the continuity conditions at the lumen-membrane and membrane-cell layer interfaces are

$$\mathbf{u}_l \cdot \mathbf{e}_r = \phi_m \mathbf{u}_m \cdot \mathbf{e}_r \quad \text{and} \quad \mathbf{e}_r \cdot \boldsymbol{\sigma}_l \cdot \mathbf{e}_r = \mathbf{e}_r \cdot \boldsymbol{\sigma}_m \cdot \mathbf{e}_r \quad \text{on } r = R_l, \tag{2.5}$$

$$\phi_m \mathbf{u}_m \cdot \mathbf{e}_r = \phi_c \mathbf{u}_c \cdot \mathbf{e}_r \quad \text{and} \quad \mathbf{e}_r \cdot \boldsymbol{\sigma}_m \cdot \mathbf{e}_r = \mathbf{e}_r \cdot \boldsymbol{\sigma}_c \cdot \mathbf{e}_r \quad \text{on } r = R_m. \tag{2.6}$$

Due to the form of the stress tensor in the membrane and cell layer, the normal stress condition on the interface between the membrane and cell layer immediately reduces to continuity of the pressure

$$p_m = p_c \quad \text{on } r = R_m. \tag{2.7}$$

At the moving boundary of the cell layer, we impose continuity of the normal fluid velocity relative to the moving boundary (*i.e.* conservation of mass) and continuity of normal stress

$$\phi_c \left(\mathbf{u}_c \cdot \mathbf{n}_c - \frac{\partial R_c}{\partial t} \right) = \mathbf{u}_e \cdot \mathbf{n}_c - \frac{\partial R_c}{\partial t}, \quad \mathbf{n}_c \cdot \boldsymbol{\sigma}_c \cdot \mathbf{n}_c = \mathbf{n}_c \cdot \boldsymbol{\sigma}_e \cdot \mathbf{n}_c \quad \text{on } r = R_c(z,t), \tag{2.8}$$

where $\mathbf{n}_c = (\mathbf{e}_r - \frac{\partial R_c}{\partial z}\mathbf{e}_z)/\sqrt{1 + \left(\frac{\partial R_c}{\partial z}\right)^2}$ is the outward-pointing unit normal to the cell layer boundary. In the lubrication limit for the flow obtained by exploiting the small aspect ratio of the bioreactor (see §2.4.1), the continuity of normal stress condition reduces to continuity of pressure. Continuity of fluid pressure at the interface between a porous medium and a free fluid has been used by several authors [17, 141, 149, 222] and justified theoretically for isotropic porous media [115, 164].

It is well known that the flow of a free fluid past a permeable boundary causes a boundary layer to develop in which the tangential component of the fluid velocity is non-vanishing

[17]. However, Shipley *et al.* [233] fitted a model of the fluid transport in the HFB (without cells in the ECS) with Beavers-Joseph conditions for the slip at the lumen-membrane and membrane-ECS interfaces to experimental measurements of the flow distribution, and found that slip had a negligible impact on the flow for the PLGA-PVA hollow fibre membranes considered here. Therefore we apply a no-slip boundary condition for the tangential component of the fluid velocity on $r = R_l$

$$\mathbf{u}_l \cdot \mathbf{e}_z = \phi_m \mathbf{u}_m \cdot \mathbf{e}_z \quad \text{on} \;\; r = R_l. \tag{2.9}$$

Since the cell layer is porous, there will also be some slip at the outer surface of the cell layer. Ideally, we would determine the magnitude of this slip from measurements of the flow distribution with a cell layer attached to the hollow fibre. However, in the absence of experimental data we assume that this slip is also negligible, and impose no slip at the outer surface of the cell layer

$$\phi_c \mathbf{u}_c \cdot \mathbf{t}_c = \mathbf{u}_e \cdot \mathbf{t}_c \quad \text{on} \;\; r = R_c(z,t), \tag{2.10}$$

where $\mathbf{t}_c = (\frac{\partial R_c}{\partial z}\mathbf{e}_r + \mathbf{e}_z)/\sqrt{1 + \left(\frac{\partial R_c}{\partial z}\right)^2}$ is the tangent vector to the surface.

The ends of the fibre are glued into place with epoxy resin and the walls of the ECS are solid, so there is no flow out of the ends of the membrane, cell layer and ECS

$$\mathbf{u}_m \cdot \mathbf{e}_z = \mathbf{u}_c \cdot \mathbf{e}_z = \mathbf{u}_e \cdot \mathbf{e}_z = 0 \quad \text{on} \;\; z = 0,\, L. \tag{2.11}$$

As stated above, we treat the ECS ports as being distributed over the entire curved wall of the ECS ($r = R_e, z \in [0, L]$), which we now refer to as 'the ECS port', and so set the fluid pressure to atmospheric pressure and the axial velocity to zero on this boundary

$$p_e = P_{atm} \quad \text{and} \quad \mathbf{u}_e \cdot \mathbf{e}_z = 0 \quad \text{on} \;\; r = R_e. \tag{2.12}$$

Shipley *et al.* [233] confirmed that this approach gives excellent agreement between model predictions and experimental measurements of the lumen and ECS flow rates, as the bulk of the pressure drop from the lumen to the ECS occurs across the membrane. We also note that we would expect a no-slip condition to hold over most of the ECS outer wall (away from the ECS ports) for the actual module with the ports open, so that the axial velocity would indeed be zero over most of the boundary.

In the experimental set-up, the volumetric flow rate of fluid into the lumen and normal stress at the lumen outlet are fixed, so

$$\int_{r=0}^{R_l} \mathbf{u}_l \cdot \mathbf{e}_z|_{z=0} \, \mathrm{d}S = Q_{l,in}, \tag{2.13}$$

$$\mathbf{e}_z \cdot \boldsymbol{\sigma}_l \cdot \mathbf{e}_z = P_{l,out} \quad \text{on} \;\; z = L,\; 0 < r < R_l. \tag{2.14}$$

Although these conditions are not sufficient to solve full Stokes flow (2.2) in the lumen, they are sufficient to determine the flow in the lubrication limit (see §2.4.1 and §2.6.1). The volumetric flow rates of fluid leaving the lumen and fluid leaving the ECS port, which are measured experimentally, are given by

$$\int_{r=0}^{R_l} \mathbf{u}_l \cdot \mathbf{e}_z|_{z=L} \, \mathrm{d}S = Q_{l,out}, \tag{2.15}$$

$$\int_{z=0}^{L} \mathbf{u}_e \cdot \mathbf{e}_r|_{r=R_e} \, \mathrm{d}S = Q_{e,out}. \tag{2.16}$$

By conservation of mass, the fluid inlet and outlet flow rates must satisfy

$$Q_{l,in} = Q_{l,out} + Q_{e,out}. \tag{2.17}$$

We use this condition to verify our numerical solution of the fluid transport problem in §2.6.3.

2.3.2 Mass transport: oxygen and lactate

We now write down the governing equations and boundary conditions for the transport and consumption/production of oxygen and lactate in the HFB. We denote the solute concentration (per unit volume of fluid) in the different regions by c_i $(i = l, m, c, e)$. As the timescales for advection and diffusion of the solutes are much shorter than the timescale for cell layer growth, we can assume that the solute transport is quasi-steady on the growth timescale. Thus, in the lumen and ECS, the solute transport is governed by the steady advection-diffusion equations

$$\boldsymbol{\nabla} \cdot (c_i \mathbf{u}_i) = D_i \nabla^2 c_i \quad \text{for } \; i = l, e, \tag{2.18}$$

where D_i $(i = l, e)$ are the solute diffusivities in the lumen and ECS, and are assumed constant. In the membrane, the transport is governed by

$$\boldsymbol{\nabla} \cdot (\phi_m c_m \mathbf{u}_m) = \boldsymbol{\nabla} \cdot (\phi_m D_m \boldsymbol{\nabla} c_m), \tag{2.19}$$

where D_m is the effective solute diffusivity (accounting for dispersion effects) in the culture medium in the membrane. In the cell layer, there is also oxygen uptake and lactate production, so the solute transport is described by the reaction-advection-diffusion equation

$$\boldsymbol{\nabla} \cdot (\phi_c c_c \mathbf{u}_c) = \boldsymbol{\nabla} \cdot (\phi_c D_c \boldsymbol{\nabla} c_c) + m \phi_c \mathcal{R}(c_c), \tag{2.20}$$

where D_c is the effective solute diffusivity in the culture medium in the cell layer, and the reaction term $m\phi_c\mathcal{R}(c_c)$ describes the rate of oxygen uptake (for $m = -1$) or lactate production (for $m = 1$) by the cells. Equations (2.19) and (2.20) are derived by volume

averaging (reaction-)advection-diffusion equations for the solute concentrations in the pore space over the membrane and cell layer, respectively (see [96] and [214] for further details).

Although the oxygen uptake and lactate production will depend on each other, we follow Shipley and Waters [231] and make the simplifying assumption that they can be treated as independent, since lactate production is approximately constant under typical bioreactor conditions (see below). For a more detailed model of cell metabolism that includes coupling between the oxygen consumption and lactate production we refer the reader to [30]. Oxygen uptake in HFBs is typically modelled by Michaelis-Menten kinetics [2, 36, 54, 206, 234], for which

$$\mathcal{R}(c_c) = \frac{V_{max} c_c}{C_{1/2} + c_c}, \tag{2.21}$$

where V_{max} (in $\mathrm{mol\,m^{-3}\,s^{-1}}$) is the maximal consumption rate per unit volume of the cell layer and $C_{1/2}$ is the concentration at which the consumption rate is half-maximal. Since (2.21) is nonlinear, to make analytical progress we assume that $c_c \gg C_{1/2}$ so that the uptake can be approximated as constant

$$\mathcal{R}(c_c) \approx V_{max}. \tag{2.22}$$

This assumption restricts the validity of the model to cell types for which the concentration in the cell layer can be maintained far above $C_{1/2}$. For cell types for which $c_c \not\gg C_{1/2}$, full Michaelis-Menten kinetics must be used and the oxygen transport equations solved numerically (as in [234]).

The lactate production rate depends on the underlying concentrations of glucose and lactate, but in glucose-rich (glucose concentration $\gg 0.5\,\mathrm{mol\,m^{-3}}$) and low lactate (lactate concentration $\ll 2.8\,\mathrm{mol\,m^{-3}}$) environments can be treated as approximately constant [232]. Since the glucose concentration in the culture medium pumped into the lumen is typically in the range $5.5-55\,\mathrm{mol\,m^{-3}}$ and the lactate concentration is kept low by lactate buffering [231], we will assume that the lactate production rate is also constant.

Since the oxygen and lactate distributions are assumed to be symmetric about the lumen axis, we impose no diffusive flux through $r = 0$

$$D_l \boldsymbol{\nabla} c_l \cdot \mathbf{e}_r = 0 \quad \text{on} \quad r = 0. \tag{2.23}$$

At the lumen-membrane and membrane-cell layer interfaces we impose continuity of concentration and flux

$$c_l = c_m \quad \text{and} \quad (c_l \mathbf{u}_l - D_l \boldsymbol{\nabla} c_l) \cdot \mathbf{e}_r = \phi_m (c_m \mathbf{u}_m - D_m \boldsymbol{\nabla} c_m) \cdot \mathbf{e}_r \quad \text{on} \quad r = R_l, \tag{2.24}$$

$$c_m = c_c \quad \text{and} \quad \phi_m (c_m \mathbf{u}_m - D_m \boldsymbol{\nabla} c_m) \cdot \mathbf{e}_r = \phi_c (c_c \mathbf{u}_c - D_c \boldsymbol{\nabla} c_c) \cdot \mathbf{e}_r \quad \text{on} \quad r = R_m. \tag{2.25}$$

At the outer surface of the cell layer we impose continuity of the concentration and flux relative to the moving boundary

$$c_m = c_c \quad \text{and} \quad \phi_c c_c \left(\mathbf{u}_c \cdot \mathbf{n}_c - \frac{\partial R_c}{\partial t} \right) - \phi_c D_c \boldsymbol{\nabla} c_c \cdot \mathbf{n}_c = (c_e \mathbf{u}_e - D_e \boldsymbol{\nabla} c_e) \cdot \mathbf{n}_c \quad \text{on} \quad r = R_c(z,t). \tag{2.26}$$

With the normal velocity continuity conditions in (2.5), (2.6) and (2.8), the flux conditions reduce to continuity of diffusive flux

$$D_l \boldsymbol{\nabla} c_l \cdot \mathbf{e}_r = \phi_m D_m \boldsymbol{\nabla} c_m \cdot \mathbf{e}_r \quad \text{on} \quad r = R_l, \tag{2.27}$$

$$\phi_m D_m \boldsymbol{\nabla} c_m \cdot \mathbf{e}_r = \phi_c D_c \boldsymbol{\nabla} c_c \cdot \mathbf{e}_r \quad \text{on} \quad r = R_m, \tag{2.28}$$

$$\phi_c D_c \boldsymbol{\nabla} c_c \cdot \mathbf{n}_c = D_e \boldsymbol{\nabla} c_e \cdot \mathbf{n}_c \quad \text{on} \quad r = R_c(z,t). \tag{2.29}$$

There is no concentration flux out of the ends of the membrane, cell-layer and ECS, so

$$D_i \boldsymbol{\nabla} c_i \cdot \mathbf{e}_z = 0 \quad \text{on} \quad z = 0, L \quad \text{for} \quad i = m, c, e. \tag{2.30}$$

Experimentally, the oxygen concentration at the lumen inlet is held constant and there is no lactate in the culture medium entering the lumen, so

$$c_l = \begin{cases} C_{in} & \text{for oxygen,} \\ 0 & \text{for lactate,} \end{cases} \quad \text{on} \quad z = 0,\ 0 < r < R_l. \tag{2.31}$$

Following Shipley and Waters [231], we assume that the culture medium leaving the lumen outlet and ECS port is well-mixed and impose zero-diffusive-flux at both for both the oxygen and lactate transport

$$D_l \boldsymbol{\nabla} c_l \cdot \mathbf{e}_z = 0 \quad \text{on} \quad z = L,\ 0 < r < R_l, \tag{2.32}$$

$$D_e \boldsymbol{\nabla} c_e \cdot \mathbf{e}_r = 0 \quad \text{on} \quad r = R_e. \tag{2.33}$$

We note that the first condition is only required to solve the reduced model derived in the small aspect ratio limit (see §2.4) when the ECS port is closed.

2.3.3 Cell layer growth

We assume that there is no movement of cells in the cell layer and that only cells at its outer surface $r = R_c(z,t)$ proliferate or die, while those in the bulk are quiescent, so that the cell layer porosity ϕ_c remains constant. Cells in the bulk are less likely to proliferate than cells at the outer surface due to contact inhibition (which is significant for the cell types we consider: cardiomyocytes [74], hepatocytes [161], and chondrocytes [99, 143]), and are also less likely to die as they experience higher oxygen concentrations and lower lactate concentrations closer to the fibre surface (see §2.7). We assume that cells at the

outer surface that proliferate form new layers on top of the existing cells and those that die become detached from the surface, so that the depth of the cell layer increases or decreases according to the net increase or decrease in the number of cells locally. We model net changes in the cell number implicitly through the movement of the outer surface of the cell layer. We do not model the ECM, and neglect cell-cell and cell-ECM interactions.

Cell proliferation and death are assumed to depend on the oxygen and lactate concentrations, c_O and c_L, and interstitial fluid shear stress σ (the shear stress on the cells due to the flow through the spaces between the cells) at the surface of the cell layer. We assume the growth depends on the interstitial shear stress rather than the shear stress on the cells from the ECS flow tangential to the surface, as the interstitial shear stress is an order of magnitude larger for the flow configuration considered here (see §2.4.3). Thus the normal velocity of the outer surface of the cell layer is given by

$$\frac{\frac{\partial R_c}{\partial t}}{\sqrt{1+\left(\frac{\partial R_c}{\partial z}\right)^2}} = G\left(c_O|_{r=R_c(z,t)}, c_L|_{r=R_c(z,t)}, \sigma|_{r=R_c(z,t)}\right), \tag{2.34}$$

where the growth function G is to be prescribed. We note that this model can be derived from a two-phase model for the cells and culture medium (treating both as fluid phases) of a similar form to the two-phase tumour growth models in [26, 35, 137, 209], for which the cell volume fraction ϕ $(= 1 - \phi_c)$ and cell velocity $\mathbf{v}$ satisfy

$$\frac{\partial \phi}{\partial t} + \boldsymbol{\nabla} \cdot (\phi \mathbf{v}) = \phi \overline{G}, \tag{2.35}$$

where $\overline{G}$ is the net cell proliferation rate. The equation for the free boundary of the cell layer (2.34) is obtained by assuming that $\phi =$ const. and that proliferation and death are localised to the free boundary, so that

$$\boldsymbol{\nabla} \cdot \mathbf{v} = \overline{G} = \boldsymbol{\delta}(\mathbf{r} - R_c(z,t)\mathbf{e}_r) G(c_O, c_L, \sigma),$$

(where $\boldsymbol{\delta}(\mathbf{r})$ is the 3D Dirac delta function in cylindrical polar coordinates $\mathbf{r} = (r, \theta, z)$), then integrating over the volume of the cell layer, and using the fact that the normal velocity of the free boundary is given by the kinematic boundary condition

$$\frac{\partial R_c}{\partial t} \mathbf{e}_r \cdot \mathbf{n}_c = \mathbf{v} \cdot \mathbf{n}_c \quad \text{on} \quad r = R_c(z,t),$$

(see Byrne and Chaplain [25]).

Following previous studies [117, 150, 171], and based on experimental evidence that the proliferation rate of many cell types increases with oxygen availability [125, 183, 269], we assume that the cell proliferation rate increases linearly with the oxygen concentration above a minimum threshold required for proliferation, C_{min}. As data on the relationships

between cell death and lactate concentration, and cell death and shear stress, is more limited, we make the simple assumption that cells die and detach from the cell layer surface at a constant rate when either the lactate concentration exceeds the threshold at which it is toxic to the cells, L_{max}, and/or the shear stress exceeds a critical threshold, Σ_d. The effects of excess lactate and shear stress are taken to be multiplicative, so that cells die at a faster rate when both $c_L > L_{max}$ and $\sigma > \Sigma_d$. The cell layer stops growing if it fills the entire ECS or recedes to the fibre surface (which is taken to represent all the cells dying), so $R_m \leq R_c(z,t) \leq R_e$. The following form for G is used to incorporate these assumptions

$$G(c_O, c_L, \sigma) = \Big[A_p \mathrm{H}(c_O - C_{min})(c_O - C_{min})\mathrm{F}(\Sigma_d - \sigma) - B_d\big[(1 + B_L \mathrm{F}(c_L - L_{max})) \times (1 + B_s \mathrm{F}(\sigma - \Sigma_d)) - 1\big]\Big]\mathrm{H}(R_c(z,t) - R_m)\mathrm{H}(R_e - R_c(z,t)), \quad (2.36)$$

where $\mathrm{H}(\cdot)$ is the Heaviside function and $\mathrm{F}(x,s) = \frac{1}{2}(1+\tanh(sx))$ is a smoothed Heaviside function with smoothing factor s; the constant A_p is the growth rate of the cell layer per unit concentration if $c_O > C_{min}$ and there is no cell death ($c_L < L_{max}$ and $\sigma < \Sigma_d$); B_d is the baseline recession rate of the cell layer if $c_L > L_{max}$ or $\sigma > \Sigma_d$ and there is no cell proliferation ($c_O < C_{min}$ or $\sigma > \Sigma_d$); and B_L and B_s are dimensionless factors that determine the rates of recession due to excess lactate, $c_L > L_{max}$ ($c_O < C_{min}$, $\sigma < \Sigma_d$), and excess shear stress, $\sigma > \Sigma_d$ ($c_L < L_{max}$), respectively. We use the smoothed Heaviside function, F, for the lactate and shear stress thresholds since using a normal Heaviside function would lead to discontinuities in $\frac{\partial R_c}{\partial t}$ and very sharp changes in $R_c(z,t)$ where c_L and σ cross the thresholds L_{max} and Σ_d, which would be difficult to resolve numerically and for which the reduced model described in the next section would not be valid.

Finally, we prescribe the initial depth of the cell layer as a function of z

$$R_c(z,0) = R_{c,init}(z). \quad (2.37)$$

2.4 Model reduction

The full system for the fluid transport, oxygen and lactate transport and cell layer growth is given by equations (2.2)–(2.37). To make analytical progress we nondimensionalise these equations and exploit the small aspect ratio of the bioreactor to neglect terms at leading order in ϵ. We nondimensionalise the variables with the following scalings:

$$r = R_l \hat{r}, \quad z = L\hat{z}, \quad t = \frac{R_l}{A_p C_{in}}\hat{t}, \quad u_{i,r} = \epsilon U \hat{u}_{i,r}, \quad u_{i,z} = U\hat{u}_{i,z}, \quad p_i = P_{atm} + P_i \hat{p}_i,$$
$$\boldsymbol{\sigma}_i = P_i \hat{\boldsymbol{\sigma}}_i, \quad c_i = \begin{cases} C_{in}\hat{c}_i & \text{for oxygen,} \\ C_L \hat{c}_i & \text{for lactate,} \end{cases} \quad i = l, m, c, e, \quad \sigma = P_c \hat{\sigma},$$
$$R_c(z,t) = R_l \hat{R}_c(\hat{z}, \hat{t}), \quad G(c_O, c_L, \sigma) = A_p C_{in} \hat{G}(\hat{c}_O, \hat{c}_L, \hat{\sigma}), \quad R_{c,init}(z) = R_l \hat{R}_{c,init}(\hat{z}), \quad (2.38)$$

where U is a typical lumen flow velocity, P_i $(i = l, m, c, e)$ are the pressure scales in the different regions (chosen as described below) and C_L is a typical lactate concentration. From here on we drop hats on dimensionless variables except where they are needed for clarity.

2.4.1 Fluid transport

In the lumen, we pick the pressure scale so that the pressure gradient and viscous terms balance in the axial momentum equation

$$P_l = \frac{\mu U}{\epsilon^2 L}.$$

In the membrane, cell layer and ECS, we choose the pressure scales so that there is an $\mathcal{O}(1)$ radial pressure gradient, as would be expected if the lumen outlet pressure is set to ensure a non-negligible radial flow through the membrane,

$$P_i = \frac{\mu \epsilon U R_l}{k_i} \quad \text{for} \quad i = m, c, \quad P_e = \frac{\mu U}{L}.$$

With these scalings the mass conservation and radial and axial momentum conservation equations in the lumen and ECS in (2.2) become

$$\frac{1}{r}\frac{\partial}{\partial r}(r u_{i,r}) + \frac{\partial u_{i,z}}{\partial z} = 0 \quad \text{for} \quad i = l, e, \tag{2.39}$$

$$\epsilon^2 \frac{1}{r}\frac{\partial}{\partial r}\left(r\frac{\partial u_{l,r}}{\partial r}\right) + \epsilon^4 \frac{\partial^2 u_{l,r}}{\partial z^2} - \epsilon^2 \frac{u_{l,r}}{r^2} = \frac{\partial p_l}{\partial r}, \quad \frac{1}{r}\frac{\partial}{\partial r}\left(r\frac{\partial u_{l,z}}{\partial r}\right) + \epsilon^2 \frac{\partial^2 u_{l,z}}{\partial z^2} = \frac{\partial p_l}{\partial z}, \tag{2.40}$$

$$\frac{1}{r}\frac{\partial}{\partial r}\left(r\frac{\partial u_{e,r}}{\partial r}\right) + \epsilon^2 \frac{\partial^2 u_{e,r}}{\partial z^2} - \frac{u_{e,r}}{r^2} = \frac{\partial p_e}{\partial r}, \quad \frac{1}{r}\frac{\partial}{\partial r}\left(r\frac{\partial u_{e,z}}{\partial r}\right) + \epsilon^2 \frac{\partial^2 u_{e,z}}{\partial z^2} = \epsilon^2 \frac{\partial p_e}{\partial z}. \tag{2.41}$$

In the membrane and cell layer the mass conservation and radial and axial velocity equations (2.3) become

$$\frac{1}{r}\frac{\partial}{\partial r}(r \phi_i u_{i,r}) + \frac{\partial}{\partial z}(\phi_i u_{i,z}) = 0, \tag{2.42}$$

$$\phi_i u_{i,r} = -\frac{\partial p_i}{\partial r}, \quad \phi_i u_{i,z} = -\epsilon^2 \frac{\partial p_i}{\partial z} \quad \text{for} \quad i = m, c. \tag{2.43}$$

Neglecting $\mathcal{O}(\epsilon^2)$ terms, the system reduces at leading order to

$$\frac{\partial p_l}{\partial r} = 0, \quad \frac{1}{r}\frac{\partial}{\partial r}\left(r\frac{\partial u_{l,z}}{\partial r}\right) = \frac{\partial p_l}{\partial z}, \quad \frac{1}{r}\frac{\partial}{\partial r}(r u_{l,r}) + \frac{\partial u_{l,z}}{\partial z} = 0, \tag{2.44a–c}$$

$$\phi_i u_{i,r} = -\frac{\partial p_i}{\partial r}, \quad u_{i,z} = 0, \quad \frac{\partial}{\partial r}\left(r\frac{\partial p_i}{\partial r}\right) = 0, \quad i = m, c, \tag{2.45a–c}$$

$$\frac{1}{r}\frac{\partial}{\partial r}\left(r\frac{\partial u_{e,r}}{\partial r}\right) - \frac{u_{e,r}}{r^2} = \frac{\partial p_e}{\partial r}, \quad \frac{\partial}{\partial r}\left(r\frac{\partial u_{e,z}}{\partial r}\right) = 0, \quad \frac{1}{r}\frac{\partial}{\partial r}(r u_{e,r}) + \frac{\partial u_{e,z}}{\partial z} = 0, \tag{2.46a–c}$$

so there is no axial flow in the membrane or cell layer at leading order.

In dimensionless coordinates the lumen-membrane and membrane-cell layer interfaces, cell layer outer surface and ECS outer boundary are given by $r = 1$, $r = R_m/R_l =: \hat{R}_m$, $r = \hat{R}_c(z,t)$ and $r = R_e/R_l =: \hat{R}_e$, respectively. The dimensionless fluid stress tensors are

$$\boldsymbol{\sigma}_l = \begin{pmatrix} -p_l + 2\epsilon^2 \frac{\partial u_{l,r}}{\partial r} & \epsilon^3 \frac{\partial u_{l,r}}{\partial z} + \epsilon \frac{\partial u_{l,z}}{\partial r} \\ \epsilon^3 \frac{\partial u_{l,r}}{\partial z} + \epsilon \frac{\partial u_{l,z}}{\partial r} & -p_l + 2\epsilon^2 \frac{\partial u_{l,z}}{\partial z} \end{pmatrix}, \quad \boldsymbol{\sigma}_i = -p_i \boldsymbol{I}, \ i = m, c,$$
$$\boldsymbol{\sigma}_e = \begin{pmatrix} -p_e + 2\frac{\partial u_{e,r}}{\partial r} & \epsilon \frac{\partial u_{e,r}}{\partial z} + \frac{1}{\epsilon} \frac{\partial u_{e,z}}{\partial r} \\ \epsilon \frac{\partial u_{e,r}}{\partial z} + \frac{1}{\epsilon} \frac{\partial u_{e,z}}{\partial r} & -p_e + 2\frac{\partial u_{e,z}}{\partial z} \end{pmatrix}. \tag{2.47}$$

Thus, the dimensionless continuity conditions at the lumen-membrane and membrane-cell layer interfaces are

$$u_{l,r} = -\frac{\partial p_m}{\partial r} \quad \text{and} \quad p_l - 2\epsilon^2 \frac{\partial u_{l,r}}{\partial r} = \kappa_m p_m \quad \text{on} \ \ r = 1, \tag{2.48}$$
$$\frac{\partial p_m}{\partial r} = \frac{\partial p_c}{\partial r} \quad \text{and} \quad p_m = \kappa_c p_c \quad \text{on} \ \ r = \hat{R}_m, \tag{2.49}$$

where $\kappa_m := \epsilon^2 R_l^2/k_m$ is a dimensionless parameter representing the permeability of the membrane and $\kappa_c := k_m/k_c$ is the ratio of the membrane and cell layer permeabilities. Both κ_m and κ_c are assumed to be $\mathcal{O}(1)$ to retain as many physical effects as possible at leading order. Thus, the normal stress condition in (2.48) becomes

$$p_l = \kappa_m p_m \quad \text{on} \ \ r = 1, \tag{2.50}$$

at leading order. At the moving surface of the cell layer, the normal velocity continuity condition in (2.8) becomes

$$\phi_c \left(u_{c,r} - \alpha_p \frac{\partial \hat{R}_c}{\partial t} - \frac{\partial \hat{R}_c}{\partial z} u_{c,z} \right) = u_{e,r} - \alpha_p \frac{\partial \hat{R}_c}{\partial t} - \frac{\partial \hat{R}_c}{\partial z} u_{e,z} \quad \text{on} \ \ r = \hat{R}_c(z,t), \tag{2.51}$$

where $\alpha_p := LA_pC_{in}/(UR_l)$ is the ratio of the advection timescale L/U to the growth timescale $R_l/(A_pC_{in})$. Since $\alpha_p = \mathcal{O}(\epsilon^2)$ (see §2.5) and $u_{c,z} = \mathcal{O}(\epsilon^2)$, this condition reduces at leading order to

$$\phi_c u_{c,r} = u_{e,r} - \frac{\partial \hat{R}_c}{\partial z} u_{e,z} \quad \text{on} \ \ r = \hat{R}_c(z,t). \tag{2.52}$$

The dimensionless normal stress condition at the moving boundary of the cell layer is

$$\kappa_m \kappa_c \hat{p}_c = \epsilon^2 \left(p_e - \frac{2}{1 + \epsilon^2 \left(\frac{\partial \hat{R}_c}{\partial z} \right)^2} \left(\frac{\partial u_{e,r}}{\partial r} - \epsilon \frac{\partial \hat{R}_c}{\partial z} \left(\epsilon \frac{\partial u_{e,r}}{\partial z} + \frac{1}{\epsilon} \frac{\partial u_{e,z}}{\partial r} \right) + \epsilon^2 \left(\frac{\partial \hat{R}_c}{\partial z} \right)^2 \frac{\partial u_{e,z}}{\partial z} \right) \right)$$
$$\text{on} \ \ r = \hat{R}_c(z,t), \tag{2.53}$$

which simplifies at leading order to

$$p_c = 0 \quad \text{on} \ \ r = \hat{R}_c(z,t), \tag{2.54}$$

so that most of the pressure drop from the lumen inlet to the ECS port occurs across the membrane and cell layer as expected. The no-slip conditions at the lumen-membrane interface and the moving boundary, (2.9) and (2.10), give

$$u_{l,z} = \phi_m u_{m,z} \quad \text{on} \quad r = 1, \tag{2.55}$$

$$\phi_c \left(\epsilon^2 u_{c,r} \frac{\partial \hat{R}_c}{\partial z} + u_{c,z} \right) = \epsilon^2 u_{e,r} \frac{\partial \hat{R}_c}{\partial z} + u_{e,z} \quad \text{on} \quad r = \hat{R}_c(z,t), \tag{2.56}$$

so that at leading order (since $u_{i,z} = \mathcal{O}(\epsilon^2)$, $i = m, c$)

$$u_{l,z} = 0 \quad \text{on} \quad r = 1, \tag{2.57}$$

$$u_{e,z} = 0 \quad \text{on} \quad r = \hat{R}_c(z,t). \tag{2.58}$$

At the outer boundary of the ECS, the dimensionless boundary conditions are

$$p_e = 0, \quad u_{e,z} = 0 \quad \text{on} \quad r = \hat{R}_e. \tag{2.59}$$

Nondimensionalising the flow rates at the lumen inlet, lumen outlet and ECS port, and pressure at the lumen outlet, gives

$$\int_{r=0}^{1} r u_{l,z}|_{z=0} \, \mathrm{d}r = \hat{Q}_{l,in}, \tag{2.60}$$

$$\int_{r=0}^{1} r u_{l,z}|_{z=1} \, \mathrm{d}r = \hat{Q}_{l,out}, \tag{2.61}$$

$$\int_{z=0}^{1} \hat{R}_e u_{e,r}|_{r=\hat{R}_e} \, \mathrm{d}z = \hat{Q}_{e,out}, \tag{2.62}$$

$$p_l = \hat{P}_{l,out} \quad \text{on} \quad z = 1, \, 0 < r < 1, \tag{2.63}$$

where

$$\hat{Q}_{l,in} := \frac{Q_{l,in}}{2\pi R_l^2 U}, \quad \hat{Q}_{l,out} := \frac{Q_{l,out}}{2\pi R_l^2 U}, \quad \hat{Q}_{e,out} := \frac{Q_{e,out}}{2\pi R_l^2 U}, \quad \hat{P}_{l,out} := \frac{\epsilon^2 L}{\mu U}(P_{l,out} - P_{atm}). \tag{2.64}$$

In dimensionless terms, the overall mass conservation equation is

$$\hat{Q}_{l,in} = \hat{Q}_{l,out} + \hat{Q}_{e,out}. \tag{2.65}$$

2.4.2 Mass transport

Nondimensionalising the advection-diffusion equations in the lumen, membrane and ECS, (2.18) and (2.19), and the reaction-advection-diffusion equation in the cell layer (2.20) with the scalings in (2.38) gives

$$\epsilon^2 \mathrm{Pe}_i \left(\frac{1}{r} \frac{\partial}{\partial r}(r c_i u_{i,r}) + \frac{\partial}{\partial z}(c_i u_{i,z}) \right) = \frac{1}{r} \frac{\partial}{\partial r} \left(r \frac{\partial c_i}{\partial r} \right) + \epsilon^2 \frac{\partial^2 c_i}{\partial z^2} \quad \text{for} \quad i = l, m, e, \tag{2.66}$$

$$\epsilon^2 \mathrm{Pe}_c \left(\frac{1}{r} \frac{\partial}{\partial r}(r c_c u_{c,r}) + \frac{\partial}{\partial z}(c_c u_{c,z}) \right) = \frac{1}{r} \frac{\partial}{\partial r} \left(r \frac{\partial c_c}{\partial r} \right) + \epsilon^2 \frac{\partial^2 c_c}{\partial z^2} + m\mathcal{M}, \tag{2.67}$$

where $\epsilon^2 \mathrm{Pe}_i := \epsilon^2 UL/D_i$ $(i = l, m, c, e)$ are the reduced Péclet numbers for the different regions and $\mathcal{M} := V^O_{max} R_l^2/(C_{in} D^O_c)$ for oxygen and $\mathcal{M} := V^L_{max} R_l^2/(C_L D^L_c)$ for lactate (where the superscript O and L specify oxygen and lactate respectively). The reduced Péclet number in each region is the ratio of the timescales for radial diffusion and axial advection of the solute in that region, R_l^2/D_i $(i = l, m, c, e)$ and L/U respectively. So, if $\epsilon^2 \mathrm{Pe}_i = \mathcal{O}(1)$ then the speed at which the solute diffuses radially is similar to that at which it is advected axially. The dimensionless parameter $\mathcal{M}$ is the ratio of the timescale for radial diffusion, R_l^2/D_c, to the timescale for oxygen uptake/lactate production in the cell layer, C/V_{max} (where $C = C_{in}$ for oxygen and $C = C_L$ for lactate).

For typical inlet flow rates used in experiments, $\epsilon^2 \mathrm{Pe}_i = \mathcal{O}(1)$ $(i = l, m, c, e)$ for both oxygen and lactate (see §2.5.2). So, at leading order, (2.66)–(2.67) reduce to

$$\epsilon^2 \mathrm{Pe}_i \left(\frac{1}{r} \frac{\partial}{\partial r}(r c_i u_{i,r}) + \frac{\partial}{\partial z}(c_i u_{i,z}) \right) = \frac{1}{r} \frac{\partial}{\partial r} \left(r \frac{\partial c_i}{\partial r} \right) \quad \text{for } i = l, e, \tag{2.68}$$

$$\epsilon^2 \mathrm{Pe}_m \frac{1}{r} \frac{\partial}{\partial r}(r c_m u_{m,r}) = \frac{1}{r} \frac{\partial}{\partial r} \left(r \frac{\partial c_m}{\partial r} \right), \tag{2.69}$$

$$\epsilon^2 \mathrm{Pe}_c \frac{1}{r} \frac{\partial}{\partial r}(r c_c u_{c,r}) = \frac{1}{r} \frac{\partial}{\partial r} \left(r \frac{\partial c_c}{\partial r} \right) + m\mathcal{M}, \tag{2.70}$$

since $u_{i,z} = \mathcal{O}(\epsilon^2)$ $(i = m, c)$.

The dimensionless zero-diffusive-flux condition on the lumen axis is

$$\frac{\partial c_l}{\partial r} = 0 \quad \text{on } r = 0. \tag{2.71}$$

The dimensionless concentration and diffusive flux continuity conditions at the interfaces between the different regions are

$$c_l = c_m, \quad \frac{\partial c_l}{\partial r} = \frac{\phi_m D_m}{D_l} \frac{\partial c_m}{\partial r} \quad \text{on } r = 1, \tag{2.72}$$

$$c_m = c_c, \quad \frac{\partial c_m}{\partial r} = \frac{\phi_c D_c}{\phi_m D_m} \frac{\partial c_c}{\partial r} \quad \text{on } r = \hat{R}_m, \tag{2.73}$$

$$c_c = c_e, \quad \frac{\partial c_c}{\partial r} - \epsilon^2 \frac{\partial \hat{R}_c}{\partial z} \frac{\partial c}{\partial z} = \frac{D_e}{\phi_c D_c} \left(\frac{\partial c_e}{\partial r} - \epsilon^2 \frac{\partial \hat{R}_c}{\partial z} \frac{\partial c_e}{\partial z} \right) \quad \text{on } r = \hat{R}_c(z, t). \tag{2.74}$$

At leading order the diffusive flux condition in (2.74) simplifies to

$$\frac{\partial c_c}{\partial r} = \frac{D_e}{\phi_c D_c} \frac{\partial c_e}{\partial r} \quad \text{on } r = \hat{R}_c(z, t). \tag{2.75}$$

The dimensionless inlet concentration is

$$c_l = \begin{cases} 1 & \text{for oxygen,} \\ 0 & \text{for lactate,} \end{cases} \quad \text{on } z = 0,\ 0 < r < 1, \tag{2.76}$$

and the zero-diffusive flux conditions at the lumen outlet and outer boundary of the ECS are

$$\frac{\partial c_l}{\partial z} = 0 \quad \text{on} \quad z = 1,\ 0 < r < 1, \tag{2.77}$$

$$\frac{\partial c_e}{\partial r} = 0 \quad \text{on} \quad r = \hat{R}_e. \tag{2.78}$$

2.4.3 Cell layer growth

In prescribing the cell layer growth in §2.3.3 we assumed that the shear stress on the cells due to the flow through the interstitial spaces in the cell layer is much higher than the shear stress on the cells at the outer surface from the ECS flow. Here we justify this assumption by estimating the magnitudes of the shear stress due to the ECS flow and the interstitial shear stress.

2.4.3.1 Shear stress from ECS flow

The dimensional shear stress at the cell layer outer surface due to the ECS flow tangential to the surface is given by

$$\begin{aligned}
&\mathbf{n}_c \cdot \boldsymbol{\sigma}_e \cdot \mathbf{t}_c|_{r=R_c(z,t)} \\
&= \frac{1}{1+\left(\frac{\partial R_c}{\partial z}\right)^2} \\
&\quad \times \left(\frac{\partial R_c}{\partial z} \left(-p_e + 2\mu \frac{\partial u_{e,r}}{\partial r} \right) + \left(1 - \left(\frac{\partial R_c}{\partial z} \right)^2 \right) \mu \left(\frac{\partial u_{e,r}}{\partial z} + \frac{\partial u_{e,z}}{\partial r} \right) + \frac{\partial R_c}{\partial z} \left(-p_e + 2\mu \frac{\partial u_{e,z}}{\partial z} \right) \right) \Big|_{r=R_c} \\
&= \frac{\mu \epsilon U}{L} \frac{1}{1 + \epsilon^2 \left(\frac{\partial \hat{R}_c}{\partial \hat{z}} \right)^2} \\
&\qquad \times \left(2 \frac{\partial \hat{R}_c}{\partial \hat{z}} \left(-\hat{p}_e + \frac{\partial \hat{u}_{e,r}}{\partial \hat{r}} + \frac{\partial \hat{u}_{e,z}}{\partial \hat{z}} \right) + \left(1 - \epsilon^2 \left(\frac{\partial \hat{R}_c}{\partial \hat{z}} \right)^2 \right) \left(\frac{\partial \hat{u}_{e,r}}{\partial \hat{z}} + \frac{1}{\epsilon^2} \frac{\partial \hat{u}_{e,z}}{\partial \hat{r}} \right) \right) \Big|_{\hat{r}=\hat{R}_c},
\end{aligned}$$

where hats denote dimensionless variables as previously. Since $\hat{p}_e = \mathcal{O}(\epsilon^2)$, $\hat{u}_{e,r} = \mathcal{O}(1)$ and $\hat{u}_{e,z} = \mathcal{O}(\epsilon^2)$ (see §2.6.1), the magnitude of this shear stress is approximately

$$|\mathbf{n}_c \cdot \boldsymbol{\sigma}_e \cdot \mathbf{t}_c|_{r=R_c} \approx \frac{\mu \epsilon U}{L} \left| 2 \frac{\partial \hat{R}_c}{\partial \hat{z}} \frac{\partial \hat{u}_{e,r}}{\partial \hat{r}} + \left(\frac{\partial \hat{u}_{e,r}}{\partial \hat{z}} + \frac{1}{\epsilon^2} \frac{\partial \hat{u}_{e,z}}{\partial \hat{r}} \right) \right| = \mathcal{O}\left(\frac{\mu \epsilon U}{L} \right).$$

2.4.3.2 Interstitial shear stress

We estimate the interstitial shear stress from the interstitial velocity following Whittaker *et al.* [272]. We assume that the flow through the interstitial spaces can be approximated as Poiseuille flow through a circular duct of diameter d with mean velocity $|\mathbf{u}_c|$. With $\tilde{r}$ as the local radial coordinate, the dimensional velocity profile is

$$u_p \approx 2|\mathbf{u}_c| \left(1 - 4 \frac{\tilde{r}^2}{d^2} \right),$$

so the dimensional interstitial shear stress on the cells is

$$\sigma = \mu \left| \frac{\partial u_p}{\partial \tilde{r}} \right|_{\tilde{r}=d/2} \approx \left| \frac{16\mu |\mathbf{u}_c| \tilde{r}}{d^2} \right|_{\tilde{r}=d/2} = \frac{8\mu |\mathbf{u}_c|}{d} = \frac{8\mu U}{d} |(\epsilon \hat{u}_{c,r}, \hat{u}_{c,z})|.$$

Since $\hat{u}_{c,r} = \mathcal{O}(1)$ and $\hat{u}_{c,z} = \mathcal{O}(\epsilon^2)$, the shear stress is

$$\sigma \approx \frac{8\mu\epsilon U}{d} |\hat{u}_{c,r}| = \mathcal{O}\left(\frac{\mu\epsilon U}{d} \right).$$

Hence, for typical estimates of d (see §2.5), the interstitial shear stress is of the order of $L/d \sim 10^3$ times higher than the shear stress due to the ECS flow.

Nondimensionalising on the cell layer pressure scale ($P_c = \mu\epsilon U R_l / k_c$) gives the dimensionless shear stress in the cell layer as

$$\hat{\sigma} \approx \kappa_s |\hat{u}_{c,r}|,$$

where $\kappa_s = 8k_c/(R_l d)$ is the dimensionless shear stress proportionality constant.

2.4.3.3 Growth law

Omitting hats on the dimensionless concentrations and shear stress, the dimensionless form of the cell layer growth law (2.34) reduces at leading order to

$$\frac{\partial \hat{R}_c}{\partial t} = \hat{G}\left(c_O|_{r=\hat{R}_c}, c_L|_{r=\hat{R}_c}, \sigma|_{r=\hat{R}_c} \right), \tag{2.79}$$

where

$$\begin{aligned} \hat{G}(c_O, c_L, \sigma) = \Big[& \mathrm{H}(c_O - c_{min})(c_O - c_{min})\mathrm{F}(\sigma_d - \sigma) \\ & - [\beta_L \mathrm{F}(c_L - l_{max}) + \beta_s \mathrm{F}(\sigma - \sigma_d) + \beta_{L,s} \mathrm{F}(c_L - l_{max})\mathrm{F}(\sigma - \sigma_d)] \Big] \mathrm{H}(\hat{R}_c - \hat{R}_m)\mathrm{H}(\hat{R}_e - \hat{R}_c), \end{aligned} \tag{2.80}$$

and $c_{min} = C_{min}/C_{in}$ and $l_{max} = L_{max}/C_L$ are the dimensionless minimum oxygen and maximum lactate concentrations for cell proliferation; $\sigma_d = k_c \Sigma_d / (\mu\epsilon U R_l)$ is the dimensionless shear stress threshold for cell death/detachment; and $\beta_L = B_L B_d/(A_p C_{in})$, $\beta_s = B_s B_d/(A_p C_{in})$ and $\beta_{L,s} = B_L B_s B_d/(A_p C_{in})$ are the ratios of the cell layer recession rates due to excess lactate and excess shear stress, and the two combined, to the cell proliferation rate.

On nondimensionalisation, the initial condition for the position of the outer surface of the cell layer becomes

$$\hat{R}_c(z, 0) = \hat{R}_{c,init}(z). \tag{2.81}$$

2.5 Parameter values

2.5.1 Fluid transport

Typical values for the bioreactor dimensions and fluid transport parameters are given in Table 2.1 along with their dimensionless counterparts.

The reduced Reynolds number for the flow, which measures the ratio of inertial to viscous forces in the fluid accounting for the small aspect ratio of the bioreactor, is defined as $\epsilon^2\mathrm{Re} = \epsilon^2\rho UL/\mu$, where ρ is the fluid density. For typical inlet flow rates used in experiments, $Q_{l,in} = 3.33\times10^{-10}$–$3.33\times10^{-8}\,\mathrm{m^3\,s^{-1}}$ (0.02–2 $\mathrm{ml\,min^{-1}}$) [231, 233], $\epsilon^2\mathrm{Re}$ lies in the range 5.3×10^{-4}–$5.3\times10^{-2} \ll 1$, which justifies our neglect of inertia in the lumen and ECS flow equations. We choose the lumen velocity scale as $U = Q_{l,in}/(2\pi R_l^2)$, so that the dimensionless lumen inlet flow rate is $\hat{Q}_{l,in} = 1$.

A rough estimate of the membrane permeability k_m can be obtained from the relationship

$$k_m = Cd_p^2, \tag{2.82}$$

where d_p is the average pore diameter and $C = 6.54\times10^{-4}$ [16] is a constant derived by modelling the flow in the membrane as Poiseuille flow in a series of embedded cylindrical pipes. For $d_p = 1\,\mu\mathrm{m}$, this gives $k_m = 6.54\times10^{-16}\,\mathrm{m^2}$. We determined k_m experimentally by measuring the lumen and ECS outlet flow rates, $Q_{l,out}$ and $Q_{e,out}$, for a prescribed lumen outlet pressure for the single-fibre HFB module without any cells as described in Appendix A. This gave a value of $k_m = 2.39\times10^{-16}\,\mathrm{m^2}$, which agrees fairly well with the rough theoretical estimate and values in the literature of $k_m = 1.86 - 2.35\times10^{-16}\,\mathrm{m^2}$ [233]. The value of the corresponding dimensionless parameter $\kappa_m = \epsilon^2R_l^2/k_m$ is 669. It should be noted that this value will vary significantly depending on how the fibre is made (see Appendix A), so we assume $\kappa_m = \mathcal{O}(1)$ to retain a radial pressure gradient in the membrane at leading order.

The permeability of the cell layer, k_c, is very difficult to measure experimentally and varies to a large degree depending on the initial seeding density and cell type. Assuming the cell layer is densely-packed with cells, we can estimate its permeability from its porosity ϕ_c and the average cell radius d_{cell} using the Kozeny-Carman equation [28, 130]

$$k_c = \frac{\phi_c^3}{(1-\phi_c)^2}\frac{d_{cell}^2}{180}. \tag{2.83}$$

For a porosity of $\phi_c = 0.6$ [231] and a typical cell diameter of $d_{cell} = 10\,\mu\mathrm{m}$, (2.83) gives $k_c \approx 7.5\times10^{-13}\,\mathrm{m^2}$, which agrees reasonably well with the range of values 10^{-12}–10^{-8} used in other studies [104, 105]. Although, these values of k_c give small values for κ_c, the large variation in k_c motivates assuming that $\kappa_c = \mathcal{O}(1)$ to retain $\mathcal{O}(\kappa_c)$ terms at leading order.

Parameter	Description	Typical value	Reference
Dimensional parameters			
R_l	lumen radius	200 µm	[233]
R_m	fibre outer radius	400 µm	[233]
R_e	ECS outer radius	1000 µm	[233]
L	lumen length	10 cm	[233]
ρ	fluid density	1000 kg m^{-3}	[68]
μ	fluid dynamic viscosity	1.00×10^{-3} Pa s	[68]
k_m	membrane permeability	2.39×10^{-16} m^2	Appendix A
k_c	cell layer permeability	7.5×10^{-13} m^2	See text
$Q_{l,in}$	lumen inlet flow rate	3.33×10^{-10}–3.33×10^{-8} m^3 s^{-1} (0.2–2 ml min^{-1})	[231, 233]
$U = Q_{l,in}/(2\pi R_l^2)$	typical axial lumen flow velocity	0.013–0.13 m s^{-1}	-
$P_{l,out}$	lumen outlet pressure	1.027×10^5–2.068×10^5 Pa (14.9–30.0 psi)	[233]
P_{atm}	atmospheric pressure	1.013×10^5 Pa (14.7 psi)	[68]
Dimensionless parameters			
$\epsilon = R_l/L$	lumen aspect ratio	2×10^{-3}	-
$\hat{R}_m$	dimensionless membrane outer surface radius	2	-
$\hat{R}_e$	dimensionless ECS outer wall radius	5	-
$\epsilon^2 \mathrm{Re} = \epsilon^2 \rho U L/\mu$	reduced Reynolds number	5.3×10^{-3}–5.3×10^{-2}	-
ϕ_m	membrane porosity	0.77	[174]
ϕ_c	cell layer porosity	0.6	[231]
$\kappa_m = \epsilon^2 R_l^2/k_m$	dimensionless inverse membrane permeability	669	-
$\kappa_c = k_m/k_c$	ratio of membrane to cell layer permeabilities	3.2×10^{-4}	-
$\hat{Q}_{l,in} = Q_{l,in}/2\pi d_l^2 U$	dimensionless inlet flow rate	1	-
$\hat{P}_{l,out} = \frac{\epsilon^2 L}{\mu U}(P_{l,out} - P_{atm})$	dimensionless lumen outlet pressure	4.2–461	-

Table 2.1: Typical fibre and bioreactor dimensions and fluid transport parameter values for the single-fibre HFB module.

2.5.2 Mass transport

Data on the diffusivities of oxygen and lactate in the different regions of the bioreactor is given in Table 2.2. Diffusion of lactate through the membrane has not been quantified experimentally, so we assume that the relationship between the lumen and membrane diffusivities is the same for lactate as for oxygen, *i.e.* $D_m^L = 0.1 D_l^L$. As far as we are aware, there is also no experimental data on the oxygen and lactate diffusivities for a multilayer cell region in the HFB. Hence, we use the values for cells seeded in alginate throughout the ECS from [231] for D_c, and the lumen diffusivity values for the free fluid region in the ECS ($D_e = D_l$). The reduced Péclet numbers for the oxygen and lactate transport in the different regions, $\epsilon^2 \mathrm{Pe}_i = \epsilon^2 UL/D_i$ $(i = l, m, c, e)$, are calculated from the diffusivities, for the range of lumen flow velocities in Table 2.1. All the reduced Péclet numbers are $\mathcal{O}(1)$ (Table 2.2), so radial diffusion and axial advection of the solute balance in each region.

Parameter	Description	Typical value	Reference
Dimensional Parameters			
Oxygen			
D_l	lumen diffusivity	$3 \times 10^{-9}\,\mathrm{m^2 s^{-1}}$	[231]
D_m	membrane diffusivity	$3 \times 10^{-10}\,\mathrm{m^2 s^{-1}}$	[231]
D_c	cell layer diffusivity	$6 \times 10^{-9}\,\mathrm{m^2 s^{-1}}$	[231]
D_e	ECS diffusivity	$3 \times 10^{-9}\,\mathrm{m^2 s^{-1}}$	[231]
Lactate			
D_l	lumen diffusivity	$1.4 \times 10^{-9}\,\mathrm{m^2 s^{-1}}$	[109]
D_m	membrane diffusivity	$1.4 \times 10^{-10}\,\mathrm{m^2 s^{-1}}$	†
D_c	cell layer diffusivity	$6 \times 10^{-9}\,\mathrm{m^2 s^{-1}}$	[67]
D_e	ECS diffusivity	$1.4 \times 10^{-9}\,\mathrm{m^2 s^{-1}}$	[109]
Dimensionless parameters			
Oxygen			
$\epsilon^2 \mathrm{Pe}_l = \epsilon^2 UL/D_l$	lumen reduced Péclet number	1.77–17.7	-
$\epsilon^2 \mathrm{Pe}_m = \epsilon^2 UL/D_m$	membrane reduced Péclet number	17.7–177	-
$\epsilon^2 \mathrm{Pe}_c = \epsilon^2 UL/D_c$	cell layer reduced Péclet number	0.884–8.84	-
$\epsilon^2 \mathrm{Pe}_e = \epsilon^2 UL/D_e$	ECS reduced Péclet number	1.77–17.7	-
Lactate			
$\epsilon^2 \mathrm{Pe}_l$	lumen reduced Péclet number	3.79–37.9	-
$\epsilon^2 \mathrm{Pe}_m$	membrane reduced Péclet number	0.379–3.79	-
$\epsilon^2 \mathrm{Pe}_c$	cell layer reduced Péclet number	0.884–8.84	-
$\epsilon^2 \mathrm{Pe}_e$	ECS reduced Péclet number	3.79–37.9	-

Table 2.2: Oxygen and lactate diffusivities and reduced Péclet numbers in the different regions of the HFB.
† No experimental data, so $D_m = 0.1 D_l$ assumed for lactate from relationship for oxygen.

Data for the maximum oxygen uptake rate V_{max}^O is available for various cell types, but data for the lactate production rate V_{max}^L is limited to chondrocytes (Table 2.3). The

dimensionless uptake/production rate, $\mathcal{M}$, clearly depends significantly on the cell type and solute, so we assume $\mathcal{M} = \mathcal{O}(1)$ throughout to retain a balance between the rates of uptake/production and diffusion at leading order.

Solute	Cell type	Cell density (cells m^{-3})	V_{max} ($\mathrm{mol\,m^{-3}\,s^{-1}}$)	$\mathcal{M} = V_{max}R_l^2/(CD_c)$ †	Reference
Oxygen	Neonatal rat cardiomyocytes	10^{12}	2.64×10^{-3}	0.08	[215]
	Primary rat hepatocytes	1.25×10^{13}	1.76×10^{-3}	0.053	[246]
	Pancreatic βTC3 cells	2.8×10^{14}	6.37×10^{-3}	0.193	[260]
	Bovine chondrocytes	1.4×10^{14}	4.8×10^{-5}	3.2×10^{-3}	[163, 188]
	Human foreskin fibroblasts (HFFs)	3.8×10^{12}	1.15×10^{-4}	4.0×10^{-3}	[129]
Lactate	Rabbit articular chondrocytes (monolayer)		3.45×10^{-4}	5.7×10^{-3}	[253]
	Bovine articular chondrocytes (3D culture)	1.4×10^{14}	1.32×10^{-5}	2.2×10^{-4}	[188]

Table 2.3: Dimensional and dimensionless oxygen uptake and lactate production rates, V_{max} and $\mathcal{M}$, for different cell types cultured in the HFB. (Adapted from [231].) † $C = C_{in}$ for oxygen and $C = C_L$ for lactate.

The oxygen concentration in the culture medium pumped into the lumen, C_{in}, is set according to cell type: $C_{in} = 0.22\,\mathrm{mol\,m^{-3}}$ for cardiomyocytes, hepatocytes and pancreatic cells [208] and $C_{in} = 0.1\,\mathrm{mol\,m^{-3}}$ for chondrocytes [156, 256]. The typical lactate concentration C_L, meanwhile, we take as $0.4\,\mathrm{mol\,m^{-3}}$ [231]. Values for the oxygen concentration at which the oxygen uptake rate is half-maximal, $C_{1/2}$, are given for various cell types in Table 2.4, along with the corresponding dimensionless values.

2.5.3 Cell layer growth

Values for the cell layer growth parameters for different cell types are summarised in Table 2.5. A detailed discussion of how these parameters are estimated (or chosen) is given in Appendix B.1.

We estimate the growth rate of the cell layer per unit concentration, A_p, for different cell types from their cell doubling times (the times they take to double in number). It is clear from the cell doubling times in Table B.1 that we are justified in assuming

Cell type	C_{in} (mol m^{-3})	$C_{1/2}$ (mol m^{-3})	$c_{1/2} = C_{1/2}/C_{in}$	Reference
Neonatal rat cardiomyocytes	0.22	6.9×10^{-3}	0.031	[215]
Primary rat hepatocytes	0.22	6.24×10^{-3}	0.028	[246]
Pancreatic βTC3 cells	0.22	1.0×10^{-2}	0.045	[241, 260]
Bovine chondrocytes	0.1	5.0×10^{-3}	0.05	[76]
HFFs	0.19	2.1×10^{-3}	0.011	[129]

Table 2.4: Inlet oxygen concentration, C_{in}, and dimensional and dimensionless half-maximal oxygen uptake concentration, $C_{1/2}$ and $c_{1/2}$, for various cell types. (Adapted from [231].)

the fluid and mass transport are quasi-steady on the timescale of cell layer growth, $R_l/(A_p C_{in}) \sim 10^5$ s. The ratio of the advection and cell layer growth timescales, for instance, is $\alpha_p = LA_pC_{in}/(UR_l) = 1.1 \times 10^{-6}$–$3.2 \times 10^{-5} = \mathcal{O}(\epsilon^2)$ for the given cell types for the range of flow rates in Table 2.1. This justifies treating the flow as steady and neglecting the contribution from the cell layer growth in the normal fluid velocity condition at the moving boundary of the cell layer (equation (2.51)). The timescales for the radial diffusion of oxygen and lactate, R_l^2/D_i^O and R_l^2/D_i^L $(i = l, m, c, e)$, are in the ranges 13–130 s and 29–290 s, respectively, so are also much shorter than the growth timescale. Likewise, the timescales for oxygen uptake and lactate production, $C_{in}/V_{max}^O \sim$ 30–2000 s and $C_L/V_{max}^L \sim$ 1000–3000 s (for the cell types in Table 2.3), are much shorter than the

Cell type	A_p (μm hr^{-1}/ (mol m^{-3}))	B_d (μm hr^{-1})	C_{min} (mol m^{-3})	L_{max} (mol m^{-3})	Σ_d (Pa)
Neonatal rat cardiomyocytes	2.3	0.5	6×10^{-3}–8×10^{-2}	0.4	0.03
Primary rat hepatocytes	2.3	0.5	2.1×10^{-2}	0.4	2
Pancreatic βTC3 cells	-	-	1.46×10^{-2}	0.4	1.4
Bovine chondrocytes	1.8	0.2	2.2×10^{-3}–1.32×10^{-2}	0.4	2
HFFs	12.1	2.3	2.1×10^{-2}	0.4	0.03

Table 2.5: Cell layer growth parameter values. Dimensionless shear stress proportionality constant, $\kappa_s = 8.9 \times 10^{-4}$, dimensionless factors for cell layer recession rate for excess lactate and excess shear stress, $B_L = 1$ and $B_s = 1$. See Appendix B.1 for sources and explanation of how A_p, L_{max} and κ_s are estimated.

growth timescale. Thus it is valid to use steady reaction-advection-diffusion equations as in (2.18)–(2.20) to model the leading order solute transport.

2.6 Solution of the reduced model

2.6.1 Fluid transport

From the lumen flow equations (2.44) we have that the lumen pressure is independent of r

$$p_l = p_l(z,t),$$

and, by (2.57) and the fact that the axial velocity must be bounded on $r = 0$, that the lumen axial velocity is given by

$$u_{l,z}(r,z,t) = -\frac{1}{4}\frac{\partial p_l}{\partial z}(1-r^2). \tag{2.84}$$

From (2.44c), the lumen radial velocity is given by

$$u_{l,r} = \frac{1}{16}\frac{\partial^2 p_l}{\partial z^2} r(2-r^2). \tag{2.85}$$

Integrating (2.45c) for the membrane pressure and applying the continuity conditions on $r = 1$ in (2.48) and (2.50), yields

$$p_m = \frac{p_l}{\kappa_m} - \frac{1}{16}\frac{\partial^2 p_l}{\partial z^2}\ln r, \tag{2.86}$$

so the interstitial radial velocity in the membrane is

$$u_{m,r} = \frac{1}{16\phi_m}\frac{\partial^2 p_l}{\partial z^2}\frac{1}{r}. \tag{2.87}$$

Repeating this process for the cell layer with the boundary conditions in (2.49) we obtain

$$p_c = \frac{p_l}{\kappa_c\kappa_m} - \frac{1}{16}\frac{\partial^2 p_l}{\partial z^2}(\ln r + (\tfrac{1}{\kappa_c} - 1)\ln \hat{R}_m). \tag{2.88}$$

The condition on the pressure in the cell layer (2.54) gives us a second order PDE for the lumen pressure

$$\frac{\partial^2 p_l}{\partial z^2} - \lambda^2 p_l = 0, \tag{2.89}$$

where

$$\lambda(z,t)^2 := \frac{16}{\kappa_m(\kappa_c \ln \hat{R}_c(z,t) + (1-\kappa_c)\ln \hat{R}_m)}. \tag{2.90}$$

The term in the denominator is always positive since $\kappa_c > 0$ and $\hat{R}_c(z,t) > \hat{R}_m$, so λ is real and we take it to be the positive root

$$\lambda(z,t) = \sqrt{\frac{16}{\kappa_m(\kappa_c \ln \hat{R}_c(z,t) + (1-\kappa_c)\ln \hat{R}_m)}}. \tag{2.91}$$

The boundary conditions on the pressure at the lumen inlet and outlet, provided by (2.60) and (2.63), are

$$\frac{\partial p_l}{\partial z}(0,t) = -16\hat{Q}_{l,in}, \quad p_l(1,t) = \hat{P}_{l,out}. \tag{2.92}$$

Since λ is a function of both z and t through $\hat{R}_c(z,t)$ (the evolution of which depends on the flow via the oxygen and lactate transport and fluid shear stress), the boundary value problem (2.89)–(2.92) does not in general have an analytical solution and must be solved numerically (see §2.6.3). We note, however, that if the cell layer is of constant depth along the fibre, so that $\hat{R}_c = \text{const.}$ and $\lambda = \text{const.}$, then there is an analytical solution for p_l of the form

$$p_l(z) = \frac{\hat{P}_{l,out}}{\cosh\lambda}\cosh(\lambda z) + \frac{16\hat{Q}_{l,in}}{\lambda\cosh\lambda}\sinh(\lambda(1-z)). \tag{2.93}$$

Using (2.89), the radial velocities in the lumen, membrane and cell layer can be written as

$$u_{l,r}(r,z,t) = \frac{\lambda(z,t)^2 p_l(z,t)}{16} r(2-r^2), \tag{2.94}$$

$$u_{m,r}(r,z,t) = \frac{\lambda(z,t)^2 p_l(z,t)}{16\phi_m r}, \tag{2.95}$$

$$u_{c,r}(r,z,t) = \frac{\lambda(z,t)^2 p_l(z,t)}{16\phi_c r}, \tag{2.96}$$

and the pressures in the membrane and cell-layer as

$$p_m(r,z,t) = \frac{1}{\kappa_m}\left(1 - \frac{\lambda(z,t)^2}{16}\kappa_m \ln r\right) p_l(z,t), \tag{2.97}$$

$$p_c(r,z,t) = \frac{1}{\kappa_c\kappa_m}\left(1 - \frac{\lambda(z,t)^2}{16}\kappa_m(\kappa_c \ln r + (1-\kappa_c)\ln\hat{R}_m)\right) p_l(z,t). \tag{2.98}$$

From (2.46b) and the boundary conditions (2.58) and (2.59) we have that there is no axial flow in the ECS at leading order, *i.e.* $u_{e,z} = 0$. With the continuity of normal velocity at the cell layer outer surface (2.52), the radial velocity in the ECS is

$$u_{e,r}(r,z,t) = \frac{\lambda^2 p_l(z,t)}{16r}. \tag{2.99}$$

Substituting this into (2.46a) gives

$$\frac{\partial p_e}{\partial r} = 0, \tag{2.100}$$

and hence by the pressure condition in (2.59)

$$p_e(r,z,t) = 0, \tag{2.101}$$

i.e. the pressure is constant to leading order in the ECS.

To verify this solution, we check that the mass conservation condition (2.65) is satisfied. By equations (2.60)–(2.62) and (2.84), (2.89) and (2.99) we have that

$$\hat{Q}_{l,in} = \int_{r=0}^{1} \frac{1}{4}\frac{\partial p_l}{\partial z}\bigg|_{z=0}(1-r^2)r\,\mathrm{d}r = -\frac{1}{16}\frac{\partial p_l}{\partial z}\bigg|_{z=0}, \tag{2.102}$$

$$\hat{Q}_{l,out} = \int_{r=0}^{1} \frac{1}{4}\frac{\partial p_l}{\partial z}\bigg|_{z=1}(1-r^2)r\,\mathrm{d}r = -\frac{1}{16}\frac{\partial p_l}{\partial z}\bigg|_{z=1}, \tag{2.103}$$

$$\hat{Q}_{e,out} = \int_{z=0}^{1} \hat{R}_e\frac{\lambda^2 p_l}{16\hat{R}_e}\,\mathrm{d}z = \frac{1}{16}\int_{z=0}^{1}\frac{\partial^2 p_l}{\partial z^2}\,\mathrm{d}z = \frac{1}{16}\left[\frac{\partial p_l}{\partial z}\right]_{z=0}^{1} = -\hat{Q}_{l,out} + \hat{Q}_{l,in}, \tag{2.104}$$

so (2.65) is indeed satisfied.

Maximum lumen outlet pressure

If the lumen outlet pressure $P_{l,out}$ is too high when the ECS port is open, there will be backflow rather than outflow at the lumen exit. We determine the threshold below which $P_{l,out}$ should be kept in our simulations to prevent backflow by requiring that

$$\hat{Q}_{l,out} = -\frac{1}{16}\frac{\partial p_l}{\partial z}\bigg|_{z=1} > 0. \tag{2.105}$$

For the values of κ_m and κ_c estimated in §2.5.1, the variations in λ as $\hat{R}_c(z,t)$ varies in z and t are small ($\mathcal{O}(10^{-5})$). Hence, to estimate $\hat{Q}_{l,out}$, we can approximate the lumen pressure by the analytical solution for constant $\hat{R}_c$ given in (2.93). Substituting this into (2.105) gives

$$\hat{Q}_{l,out} \approx \frac{1}{16\cosh\lambda}(16\hat{Q}_{l,in} - \hat{P}_{l,out}\lambda\sinh\lambda) > 0,$$

so that the maximum lumen outlet pressure is approximately

$$\hat{P}_{l,out}^{max} \approx \frac{16\hat{Q}_{l,in}}{\lambda\sinh\lambda}, \tag{2.106}$$

or in dimensional terms

$$P_{l,out}^{max} \approx P_{atm} + \frac{\mu U}{\epsilon^2 L}\frac{16\hat{Q}_{l,in}}{\lambda\sinh\lambda}. \tag{2.107}$$

The maximum lumen outlet pressure that can be used therefore increases approximately linearly as the inlet flow rate $Q_{l,in}$ increases. The radial flow through the membrane, cell layer and ECS is proportional to p_l (see (2.95), (2.96) and (2.99)), so to maximise oxygen delivery and lactate clearance to and from the cell layer the maximum lumen outlet pressure $P_{l,out}^{max}$ and flow rate should be used. Since $P_{l,out}^{max}$ depends on the membrane and cell layer depths and permeabilities through λ, it is useful to know how it varies with these parameters. For the parameter values given in §2.5.1 and a cell layer of even depth along the fibre, $P_{l,out}^{max}$ is an increasing function of the depths of the membrane and cell layer, $(R_c - R_m)$ and $(R_m - R_l)$, and a decreasing function of their permeabilities, k_m and k_c (Figures 2.2(a) and

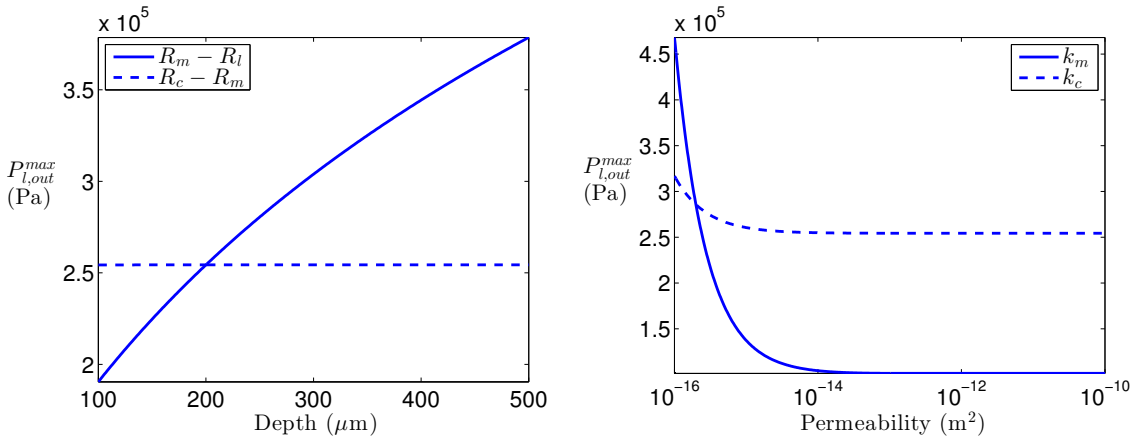

Figure 2.2: Variation in the maximum lumen outlet pressure without backflow, $P^{max}_{l,out}$, with (a) the membrane and cell layer depths, $(R_m - R_l)$ and $(R_c - R_m)$, and (b) the membrane and cell layer permeabilities, k_m and k_c, for a cell layer of uniform depth. Parameter values (when held constant): $Q_{l,in} = 3.33 \times 10^{-8}\,\mathrm{m^3\,s^{-1}}$, $P_{l,out} = 1.379 \times 10^5\,\mathrm{Pa}$, $R_m = 400\,\mu\mathrm{m}$, $R_c(z,t) = 450\,\mu\mathrm{m}$, $k_m = 2.39 \times 10^{-16}\,\mathrm{m^2}$, $k_c = 7.5 \times 10^{-13}\,\mathrm{m^2}$. All other parameter values as in Table 2.1.

2.2(b)). This is because the resistance to the flow provided by the membrane and cell layer increases as their depths increase and as their permeabilities decrease, and $P^{max}_{l,out}$ increases as the resistance increases. It is evident from Figure 2.2, however, that for our experimentally-determined value for k_m ($2.39 \times 10^{-16}\,\mathrm{m^2}$) and estimate for k_c ($7.5 \times 10^{-13}\,\mathrm{m^2}$), $P^{max}_{l,out}$ is more sensitive to variation in $(R_m - R_l)$ and k_m than in $(R_c - R_m)$ and k_c. This is due to the experimentally-determined value for k_m being much smaller than the estimate for k_c, which means that the membrane provides most of the resistance to flow.

2.6.2 Mass transport

To solve the reduced system for the solute transport we first substitute the flow velocities (2.84), (2.94)–(2.96) and (2.99) into (2.68)-(2.70) (noting that $u_{i,z} = \mathcal{O}(\epsilon^2)$ for $i = m, c, e$), to obtain the leading order system

$$\epsilon^2 \mathrm{Pe}_l \left(\frac{\lambda^2 p_l}{16r} \frac{\partial}{\partial r}(c_l r^2(2 - r^2)) - \frac{1}{4}(1 - r^2) \frac{\partial}{\partial z}\left(c_l \frac{\partial p_l}{\partial z} \right) \right) = \frac{1}{r} \frac{\partial}{\partial r}\left(r \frac{\partial c_l}{\partial r} \right), \tag{2.108}$$

$$\epsilon^2 \mathrm{Pe}_i \frac{\lambda^2 p_l}{16} \frac{\partial c_i}{\partial r} = \frac{\partial}{\partial r}\left(r \frac{\partial c_i}{\partial r} \right) \quad \text{for } i = m, e, \tag{2.109}$$

$$\epsilon^2 \mathrm{Pe}_c \frac{\lambda^2 p_l}{16} \frac{\partial c_c}{\partial r} = \frac{\partial}{\partial r}\left(r \frac{\partial c_c}{\partial r} \right) + m\mathcal{M} r. \tag{2.110}$$

Solving (2.109) and (2.110) gives

$$c_i(r,z,t) = A_i(z,t) + B_i(z,t)r^{n_i(z,t)} \quad \text{for } i = m, e, \tag{2.111}$$

$$c_c(r,z,t) = A_c(z,t) + B_c(z,t)r^{n_c(z,t)} + \frac{m\mathcal{M}}{2(n_c(z,t)-2)}r^2, \tag{2.112}$$

where

$$n_i(z,t) := \frac{\epsilon^2 \mathrm{Pe}_i \lambda^2 p_l(z,t)}{16}, \quad i = m, c, e, \tag{2.113}$$

and $A_i(z,t)$, $B_i(z,t)$ $(i = m, c, e)$ remain to be determined from the boundary conditions. By (2.78) we have

$$\frac{\partial c_e}{\partial r}(\hat{R}_e, z, t) = n_e B_e(z,t)\hat{R}_e^{n_e - 1} = 0,$$

so $B_e(z,t) = 0$ and

$$c_e(r,z,t) = A_e(z,t), \tag{2.114}$$

i.e. the ECS concentration is constant in r at leading order.

By the flux continuity conditions on $r = \hat{R}_c(z,t)$ and $r = \hat{R}_m$

$$B_c(z,t) = -\frac{m\mathcal{M}\hat{R}_c^{2-n_c}}{n_c(n_c-2)}, \tag{2.115}$$

$$\begin{aligned} B_m(z,t) &= \frac{\phi_c D_c}{\phi_m D_m}\frac{1}{n_m}\left(n_c B_c(z,t)\hat{R}_m^{n_c - n_m} + \frac{m\mathcal{M}\hat{R}_m^{2-n_m}}{n_c - 2}\right) \\ &= -\frac{\phi_c D_c}{\phi_m D_m}\frac{m\mathcal{M}}{n_m(n_c-2)}(\hat{R}_m^{n_c-n_m}\hat{R}_c^{2-n_c} - \hat{R}_m^{2-n_m}). \end{aligned} \tag{2.116}$$

Substituting (2.111) into the flux continuity condition on $r = 1$ in (2.48) gives

$$\frac{\partial c_l}{\partial r}(1,z,t) = \frac{\phi_m D_m}{D_l}\frac{\partial c_m}{\partial r}(1,z,t) = \frac{\phi_m D_m}{D_l} n_m(z,t) B_m(z,t). \tag{2.117}$$

Analysis of the right-hand side of (2.117) for typical parameter values (as given in §2.5) reveals that it is $\mathcal{O}(\epsilon^2)$ or smaller so can be neglected at leading order [231]. Thus, at leading order, there is no diffusive flux of oxygen or lactate across $r = 1$ (solute transport across $r = 1$ is purely advective). By (2.71) we know that $\frac{\partial c_l}{\partial r}(0,z,t) = 0$, and substituting $c_l = \text{const.}$ into (2.108) reduces it to a multiple of the PDE for p_l

$$\frac{1}{4}\epsilon^2 \mathrm{Pe}_l(1-r^2)\left(\lambda^2 p_l - \frac{\partial^2 p_l}{\partial z^2}\right) = 0,$$

so we know that $c_l = \text{const.}$ is a solution. Therefore, by (2.76), we have that

$$c_l(r,z,t) = \begin{cases} 1 & \text{for oxygen,} \\ 0 & \text{for lactate,} \end{cases} \tag{2.118}$$

i.e. the fluid pumped into the lumen passes through it too quickly to register the oxygen uptake and lactate production in the cell layer. Hence, the concentration continuity condition on $r = 1$ in (2.72) gives

$$A_m(z,t) = c_l(1,z,t) - B_m(z,t) \approx c_l(1,z,t) = \begin{cases} 1 & \text{for oxygen,} \\ 0 & \text{for lactate,} \end{cases} \tag{2.119}$$

and those on $r = \hat{R}_m$ and $r = \hat{R}_c(z,t)$ in (2.73) and (2.74) give

$$\begin{aligned} A_c(z,t) &= c_l + B_m(z,t)\hat{R}_m^{n_m} - B_c(z,t)\hat{R}_m^{n_c} - \frac{m\mathcal{M}\hat{R}_m^2}{2(n_c-2)} \\ &= c_l + \frac{m\mathcal{M}}{n_c-2}\left(-\frac{\phi_c D_c}{\phi_m D_m}\frac{1}{n_m}(\hat{R}_m^{n_c}\hat{R}_c^{2-n_c} - \hat{R}_m^2) + \frac{\hat{R}_c^{2-n_c}\hat{R}_m^{n_c}}{n_c} - \frac{\hat{R}_m^2}{2}\right), \end{aligned} \tag{2.120}$$

$$\begin{aligned} A_e(z,t) &= A_c(z,t) + B_c(z,t)\hat{R}_c^{n_c} + \frac{m\mathcal{M}\hat{R}_c^2}{2(n_c-2)} \\ &= c_l + \frac{m\mathcal{M}}{n_c-2}\left(-\frac{\phi_c D_c}{\phi_m D_m}\frac{1}{n_m}(\hat{R}_m^{n_c}\hat{R}_c^{2-n_c} - \hat{R}_m^2) + \frac{\hat{R}_c^{2-n_c}\hat{R}_m^{n_c}}{n_c} - \frac{\hat{R}_m^2}{2} + \left(\frac{1}{2} - \frac{1}{n_c}\right)\hat{R}_c^2\right). \end{aligned} \tag{2.121}$$

2.6.3 Numerical solution of the leading order system

The leading order system for the fluid flow, oxygen and lactate transport and cell layer growth is given by equations (2.79)–(2.81), (2.89)–(2.92), (2.94)–(2.99), (2.111)–(2.113), (2.115)–(2.116), and (2.118)–(2.121). Since derivatives with respect to r have been integrated out in deriving these equations, they constitute a system of PDEs and boundary and initial conditions in z and t. Due to the interdependence between the flow, solute transport and cell layer growth, the system must be solved numerically. We do this using the method of lines, *i.e.* by discretising the system in z (with a grid space of $\Delta z = 2 \times 10^{-3}$) and then solving the resulting system of time-dependent ordinary differential equations (ODEs) using the MATLAB ODE solver `ode113`.

At each time step, the steady flow and solute transport problems are solved for the current position of the cell layer outer surface, and the solutions used to update the position of the outer surface via the growth law (2.79). We solve the boundary value problem for the lumen fluid pressure (2.89)–(2.92) at each time step using the MATLAB boundary value problem solver `bvp4c` with $\Delta z = 2 \times 10^{-3}$, and verify that the solution for p_l satisfies the conservation of mass condition in (2.65). The convergence of the numerical scheme was verified by reducing Δz and the time step and checking that the results were the same to a relative tolerance of 0.01%.

The algorithm for determining the cell layer growth can be summarised as follows:

1. Prescribe the initial position of the cell layer outer surface, *i.e.* set $\hat{R}_c(z,0) = \hat{R}_{c,init}(z)$.
2. Determine the fluid pressures and velocities and solute concentrations throughout the bioreactor for the given position of the cell layer outer surface, by solving (2.89)–(2.92) for p_l and evaluating (2.94)–(2.99), (2.111)–(2.113), (2.115)–(2.116), and (2.120)–(2.121).
3. Evaluate the oxygen and lactate concentrations and shear stress at $r = \hat{R}_c(z,t)$ and use these to update $\hat{R}_c(z,t)$ according to the growth law (2.79).
4. Repeat Steps 1–3 until the simulation time (60 days) elapses, or the system reaches a steady state, or the cell layer grows to fill the entire ECS or recedes to the fibre surface (whichever occurs first).

2.7 Flow profiles and oxygen and lactate distributions

Before simulating the growth of the cell layer we compare the fluid flow and oxygen and lactate distributions in the bioreactor for layers of rat cardiomyocytes of uniform and non-uniform depths. For simplicity we consider a layer with a uniform depth of 50 µm (*i.e.* $R_c(z,t) = 450\,\mu\text{m}$) and a cell layer of the same volume whose depth decreases linearly with z from 80 µm at the upstream end of the bioreactor to 19 µm at the downstream end. We use the parameter values for rat cardiomyocytes given in Tables 2.1–2.4, together with $V_{max}^L = 1.32 \times 10^{-3}\,\text{mol}\,\text{m}^{-3}\,\text{s}^{-1}$ [231]. All results are displayed in dimensional variables.

2.7.1 Fluid pressures and velocities

Figures 2.3(a) and 2.3(b) show the fluid pressure throughout the bioreactor for the uniform cell layer and non-uniform cell layer respectively. There is very little difference between the two, as most of the pressure drop from the lumen to the ECS occurs across the membrane and there is little change in the pressure across the cell layer (which is marginally above atmospheric pressure). This is due to the considerably higher permeability of the cell layer. The lumen pressure p_l decreases approximately linearly with z. The lumen axial velocity $u_{l,z}$ is therefore close to identical for the uniform and non-uniform cell layers (the maximum difference between the two being approximately $2 \times 10^{-9}\,\text{m}\,\text{s}^{-1}$). It decreases with z since it is proportional to the pressure gradient $\frac{\partial p_l}{\partial z}$ (which is determined by $Q_{l,in}$ and $P_{l,out}$), and decreases quadratically with r (Figure 2.4(a)). The radial flow velocity, u_r, defined as

$$u_r = \begin{cases} u_{l,r} & \text{for } r \in [0, R_l],\ z \in [0, L], \\ \phi_m u_{m,r} & \text{for } r \in [R_l, R_m],\ z \in [0, L], \\ \phi_c u_{c,r} & \text{for } r \in [R_m, R_c(z)],\ z \in [0, L], \\ u_{e,r} & \text{for } r \in [R_c(z), R_e],\ z \in [0, L], \end{cases}$$

is also virtually identical for the uniform and non-uniform cell layers (the maximum difference again being approximately $2 \times 10^{-9}\,\mathrm{m\,s^{-1}}$); it is proportional to p_l so decreases with z and increases with r from 0 along the lumen axis to a maximum of $77\,\mu\mathrm{m\,s^{-1}}$ at $r = 163\,\mu\mathrm{m}$ at the inlet, then like $1/r$ in the membrane, cell layer and ECS (Figure 2.4(b)).

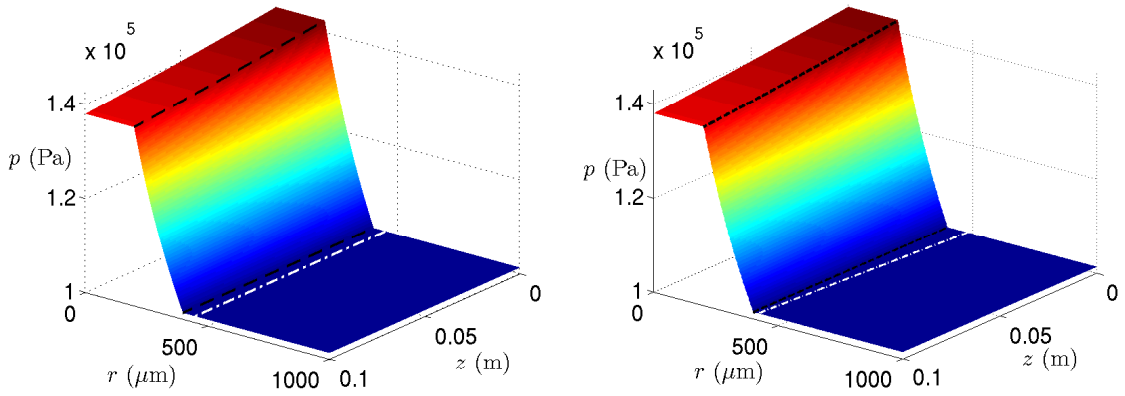

Figure 2.3: Typical fluid pressure in the bioreactor, p, for (a) a uniform depth cell layer, $R_c = 450\,\mu\mathrm{m}$, and (b) a non-uniform cell layer, $R_c = (480 - 6.1 \times 10^{-4} z)\,\mu\mathrm{m}$. All parameter values as in Figure 2.2. Lumen axis running from right to left. Black dashed lines indicate the membrane surfaces and the white dashed lines the outer surface of the cell layer.

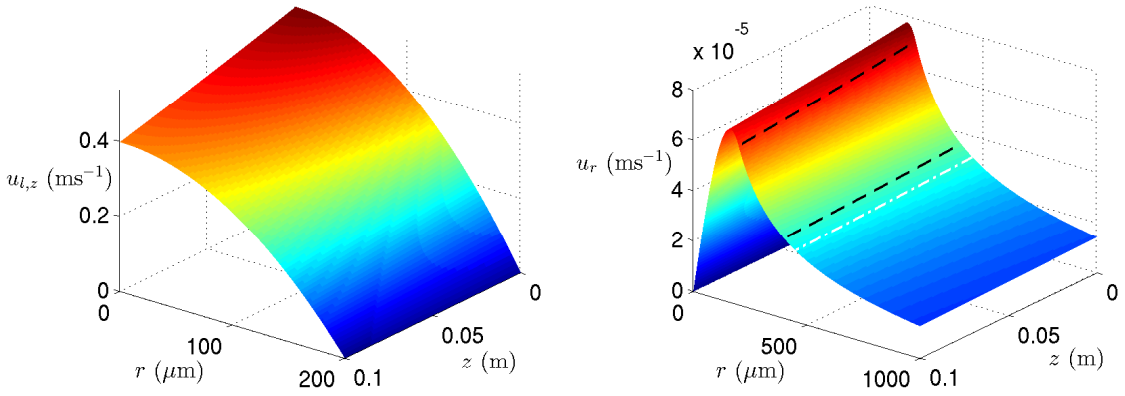

Figure 2.4: (a) Lumen axial flow velocity $u_{l,z}$ and (b) radial flow velocity u_r for the uniform depth cell layer in Figure 2.3(a). Profiles for the non-uniform cell layer in Figure 2.3(b) are almost identical. All parameter values and dashed lines as in Figure 2.3.

2.7.2 Oxygen and lactate concentrations

The oxygen and lactate concentrations throughout the bioreactor for the uniform and non-uniform cell layers are shown in Figures 2.5(a) and 2.5(b). For the uniform cell layer, the oxygen concentration is a decreasing function of r and z as far as the ECS, where it is constant in r, and so reaches a minimum of $0.216\,\mathrm{mol\,m^{-3}}$ at the ECS wall surrounding the lumen outlet ($r \in [R_c, R_e]$, $z = L$). For the non-uniform cell layer, the oxygen concentration decreases with r, but increases with z in the ECS since less oxygen is taken up where the cell layer is thinner. The minimum oxygen concentration, $0.207\,\mathrm{mol\,m^{-3}}$, is therefore reached on the wall surrounding the lumen inlet ($r \in [R_c(0), R_e]$, $z = 0$), and is lower than for the uniform cell layer as the non-uniform layer is deeper than it at that point.

The lactate concentration increases with r and z to a maximum of $1.8 \times 10^{-3}\,\mathrm{mol\,m^{-3}}$ on $z = L$, $r \in [R_c, R_e]$ for the uniform depth cell layer (Figure 2.6(a)). For the non-uniform cell layer, the lactate concentration still increases with r, but decreases with z in the ECS as less lactate is produced as the cell layer depth decreases (Figure 2.6(b)). Hence, the lactate concentration reaches a maximum of $2.7 \times 10^{-3}\,\mathrm{mol\,m^{-3}}$ on the wall around the inlet.

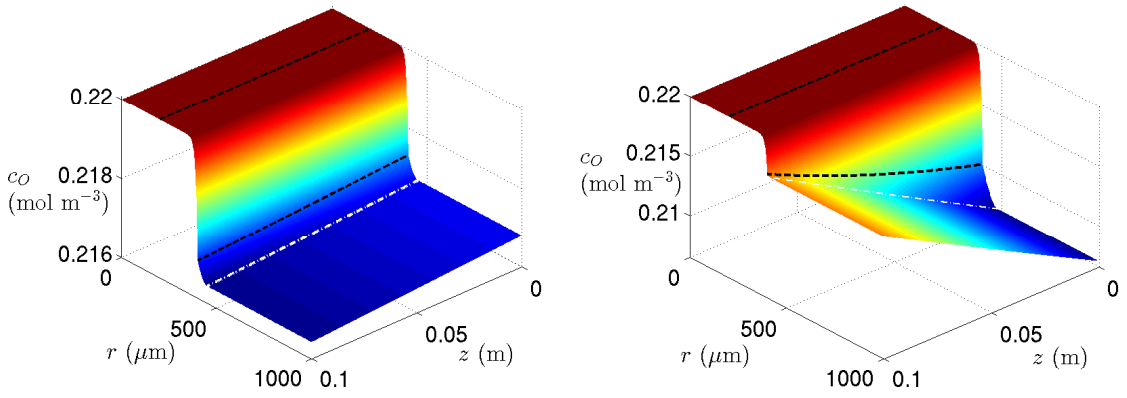

Figure 2.5: Oxygen concentration in the bioreactor, c_O for (a) the uniform depth rat cardiomyocyte layer, and (b) the non-uniform depth rat cardiomyocyte layer. Fluid transport parameter values as in Figure 2.3, and oxygen transport parameter values for rat cardiomyocytes as in Tables 2.3–2.4. Dashed lines as in Figure 2.3.

2.7.3 Changes in flow and oxygen and lactate distributions with cell layer growth

So far we have described the fluid flow and oxygen and lactate distributions in the bioreactor for a static cell layer. We now describe briefly how they change as the cell layer grows to explain the feedback effects this has on the growth.

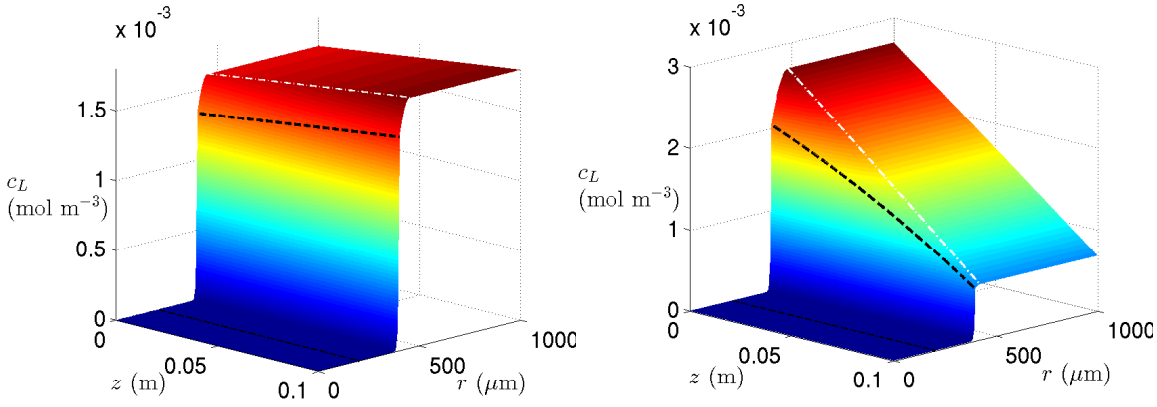

Figure 2.6: Lactate concentration in the bioreactor, c_L, for (a) the uniform depth rat cardiomyocyte layer, and (b) the non-uniform rat cardiomyocyte layer. Parameters as in Figure 2.5 with $V_{max}^L = 1.32 \times 10^{-3}\,\mathrm{mol\,m^{-3}}$. Lumen axis running from left to right.

If $\sigma|_{r=R_c} < \Sigma_d$, $c_O|_{r=R_c} > C_{min}$ and $c_L|_{r=R_c} < L_{max}$ (or $c_L|_{r=R_c} > L_{max}$ and the positive effect of oxygen on growth outweighs the negative effect of lactate), then the cell layer grows outwards. As it does so, the surface oxygen concentration $c_O|_{r=R_c}$ decreases and the surface lactate concentration $c_L|_{r=R_c}$ increases, so that the growth slows with time. If $c_L|_{r=R_c} < L_{max}$ and $c_O|_{r=R_c}$ decreases to C_{min}, or $c_O|_{r=R_c} > C_{min}$ and $c_L|_{r=R_c} > L_{max}$ and the positive and negative effects of oxygen and lactate on the growth come to balance each other, then the cell layer reaches a steady state depth. For fixed $Q_{l,in}$ and $P_{l,out}$, the radial flow decreases slightly as the cell layer grows, due to the increase in resistance to the flow through the ECS. Combined with the decrease in the radial velocity with r, this means that the shear stress on the cells at the cell layer surface decreases as the layer grows. Hence, if $\sigma|_{r=R_c}$ is initially below Σ_d, it will remain so as the cell layer grows. Conversely, if $\sigma|_{r=R_c}$ is initially above Σ_d, then the cell layer recedes and the shear stress on the surface cells increases. Hence, the layer will continue to recede until it reaches the fibre surface.

2.8 Numerical simulations of cell layer growth

Given how c_O, c_L and σ change as the cell layer grows, to maximise the growth of the cell layer we require $c_O|_{r=R_c} > C_{min}$, $c_L|_{r=R_c} < L_{max}$, and $\sigma|_{r=R_c} < \sigma_d$ where possible. For the purposes of this investigation we assume that the bioreactor dimensions and properties of the membrane (its depth and permeability) are fixed, and that we can only vary the operating parameters $Q_{l,in}$ and $P_{l,out}$ and the initial depth of the cell layer $(R_{c,init}(z) - R_m)$.

As the leading order system for the flow, solute transport and cell layer growth must be solved numerically, we do not attempt to define operating equations for $Q_{l,in}$ and $P_{l,out}$ based on the conditions on c_O, c_L and σ as in [231, 234]. Instead, we simulate and compare the growth of cell types with different oxygen demands and shear stress tolerances for typical flow rate and outlet pressure ranges used in experiments, $Q_{l,in} \in [3.33\times10^{-9}\,\mathrm{m^3\,s^{-1}}, 3.33\times10^{-8}\,\mathrm{m^3\,s^{-1}}]$ and $P_{l,out} \in [1.027\times10^5\,\mathrm{Pa}, 2.068\times10^5\,\mathrm{Pa}]$. The cell types we consider are rat cardiomyocytes, which have high oxygen requirements ($V^O_{max} = 2.64^{-3}\,\mathrm{mol\,m^{-3}\,s^{-1}}$, $C_{min} = 8\times10^{-2}\,\mathrm{mol\,m^{-3}}$) and are assumed to have low shear stress tolerance ($\Sigma_d = 0.03\,\mathrm{Pa}$), and bovine chondrocytes, which have low oxygen requirements ($V^O_{max} = 4.8^{-5}\,\mathrm{mol\,m^{-3}\,s^{-1}}$, $C_{min} = 5\times10^{-3}\,\mathrm{mol\,m^{-3}}$) and can withstand much higher shear stresses ($\Sigma_d = 2\,\mathrm{Pa}$). We assume for these simulations that the cell layer initially has an even depth along the fibre of 50 µm, *i.e.* $R_{c,init}(z) = 450\,\mu\mathrm{m}$. From the simulations we are able to predict for each cell type optimal values of $Q_{l,in}$ and $P_{l,out}$ to maximise the cell layer growth, *i.e.* to grow the cell layer to the maximum possible depth or to fill the ECS in the shortest time. We also briefly consider the impact of variation in the initial cell layer depth with z on the cell layer growth, and the sensitivity of the growth to the lactate toxicity threshold, L_{max}.

The simulations are run until the cell layer grows to fill the whole of the ECS (or completely recedes to the fibre surface, or reaches a steady state), in which case the time at which this happens is recorded, or until $T = 60$ days have elapsed, in which case the mean and standard deviation of the final outer radius of the cell layer, $\overline{R}_c = \frac{1}{L}\int_0^L R_c(z,T)\,\mathrm{d}z$ and $\mathrm{SD} = \frac{1}{L}\int_0^L (R_c(z,T) - \overline{R}_c)^2\,\mathrm{d}z$, are recorded. The culture time of 60 days is chosen on the basis that major degradation of the PLGA in the membrane would occur with a longer culture time [13, 111], resulting in a significant increase in the membrane permeability and invalidating our assumption that it remains constant. All of the simulation results are presented in dimensional variables to facilitate comparison between the two cell types.

2.8.1 Impact of flow rate and outlet pressure on growth

The oxygen and lactate concentrations and shear stress at the surface of the cell layer, which determine the rate of growth, depend on $Q_{l,in}$ and $P_{l,out}$. Figures 2.7(a) and 2.7(b) show how $\overline{R}_c$ varies with $Q_{l,in}$ and $P_{l,out}$ for cardiomyocytes and chondrocytes respectively.

The cell layer does not grow to fill the ECS in 60 days for either cell type for any combination of the flow rate and outlet pressure in the ranges considered. However for the cardiomyocytes, $\overline{R}_c$ increases up to 871 µm as $Q_{l,in}$ increases up to $3.33\times10^{-8}\,\mathrm{m^3\,s^{-1}}$ and $P_{l,out}$ increases up to $1.965\times10^5\,\mathrm{Pa}$, and then decreases sharply as $P_{l,out}$ increases above $1.965\times10^5\,\mathrm{Pa}$. This is due to the balance of the effects of increased oxygen concentration and increased shear stress at the surface of the cell layer as $Q_{l,in}$ and $P_{l,out}$ increase

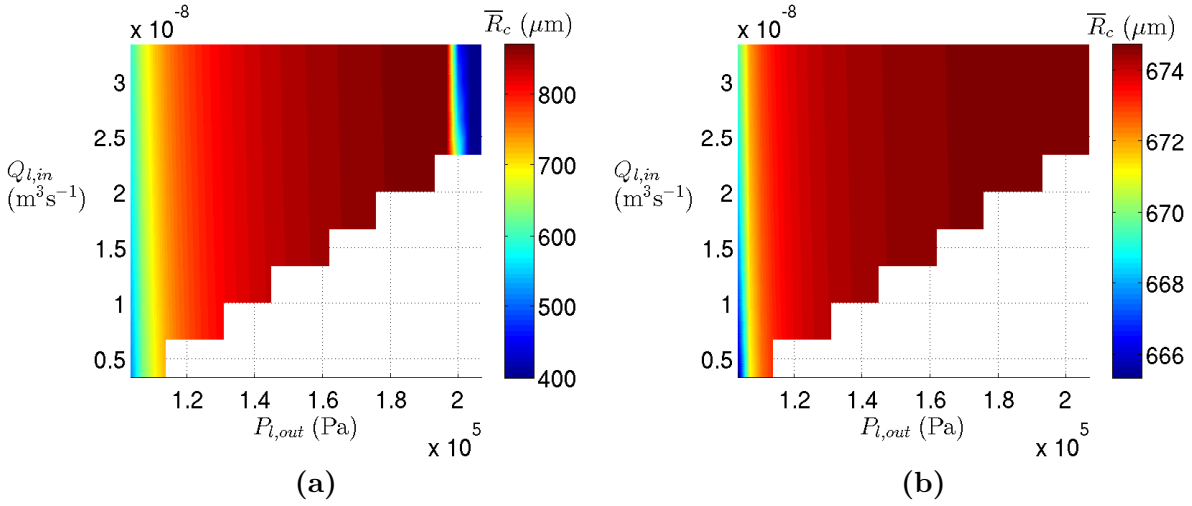

Figure 2.7: Variation in the mean final outer radius of the cell layer $\overline{R}_c$ with the lumen inlet flow rate $Q_{l,in}$ and lumen outlet pressure $P_{l,out}$ for (a) rat cardiomyocytes, and (b) bovine chondrocytes, after 60 days of culture with the ECS port open. Initial cell layer outer radius: $R_{c,init}(z) = 450\,\mu\text{m}$. Parameter values: (a) $V^O_{max} = 2.64 \times 10^{-3}\,\text{mol}\,\text{m}^{-3}\,\text{s}^{-1}$, $V^L_{max} = 1.32 \times 10^{-3}\,\text{mol}\,\text{m}^{-3}\,\text{s}^{-1}$, $C_{min} = 8 \times 10^{-2}\,\text{mol}\,\text{m}^{-3}$, $L_{max} = 0.4\,\text{mol}\,\text{m}^{-3}$, $\Sigma_d = 0.03\,\text{Pa}$, (b) $V^O_{max} = 4.8 \times 10^{-5}\,\text{mol}\,\text{m}^{-3}\,\text{s}^{-1}$, $V^L_{max} = 1.32 \times 10^{-5}\,\text{mol}\,\text{m}^{-3}\,\text{s}^{-1}$, $C_{min} = 1.32 \times 10^{-2}\,\text{mol}\,\text{m}^{-3}$, $L_{max} = 0.4\,\text{mol}\,\text{m}^{-3}$, $\Sigma_d = 2\,\text{Pa}$; all other parameter values as in Tables 2.1, 2.2, 2.4 and 2.5.

($c_L \ll L_{max}$ for both cell types over the range of flow rates and outlet pressures considered). For $P_{l,out} < 1.965 \times 10^5\,\text{Pa}$, the shear stress σ is below the cell death threshold, $\Sigma_d = 0.03\,\text{Pa}$, so there is no cell death (Figure 2.8), and cell proliferation increases as $Q_{l,in}$ and $P_{l,out}$ increase due to improved oxygen delivery. For $P_{l,out} > 1.965 \times 10^5\,\text{Pa}$, $\sigma > \Sigma_d$ so cells die and the cell layer recedes towards the fibre surface (Figure 2.9). For chondrocytes $\overline{R}_c$ increases monotonically as $Q_{l,in}$ and $P_{l,out}$ increase, since the shear stress remains far below the threshold at which they die, $\Sigma_d = 2\,\text{Pa}$.

The model therefore predicts that to maximise the growth of the cardiomyocyte layer the maximum flow rate, $Q_{l,in} = 3.33 \times 10^{-8}\,\text{m}^3\,\text{s}^{-1}$, and an outlet pressure of $P_{l,out} = 1.965 \times 10^5\,\text{Pa}$ should be used; while for the chondrocytes the maximum flow rate and maximum outlet pressure, $P_{l,out} = 2.068 \times 10^5\,\text{Pa}$, should be used.

For the cardiomyocytes, the standard deviation in the final outer radius of the cell layer, SD, decreases as $Q_{l,in}$ decreases and as $P_{l,out}$ increases for $P_{l,out} < 1.931 \times 10^5\,\text{Pa}$, ranging from $0.2\,\mu\text{m}$ with $Q_{l,in} = 2 \times 10^{-8}\,\text{m}^3\,\text{s}^{-1}$ and $P_{l,out} = 1.931 \times 10^5\,\text{Pa}$ to $44\,\mu\text{m}$ with $Q_{l,in} = 3.33 \times 10^{-8}\,\text{m}^3\,\text{s}^{-1}$ and $P_{l,out} = 1.034 \times 10^5\,\text{Pa}$. For the chondrocytes, SD also decreases as $Q_{l,in}$ decreases and $P_{l,out}$ increases, but is much smaller, SD = 0–2 μm. The greater variation in the final depth of the cell layer for the cardiomyocytes is due to their

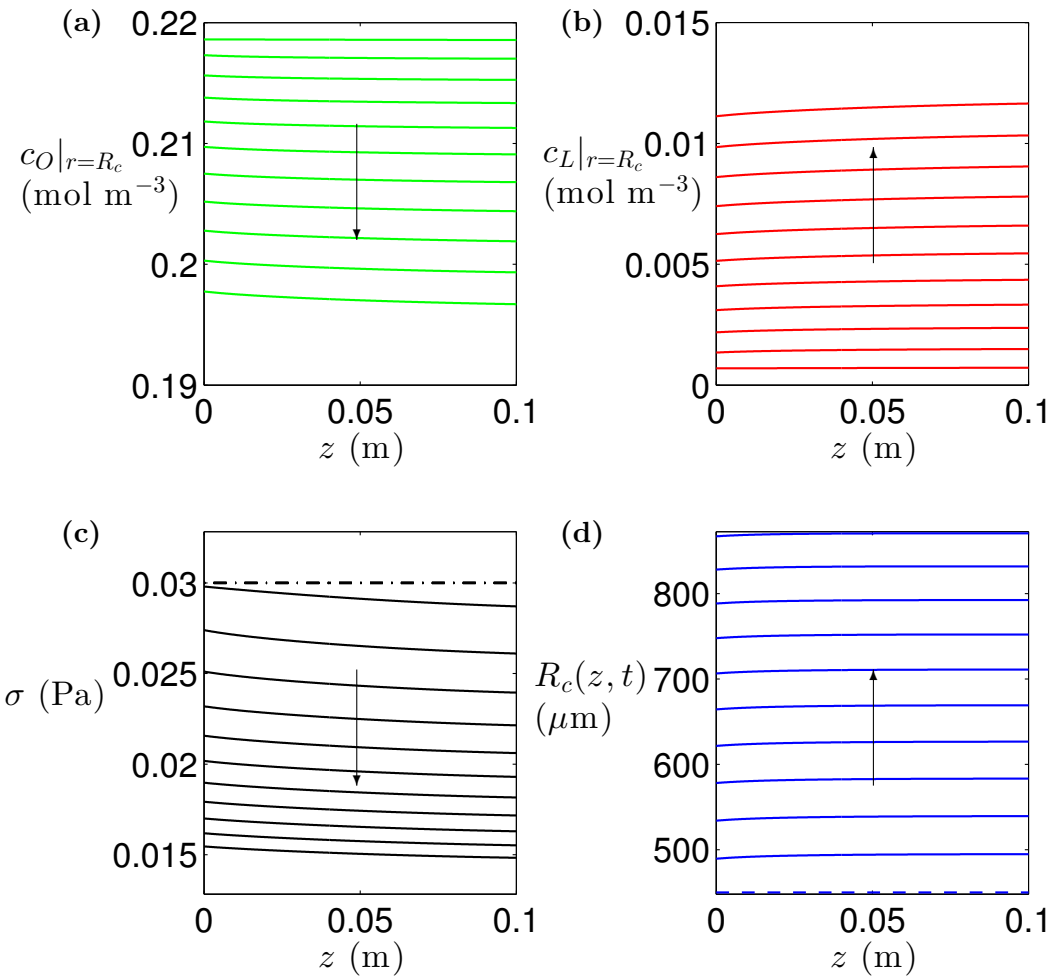

Figure 2.8: Evolution of (a) the surface oxygen concentration $c_O|_{r=R_c}$, (b) surface lactate concentration $c_L|_{r=R_c}$, (c) surface interstitial shear stress $\sigma|_{r=R_c}$ and (d) outer surface $r = R_c(z,t)$ of a layer of rat cardiomyocytes at the optimal flow rate and outlet pressure. Mean final outer radius $\overline{R}_c = 871\,\mu\text{m}$, standard deviation in final outer radius SD $= 3\,\mu\text{m}$. Initial cell layer depth and parameter values as in Figure 2.7(a) with $Q_{l,in} = 3.33 \times 10^{-8}\,\text{m}^3\,\text{s}^{-1}$, $P_{l,out} = 1.965 \times 10^5\,\text{Pa}$. Arrows show direction of increasing time, solid lines the variables at regular time intervals, black dashed line the shear stress cell death threshold Σ_d, and blue dashed line the initial cell layer outer radius $R_{c,init}(z)$.

higher oxygen uptake rate, which means that at low outlet pressures increasing the flow rate only increases oxygen delivery to the upstream end of the cell layer, which therefore grows much more quickly than the downstream end.

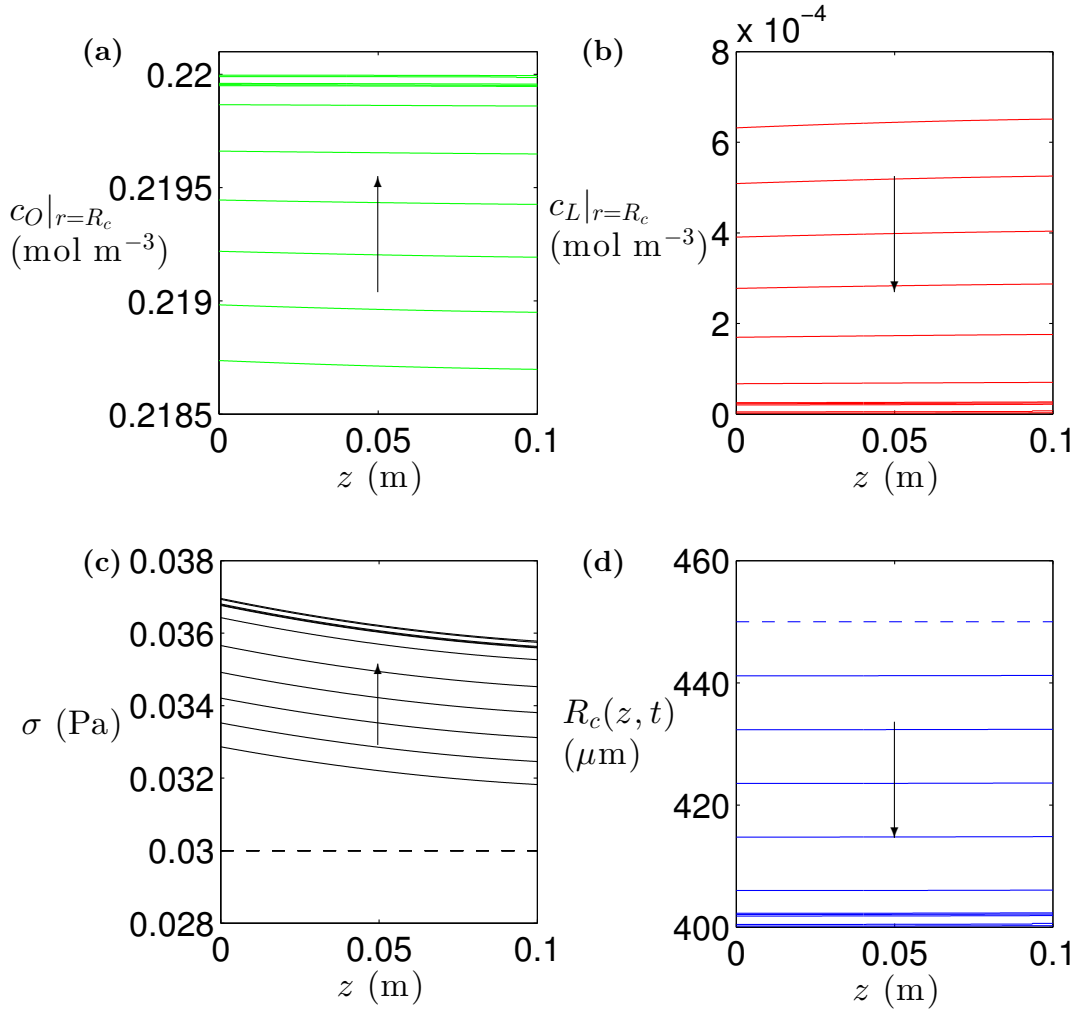

Figure 2.9: Evolution of (a) $c_O|_{r=R_c}$, (b) $c_L|_{r=R_c}$, (c) $\sigma|_{r=R_c}$ and (d) $R_c(z,t)$ for a layer of rat cardiomyocytes with too high an outlet pressure. Parameter values as in Figure 2.8 with $Q_{l,in} = 3.33 \times 10^{-8}\,\mathrm{m^3\,s^{-1}}$, $P_{l,out} = 2.068 \times 10^5\,\mathrm{Pa}$. Lines and arrows as in Figure 2.8.

2.8.2 Impact of variation in initial cell layer depth on growth

In the simulations in the previous section we assumed that the initial cell layer had a uniform depth along the fibre. However, as we saw in §2.7.2, the oxygen and lactate distributions vary with the uniformity of the cell layer, so it is likely that non-uniformity in the initial depth of the cell layer will affect its subsequent growth. Here we demonstrate that variation in the depth can have a major impact on the growth.

Take, for example, the predicted optimal conditions for the growth of the rat cardiomyocyte layer in the previous section, $Q_{l,in} = 3.33 \times 10^{-8}\,\mathrm{m^2 s^{-1}}$ and $P_{l,out} = 1.965 \times 10^5\,\mathrm{Pa}$. If we simulate the growth of the non-uniform layer of rat cardiomyocytes in §2.7.2 (which

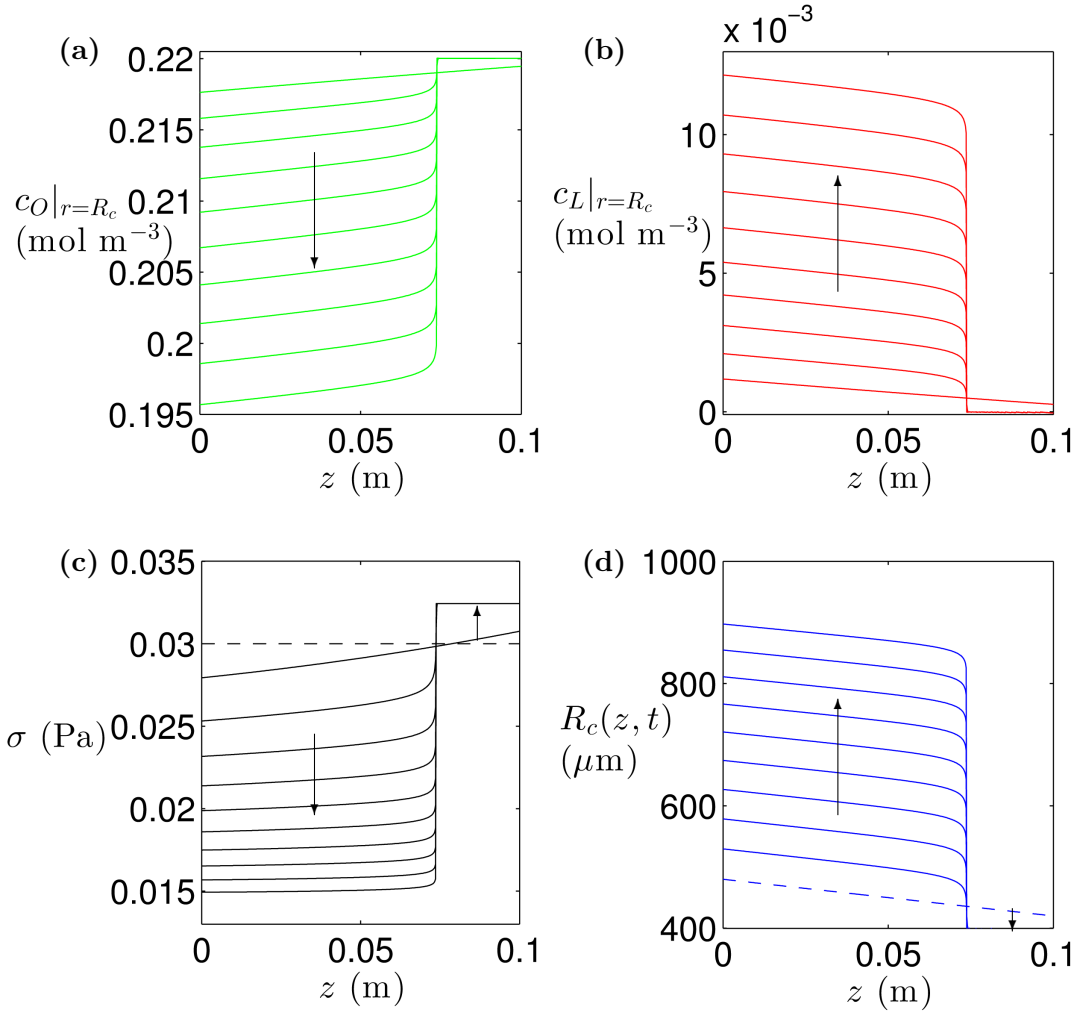

Figure 2.10: Evolution of (a) $c_O|_{r=R_c}$, (b) $c_L|_{r=R_c}$, (c) $\sigma|_{r=R_c}$ and (d) $R_c(z,t)$ for an initially non-uniform layer of rat cardiomyocytes. Initial cell layer outer radius $R_{c,init}(z) = (480 - 6.1 \times 10^{-4} z)\,\mu$m. Mean final outer radius $\overline{R}_c = 750\,\mu$m. Parameter values as in Figure 2.8 ($Q_{l,in} = 3.33 \times 10^{-8}\,\mathrm{m^3\,s^{-1}}$, $P_{l,out} = 1.965 \times 10^5\,$Pa).

has the same volume as the uniform layer but a depth that decreases linearly with z) at the same flow rate and outlet pressure, we obtain a very different result from Figure 2.8 as shown in Figure 2.10. Since the non-uniform cell layer is initially thinner at its downstream end, the shear stress on the cells at the surface is higher than for the uniform layer and exceeds Σ_d. Hence the cell layer recedes towards the fibre surface at its downstream end, but grows outwards over the upstream part of the fibre, where $\sigma < \Sigma_d$. The shear stress on the cells at the downstream end increases as the cell layer recedes, so the layer continues to recede until it reaches the membrane. Consequently, after 60 days the mean final outer radius of the cell layer, $\overline{R}_c = 750\,\mu$m, is much smaller (and the standard deviation in the

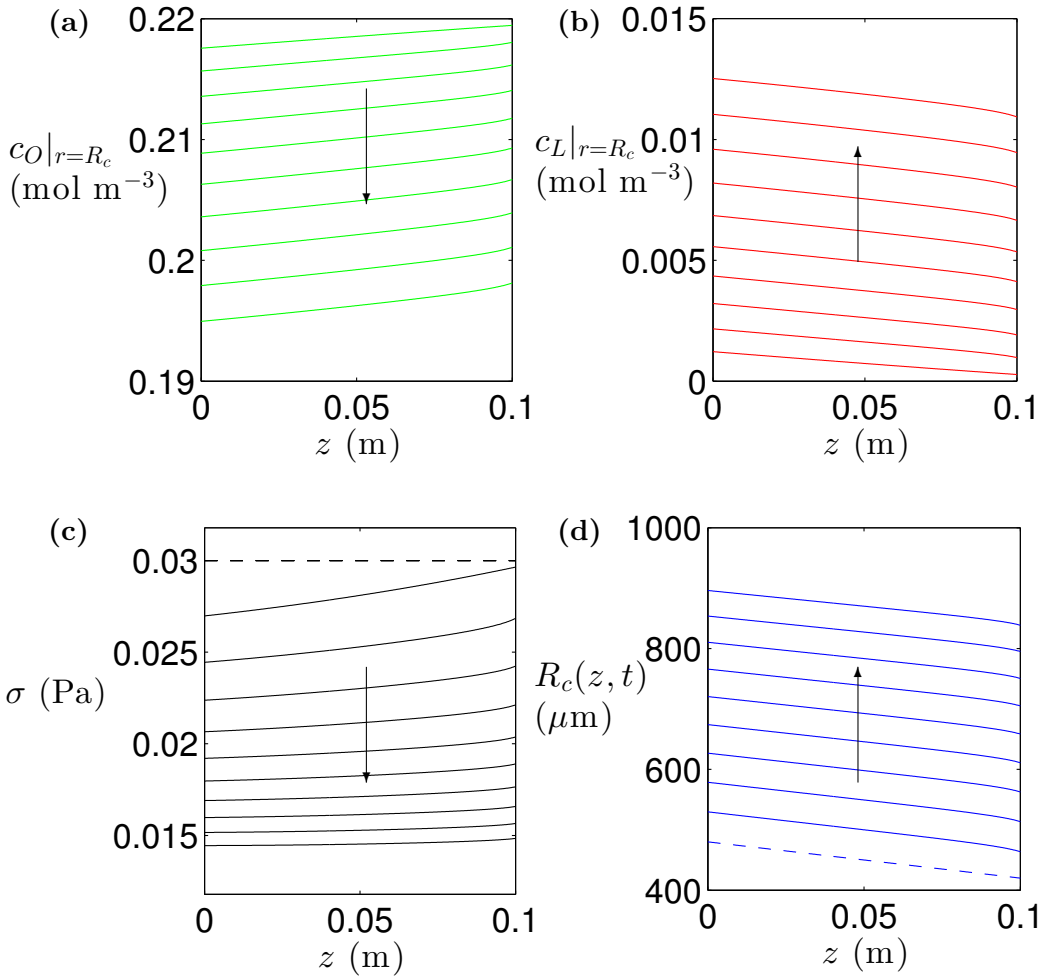

Figure 2.11: Evolution of (a) $c_O|_{r=R_c}$, (b) $c_L|_{r=R_c}$, (c) $\sigma|_{r=R_c}$ and (d) $R_c(z,t)$ with the initial layer of rat cardiomyocytes in Figure 2.10 at lower outlet pressure. Parameter values as in Figure 2.10 with $P_{l,out} = 1.930 \times 10^5$ Pa.

final outer radius, SD = 211 µm, much larger) than for the initially uniform cell layer with the same flow rate and outlet pressure.

Reducing $P_{l,out}$ brings the shear stress on the cells near the outlet below Σ_d, so that the cell layer grows outwards over its whole length to a mean outer radius of $\overline{R}_c = 870$ µm after 60 days (Figure 2.11). However, the cell layer remains thicker at its upstream end as it grows and the standard deviation in the final outer radius, SD = 16 µm, is larger than for the uniform cell layer. Similar results are observed with a cell layer whose depth *increases* with z ($R_{c,init} = (419 + 6.1 \times 10^{-4} z)$ µm)—the cell layer recedes at the downstream end, where $\sigma > \Sigma_d$ if $Q_{l,in} = 3.33 \times 10^{-8}$ m^3 s^{-1} and $P_{l,out} = 1.965 \times 10^5$ Pa, so that $\overline{R}_c = 705$ µm and SD = 14 µm, but grows over its whole length at lower outlet pressures.

These results suggest that the uniformity of the initial cell layer can make a large difference to the cell layer growth if the cells are shear-sensitive, and that care is needed to pick the optimal flow rate and outlet pressure if the cell layer is initially non-uniform.

2.9 Comparison with flow, solute transport and growth with ECS port closed

Thus far, we have described how the flow, solute transport and cell layer growth vary when the ECS port is open. Here we briefly describe the key differences in each of these components when the ECS port is closed.

2.9.1 Flow

When the ECS port is closed, there is no normal flow out of, or axial flow along, the ECS outer boundary, so (in terms of dimensionless variables)

$$u_{e,r} = 0 \quad \text{and} \quad u_{e,z} = 0 \quad \text{on} \quad r = \hat{R}_e.$$

As a result, at leading order there is only flow in the lumen (steady Poiseuille flow) and no axial or radial flow in the rest of the bioreactor,

$$p_l(z,t) = 16\hat{Q}_{l,in}(1-z) + \hat{P}_{l,out}, \quad u_{l,z}(r,z,t) = 4\hat{Q}_{l,in}(1-r^2), \quad u_{l,r} = \mathcal{O}(\epsilon^2), \tag{2.122}$$

$$p_m(z,t) = \frac{p_l(z)}{\kappa_m}, \quad p_c(z,t) = \frac{p_l(z)}{\kappa_m \kappa_c}, \quad u_{i,r}, u_{i,z} = \mathcal{O}(\epsilon^2),\ i = m, c, e. \tag{2.123}$$

The interstitial fluid shear stress in the cell layer is still an order of magnitude larger than the shear stress on the cells due to the ECS flow, but for the cell types and range of flow rates considered here, is far below the cell death threshold, Σ_d. Thus changes in the interstitial shear stress due to changes in $Q_{l,in}$ and $P_{l,out}$ do not affect the growth of the cell layer.

2.9.2 Solute transport

The mass transport problem for the oxygen and lactate reduces in the small aspect ratio limit to solving an advection-diffusion equation for the lumen concentration at each time step (see Appendix C.1). Due to the much weaker radial flow through the bioreactor than when the ECS port is open, the rates at which oxygen is transported through the membrane to the cells and lactate is advected away from the cell layer are much lower. Consequently the minimum oxygen and maximum lactate concentrations reached are much lower and higher respectively, *e.g.* for the uniform cell layer in Figures 2.5(a) and 2.6(a) ($R_c = 450\,\mu\text{m}$) the minimum oxygen concentration with the ECS port closed is $0.108\,\text{mol}\,\text{m}^{-3}$ (compared to

$0.216\,\mathrm{mol\,m^{-3}}$ with the port open) and the maximum lactate concentration is $0.119\,\mathrm{mol\,m^{-3}}$ (more than 60 times higher than with the port open).

With the ECS port closed, the leading order oxygen and lactate concentrations at the outer surface of the cell layer, and therefore the cell layer growth, only depend on $Q_{l,in}$ (through its effect on the oxygen and lactate transport through the lumen) and not on $P_{l,out}$. Similarly to when the ECS port is open, the growth rate of the cell layer decreases as it grows out into the ECS due to the decrease in the surface oxygen concentration with distance from the fibre. As the cell layer growth does not affect the flow at leading order, the only feedback effect from the growth is through changes in the oxygen and lactate distributions caused by changes in uptake/production and diffusion through the ECS.

2.9.3 Growth

The leading order system for the flow, solute transport and growth with the ECS port closed is solved as described in Appendix C.2, and used to simulate the growth of initially uniform layers of rat cardiomyocytes and bovine chondrocytes as in §2.8.1. Figures 2.12(a) and 2.12(b) show how the mean final outer radius of the cell layer, $\overline{R}_c$, varies with $Q_{l,in}$ for the cardiomyocytes and chondrocytes respectively ($R_{c,init}(z) = 450\,\mu\mathrm{m}$ as in Figure 2.7). The cardiomyocyte layer grows very little, $\overline{R}_c = 463$–$466\,\mu\mathrm{m}$, since the surface oxygen concentration $c_O|_{r=R_c}$ rapidly approaches C_{min} as the cell layer grows outwards and the cell layer approaches a steady state depth. The depth of the chondrocyte layer, meanwhile, does not approach an equilibrium and is much greater after 60 days growth, $\overline{R}_c = 656$–$657\,\mu\mathrm{m}$, since the chondrocyte oxygen uptake rate is much lower, so $c_O|_{r=R_c}$ remains well above C_{min} as the cell layer grows. For both cardiomyocytes and chondrocytes the lactate concentration remains well below the threshold for cell death, $L_{max} = 0.4\,\mathrm{mol\,m^{-3}}$, throughout the growth.

The cardiomyocyte layer grows far less than when the ECS port is open (for $P_{l,out} < 1.965 \times 10^5\,\mathrm{Pa}$) ($\overline{R}_c = 463$–$466\,\mu\mathrm{m}$ compared to 516–871 μm), but the chondrocyte layer grows only slightly less ($\overline{R}_c = 656$–$657\,\mu\mathrm{m}$ compared to 665–675 μm). The decreased growth with the ECS port closed is due to the reduced radial flow and therefore oxygen delivery to the cells. The greater decrease in the growth of the cardiomyocytes is due to a greater decrease in the surface oxygen concentration from closing the ECS port (due to their higher uptake rate).

Figure 2.12 shows that increasing $Q_{l,in}$ only produces a slight increase in the final cell layer depth for both cardiomyocytes and chondrocytes. This is because increasing $Q_{l,in}$ only increases the advective transport through the lumen at leading order when the ECS port is closed, leading to a marginal increase in the oxygen concentration at the inner surface of the membrane, which is carried through the membrane and cell layer by diffusion. The

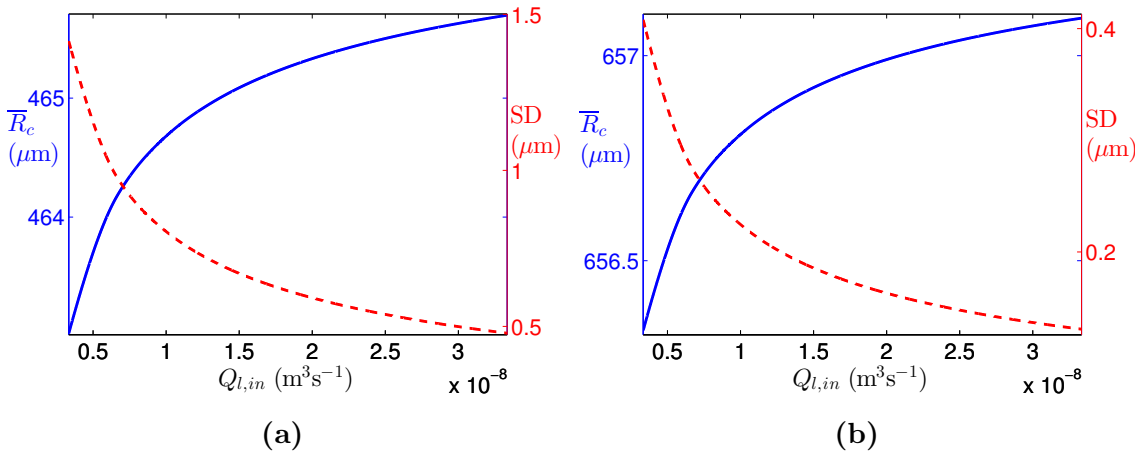

Figure 2.12: Variation in the mean, $\overline{R}_c$, and standard deviation, SD, of the final cell layer outer radius with $Q_{l,in}$ for (a) rat cardiomyocytes, and (b) bovine chondrocytes, after 60 days of culture with the ECS port closed. Parameter values: (a) as in Figure 2.7(a), (b) as in Figure 2.7(b). Blue solid line shows $\overline{R}_c$, red dashed line SD.

variation in the final cell layer depth is much smaller than when the ECS port is open for the cardiomyocytes (SD = 0.5–1.4 µm compared to SD = 0.2–44 µm), as expected given how little the cardiomyocyte layer grows, and slightly smaller for the chondrocytes (SD = 0.1–0.4 µm compared to SD = 0–2 µm).

From these results it is clear that opening the ECS port and using higher flow rates and outlet pressures can significantly improve cell layer growth, but it is important to know the level of shear stress that the cells can withstand as high outlet pressures can adversely affect the growth. We anticipate that opening the ECS port and using a high flow rate and outlet pressure would lead to similar improvements in growth to those for rat cardiomyocytes for rat hepatocytes and pancreatic beta cells, given their similar oxygen requirements and higher shear stress tolerances (Tables 2.3, 2.5).

2.9.4 Sensitivity of growth to lactate concentration

So far, we have assumed that the lactate concentration at which cell death occurs is the same for all cells ($L_{max} = 0.4\,\text{mol}\,\text{m}^{-3}$), and have found that for the cell types and operating conditions considered the lactate concentration at the outer surface of the cell layer remains much lower than L_{max}. Since there is a lack of cell-type-specific data for L_{max}, the sensitivity of the cell layer growth to L_{max} warrants further investigation. We therefore simulate the growth of the uniform rat cardiomyocyte layer for L_{max} in the range 0.001–0.4 mol m^{-3} with the ECS port closed and with it open. Figures 2.13(a) and 2.13(b)

show how the growth of the cell layer (measured as the difference, $\overline{\Delta R_c}$, between its mean final outer radius, $\overline{R}_c$, and initial outer radius, $R_{c,init} = 450\,\mu\text{m}$) varies with L_{max} when the ECS port is closed and when it is open. With the ECS port closed, the cell layer recedes if $L_{max} < 0.14\,\text{mol}\,\text{m}^{-3}$ (by an increasing amount as L_{max} decreases), but grows if $L_{max} > 0.14\,\text{mol}\,\text{m}^{-3}$. For $L_{max} > 0.25\,\text{mol}\,\text{m}^{-3}$, the growth is approximately constant. With the ECS port open, the cell layer grows even for very low values of L_{max}, and by an increasing amount as L_{max} increases, up to $L_{max} = 0.15\,\text{mol}\,\text{m}^{-3}$. For $L_{max} > 0.15\,\text{mol}\,\text{m}^{-3}$ the growth does not change with L_{max}. The fact that the growth is more sensitive to the value of L_{max} when the ECS port is closed, and that the cell layer can recede if L_{max} is low, provides further motivation for operating the bioreactor with the ECS port open.

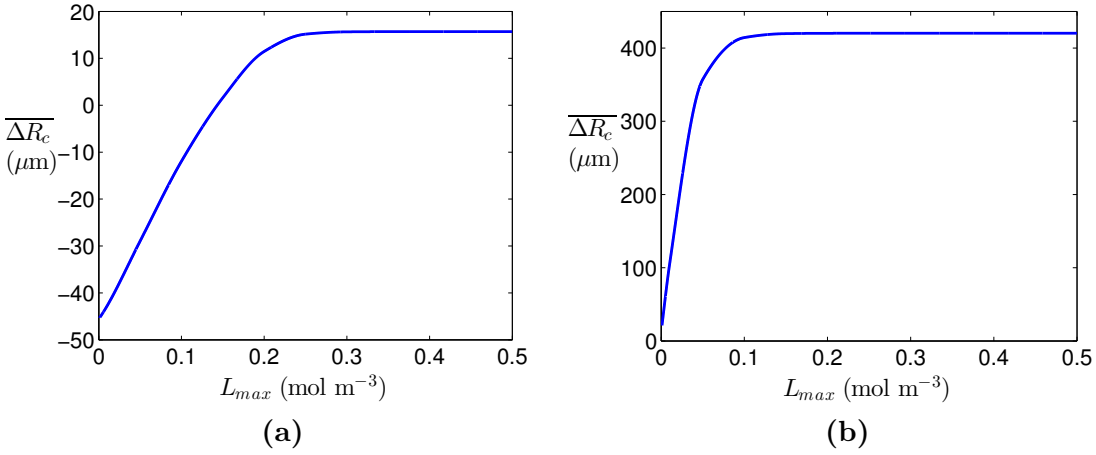

Figure 2.13: Variation in the growth of a rat cardiomyocyte cell layer with the lactate cell death threshold L_{max} with the ECS port (a) closed and (b) open. Initial cell layer outer radius $R_{c,init}(z) = 450\,\mu\text{m}$. Cell layer growth measured by $\overline{\Delta R_c} = \overline{R}_c - R_{c,init}$. Parameter values as in Figure 2.8.

2.10 Discussion

We have developed a model of cell layer growth in a single-fibre HFB by extending the model of fluid and mass transport in a HFB of Shipley and Waters [231] to include a growing layer of cells on the outer surface of the fibre. We have assumed that cell layer growth is localised to the outer surface of the cell layer and that it depends on the oxygen and lactate concentrations and fluid shear stress there. Considering both the case in which the ECS ports are open and that in which they are closed, we have exploited the small aspect ratio of the bioreactor to reduce the governing equations for the fluid flow, oxygen and lactate transport, and cell layer growth, and solved the resulting leading order system

numerically. We have used the model to compare the growth of a layer of rat cardiomyocytes and a layer of bovine chondrocytes with the ECS ports open and with them closed, and to investigate how the lumen inlet flow rate $Q_{l,in}$ and lumen outlet pressure $P_{l,out}$ affect the growth.

As described in §1.2.5, Pearson *et al.* [205] have also developed a model of cell proliferation in a cell layer in the ECS of the single-fibre HFB. There are a number of key differences between their model and ours, however. Firstly, they considered a set-up in which fluid is pumped into the bioreactor both via the upstream ECS port and the lumen inlet, rather than only via the lumen inlet. Secondly, they assumed that the depth of the cell layer remains constant in time and described cell proliferation and death via shear-mediated mass transfer between the culture medium and cells. In contrast, we have assumed that the cell volume fraction remains constant as cells proliferate and die, so that net cell proliferation and death are represented by changes in the depth of the cell layer. Thirdly, they considered much lower flow rates, so in their model the timescales for advection in the membrane and cell layer are of the same order as the timescale for proliferation, rather than being much shorter as in our model. Finally, their investigation focussed on the effect of fluid shear stress on cell yield and distribution, whereas we have considered both oxygen- and shear-limited growth. Despite these differences, their study also highlighted the importance of avoiding exposing cells to excess shear stress for maximising the cell yield.

2.10.1 Summary of model predictions

The simulation results show that opening the ECS ports, increasing $Q_{l,in}$ and increasing $P_{l,out}$ all improve growth, provided that the shear stress on the cells at the surface does not reach the level at which the cells die or detach from the layer. The results also show that the improvement in growth with the opening of the ECS ports is greater for cells with higher oxygen demands (Figure 2.7).

Increasing $Q_{l,in}$ and/or $P_{l,out}$ increases the oxygen concentration and decreases the lactate concentration at the cell layer surface, but also increases the shear stress on the cells. For shear-sensitive cells it is therefore necessary to avoid imposing too high an outlet pressure and flow rate. In view of this, we have used the model to predict the flow rate and outlet pressure that maximise the growth of initially uniform layers of rat cardiomyocytes (assumed to be shear-sensitive) and bovine chondrocytes (shear-tolerant) when the ECS ports are open, and have predicted a lower optimal $P_{l,out}$ for rat cardiomyocytes (Figure 2.7). This indicates that the optimal flow rate and outlet pressure are cell-type-specific. Cells that are able to tolerate the maximum interstitial shear stress reached in the cell layer over the whole range of $Q_{l,in}$ and $P_{l,out}$ (*i.e.* for which σ is always less than Σ_d) should be

cultured with the highest possible $Q_{l,in}$ and $P_{l,out}$ to maximise oxygen delivery and lactate clearance. Cells for which the shear stress exceeds Σ_d at higher flow rates and outlet pressures should be cultured with the highest possible $Q_{l,in}$ and $P_{l,out}$ for which the shear stress remains below Σ_d.

Although cells such as cardiomyocytes with high oxygen demands (high V_{max}^O and C_{min}) should be grown with the ECS ports open to promote oxygen delivery to the cell layer, it may be better to keep the ECS ports closed for cells that are very sensitive to shear stress (have a very low Σ_d) or have sufficiently low oxygen requirements that the culture medium can be recycled directly from the outlet to the inlet without any significant adverse effect on the growth.

For the cell types we have considered, the surface lactate concentration remains well below the estimated toxicity threshold, L_{max}, for typical operating conditions (as shown in Figures 2.8–2.11), and oxygen is instead the limiting solute with respect to cell layer growth. However, given the lack of experimental data for L_{max}, we have used the model to predict the sensitivity of the cell layer growth to this threshold. The results suggest that the growth is less sensitive to L_{max} at low values when the ECS ports are open, so that it is better for the ECS ports to be open if L_{max} is not known for the cell type being cultured (provided the cells are not highly shear-sensitive).

It is clear from the simulations for the initially non-uniform cell layer that cell layer growth (and optimal flow rate and outlet pressure) can be sensitive to variation in the initial cell layer depth along the fibre (Figures 2.10 and 2.11). The cell layer depth is likely to be non-uniform in practice, so it would be interesting to test experimentally the sensitivity of the growth to this non-uniformity by measuring the initial and final outer radii of multiple cell layers of a certain cell type. From the simulations it appears that the cell layer grows less and has a less uniform final depth if its initial depth varies along the fibre. This suggests that the cell seeding and initial culture conditions should be aimed at producing a uniform cell layer depth to maximise growth and the uniformity of the final cell layer. However, further investigation with a range of choices for $R_{c,init}(z)$ is needed to confirm whether this hypothesis is correct. Simulating the growth with different $R_{c,init}(z)$ across a range of values of $Q_{l,in}$ and $P_{l,out}$ would also enable the prediction of optimal combinations of $R_{c,init}(z)$, $Q_{l,in}$ and $P_{l,out}$.

2.10.2 Possible extensions

Although the functional form chosen for $G(c_O, c_L, \sigma)$ in the cell layer growth law is relatively simple, it has allowed us to predict the possible effects of changes in the fluid flow and oxygen and lactate transport on the cell layer growth. Alternative functional forms, even

cell-type-specific ones, could easily be considered. In addition, rather than assuming that cell proliferation and death are concentrated at the free surface of the cell layer $r = R_c(z,t)$, we could assume that they occur throughout the cell layer so that its growth is volumetric, and compare simulations based on this assumption with those presented here. Different model assumptions could be validated by comparing the growth predicted by simulations against experimental measurements, so that the model can be used to determine optimal operating conditions for different cell types.

In addition to experimentally validating the growth law, a number of key parameters need to be measured to use the model to make accurate quantitative predictions of the growth of specific cell types. These include the lactate diffusivity in the membrane, D_m^L, the lactate concentration that is toxic to the cells, L_{max}, and the rates of recession of the cell layer due to cell death from excess lactate and shear stress, $B_L B_d$ and $B_s B_d$. The lactate diffusivity in the membrane can be determined by measuring the lactate concentration in the permeate from the single-fibre HFB when the ECS is filled with cells with a known lactate production rate, and fitting the results to the solute transport model with $R_c = R_e$. Although a generic value for L_{max} has been estimated, it is likely to vary with cell type, so should be measured for the cell type being cultured, *e.g.* by exposing monolayers of the cells to solutions of different lactate concentrations. The values of B_L, B_s and B_d may be harder to measure experimentally. As a first step, it would be useful to determine the sensitivity of the cell layer growth to B_L, B_s and B_d. A thorough parameter sensitivity analysis to determine how the cell layer growth varies with the values of the other growth parameters A_p, C_{min} and L_{max} should also be carried out as part of any further work.

We have treated the porosities and permeabilities of the membrane and cell layer as constant, but they will exhibit some spatial heterogeneity and change to some degree over time. Although the membrane porosity may remain fairly constant in time for the culture times we have considered, over longer timescales it will increase due to degradation of the PLGA in the membrane [13, 111, 233]. The porosity of the cell layer is likely to decrease with time due to cell growth and proliferation and ECM deposition within the cell layer. One way to incorporate this into the model would be to use a multiphase description for the cell layer, with volume fractions for the culture medium and cells and mass transfer between the phases, similar to that developed by Pearson *et al.* [205]. A multiphase description with varying fluid and solid fractions, similar to that in [194], could also be used to model spatial heterogeneity and PLGA degradation in the membrane.

Given that the membrane permeability k_m is the key determinant of the flow through the bioreactor when the ECS ports are open, it would be interesting to investigate the sensitivity of the cell layer growth to k_m as part of any further work. The impact of spatial

and temporal variation in the permeability on the flow, solute transport and growth could also be investigated by making k_m a function of r, z and t (or via a multiphase description for the membrane with k_m as a function of the porosity).

A further extension to the model would be to add transport equations for other species dissolved in the culture medium, such as glucose, growth factors and other proteins. This would enable the incorporation of a detailed model for cell metabolism (such as that in Casciari *et al.* [30]), with coupling between the oxygen, glucose and lactate concentrations. As some proteins in standard culture medium are large enough to constrict or block pores in the membrane or become 'caked' on its inner surface, adding protein transport would require a description of the effect of fouling on the membrane permeability and the protein concentration reaching the cell layer over time. Shipley *et al.* [235] have investigated membrane fouling in the transport of bovine serum albumin (BSA) through a cell-free single-fibre HFB via a combination of experimental measurements and theoretical analysis. Their model of BSA transport could be incorporated into the present model by adding a reaction-advection-diffusion equation for the uptake of BSA in the cell layer.

As discussed in Chapter 1, there is still a large amount of work to be done to scale up laboratory tissue engineering experiments for clinical use. To help the process of scaling up cell expansion in HFBs, our model could be extended to describe fluid and mass transport and cell proliferation in a multi-fibre HFB, with growing cell layers attached to the outer surfaces of the fibres and coupling of the flows between adjacent fibres. Nonetheless, in characterising cell layer growth in a single-fibre HFB subject to oxygen delivery, lactate clearance and fluid shear stress, the results of this chapter provide a useful starting point for optimising cell expansion in HFBs.

Chapter 3

Cell aggregate growth in the HFB

3.1 Introduction

In Chapter 2 we investigated the effects of solute transport and fluid shear stress on the growth of a cell layer on the outer surface of the fibre in the HFB. We assumed that the cells initially seeded on the fibre surface had already proliferated to confluence over the surface and then outwards into the ECS, so that the cell layer was already multiple cells deep at the point from which the growth was modelled. To investigate the impact of solute transport and shear stress on cell proliferation in the stage of culture preceding confluence, we now model the cell population at a smaller spatial scale. We consider the growth of cell aggregates that form on the outer surface of the fibre shortly after seeding, and that are a single cell thick, along the fibre surface.

In Chapter 2 we showed that operating the HFB with the ECS ports open rather than closed leads to increased growth of the cell layer, provided the shear stress on the cells is kept below the threshold at which cell death occurs. Here we consider a different flow configuration, with the ECS port nearest the lumen inlet closed and that nearest the lumen outlet open. With this configuration, the axial flow in the ECS is dominant rather than the radial flow. The motivation for considering this configuration is that cells in aggregates on the membrane surface experience higher shear stresses than cells at the surface of the cell layer for lumen-driven flow, so closing the upstream ECS port should reduce the shear stress on the cells on the membrane surface (by reducing the radial flow through the membrane) but still provide greater oxygen delivery than closing both ports. We assume that the cell aggregates are distributed over the outer surface of the fibre and grow or shrink over the surface as cells proliferate and die. For simplicity we consider a representative 2D cross-section of the bioreactor module that excludes the open ECS port (see Figure 3.1), rather than the full 3D set-up. Including the ECS port and modelling the set-up in 3D would require a numerical approach and consideration of the azimuthal-dependence of the cell

aggregate distribution, and would be computationally expensive. Modelling the 2D cross-section instead enables us to make analytical progress and gain an understanding of how the coupled fluid flow, solute transport and cell aggregate growth in the bioreactor depend on the operating parameters and initial cell aggregate distribution.

The rate at which the aggregates elongate or shorten along the membrane is assumed to depend on the oxygen concentration at the membrane surface and the shear stress exerted on them by the flow. Greater oxygen delivery is known to promote cell proliferation and excess shear stress to lead to cell death [47, 215], but insufficient oxygen can also result in cell death and increasing shear stress can stimulate proliferation, *e.g.* for osteoblasts [121], chondrocytes [162] and embryonic and mesenchymal stem cells [279, 289]. Hence, in addition to considering proliferation at sufficiently high oxygen concentrations and cell death due to excess shear stress as in Chapter 2, we consider cell death and quiescence at low oxygen concentrations and shear-stimulated proliferation at intermediate shear stresses. However, here we neglect the effect of lactate concentration on the cell aggregate growth, as for thin cell aggregates, at typical lactate production rates and flow rates, lactate does not build up to toxic levels. The dominant shear stress exerted by the flow on the cells arises from the ECS flow over the top of the aggregates, and we consider the effect of variations in this shear stress on the cell aggregate growth. We consider the timescale of cell proliferation, on which the fluid and oxygen transport are quasi-steady, and account for the feedback effect of the aggregate growth on the flow and oxygen distribution in the bioreactor via changes in the permeability of the outer surface of the membrane and oxygen uptake as the aggregates grow.

As discussed previously, increasing the flow rate of the culture medium into the lumen inlet and/or the pressure imposed at the lumen outlet promotes flow through the membrane into the ECS, increasing oxygen delivery to, and the shear stress experienced by, the cells. Oxygen demands and shear stress tolerance vary considerably with cell type and different aggregate distributions experience different oxygen and shear stress conditions. For a given cell type, it is therefore necessary to determine the flow parameters and initial seeding distribution that give the optimal balance of oxygen delivery and shear stress for growth.

We use our model to simulate cell aggregate growth for different cell types and different initial aggregate distributions. In particular, we assess the combined effects of seeding and flow on the growth. We use the results to predict optimal lumen inlet flow rates, lumen outlet pressures and seeding distributions for minimising the time the aggregates take to reach confluence or, if they do not reach confluence, maximising their final total length.

3.1.1 Chapter outline

The structure of this chapter is as follows. In §3.2 we briefly describe the model set-up. In §3.3 we present the governing equations for the fluid and oxygen transport and cell aggregate growth. We describe how the model is parameterised for specific cell types, simplified using lubrication theory and solved numerically in §§3.5–3.6. In §3.7 we assess the impact of varying the inlet flow rate, outlet pressure and initial aggregate distribution on the aggregate growth, and identify optimal operating conditions for growth of specific cell types. In §3.8, we summarise our findings and explain how they may be used to try to maximise the cell yield for different cell types, as well as briefly discussing possible extensions and improvements to the model and the experiments necessary to validate it.

3.2 Model set-up

We consider a 2D cross-section of the upper half of the bioreactor running from the lumen inlet to just upstream of the ECS outlet, as shown in Figure 3.1, and make the simplifying assumption that the flow and oxygen distribution can be treated as symmetric about the lumen centreline. The lumen centreline and membrane surfaces are assumed to be straight, so the model domain consists of three rectangular regions, representing the lumen, membrane and ECS. We describe the domain using Cartesian coordinates (x, y), with corresponding unit vectors $\mathbf{e}_x$ and $\mathbf{e}_y$, where x is the distance along the lumen centreline with the inlet at $x = 0$ and the downstream end at $x = L$, and y is the distance perpendicular to the lumen centreline. The lumen, membrane and ECS radii are denoted by R_l, R_m and R_e, so the lumen occupies the region $0 < x < L$, $0 < y < R_l$; the membrane occupies $0 < x < L$, $R_l < y < R_m$; and the ECS occupies $0 < x < L$, $R_m < y < R_e$.

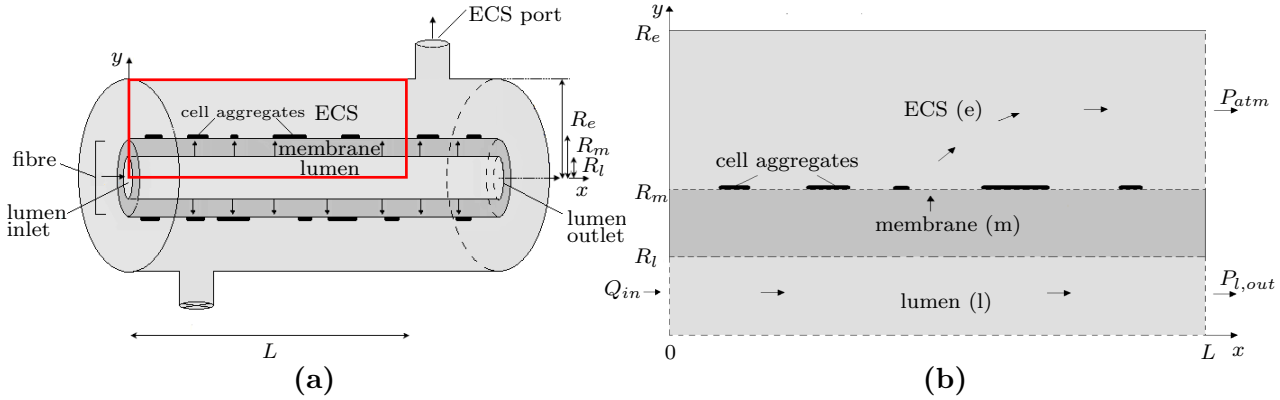

Figure 3.1: (a) Schematic of the HFB module with the model domain outlined in red. (b) Model domain. Cell aggregates on membrane shown in black. Arrows show direction of fluid flow.

Culture medium containing oxygen at a fixed concentration, C_{in}, is pumped into the lumen inlet at a prescribed rate, Q_{in}. To mimic the lumen outlet and open ECS port, we prescribe the normal fluid stresses at the downstream ends of the lumen and ECS regions to be $P_{l,out}$ and P_{atm} (atmospheric pressure), respectively. The ratio of flow through the ECS to flow through the lumen is thus determined by $P_{l,out}$. From here on, we refer to the ends of the lumen and ECS at the downstream end of the domain as the lumen outlet and ECS outlet for convenience. The cell aggregates are distributed along the outer surface of the membrane and are treated as being infinitesimally thin to facilitate modelling the effects of their growth on the flow and oxygen distribution. This is a reasonable simplification given that a typical cell diameter (10 µm) is small compared with the depths of the membrane (200 µm) and ECS (600 µm) and the aggregates are one cell thick. The aggregates are assumed to absorb oxygen, and elongate or shorten at a rate that depends on the local oxygen concentration and fluid shear stress. As the aggregates elongate/shorten, the flow and oxygen profiles along the membrane change through increased/decreased oxygen uptake and reduced/increased permeability of the membrane outer surface to fluid.

3.3 Governing equations

Much of the modelling framework used here is similar to that in Chapter 3. The key differences are that here we only require equations to describe the flow and solute transport in the lumen, membrane and ECS as there is no cell layer; we model resistance to the flow and oxygen uptake due to the aggregates via the conditions at the outer surface of the membrane; and we require additional equations to describe the elongation/shortening of the cell aggregates. Below we state the governing equations and boundary conditions for the model for completeness.

3.3.1 Fluid transport

We assume that the flow in the lumen and ECS is governed by the steady incompressible Stokes flow equations (*i.e.* we neglect inertia, see §3.5.1)

$$\boldsymbol{\nabla} \cdot \mathbf{u}_i = 0, \quad \mu \nabla^2 \mathbf{u}_i = \boldsymbol{\nabla} p_i, \quad i = l, e, \tag{3.1}$$

where $\mathbf{u}_i = (u_i, v_i)$ and p_i are the fluid velocity and pressure, μ is the dynamic fluid viscosity, and $i = l, e$ denote the lumen and ECS. We use incompressible Darcy flow to describe the fluid transport in the porous membrane

$$\boldsymbol{\nabla} \cdot \mathbf{u}_m = 0, \quad \phi_m \mathbf{u}_m = -\frac{k_m}{\mu} \boldsymbol{\nabla} p_m, \tag{3.2}$$

where $\mathbf{u}_m$ and p_m are the pore-averaged fluid velocity and pressure, ϕ_m is the membrane porosity, and k_m is the permeability of the membrane.

At the lumen-membrane interface, $y = R_l$, we impose no slip and continuity of normal velocity and normal stress

$$\mathbf{u}_l \cdot \mathbf{e}_x = \phi_m \mathbf{u}_m \cdot \mathbf{e}_x, \quad \mathbf{u}_l \cdot \mathbf{e}_y = \phi_m \mathbf{u}_m \cdot \mathbf{e}_y, \quad \mathbf{e}_y \cdot \boldsymbol{\sigma}_l \cdot \mathbf{e}_y = \mathbf{e}_y \cdot \boldsymbol{\sigma}_m \cdot \mathbf{e}_y, \quad \text{on } \ y = R_l. \tag{3.3}$$

At the outer surface of the membrane, $y = R_m$, we impose no slip and continuity of normal fluid velocity, but assume there is a jump in the normal stress proportional to the fluid flux, so that

$$\phi_m \mathbf{u}_m \cdot \mathbf{e}_x = \mathbf{u}_e \cdot \mathbf{e}_x, \quad \phi_m \mathbf{u}_m \cdot \mathbf{e}_y = \mathbf{u}_e \cdot \mathbf{e}_y, \tag{3.4a,b}$$

$$\mathbf{e}_y \cdot \boldsymbol{\sigma}_e \cdot \mathbf{e}_y - \mathbf{e}_y \cdot \boldsymbol{\sigma}_m \cdot \mathbf{e}_y = \frac{1}{K(x,t)} \mathbf{u}_e \cdot \mathbf{e}_y \quad \text{on } \ y = R_m, \tag{3.4c}$$

where $K(x,t)$ represents the permeability of the outer surface of the membrane. We assume that the aggregates provide resistance to the flow such that $K(x,t)$ has a low value, K_{lo}, in regions covered by aggregates and a higher but finite value, K_{hi}, in regions not covered by aggregates (to model a reduction in surface permeability caused by ECM and protein deposition by the cells). We suppose that the cell density within an aggregate remains constant as the aggregate grows/shrinks, so that K_{lo} and K_{hi} are fixed. Thus, $K(x,t)$ is given by

$$K(x,t) = K_{lo} I_a(x,t) + K_{hi}(1 - I_a(x,t)), \tag{3.5}$$

where the aggregate indicator function, $I_a(x,t)$, is defined as

$$I_a(x,t) = \begin{cases} 1 & \text{for } x \in (0,L),\ y = R_m \text{ covered by an aggregate at time } t, \\ 0 & \text{for } x \in (0,L),\ y = R_m \text{ not covered by an aggregate at time } t. \end{cases} \tag{3.6}$$

In the lubrication limit we derive in §3.4.1 by exploiting the small aspect ratio of the fibre, the normal stress boundary condition (3.4c) reduces to Starling's equation for the fluid flux across a thin membrane, *i.e.* to the fluid flux being proportional to the pressure difference across the membrane.

Symmetry about the lumen centreline gives

$$\mathbf{u}_l \cdot \mathbf{e}_y = 0, \quad \boldsymbol{\nabla} u_l \cdot \mathbf{e}_y = 0 \quad \text{on } \ y = 0. \tag{3.7}$$

At the outer boundary of the ECS we impose no slip and no flux, so that

$$\mathbf{u}_e = 0 \quad \text{on } \ y = R_e. \tag{3.8}$$

We also impose no-flux conditions at the ends of the membrane and the upstream end of the ECS

$$\begin{aligned} \mathbf{u}_m \cdot \mathbf{e}_x &= 0 \quad \text{on } x = 0, L,\ R_l < y < R_m, \\ \mathbf{u}_e \cdot \mathbf{e}_x &= 0 \quad \text{on } x = 0,\ R_m < y < R_e, \end{aligned} \tag{3.9}$$

and prescribe the lumen inlet flow rate and normal stress at the lumen outlet

$$\int_0^{R_l} \mathbf{u}_l \cdot \mathbf{e}_x|_{x=0}\, \mathrm{d}y = Q_{in}, \tag{3.10}$$

$$\mathbf{e}_x \cdot \boldsymbol{\sigma}_l \cdot \mathbf{e}_x = -P_{l,out} \quad \text{on } x = L,\ 0 < y < R_l. \tag{3.11}$$

We note that in the lubrication limit, (3.11) reduces to a condition on the lumen pressure, and (3.10) and (3.11) are sufficient to determine the flow (see §3.4.1). At the ECS outlet we impose continuity of normal stress

$$\mathbf{e}_x \cdot \boldsymbol{\sigma}_e \cdot \mathbf{e}_x = -P_{atm} \quad \text{on } x = L,\ R_m < y < R_e. \tag{3.12}$$

3.3.2 Oxygen transport

We model oxygen transport in the lumen, membrane and ECS via the steady advection-diffusion equations

$$\mathbf{u}_i \cdot \boldsymbol{\nabla} c_i = D_i \nabla^2 c_i, \quad i = l, m, e, \tag{3.13}$$

where c_i and D_i $(i = l, e)$ are the oxygen concentration (per unit volume of fluid) and diffusivity in the lumen and ECS, and c_m and D_m are the average oxygen concentration (over the pore space) and effective oxygen diffusivity in the membrane.

At the lumen-membrane interface we impose continuity of the oxygen concentration and flux

$$c_l = c_m, \quad D_l \boldsymbol{\nabla} c_l \cdot \mathbf{e}_y = \phi_m D_m \boldsymbol{\nabla} c_m \cdot \mathbf{e}_y \quad \text{on } y = R_l. \tag{3.14}$$

However, at the membrane-ECS interface, we impose continuity of concentration and a jump in the flux across the aggregates due to cellular uptake of oxygen

$$c_m = c_e, \quad (D_e \boldsymbol{\nabla} c_e - \phi_m D_m \boldsymbol{\nabla} c_m) \cdot \mathbf{e}_y = I_a(x,t) R(c_e) \quad \text{on } y = R_m, \tag{3.15}$$

where the oxygen uptake flux $R(c_e)$ is an increasing saturating function of c_e

$$R(c_e) = M \frac{c_e}{C_{1/2} + c_e},$$

with the constant $M > 0$ denoting the maximal oxygen uptake flux and $C_{1/2}$ the concentration at which the flux is half-maximal. Symmetry about the lumen centreline corresponds to no diffusive flux through $y = 0$

$$\boldsymbol{\nabla} c_l \cdot \mathbf{e}_y = 0 \quad \text{on } y = 0. \tag{3.16}$$

We impose the following no-flux boundary conditions at the ends of the membrane and outer walls of the ECS

$$\boldsymbol{\nabla} c_m \cdot \mathbf{e}_x = 0 \quad \text{on} \quad x = 0, 1, \; R_l < y < R_m, \tag{3.17}$$

$$\boldsymbol{\nabla} c_e \cdot \mathbf{e}_x = 0 \quad \text{on} \quad x = 0, \; R_m < y < R_e, \tag{3.18}$$

$$\boldsymbol{\nabla} c_e \cdot \mathbf{e}_y = 0 \quad \text{on} \quad y = R_e. \tag{3.19}$$

The inlet oxygen concentration is prescribed by

$$c_l = C_{in} \quad \text{on} \quad x = 0. \tag{3.20}$$

Finally, we impose zero-diffusive-flux conditions at the outlets

$$\begin{aligned} \boldsymbol{\nabla} c_l \cdot \mathbf{e}_x = 0 \quad &\text{on} \quad x = L, \; 0 < y < R_l, \\ \boldsymbol{\nabla} c_e \cdot \mathbf{e}_x = 0 \quad &\text{on} \quad x = L, \; R_m < y < R_e. \end{aligned} \tag{3.21}$$

3.3.3 Cell aggregate growth

Net increases/decreases in the cell population are modelled by elongation/shortening of the aggregates, whose initial distribution and lengths along the membrane are prescribed. It is assumed that cell proliferation occurs over the whole length of each aggregate, and that when cells in the middle of an aggregate divide they push neighbouring cells outwards, so that the cell density in the aggregate remains constant as it grows. This assumption is motivated by cell migration and proliferation assays on 2D substrates, which show that cells distant from a growing edge continue to proliferate and exert a mitotic pressure on their neighbouring cells [135, 224, 255, 284]. When two aggregates come into contact, they are assumed to coalesce and are thereafter treated as one larger aggregate. If one end of an aggregate reaches either end of the membrane ($x = 0$ or $x = L$), any further growth is taken to occur at its opposite end. When cells die we assume they detach from the membrane and are removed with the flow, causing the aggregates to shrink. For simplicity, we assume that the effects of the oxygen concentration and fluid shear stress on the cell proliferation rate G_p and death rate G_d, and hence on the net rate of aggregate elongation, are multiplicative (see equations (3.22a,b)). This means that the aggregates cannot grow in either hypoxic or excess shear conditions, which would be possible if the effects were assumed to be additive (*e.g.* if the shear stress was high enough to kill cells, but the oxygen concentration was also very high and promoted proliferation sufficiently for the net effect to be positive). A strength of our modelling approach is its modular nature, which means that alternative growth laws (based on different assumptions, such as assuming proliferation only occurs near the aggregate ends) could easily be incorporated.

Several authors use Monod kinetics to describe the relationship between oxygen concentration and cell proliferation [22, 136, 229, 236], for which the proliferation rate is approximately constant at low concentrations, increases with concentration for intermediate concentrations, and plateaus to a maximum at high concentrations. Following McElwain and Ponzo [171], we approximate Monod kinetics in a piecewise linear fashion, as shown in Figure 3.2(a), and assume that cells die below a certain oxygen concentration. Following O'Dea *et al.* [192], we take the cell proliferation/death rate to be a stepped function of the fluid shear stress on the cells along the membrane outer surface, $\sigma_{e,xy}|_{y=R_m} = \mu(\frac{\partial u_e}{\partial y} + \frac{\partial v_e}{\partial x})|_{y=R_m}$ (see §3.4.3 for details of how this is approximated in the reduced model), with faster cell proliferation at intermediate shear stresses and cell death at high shear stresses as shown in Figure 3.2(b). This relationship is based on experimental observations (see Table B.7 and references therein).

In any given simulation, the number of aggregates on the membrane can only decrease from the number in the initial distribution due to aggregates merging with one another (new aggregates cannot be created). Assuming that there are N cell aggregates at time t, such that the jth aggregate occupies the interval $[x_{2j-1}(t), x_{2j}(t)]$ $(j = 1, \ldots, N)$, the evolution equation for the length of the jth aggregate, $L_j = x_{2j} - x_{2j-1}$, is

$$\frac{\mathrm{d}L_j}{\mathrm{d}t} = \int_{x_{2j-1}(t)}^{x_{2j}(t)} (G_p(c_e|_{y=R_m}, \sigma_{e,xy}|_{y=R_m}) - G_d(c_e|_{y=R_m}, \sigma_{e,xy}|_{y=R_m}))\,\mathrm{d}x, \tag{3.22}$$

where G_p and G_d are the cell proliferation rate and death rate, respectively, at each point in the aggregate due to the combined effects of the oxygen concentration and shear stress (see Figure 3.2(c)). The cell proliferation and death functions are integrated over the length of the aggregate (from x_{2j-1} to x_{2j}) to give the net rate of change of its length. (We note that in our model if an aggregate shortens it cannot completely disappear, since the rate at which it shortens is proportional to its length.)

There is little quantitative data available with which to pose and parameterise forms for G_p and G_d, so we use the following constitutive relationships to capture the key effects of oxygen and shear stress on growth described above

$$\begin{aligned} G_p(c_e, \sigma_{e,xy}) = {} & (\mathrm{H}(c_e - C_p)\mathrm{H}(C_{max} - c_e)(c_e - C_p) + \mathrm{H}(c_e - C_{max})(C_{max} - C_p)) \\ & \times (A_1\mathrm{H}(\Sigma_p - \sigma_{e,xy}) + A_2\mathrm{H}(\sigma_{e,xy} - \Sigma_p)\mathrm{H}(\Sigma_d - \sigma_{e,xy})), \end{aligned} \tag{3.22a}$$

$$G_d(c_e, \sigma_{e,xy}) = B_0(1 + B_1\mathrm{H}(C_d - c_e))(1 + B_2\mathrm{H}(\sigma_{e,xy} - \Sigma_d)) - 1. \tag{3.22b}$$

In (3.22a) and (3.22b), H is the Heaviside function; C_d the oxygen concentration below which cells die; C_p the minimum concentration for cell proliferation; C_{max} the concentration above which the aggregate growth rate is a constant maximum (Figure 3.2(a)); Σ_p the shear stress

threshold for elevated cell proliferation rate; A_1 the constant baseline aggregate growth rate per unit concentration for low shear stress ($\sigma_{e,xy}|_{y=R_m} < \Sigma_p$); A_2 the elevated growth rate per unit concentration for intermediate shear stress ($\Sigma_p < \sigma_{e,xy}|_{y=R_m} < \Sigma_d$); Σ_d the shear stress above which cells die (Figure 3.2(b)); B_0 the baseline aggregate shortening rate due to cell death from insufficient oxygen ($c_e|_{y=R_m} < C_d$, $\sigma_{e,xy}|_{y=R_m} < \Sigma_d$) or excess shear stress ($\sigma_{e,xy}|_{y=R_m} > \Sigma_d$, $c_e|_{y=R_m} > C_d$); and B_1 and B_2 dimensionless factors that determine the aggregate shortening rates for insufficient oxygen and excess shear stress, respectively (Figure 3.2(c)). These forms of G_p and G_d capture the fact that most cells die if they receive insufficient oxygen ($c_e|_{y=R_m} < C_d$, blue band on left of Figure 3.2(c)), remain quiescent in low oxygen conditions ($C_d < c_e|_{y=R_m} < C_p$, green region in Figure 3.2(c)), proliferate at an increasing rate with increasing oxygen concentration ($C_p < c_e|_{r=R_m} < C_{max}$, yellow to red region in bottom centre and right of Figure 3.2(c)) and die if the fluid shear stress they experience is too high ($\sigma_{e,xy}|_{y=R_m} > \Sigma_d$, blue band at top of Figure 3.2(c)). Despite the lack of experimental data for parameterisation, the model can be used to test the impact of promoting either sensitivity to oxygen or shear stress, through the concentration and shear stress thresholds and growth and death rate constants.

We make the further assumption that cell division forces cells outwards in such a way

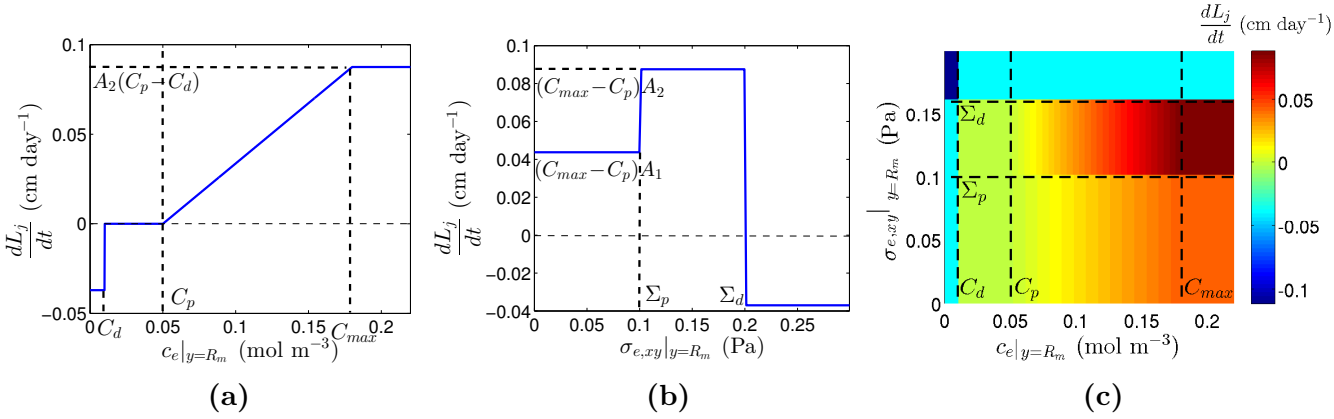

Figure 3.2: Prescribed variation in aggregate growth rate $\frac{dL_j}{dt}$ with (a) oxygen concentration c_e for fixed shear stress ($\sigma_{e,xy} = 0.15\,\text{Pa}$), (b) shear stress $\sigma_{e,xy}$ for fixed oxygen concentration ($c_e = 0.19\,\text{mol m}^{-3}$), and (c) oxygen concentration and shear stress. Concentration thresholds: $C_d = 0.01\,\text{mol m}^{-3}$, $C_p = 0.05\,\text{mol m}^{-3}$ and $C_{max} = 0.18\,\text{mol m}^{-3}$. Shear stress thresholds: $\Sigma_p = 0.1\,\text{Pa}$, $\Sigma_d = 0.2\,\text{Pa}$. Growth rate parameters: $A_1 = 0.68\,\text{day}^{-1}\,(\text{mol m}^{-3})^{-1}$, $A_2 = 1.35\,\text{day}^{-1}\,(\text{mol m}^{-3})^{-1}$, $B_0 = 0.075\,\text{day}^{-1}$, $B_1 = B_2 = 1$.

that the growth at the ends of the aggregate is equal, *i.e.*

$$\frac{\mathrm{d}x_{2j}}{\mathrm{d}t} = -\frac{\mathrm{d}x_{2j-1}}{\mathrm{d}t} = \frac{1}{2}\int_{x_{2j-1}(t)}^{x_{2j}(t)} \left(G_p(c_e|_{y=R_m}, \sigma_{e,xy}|_{y=R_m}) - G_d(c_e|_{y=R_m}, \sigma_{e,xy}|_{y=R_m})\right) \mathrm{d}x, \tag{3.23}$$

except when one end of the aggregate reaches the end of the membrane, in which case there is only growth at the opposite end and the total growth is halved. This gives $2N$ equations for the $2N$ unknown positions of the aggregate ends x_i $(i = 1, \ldots, 2N)$. To close the system given by (3.1)–(3.23) we prescribe the initial distribution of aggregates via $x_i(0)$ $(i = 1, \ldots, 2N)$.

3.4 Model reduction

The full model for the fluid flow, oxygen transport and aggregate growth in the HFB is given by equations (3.1)–(3.23). Rather than solve this system numerically, which is computationally expensive due to the coupling between the flow, oxygen transport and growth and the nonlinearity in the oxygen uptake, we first nondimensionalise and asymptotically reduce it. We nondimensionalise as follows

$$\begin{aligned}
&x = L\hat{x}, \quad y = R_l\hat{y}, \quad u_i = U\hat{u}_i, \quad v_i = \epsilon U\hat{v}_i, \quad t = \frac{2}{A_1 C_{in}}\hat{t}, \quad c_i = C_{in}\hat{c}_i, \quad i = l, m, e,\\
&p_i = P_{atm} + \frac{\mu U}{\epsilon^2 L}\hat{p}_i, \quad i = l, e, \quad p_m = P_{atm} + \frac{\epsilon^2 \mu U L}{k_m}\hat{p}_m, \quad \boldsymbol{\sigma}_i = \frac{\mu U}{\epsilon^2 L}\hat{\boldsymbol{\sigma}}_i, \quad i = l, e,\\
&\boldsymbol{\sigma}_m = \frac{\epsilon^2 \mu U L}{k_m}\hat{\boldsymbol{\sigma}}_m, \quad x_i = L\hat{x}_i, \; i = 1, \ldots, 2N, \quad R_m = R_l\hat{R}_m, \quad R_e = R_l\hat{R}_e,\\
&\hat{P}_{l,out} = \frac{\epsilon^2 L}{\mu U}(P_{l,out} - P_{atm}),
\end{aligned} \tag{3.24}$$

where hats denote dimensionless variables, the typical lumen flow velocity U is determined from the inlet flow rate by $U = Q_{in}/R_l$, and $\epsilon = R_l/L \ll 1$ as previously. The timescale is chosen as that for aggregate growth, $2/(A_1 C_{in})$, and represents the time taken for the cell population to double at high oxygen concentration ($c_e > C_{max}$) and low shear stress ($\sigma_{e,xy} < \Sigma_p$) (see Appendix B.2.2). On this timescale, the fluid and oxygen transport problems are quasi-steady (see §3.5.3). The pressure scale in the lumen, $\mu U/(\epsilon^2 L)$, is chosen to balance the axial pressure gradient with the transverse viscous terms in equation (3.1), and the pressure scale in the membrane, $\epsilon^2 \mu U L/k_m$, ensures that there is an $\mathcal{O}(1)$ pressure gradient in the y-direction in the membrane. In contrast to Chapter 2, the pressure scale in the ECS is chosen to be the same as that in the lumen to reflect the fact that we expect the axial flow to dominate in the ECS. In §§3.4.1–3.4.3 we exploit the small aspect ratios of the lumen, $\epsilon = R_l/L = 2 \times 10^{-3} \ll 1$, membrane and ECS to simplify the governing equations

by neglecting terms of $\mathcal{O}(\epsilon^2)$. From here on, we omit hats on dimensionless variables for ease of notation.

3.4.1 Fluid transport

The dimensionless versions of the lumen, ECS and membrane flow equations (3.1)–(3.2) are

$$\frac{\partial u_i}{\partial x}+\frac{\partial v_i}{\partial y}=0, \quad \epsilon^2\frac{\partial^2 u_i}{\partial x^2}+\frac{\partial^2 u_i}{\partial y^2}=\frac{\partial p_i}{\partial x}, \quad \epsilon^4\frac{\partial^2 v_i}{\partial x^2}+\epsilon^2\frac{\partial^2 v_i}{\partial y^2}=\frac{\partial p_i}{\partial y}, \quad i=l,e. \tag{3.25}$$

$$\frac{\partial u_m}{\partial x}+\frac{\partial v_m}{\partial y}=0, \quad u_m=-\epsilon^2\frac{\partial p_m}{\partial x}, \quad v_m=-\frac{\partial p_m}{\partial y}. \tag{3.26}$$

The dimensionless fluid stress tensors in the lumen, ECS and membrane are

$$\boldsymbol{\sigma}_i=\begin{pmatrix}\sigma_{i,xx} & \sigma_{i,xy}\\ \sigma_{i,xy} & \sigma_{i,yy}\end{pmatrix}=\begin{pmatrix}-p_i+2\epsilon^2\frac{\partial u_i}{\partial x} & \epsilon\frac{\partial u_i}{\partial y}+\epsilon^3\frac{\partial v_i}{\partial x}\\ \epsilon\frac{\partial u_i}{\partial y}+\epsilon^3\frac{\partial v_i}{\partial x} & -p_i+2\epsilon^2\frac{\partial v_i}{\partial y}\end{pmatrix}, \quad i=l,e, \quad \boldsymbol{\sigma}_m=-p_m\boldsymbol{I}. \tag{3.27}$$

The dimensionless boundary conditions at the lumen-membrane and membrane-ECS interfaces from (3.3) and (3.4) are

$$u_l=\phi_m u_m, \quad v_l=\phi_m v_m, \quad p_l-2\epsilon^2\frac{\partial v_l}{\partial y}=\kappa_m p_m \quad \text{on } \ y=1, \tag{3.28}$$

$$\phi_m u_m=u_e, \quad \phi_m v_m=v_e=k(x,t)\left(\kappa_m p_m-\left(p_e-2\epsilon^2\frac{\partial v_e}{\partial y}\right)\right) \quad \text{on } \ y=\hat{R}_m, \tag{3.29}$$

where

$$k(x,t)=k_{lo}I_a(x,t)+k_{hi}(1-I_a(x,t)), \tag{3.30}$$

and $k_{lo}=\mu K_{lo}/(\epsilon^3 L)$ and $k_{hi}=\mu K_{hi}/(\epsilon^3 L)$ are the dimensionless aggregate and membrane outer surface permeabilities (assumed to be $\mathcal{O}(1)$, see §3.5.1). Neglecting $\mathcal{O}(\epsilon^2)$ terms, the continuity and momentum equations (3.25) and (3.26) reduce to

$$\frac{\partial u_i}{\partial x}+\frac{\partial v_i}{\partial y}=0, \quad i=l,m,e, \tag{3.31}$$

$$\frac{\partial^2 u_i}{\partial y^2}=\frac{\partial p_i}{\partial x}, \quad \frac{\partial p_i}{\partial y}=0 \quad \Rightarrow \quad p_i=p_i(x,t), \quad i=l,e, \tag{3.32}$$

$$u_m=0, \quad \phi_m v_m=-\frac{\partial p_m}{\partial y}, \tag{3.33}$$

Since $u_m=\mathcal{O}(\epsilon^2)$, the boundary conditions (3.28) and (3.29) reduce at leading order in ϵ to

$$u_l=0, \quad v_l=\phi_m v_m, \quad p_l=\kappa_m p_m \quad \text{on } \ y=1, \tag{3.34}$$

$$u_e=0, \quad \phi_m v_m=v_e=k(x,t)(\kappa_m p_m-p_e) \quad \text{on } \ y=\hat{R}_m, \tag{3.35}$$

where the normal stress condition (3.4c) has reduced to Starling's equation in (3.35).

The remaining dimensionless conditions on the outer boundaries, from (3.7) and (3.8), are

$$v_l = 0, \quad \frac{\partial u_l}{\partial y} = 0 \quad \text{on} \quad y = 0, \tag{3.36}$$

$$u_e = 0, \quad v_e = 0 \quad \text{on} \quad y = \hat{R}_e, \tag{3.37}$$

$$u_e = 0 \quad \text{on} \quad x = 0, \ \hat{R}_m < y < \hat{R}_e, \tag{3.38}$$

and the dimensionless conditions at the inlet and outlets, from (3.10) and (3.11), are

$$\int_0^1 u_l|_{x=0} \, \mathrm{d}y = 1, \tag{3.39}$$

$$p_l = \hat{P}_{l,out} \quad \text{on} \quad x = 1, \ 0 < y < 1, \tag{3.40}$$

$$p_e = 0 \quad \text{on} \quad x = 1, \ \hat{R}_m < y < \hat{R}_e. \tag{3.41}$$

We note that the assumption that the y length scale for the flow is much shorter than the x length scale is strictly only valid away from the lumen inlet, so it is necessary to confirm that any boundary layers near the inlet do not affect the flow in the rest of the bioreactor. We do this in Appendix D, where we solve the full flow problem given by (3.2)–(3.21) with steady Navier-Stokes equations for the flow in the lumen.

3.4.2 Oxygen transport

On nondimensionalisation the oxygen transport equations in (3.13) become

$$\epsilon^2 \mathrm{Pe}_i \left(u_i \frac{\partial c_i}{\partial x} + v_i \frac{\partial c_i}{\partial y} \right) = \epsilon^2 \frac{\partial^2 c_i}{\partial x^2} + \frac{\partial^2 c_i}{\partial y^2}, \quad i = l, m, e, \tag{3.42}$$

where $\epsilon^2 \mathrm{Pe}_i = \epsilon^2 UL/D_i$ $(i = l, m, e)$ are the reduced Péclet numbers (the ratios of the timescales for radial diffusion and axial advection of oxygen) in the different regions, which are $\mathcal{O}(1)$ for the flow rates we consider (see Table 3.1). At leading order in ϵ, (3.42) therefore simplifies to

$$\epsilon^2 \mathrm{Pe}_i \left(u_i \frac{\partial c_i}{\partial x} + v_i \frac{\partial c_i}{\partial y} \right) = \frac{\partial^2 c_i}{\partial y^2}, \quad i = l, m, e. \tag{3.43}$$

The lumen-membrane and membrane-ECS interface conditions, (3.14) and (3.15), become

$$c_l = c_m, \quad \frac{D_l}{\phi_m D_m} \frac{\partial c_l}{\partial y} = \frac{\partial c_m}{\partial y} \quad \text{on} \quad y = 1, \tag{3.44}$$

$$c_m = c_e, \quad \frac{\partial c_e}{\partial y} - \frac{\phi_m D_m}{D_e} \frac{\partial c_m}{\partial y} = \mathrm{Da} \, I_a(x,t) \frac{c_e}{c_{1/2} + c_e} \quad \text{on} \quad y = \hat{R}_m, \tag{3.45}$$

where $\mathrm{Da} = R_l M/(D_e C_{in})$ is the dimensionless uptake flux, or second Damköhler number, (the ratio of the rate of oxygen uptake by the cells, $M/(R_l C_{in})$, to the rate of diffusive transport, D_e/R_l^2), and $c_{1/2} = C_{1/2}/C_{in}$ is the dimensionless half-maximal uptake flux

concentration. For the diffusive flux condition in (3.45) to hold at leading order, it is necessary that $\epsilon^2 \ll \mathrm{Da} \ll 1/\epsilon^2$, which we verify *a posteriori* in §3.5.2.

Finally, the dimensionless forms of the inlet concentration and zero-diffusive-flux boundary conditions (3.16)–(3.21) are

$$c_l = 1 \quad \text{on} \quad x = 0, \qquad \frac{\partial c_l}{\partial x} = 0 \quad \text{on} \quad x = 1, \qquad \frac{\partial c_l}{\partial y} = 0 \quad \text{on} \quad y = 0, \tag{3.46}$$

$$\frac{\partial c_m}{\partial x} = 0 \quad \text{on} \quad x = 0, 1, \ 1 < y < \hat{R}_m, \tag{3.47}$$

$$\frac{\partial c_e}{\partial x} = 0 \quad \text{on} \quad x = 0, 1, \ \hat{R}_m < y < \hat{R}_e, \qquad \frac{\partial c_e}{\partial y} = 0 \quad \text{on} \quad y = \hat{R}_e. \tag{3.48}$$

3.4.3 Cell aggregate growth

From (3.27), the shear stress along the membrane in the ECS is

$$\mathbf{e}_y \cdot \boldsymbol{\sigma}_e \cdot \mathbf{e}_x|_{y=\hat{R}_m} = \sigma_{e,xy}|_{y=\hat{R}_m} = \left(\epsilon \frac{\partial u_e}{\partial y} + \epsilon^3 \frac{\partial v_e}{\partial x} \right) \Bigg|_{y=\hat{R}_m},$$

the dominant component of which is $\epsilon \frac{\partial u_e}{\partial y}\big|_{y=\hat{R}_m}$, so we approximate the shear stress by this component. The dimensionless form of the evolution equation for the aggregate lengths (3.23) is then given by

$$\frac{\mathrm{d}x_{2j}}{\mathrm{d}t} = -\frac{\mathrm{d}x_{2j-1}}{\mathrm{d}t} = \int_{x_{2j-1}(t)}^{x_{2j}(t)} \left(\hat{G}_p \left(c_e|_{y=\hat{R}_m}, \frac{\partial u_e}{\partial y}\Big|_{y=R_m} \right) - \hat{G}_d \left(c_e|_{y=R_m}, \frac{\partial u_e}{\partial y}\Big|_{y=R_m} \right) \right) \mathrm{d}x, \tag{3.49}$$

where

$$\hat{G}_p \left(c_e, \tfrac{\partial u_e}{\partial y} \right) = \left[\mathrm{H}(c_e - c_p)\mathrm{H}(c_{max} - c_e)(c_e - c_p) + \mathrm{H}(c_e - c_{max})(c_{max} - c_p) \right], \\ \times \left[\mathrm{H}\left(\sigma_p - \tfrac{\partial u_e}{\partial y} \right) + \alpha \mathrm{H}\left(\tfrac{\partial u_e}{\partial y} - \sigma_p \right) \mathrm{H}\left(\sigma_d - \tfrac{\partial u_e}{\partial y} \right) \right] \tag{3.50}$$

$$\hat{G}_d \left(c_e, \tfrac{\partial u_e}{\partial y} \right) = \beta_1 \mathrm{H}(c_d - c_e) + \beta_2 \mathrm{H}\left(\tfrac{\partial u_e}{\partial y} - \sigma_d \right) + \beta_3 \mathrm{H}(c_d - c_e) \mathrm{H}\left(\tfrac{\partial u_e}{\partial y} - \sigma_d \right), \tag{3.51}$$

with $c_d = C_d/C_{in}$, $c_p = C_p/C_{in}$ and $c_{max} = C_{max}/C_{in}$ being the dimensionless concentration thresholds for cell survival, proliferation and maximal proliferation; $\sigma_k = \epsilon L \Sigma_k/(\mu U)$ $(k = p, d)$ the dimensionless shear stress thresholds for faster proliferation and cell death; $\alpha = A_2/A_1 > 1$ the ratio of the elevated growth rate for intermediate shear stress to the baseline growth rate for low shear stress; and $\beta_k = B_0 B_k/(A_1 C_{in})$ $(k = 1, 2)$ and $\beta_3 = B_0 B_1 B_2/(A_1 C_{in})$ the ratio of the shortening rates due to insufficient oxygen and excess shear stress, and the combination of the two, to the baseline growth rate.

3.5 Parameter values

Currently, not all the values of the model parameters have been determined for the single-fibre HFB. Hence, as in Chapter 2, we use a combination of values determined from experiments with the single-fibre HFB and values for the same or similar systems from the literature.

3.5.1 Fluid transport

We use the same values for the bioreactor dimensions and flow parameters as given in Table 2.1 in Chapter 2 apart from for the lumen inlet flow rate Q_{in} (and therefore the typical lumen flow velocity U), and the outlet pressure $P_{l,out}$ (Table 3.1). We consider a slightly larger range of inlet flow rates, 0.023–2.3 ml min^{-1}, and convert these to 2D flow rates into the lumen cross-section (in m^{2}s^{-1}) by dividing by the lumen circumference ($2\pi R_l$), so that $Q_{in} = 3\times10^{-7}$–3×10^{-5} m^{2}s^{-1}. For this range of Q_{in}, $U = Q_{in}/R_l = 1.5\times10^{-3}$–$0.15$ m s^{-1}, and the reduced Reynolds number, $\epsilon^2\mathrm{Re} = \epsilon^2\rho UL/\mu$, is in the range 6×10^{-4}–6×10^{-2}, so we are justified in neglecting inertia in the lumen and ECS flow equations in (3.1). We consider a smaller range for $P_{l,out}$ of 14.9–19.0 psi (1.027×10^5–1.310×10^5 Pa) than in the cell layer growth model, as we anticipate that cell aggregates at the outer surface of the membrane will generally experience higher shear stresses than cells at the surface of the cell layer at a given inlet flow rate and outlet pressure. As in Chapter 2, in all simulations $P_{l,out}$ is chosen so that there is no backflow at the lumen exit (see §3.6.5).

The value of the aggregate permeability K_{lo} has not been measured experimentally but represents the degree of resistance to the flow at the outer surface of the membrane provided by the cell aggregates (a value of 0 means that they block the flow completely, while a very large value means they offer little resistance to the flow). The value of the membrane outer surface permeability K_{hi} represents the extent to which pores in the outer surface of the membrane are blocked by ECM and protein deposition by the cells (low values correspond to significant blocking, high values to little blocking). In order for the fluid flux condition at the outer surface of the membrane in (3.35) to hold at leading order, the dimensionless aggregate permeability, $k_{lo} = \mu K_{lo}/(\epsilon^3 L)$, and dimensionless membrane outer surface permeability, $k_{hi} = \mu K_{hi}/(\epsilon^3 L)$, must satisfy $\epsilon^2 \ll k_{lo}, k_{hi} \ll 1/\epsilon^2$. We assume that $k_{lo} = \mathcal{O}(1)$, so that there is an $\mathcal{O}(1)$ flux through the aggregates, and take $k_{hi} = 10k_{lo}$. Although larger values of $k_{hi} \gg 1$ can be considered, we note that taking $k_{hi} \gg 1$ and $k_{lo} = \mathcal{O}(1)$ leads to numerical issues with resolving sharp gradients in $k(x,t)$ at the ends of the aggregates (see §3.6.2).

3.5.2 Oxygen transport

We use the same values for the oxygen diffusivities in the different regions of the bioreactor as for the cell layer growth model. The reduced Péclet numbers in the different regions cover slightly larger ranges than for the cell layer growth model due to the greater range of flow rates considered (Table 3.1).

Values for the other transport parameters—the inlet oxygen concentration C_{in}, the half-maximal uptake flux concentration $C_{1/2}$, and the maximal uptake flux M—are cell-type-dependent. Experimental data for these parameters for different cell types is presented in Tables 2.4 and B.4. For the aggregate growth simulations in §3.7, we follow Shipley and Waters [231] and use values of the transport and uptake parameters appropriate to rat cardiomyocytes from [215]. We convert the estimate of the maximal volumetric oxygen uptake rate V_{max} (the maximum rate of oxygen uptake per unit volume of cells, in $\mathrm{mol\,m^{-3}\,s^{-1}}$) of the rat cardiomyocytes in [215] to a value for M (the maximum rate of oxygen uptake per unit surface area covered by cells, in $\mathrm{mol\,m^{-2}\,s^{-1}}$) by multiplying it by the estimated cell volume V_c (to estimate the cellular uptake rate M_c, in $\mathrm{mol\,cell^{-1}\,s^{-1}}$) and the surface density of cells on the membrane ρ_s,

$$\begin{aligned} M &= M_c\rho_s = V_{max}V_c\rho_s \\ &= 2.64\times10^{-3}\,\mathrm{mol\,m^{-3}\,s^{-1}} \times 1.6\times10^{-15}\,\mathrm{m^3} \times 7.3\times10^{10}\,\mathrm{cells\,m^{-2}} \\ &= 3.08\times10^{-7}\,\mathrm{mol\,m^{-2}\,s^{-1}}, \end{aligned}$$

where the value of ρ_s is taken from [251] and V_c is estimated from the data in Table B.5 (see Table B.4 for further details). The corresponding value of the dimensionless uptake flux is $\mathrm{Da} = 0.093$, which satisfies $4\times10^{-6} = \epsilon^2 \ll \mathrm{Da} \ll 1/\epsilon^2 = 2.5\times10^5$, so the uptake condition in (3.45) is valid at leading order.

3.5.3 Seeding and growth parameters

The growth parameter values used in the simulations in §3.7 are given in Table 3.1 (a discussion of how these values are estimated can be found in Appendix B.2.2). We use experimental data to estimate the typical fraction of the fibre surface area that is initially covered by cell aggregates and the aggregate elongation rate as described in Appendix B.2.2. In our simulations, 25% of the membrane is initially covered by cell aggregates (*i.e.* the initial total aggregate length is 2.5 cm, equivalent to 625 cells). For the estimated baseline growth rate, $A_1 = 0.68\,\mathrm{day^{-1}\,(mol\,m^{-3})^{-1}}$, the growth timescale is $2/(A_1C_{in}) \sim 13.5\,\mathrm{days} = 1.2\times10^6\,\mathrm{s}$. This is much longer than the advection timescale, $L/U = 0.67$–$67\,\mathrm{s}$, and the diffusion and uptake timescales, $R_l^2/D_i = 13$–$130\,\mathrm{s}$ $(i = l, m, e)$ and $C_{in}R_l/M = 7$–$4.7\times10^4\,\mathrm{s}$, which justifies treating the fluid and oxygen transport as steady at leading order.

Parameter	Description	Value(s)	Reference
Dimensional Parameters			
Q_{in}	2D lumen inlet flow rate	3×10^{-7}–$3 \times 10^{-5}\,\mathrm{m^2 s^{-1}}$	[231, 233]
U	typical lumen flow velocity	1.5×10^{-3}–$0.15\,\mathrm{m\,s^{-1}}$	-
$P_{l,out}$	lumen outlet pressure	1.027×10^5–1.310×10^5 Pa	[233]
K_{lo}	cell aggregate permeability	$8 \times 10^{-8}\,\mathrm{m^2\,s\,kg^{-1}}$	See §3.5.1
K_{hi}	membrane outer surface permeability	$8 \times 10^{-7}\,\mathrm{m^2\,s\,kg^{-1}}$	See §3.5.1
M	maximal oxygen uptake flux	$3.08 \times 10^{-7}\,\mathrm{mol\,m^{-2}\,s^{-1}}$	[215] †
C_{in}	inlet oxygen concentration	$0.22\,\mathrm{mol\,m^{-3}}$	[215] †
$C_{1/2}$	half maximal uptake rate concentration	$6.9 \times 10^{-3}\,\mathrm{mol\,m^{-3}}$	[215] †
C_d	minimum oxygen concentration for cell survival	$6 \times 10^{-3}\,\mathrm{mol\,m^{-3}}$	[215] †
C_p	minimum oxygen concentration for cell proliferation	0.05–$0.1\,\mathrm{mol\,m^{-3}}$	‡
C_{max}	maximal growth rate oxygen concentration	0.18–$0.21\,\mathrm{mol\,m^{-3}}$	‡
Σ_p	shear stress threshold for elevated proliferation rate	0.01–0.05 Pa	Appendix B.2.2.3
Σ_d	shear stress threshold for cell death	0.05–0.16 Pa	[215], Appendix B.2.2.3
A_1	baseline growth rate for low shear stress	$0.68\,\mathrm{day^{-1}\,(mol\,m^{-3})^{-1}}$	[70], Appendix B.2.2.2
A_2	elevated growth rate for intermediate shear stress	$1.35\,\mathrm{day^{-1}\,(mol\,m^{-3})^{-1}}$	‡
B_0	baseline aggregate shortening rate for insufficient oxygen or excess shear stress	$0.075\,\mathrm{day^{-1}}$	‡
Dimensionless Parameters			
$\epsilon^2\mathrm{Re}$	reduced Reynolds number	6×10^{-4}–6×10^{-2}	-
$\hat{P}_{l,out}$	dimensionless lumen outlet pressure	6.45–645	-
k_{lo}	dimensionless aggregate permeability	0.1	-
k_{hi}	dimensionless membrane outer surface permeability	1	-
$\epsilon^2\mathrm{Pe}_l$	lumen reduced Péclet number	0.2–20	-
$\epsilon^2\mathrm{Pe}_m$	membrane reduced Péclet number	2–200	-
$\epsilon^2\mathrm{Pe}_e$	ECS reduced Péclet number	0.2–200	-
Da	dimensionless uptake flux	0.093	-
B_1	weight factor for aggregate shortening rate due to insufficient oxygen	1	-
B_2	weight factor for aggregate shortening rate due to excess shear stress	1	-

Table 3.1: Parameter values used in aggregate growth simulations. Bioreactor and other flow parameter values used are as in Table 2.1 in Chapter 2.
† Values stated are for rat cardiomyocytes (see Tables 2.4 and B.2–B.4 for values for other cell types).
‡ Parameter values for which there is limited experimental data and that are varied in the growth simulations.

3.6 Solution of the reduced model

We now describe how we solve the reduced model for the fluid flow, oxygen transport and aggregate growth given by equations (3.31)–(3.41), (3.43)–(3.48) and (3.49)–(3.51).

3.6.1 Fluid transport

First we derive the governing PDE and boundary conditions for the lumen pressure. Integrating the leading order fluid transport equations, (3.31)–(3.33), subject to the boundary conditions (3.34)–(3.41), gives the velocity components in each region as

$$u_l = \frac{1}{2}\frac{\partial p_l}{\partial x}(y^2-1), \quad v_l = \frac{1}{6}\frac{\partial^2 p_l}{\partial x^2}y(3-y^2), \tag{3.52}$$

$$u_m = 0, \quad v_m = \frac{1}{3\phi_m}\frac{\partial^2 p_l}{\partial x^2}, \tag{3.53}$$

$$u_e = \frac{1}{2}\frac{\partial p_e}{\partial x}(y-\hat{R}_m)(y-\hat{R}_e), \quad v_e = -\frac{1}{12}\frac{\partial^2 p_e}{\partial x^2}(y-\hat{R}_e)^2(2y-3\hat{R}_m+\hat{R}_e), \tag{3.54}$$

i.e. the flow in the lumen and ECS has a Poiseuille profile. The pressures in the membrane and ECS are

$$p_m = \frac{p_l}{\kappa_m} - \frac{1}{3}\frac{\partial^2 p_l}{\partial x^2}(y-1), \quad p_e = \frac{1}{(\hat{R}_e-\hat{R}_m)^3}(12(1-x)-4(p_l-\hat{P}_{l,out})). \tag{3.55}$$

Starling's equation on the interface between the membrane and the ECS in (3.35) gives the following second-order PDE for p_l

$$\frac{1}{3}(1+\kappa_m(\hat{R}_m-1)k(x,t))\frac{\partial^2 p_l}{\partial x^2} - \left(1+\tfrac{4}{(\hat{R}_e-\hat{R}_m)^3}\right)k(x,t)p_l = -\tfrac{k(x,t)}{(\hat{R}_e-\hat{R}_m)^3}(12(1-x)+4\hat{P}_{l,out}), \tag{3.56}$$

and (3.39) and (3.40) supply the boundary conditions for p_l at the inlet and outlet

$$\frac{\partial p_l}{\partial x}(0,t) = -3, \quad p_l(1,t) = \hat{P}_{l,out}. \tag{3.57}$$

The leading order system of equations for the fluid flow, oxygen transport and aggregate growth is thus given by equations (3.56)–(3.57), (3.30), and (3.43)–(3.54). We solve this system numerically as described in §3.6.3. First, however, we describe how we smooth the aggregate indicator function, $I_a(x,t)$, to overcome issues associated with its discrete form in equation (3.6).

3.6.2 Smoothed aggregate indicator function

With $I_a(x,t)$ as defined in (3.6), the permeability of the outer surface of the membrane, $k(x,t)$, and oxygen uptake, $\mathrm{Da}\, I_a(x,t)c_e/(c_{1/2}+c_e)$, are discontinuous at the ends of the cell aggregates. To solve the boundary value problem for p_l given by (3.56) and (3.57) we

would therefore need to specify two boundary conditions at each end of each cell aggregate and integrate (3.56) piecewise. A bigger problem with using the piecewise continuous I_a in (3.6), however, is that $\frac{\partial^2 p_l}{\partial x^2}$, and therefore the y-velocity components in (3.52)–(3.54), are discontinuous at the ends of the cell aggregates.

To circumvent these problems, we use a smoothed version of the indicator function, which is continuous at the ends of the aggregates, to represent the membrane outer surface permeability and oxygen uptake. For N aggregates with ends at $x_i(t)$ $(i = 1, \ldots, 2N)$, the smoothed indicator function is

$$I_a(x,t) = \sum_{j=1}^{N} \frac{1}{2}\big[\tanh(s(x - x_{2j-1}(t))) + \tanh(s(x_{2j}(t) - x))\big], \tag{3.58}$$

where the constant s determines the sharpness of the transition between the values of the permeability and uptake inside and outside the cell aggregate (Figure 3.3). The higher the value of s, the sharper the transition in the indicator function at the ends of the aggregates and the more closely it approximates the discrete indicator function. Defined in this way, $I_a(x,t)$ can be viewed as a cell density. Since the permeability $k(x,t)$, as defined in (3.30), is continuous with this definition of I_a there is no need to specify extra conditions at the ends of the aggregates and we can integrate (3.56) over the whole length of the membrane rather than piecewise.

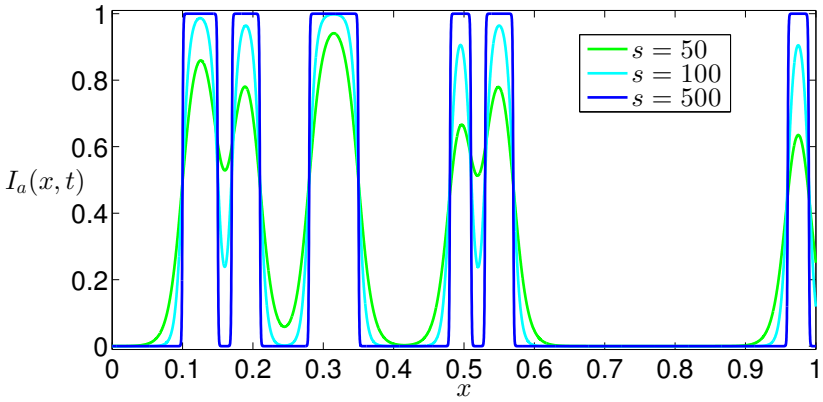

Figure 3.3: Smoothed aggregate indicator function $I_a(x,t)$ defined in (3.58) for an example aggregate distribution. The sharpness of the transitions in I_a at the ends of the aggregates is shown for different values of the smoothing factor s.

Using a larger value of s increases the computational cost of simulations as a finer mesh is required to resolve the transitions in I_a. So that the discrete indicator function is closely approximated by (3.58), but the computational cost remains reasonable, we use $s = 500$ in all simulations. The flow and oxygen distributions for $s = 500$ were compared with

those for larger values of s for various static aggregate distributions and showed negligible differences. Using $s = 500$ imposes a lower limit on the aggregate length that can be used in the model for I_a to reach 1 inside the aggregate. The shortest aggregate length that can be resolved is approximately -five times the length scale over which the transitions in I_a occur, $L_{agg} \approx 5L/s = 1\,\text{mm}$. In our simulations the shortest aggregates we use are 5 mm long. We note that there is an analytical lower bound on the aggregate length, $L_{agg} > R_l$, necessary for the leading order growth equation (3.49) to hold, but this is a weaker constraint than that due to the value of s.

3.6.3 Numerical solution of the leading order system

We solve the leading order system for the flow, oxygen transport and growth numerically using code developed in MATLAB. At each time step, the steady flow and oxygen transport equations ((3.56)–(3.57) and (3.43)–(3.48)-, respectively) are solved for the current aggregate distribution (starting from a chosen initial distribution of N cell aggregates), and the solutions used to update the aggregate lengths via (3.49). The aggregate distribution affects the flow (through the outer surface membrane permeability, $k(x,t)$, in (3.56)) and the oxygen transport (through the nonlinear uptake term in the diffusive flux condition at the outer surface of the membrane (3.45)). The flow equations (3.56) and (3.57) are solved using the MATLAB boundary value problem solver `bvp4c`. The oxygen advection-diffusion equations are solved using the Galerkin finite element method (FEM) with piecewise linear basis functions on a regular triangular mesh with 320,000 elements (160,801 nodes) (the nodes of the mesh have spacings of $\Delta x = 2.5\times10^{-3}$ and $\Delta y = 1.25\times10^{-2}$, corresponding to dimensional spacings of 2.5×10^{-4} m in the x-direction and 2.5×10^{-6} m in the y-direction). To solve equations (3.43)–(3.48) in this way as a linear system, it is necessary to use the concentration at the outer surface of the membrane from the previous time step in the denominator of the nonlinear uptake term at each time step, *i.e.* to evaluate the uptake condition in (3.45) at time $t = t_n = n\Delta t$ as

$$\frac{\partial c_e^{(n+1)}}{\partial y} - \frac{\phi_m D_m}{D_e}\frac{\partial c_m^{(n+1)}}{\partial y} = \text{Da}\, I_a(x,t_n)\frac{c_e^{(n+1)}}{c_{1/2}+c_e^{(n)}} \quad \text{on} \quad y = \hat{R}_m, \tag{3.59}$$

where the superscript (n) denotes evaluation at time t_n. At the first time step this requires an estimate for $c^{(0)}|_{y=\hat{R}_m}$. This is found by solving the oxygen transport equations (3.43)–(3.48) and (3.59) iteratively with the initial aggregate distribution fixed and an initial guess of $c_e|_{y=\hat{R}_m} \equiv 1$ until a fixed point is reached (in practice, until the maximum difference between consecutive concentration solutions is less than 10^{-4}).

The algorithm for simulating the aggregate growth then proceeds as follows:

1. Evaluate I_a for the current aggregate distribution, $x_i(t)$ $(i = 1, \ldots, 2N)$, (the prescribed initial distribution is used at the first time step) using (3.58).

2. Solve the boundary value problem for p_l given by (3.56), (3.30) (with I_a given by (3.58)) and (3.57) using the MATLAB solver `bvp4c` and evaluate the fluid velocities (3.52)–(3.54).

3. Solve the oxygen transport problems given by (3.43) (with (3.52)–(3.54)) and (3.44)–(3.48) using the Galerkin FEM.

4. Calculate the growth rate of each aggregate by evaluating the right-hand side of the growth law (3.49) and update the positions of the aggregate ends using an explicit Euler discretisation of the growth law. If the growth of an aggregate is larger than the space to the next aggregate either to the left or right, take the aggregate to grow until it touches the next aggregate in that direction, and thereafter treat the touching aggregates as a single aggregate. If one end of an aggregate reaches either end of the model domain ($x = 0$ or $x = L$), fix that end of the aggregate, take all growth to occur at its opposite end and take the overall growth to be halved.

5. Repeat Steps 1–4 until either the aggregates cover the entire membrane or the simulation time has elapsed.

3.6.4 Verification of numerical scheme

Several checks were performed and the accuracy of the numerical scheme verified as described in Appendix D. The convergence of the finite element (FE) scheme was verified on a test problem, and solutions for the fluid and oxygen transport obtained using the code in simplified regimes were checked. The accuracy of the numerical solutions of the reduced model for the fluid and oxygen transport was then verified by solving the full fluid and oxygen transport model (given by equations (3.1)–(3.21), but with inertial terms added to the lumen and ECS flow equations (3.1) and the smoothed version of the aggregate indicator function (3.58)) for a static distribution of five aggregates using the FE software COMSOL Multiphysics 4.3[1]. Over the range of parameter values for which the reduced model is valid, the error in the reduced model solutions was consistent with the size of the terms neglected.

3.6.5 Maximum lumen outlet pressure

As for the HFB set-up with the ECS port open in Chapter 2, for a given inlet flow rate there is a maximum lumen outlet pressure, $P_{l,out}^{max}$, that can be applied without backflow occurring.

[1] See http://www.comsol.com

However, here it is not straightforward to approximate this analytically because of the dependence of the lumen pressure on the aggregate distribution. We therefore determine the relationship between $P_{l,out}^{max}$ and Q_{in} in the reduced model numerically. For a single cell aggregate of fixed length 1 cm in the middle of the membrane we obtain the relationship shown in Figure 3.4. We note that $P_{l,out}^{max}$ increases with the fraction of the membrane surface covered by cell aggregates, due to the associated decrease in permeability of the surface, $K(x,t)$, so that the relationship with a single relatively short aggregate provides an approximate lower bound for $P_{l,out}^{max}$.

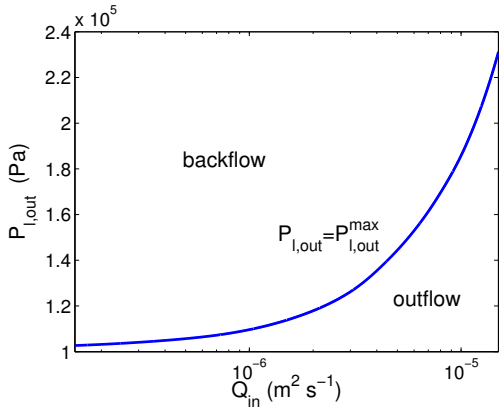

Figure 3.4: Relationship between maximum lumen outlet pressure without backflow $P_{l,out}^{max}$ and flow rate Q_{in}. Scale on horizontal axis is logarithmic. Parameter values as in Table 3.1.

3.7 Numerical results

In the following sections, we investigate the influence of the flow conditions and seeding distribution on the cell aggregate growth by simulating the growth for a range of flow rates and outlet pressures and initial aggregate distributions. Our aim is to identify the flow conditions and seeding distributions that give the most rapid overall growth, and to determine how these vary with the sensitivity of the cells to oxygen levels and shear stress. We focus on rat cardiomyocytes (the cell type for which we have most experimental data for the parameter values), but consider different values of the concentration thresholds, C_p and C_d, and shear stress thresholds, Σ_p and Σ_d. First we give an example of how the oxygen and shear stress distributions in the bioreactor evolve as the cell aggregates grow. All results are presented in dimensional variables.

3.7.1 Evolution of oxygen, shear stress and aggregate distributions

Figure 3.5 shows the growth of a distribution of rat cardiomyocyte aggregates along the membrane and the corresponding evolution of the oxygen and shear stress distributions in

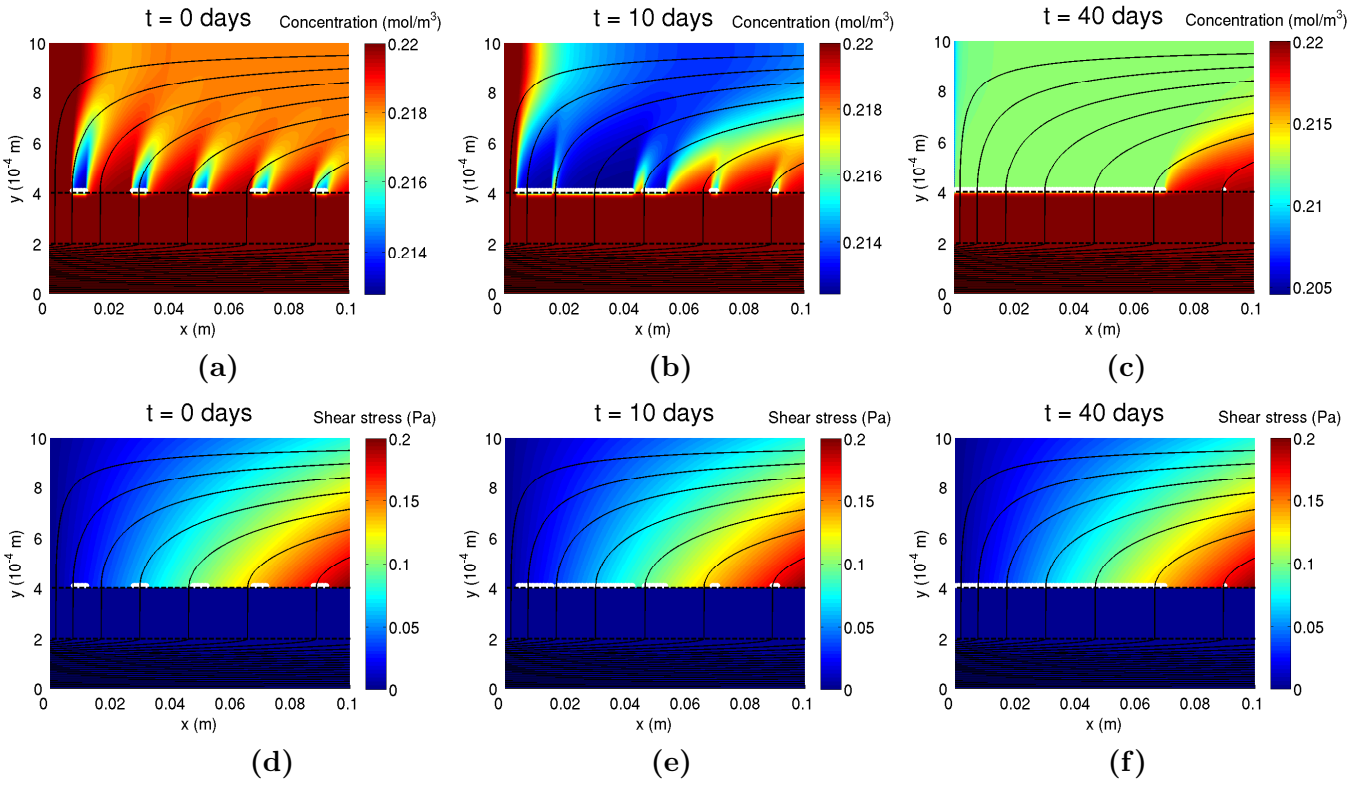

Figure 3.5: Evolution of (a)–(c) the oxygen distribution and (d)–(f) the shear stress distribution with the growth of a distribution of rat cardiomyocyte aggregates over 40 days. Aggregates shown in white. Solid black lines are flow streamlines. The dark blue in the lumen and membrane in (d)–(f) indicates very low and negative fluid shear stress in these regions, respectively. Parameter values: $N = 5$, $L_{agg} = 0.5\,\text{cm}$, $Q_{in} = 3 \times 10^{-5}\,\text{m}^2\text{s}^{-1}$, $P_{l,out} = 1.310 \times 10^5\,\text{Pa}$, $C_p = 0.05\,\text{mol}\,\text{m}^{-3}$, $C_{max} = 0.18\,\text{mol}\,\text{m}^{-3}$, $\Sigma_p = 0.03\,\text{Pa}$, $\Sigma_d = 0.08\,\text{Pa}$; A_1, A_2, B_0, B_1 and B_2 as in Figure 3.2. All other parameter values as in Table 3.1.

the ECS for typical parameter values (see legend). The initial aggregate distribution (shown in Figure 3.5(a),(d)) consists of five aggregates of length $L_{agg} = 0.5\,\text{cm}$ distributed evenly along the membrane (such that $x_{2j-1}(0) = (2j - 1.25)\,\text{cm}$, $x_{2j}(0) = x_{2j-1}(0) + 0.5\,\text{cm}$, $j = 1, \ldots, 5$). This distribution is used for all subsequent simulations, unless otherwise stated, so that we can isolate and compare the impacts of oxygen delivery and fluid shear stress on growth. Due to uptake by the cells, oxygen is depleted in regions surrounding each aggregate that extend outwards from the membrane into the ECS. These regions increase in size as the aggregates grow and eventually merge to form one large region (Figures 3.5(a)–(c)). The flow of the culture medium ensures that the oxygen concentration remains highest at the upstream wall of the ECS until the aggregates come into contact with it. The shear stress profile along the membrane remains fairly constant in time as the aggregates grow

(Figures 3.5(d)–(f)), because the aggregates have only a small effect on the membrane outer surface permeability, and therefore on the flow (for the chosen values of K_{lo} and K_{hi}). The aggregates do not reach confluence after 40 days (the chosen simulation time) as the shear stress exceeds the cell death threshold ($\sigma_{e,xy}|_{y=R_m} > \Sigma_d$) towards the outlet. Thus the three aggregates nearest the inlet grow and coalesce to form one large aggregate, while the fourth aggregate neither grows nor shrinks and the rightmost one shrinks.

3.7.2 Impact of flow on oxygen flux and shear stress

To understand how the inlet flow rate, Q_{in}, and outlet pressure, $P_{l,out}$, affect the growth of the aggregates we first determine how they affect the oxygen concentration around, and shear stress on, the aggregates.

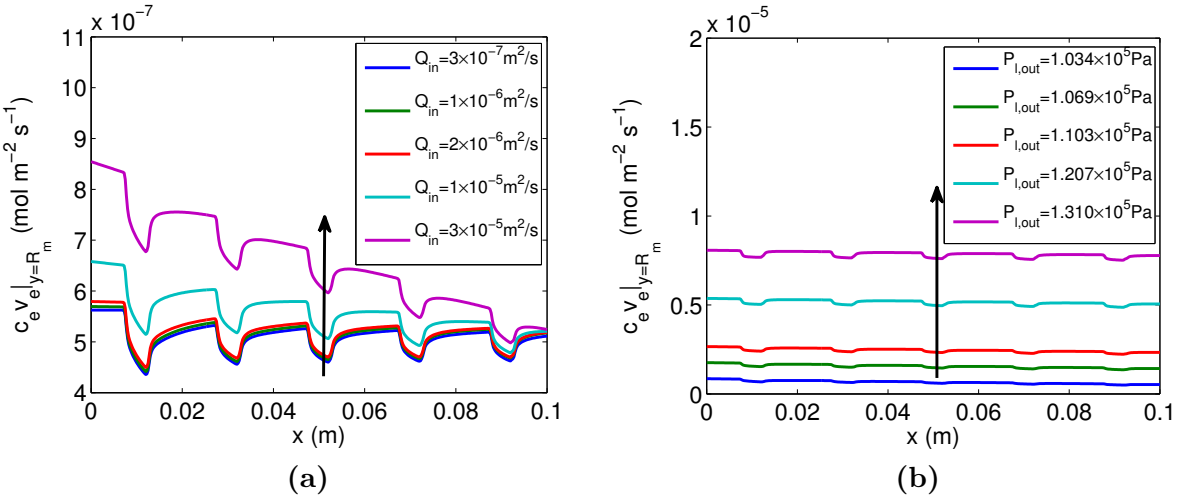

Figure 3.6: Advective oxygen flux across the membrane outer surface, $c_e v_e|_{y=R_m}$, for (a) different flow rates and (b) different outlet pressures for the distribution of rat cardiomyocyte aggregates in Figure 3.5(a). Arrow shows direction of increasing Q_{in} in (a) and increasing $P_{l,out}$ in (b). Parameter values: (a) $P_{l,out} = 1.034 \times 10^5$ Pa, (b) $Q_{in} = 3 \times 10^{-5}\,\mathrm{m^2 s^{-1}}$. All other parameter values as in Figure 3.5.

Figures 3.6(a) and 3.6(b) show how the advective oxygen flux through the outer surface of the membrane, $c_e v_e|_{y=R_m}$, changes when Q_{in} and $P_{l,out}$ are varied for the rat cardiomyocyte aggregate distribution in Figure 3.5(a). The flux dips in the regions of the membrane covered by aggregates because of the oxygen uptake and reduced fluid permeability there. Increasing Q_{in} or $P_{l,out}$ increases the oxygen flux through the membrane. However, the system is more sensitive to changes in $P_{l,out}$ than Q_{in}: a 100-fold increase in Q_{in} (from $3 \times 10^{-7}\,\mathrm{m^2 s^{-1}}$ to $3 \times 10^{-5}\,\mathrm{m^2 s^{-1}}$) leads to an increase of at most 50% in the flux, while a 14-fold increase in $(P_{l,out} - P_{atm})$ (the outlet pressure relative to atmospheric pressure, from 2.1 kPa to 29.6 kPa, or 0.3 to 4.3 psi) produces an 8-fold increase. This is because

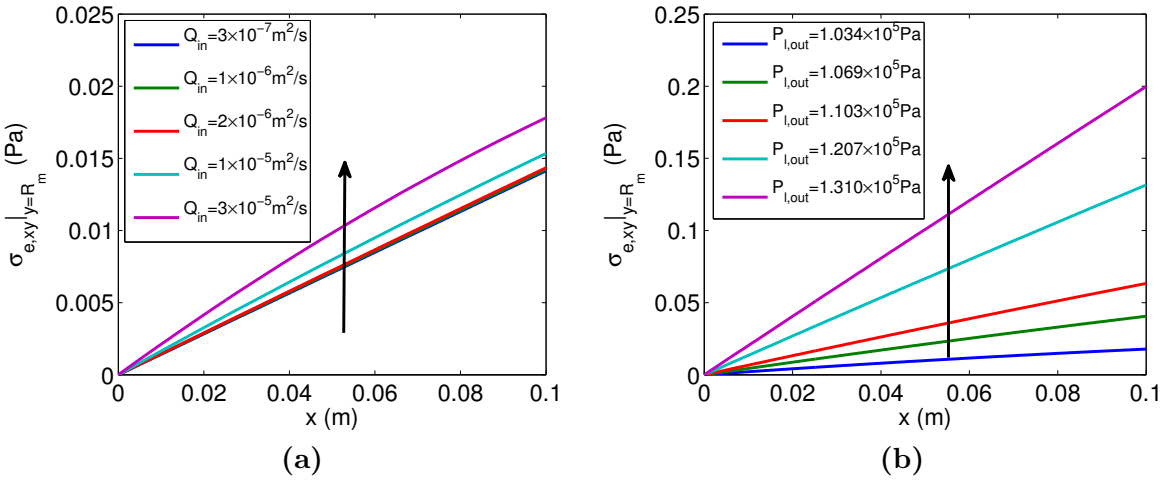

Figure 3.7: Shear stress along the membrane, $\sigma_{e,xy}|_{y=R_m}$, for (a) different flow rates and (b) different outlet pressures. Arrow shows direction of increasing Q_{in} in (a) and increasing $P_{l,out}$ in (b). Parameter values: (a) $P_{l,out} = 1.034 \times 10^5$ Pa, (b) $Q_{in} = 3 \times 10^{-5}\,\mathrm{m^2 s^{-1}}$. All other parameter values as in Figure 3.6.

the bulk of the pressure drop from the lumen inlet to the ECS outlet occurs across the membrane, so increasing $P_{l,out}$ gives a much bigger pressure gradient across, and therefore flow through, the membrane. As shown in Figure 3.7, the shear stress, $\sigma_{e,xy}|_{y=R_m}$, increases with distance along the membrane surface (from 0 at the upstream end of the ECS, which is closed) and as Q_{in} and $P_{l,out}$ are increased. The shear stress reached at the outlet ranges between 0.01 Pa and 0.2 Pa for the ranges of Q_{in} and $P_{l,out}$ considered. The increase in the shear stress as $P_{l,out}$ increases is more pronounced than that as Q_{in} increases: the 100-fold increase in Q_{in} produces a 26% increase in the maximum shear stress over the membrane, whereas the 14-fold increase in $(P_{l,out} - P_{atm})$ causes a 10-fold increase in the maximum shear stress.

3.7.3 Impact of flow on aggregate growth

First we distinguish the effects of oxygen and shear stress on aggregate growth as Q_{in} and $P_{l,out}$ are varied by comparing simulations for which growth is purely oxygen-dependent with those for which it is purely shear-stress-dependent. Oxygen-dependent growth is appropriate to cell types such as endothelial cells and hepatocytes, which are tolerant to high shear stresses or have high oxygen demands, while shear-stress-dependent growth is appropriate to cell types such as chondrocytes and mouse embryonic stem cells, which have low oxygen demands or are sensitive to changes in shear stress (see Tables B.3, B.4 and B.7). In the model, purely oxygen-dependent growth is achieved by setting the shear stress growth

parameters $A_2 = B_2 = 0$ in (3.22a,b) and choosing Σ_p such that $\sigma_{e,xy}|_{y=R_m} < \Sigma_p$ always; and purely shear-stress-dependent growth is achieved by taking $B_1 = 0$ in (3.22b) and C_{max} low enough such that $c_e|_{y=R_m} > C_{max}$ always.

Following this, we consider aggregate growth for cells that are sensitive to both oxygen levels and shear stress. We choose the concentration thresholds $C_p = 0.05\,\mathrm{mol\,m^{-3}}$ and $C_{max} = 0.18\,\mathrm{mol\,m^{-3}}$ in (3.22a), such that the growth rate is linearly proportional to the concentration over a wide concentration range, and use low values for the shear stress thresholds $\Sigma_p = 0.01\,\mathrm{Pa}$ and $\Sigma_d = 0.05\,\mathrm{Pa}$ that are within the range of shear stresses produced by typical values of Q_{in} and $P_{l,out}$. Oxygen- and shear-stress-dependent growth is relevant to cell types such as cardiomyocytes, mesenchymal stem cells and fibroblasts (see Tables B.3 and B.4).

Simulations are run until either the aggregates reach confluence or 40 days have elapsed (as this is the longest culture period reported in the literature for similar exposure of cells to fluid shear stress [288]). In the former case the confluence time, t_c, is recorded, in the latter case the final total length of the aggregates, L_{tot}, is recorded (at confluence $L_{tot} = L = 10\,\mathrm{cm}$).

3.7.3.1 Oxygen-dependent growth

Figure 3.8(a) shows how the confluence time, t_c, varies with Q_{in} and $P_{l,out}$ for oxygen-dependent growth of rat cardiomyocyte aggregates. For each fixed value of Q_{in}, the curve of t_c against $P_{l,out}$ ends at the maximum outlet pressure for which there is no backflow, $P_{l,out}^{max}$. As expected, t_c decreases as Q_{in} and $P_{l,out}$ increase, the effect being more marked for changes in $P_{l,out}$. This is because increasing Q_{in} or $P_{l,out}$ increases the advective flux of oxygen through the membrane, and therefore the oxygen concentration around the aggregates and their growth rate.

3.7.3.2 Shear-stress-dependent growth

Figure 3.8(b) shows how the confluence time varies with $P_{l,out}$ and Q_{in} for shear-stress-dependent growth. As $P_{l,out}$ increases, there is a sharp decrease in the confluence time at around $P_{l,out} = 1.089 \times 10^5\,\mathrm{Pa}$ (15.8 psi), but changes in Q_{in} have little effect on t_c. As $P_{l,out}$ increases through $P_{l,out} = 1.089 \times 10^5\,\mathrm{Pa}$, it is observed in the simulations that the number of aggregates on which the shear stress is higher than Σ_p increases sharply, leading to a significant increase in the net aggregate growth. There is barely any effect when Q_{in} is increased because the associated increase in the fluid flux through the membrane is much smaller.

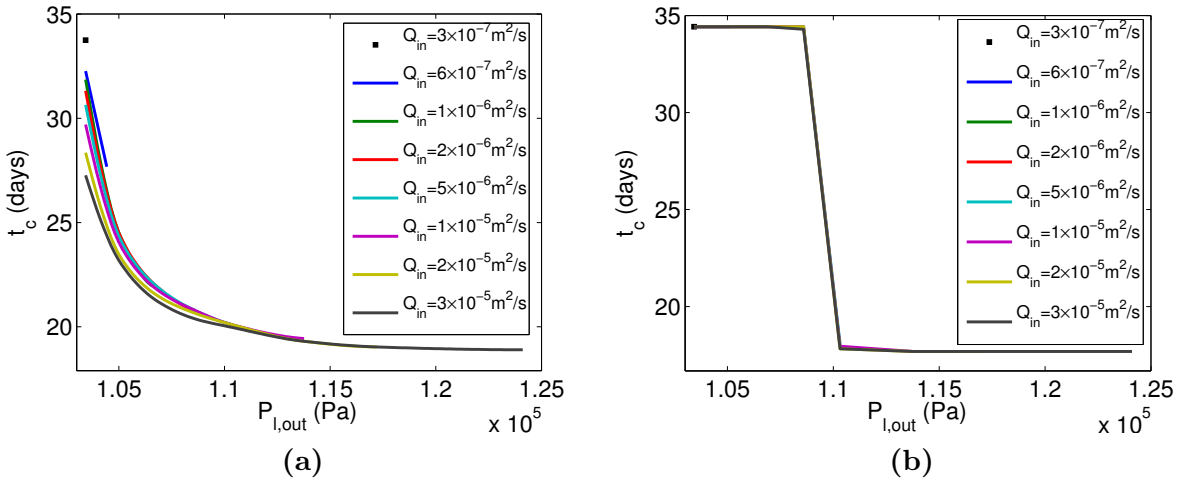

Figure 3.8: Relationship between confluence time t_c and outlet pressure for different flow rates for (a) oxygen-dependent growth and (b) shear-stress-dependent growth of rat cardiomyocyte aggregates. Time step: $\Delta t = 3.24\,\text{hrs}$ (dimensionless time step 0.01). Parameter values: (a) $C_p = 0.1\,\text{mol}\,\text{m}^{-3}$, $C_{max} = 0.21\,\text{mol}\,\text{m}^{-3}$, $\Sigma_p = 1\,\text{Pa}$, $\Sigma_d = 2\,\text{Pa}$, $A_2 = 0$, $B_0 = 0.075\,\text{day}^{-1}$, $B_1 = 1$, $B_2 = 0$, (b) $C_p = 0.02\,\text{mol}\,\text{m}^{-3}$, $C_{max} = 0.08\,\text{mol}\,\text{m}^{-3}$, $\Sigma_p = 0.05\,\text{Pa}$, $\Sigma_d = 0.16\,\text{Pa}$, $A_2 = 1.35\,\text{day}^{-1}\,(\text{mol}\,\text{m}^{-3})^{-1}$, $B_0 = 0.15\,\text{day}^{-1}$, $B_1 = 0$, $B_2 = 1$. All other parameter values as in Figure 3.5. Curve for each Q_{in} stops at maximum outlet pressure that can be used without backflow, $P_{l,out}^{max}$.

3.7.3.3 Combined oxygen-concentration- and shear-stress-dependent growth

Figure 3.9(a) shows that aggregates of rat cardiomyocytes sensitive to both oxygen levels and shear stress only reach confluence when $P_{l,out} < 1.089 \times 10^5\,\text{Pa}$, and that for $P_{l,out} > 1.089 \times 10^5\,\text{Pa}$, L_{tot} decreases as $P_{l,out}$ increases, up to $1.172 \times 10^5\,\text{Pa}$ (17 psi) (above which it is constant). This is because at outlet pressures above $1.089 \times 10^5\,\text{Pa}$ the shear stress exceeds the cell death threshold Σ_d over more of the membrane and this effect outweighs the positive effect of greater oxygen delivery to the cells.

Figure 3.9(b) shows how the confluence time changes with flow rate and outlet pressure for flow rates between $3 \times 10^{-7}\,\text{m}^2\text{s}^{-1}$ and $3 \times 10^{-5}\,\text{m}^2\text{s}^{-1}$ and outlet pressures ranging from $1.035 \times 10^5\,\text{Pa}$ to $1.089 \times 10^5\,\text{Pa}$ (or 15 psi to 15.8 psi) (ranges achievable with standard laboratory equipment). As $P_{l,out}$ increases, the confluence time first decreases, for $P_{l,out}$ up to $1.083 \times 10^5\,\text{Pa}$ (15.7 psi), and then increases. This is because the section of the membrane over which the proliferation rate is elevated (*i.e.* where $\Sigma_p < \sigma_{e,xy}|_{y=R_m} < \Sigma_d$) increases in extent, covering more of the aggregates, as $P_{l,out}$ increases up to $P_{l,out} = 1.083 \times 10^5\,\text{Pa}$, but the region in which the shear stress exceeds the death threshold Σ_d becomes larger for $P_{l,out} > 1.083 \times 10^5\,\text{Pa}$. For $P_{l,out} \leq 1.052 \times 10^5\,\text{Pa}$ (15.25 psi), the confluence time decreases marginally as Q_{in} increases due to greater oxygen flux through the membrane.

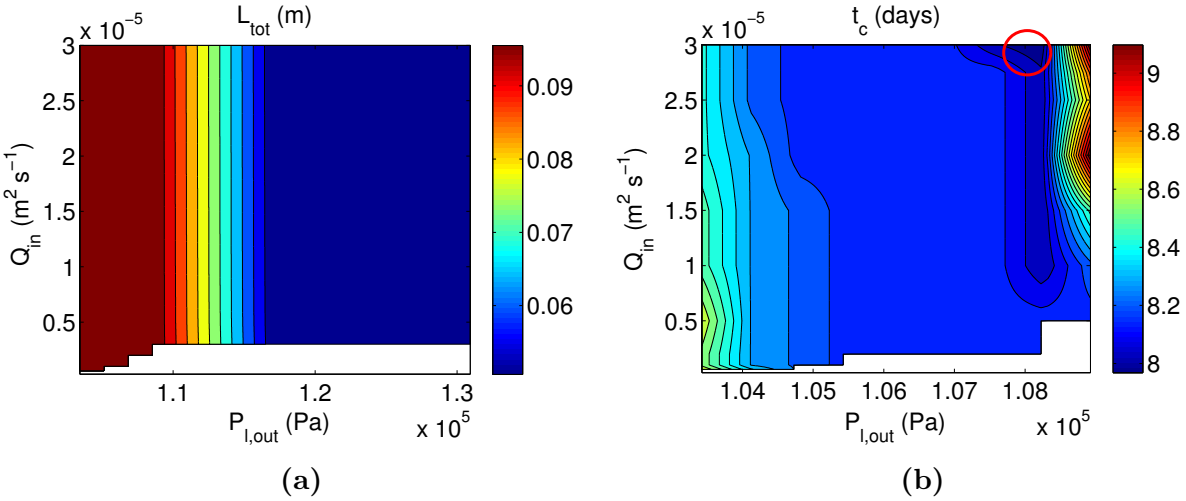

Figure 3.9: Oxygen-concentration- and shear-stress-dependent growth of shear-sensitive rat cardiomyocytes: variation in (a) the final total aggregate length L_{tot} and (b) the confluence time t_c with flow rate and outlet pressure. Red circle in (b) shows flow rate and outlet pressure ranges that minimise t_c. Parameter values: $C_p = 0.05\,\text{mol}\,\text{m}^{-3}$, $C_{max} = 0.18\,\text{mol}\,\text{m}^{-3}$, $\Sigma_p = 0.01\,\text{Pa}$, $\Sigma_d = 0.05\,\text{Pa}$. All other parameter values as in Figure 3.5.

In the range $P_{l,out} = 1.052 \times 10^5$–$1.069 \times 10^5\,\text{Pa}$ (15.25–15.5 psi), the confluence time remains approximately constant as Q_{in} increases. For $P_{l,out} = 1.069 \times 10^5$–$1.083 \times 10^5\,\text{Pa}$, the confluence time decreases as Q_{in} increases, reaching a minimum of 7.9 days for $Q_{in} = 2.75 \times 10^{-5}$–$3 \times 10^{-5}\,\text{m}^2\text{s}^{-1}$ and $P_{l,out} = 1.077 \times 10^5$–$1.083 \times 10^5\,\text{Pa}$. For $P_{l,out} = 1.083 \times 10^5$–$1.089 \times 10^5\,\text{Pa}$, the confluence time increases with increasing Q_{in}, since the detrimental effects of the shear stress exceeding Σ_d start to outweigh those of increased oxygen delivery. Hence, $Q_{in} = 2.75 \times 10^{-5}$–$3 \times 10^{-5}\,\text{m}^2\text{s}^{-1}$ (equivalent to 2.07–2.26 ml min^{-1}) and $P_{l,out} = 1.077 \times 10^5$–$1.083 \times 10^5\,\text{Pa}$ ($P_{l,out} = 15.6$–15.7 psi) are predicted to be the optimal flow rate and outlet pressure ranges for proliferation of these shear-sensitive rat cardiomyocytes.

3.7.4 Influence of seeding on growth

The model can be used to simulate the growth of experimentally-realised seeding distributions. However, since sufficient seeding data is currently not available to do this, we use three different simple initial aggregate distributions to test the impact of skew in the distribution (towards the inlet end or outlet end of the membrane) on the growth. We expect the skew to have an effect because the oxygen and shear stress distributions that arise are spatially non-uniform and evolve as the aggregates grow. Each of the distributions we consider has five aggregates each of initial length 0.5 cm, and the aggregate growth is simulated for a low

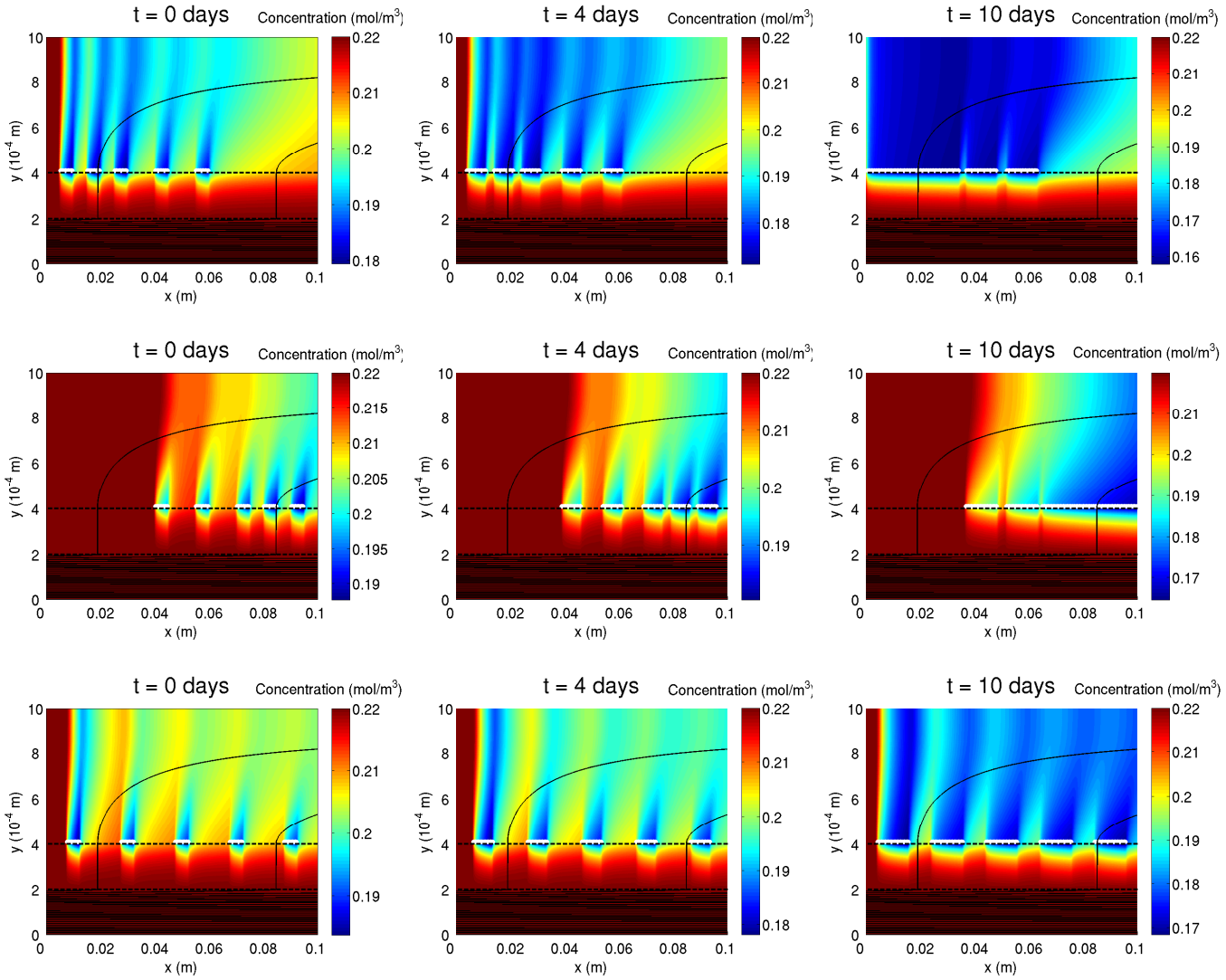

Figure 3.10: Aggregate growth and oxygen distribution at different time points for different initial aggregate distributions and a low outlet pressure. First row: left-skewed distribution. Second row: right-skewed distribution. Third row: even distribution. Solid black lines are flow streamlines. Parameter values: $N = 5$, $L_{agg} = 0.5\,\text{cm}$, $Q_{in} = 3 \times 10^{-5}\,\text{m}^2\text{s}^{-1}$, $P_{l,out} = 1.034 \times 10^5\,\text{Pa}$, $C_p = 0.05\,\text{mol}\,\text{m}^{-3}$, $C_{max} = 0.18\,\text{mol}\,\text{m}^{-3}$, $\Sigma_p = 0.03\,\text{Pa}$, $\Sigma_d = 0.08\,\text{Pa}$. All other parameter values as in Figure 3.5.

outlet pressure ($P_{l,out} = 1.034 \times 10^5\,\text{Pa}$) and a high outlet pressure ($P_{l,out} = 1.310 \times 10^5\,\text{Pa}$). (We do not vary Q_{in} since its effect on the transmembrane fluid flux is much weaker.) The initial distributions we consider are: (i) *left-skewed* (*i.e.* aggregates concentrated towards the inlet); (ii) *right-skewed* (*i.e.* aggregates concentrated towards the outlet); and (iii) *even* (*i.e.* aggregates spaced uniformly across the membrane) (see $t = 0$ panels in Figure 3.10).

With the lower outlet pressure the aggregates grow to confluence in all three cases, albeit at differing rates. The aggregates reach confluence fastest if they are right-skewed

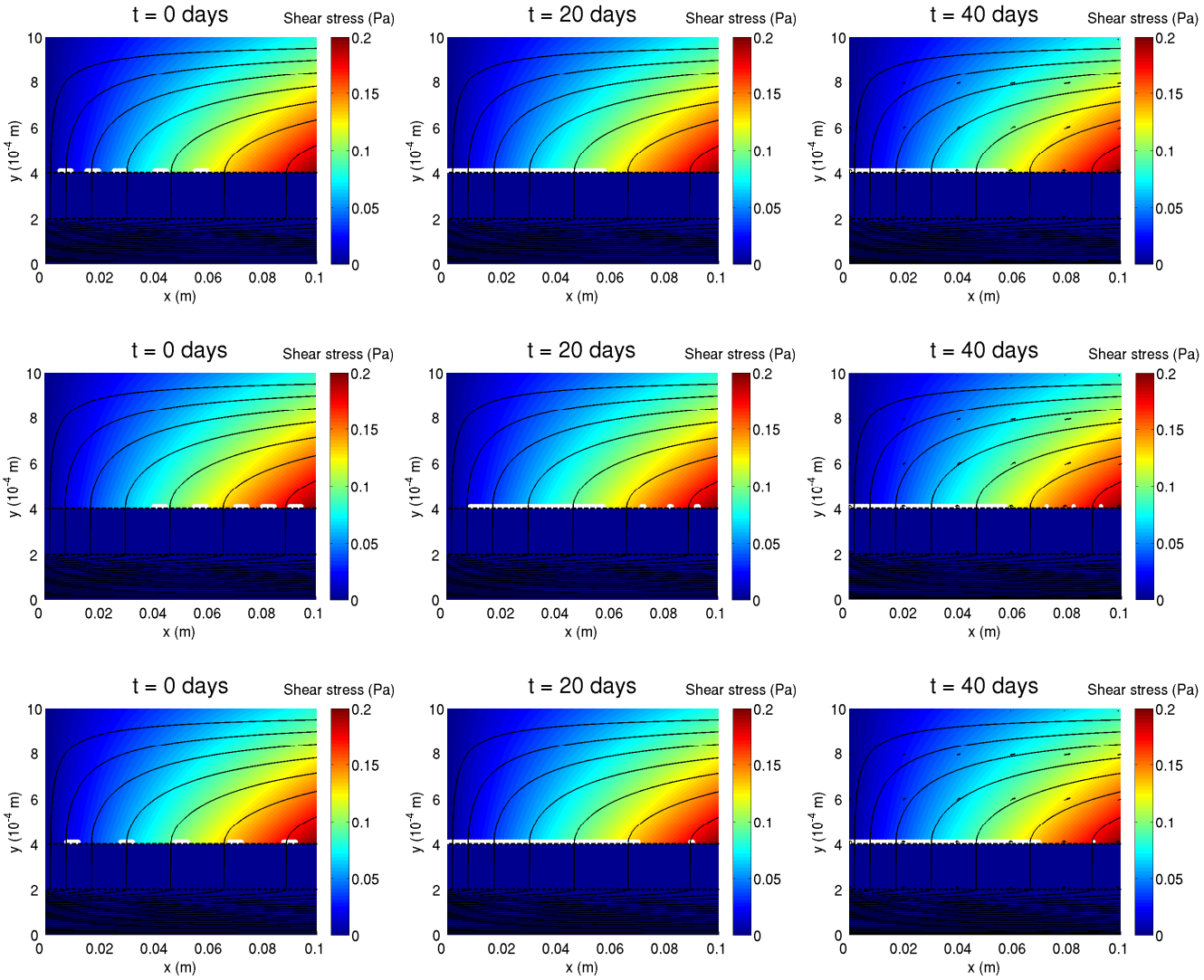

Figure 3.11: Aggregate growth and shear stress distribution at different time points for the different initial aggregate distributions in Figure 3.10 and a high outlet pressure. First row: left-skewed distribution. Second row: right-skewed distribution. Third row: even distribution. Parameter values as in Figure 3.10 except with $P_{l,out} = 1.310 \times 10^5$ Pa.

($t_c = 10.5$ days), take longer if they are evenly distributed ($t_c = 17$ days), and take more than twice as long ($t_c = 24.8$ days) if they are left-skewed. For the right-skewed distribution the aggregates start further away from, and grow towards, the inlet. Hence, once the aggregates have merged to form one large aggregate, the end of the aggregate nearest the inlet continues to experience a high oxygen concentration as it grows, despite the weak oxygen flux through the membrane from the low outlet pressure (Figure 3.10). Changes in the shear stress along the membrane with the initial aggregate distribution do not have any

impact on the rate of growth to confluence as the shear stress is always below the threshold for increased proliferation ($\Sigma_p = 0.03\,\text{Pa}$) for all three distributions.

With the higher outlet pressure, the aggregates fail to reach confluence after 40 days for all three initial distributions. The total aggregate length at 40 days is greatest for the even distribution (7 cm) and slightly less for the left-skewed and right-skewed distributions (5.76 cm and 5.84 cm respectively). This is because when the outlet pressure is large the oxygen concentration around the aggregates is similar for the different distributions but the shear stress exceeds the threshold for cell death ($\Sigma_d = 0.08\,\text{Pa}$) near the outlet end of the membrane (Figure 3.11). Aggregates at the outlet end therefore tend to shrink, so initial differences in growth between the distributions disappear over time and the aggregates merge to form one large aggregate at the inlet.

3.8 Discussion

We have developed a model of cell aggregate growth in the single-fibre HFB to provide insight into optimising cell expansion in HFBs. The model has been used to investigate how the flow of culture medium through the HFB and the seeding distribution affect the cell aggregate growth when it is mediated by oxygen delivery and fluid shear stress. We have considered how the lumen inlet flow rate, Q_{in}, and outlet pressure, $P_{l,out}$, affect the growth of cell aggregates with different oxygen and shear stress sensitivities. Our numerical results indicate that increasing Q_{in} or $P_{l,out}$ increases the transmembrane fluid flux, the increase being more pronounced for increments in $P_{l,out}$ over the range of flow rates and pressures typically used in experiments. The increase in transmembrane fluid flux has two effects: more oxygen is advected through the membrane to the aggregates, and the horizontal flow in the ECS is stronger so the aggregates experience higher shear stress. The higher oxygen concentration increases the rate of aggregate growth, but the effect of the increased shear stress depends on the shear-sensitivity of the cells (*i.e.* the shear thresholds Σ_p and Σ_d, which mark the transitions to elevated proliferation rate and cell death, respectively) and the aggregate distribution, since the shear stress increases with distance along the membrane from the inlet.

Figure 3.12 summarises the operating conditions and basic seeding strategy that maximise the cell yield, either in terms of minimising the time to confluence or maximising the final total aggregate length if confluence is not reached, for cells with different oxygen uptake rates and shear stress tolerances. The optimal initial position of the aggregates is described in terms of the skew of the aggregate distribution towards the ECS outlet. For rat cardiomyocytes with an uptake rate of $4.22 \times 10^{-18}\,\text{mol}\,\text{cell}^{-1}\,\text{s}^{-1}$ and shear tolerance of

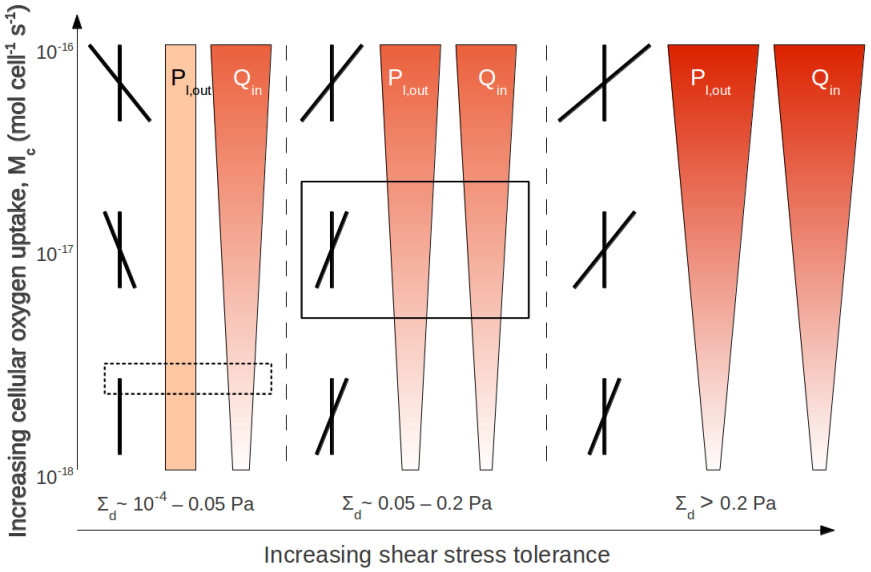

Figure 3.12: Optimal HFB operating conditions for proliferation of cell types with different oxygen uptake rates and shear stress tolerances. Wedge width and shading show relative values of flow rate Q_{in} and outlet pressure $P_{l,out}$ that give maximum cell yield (*i.e.* minimum confluence time, or maximum final total aggregate length if confluence is not reached), for cells with different oxygen demands and shear tolerance; greater widths/darker shades representing greater values, up to $Q_{in} = 3 \times 10^{-5}\,\mathrm{m^2 s^{-1}}$ and $P_{l,out} = 1.310 \times 10^5\,\mathrm{Pa}$. Crossed lines show whether the aggregates should be seeded towards the inlet (left-slanted line) or outlet (right-slanted line), or distributed evenly along the membrane (overlapping vertical line), to maximise the cell yield. The greater the angle of the slanted line the more concentrated towards the inlet/outlet the initial aggregate distribution should be. Dashed box marks optimal operating conditions for rat cardiomyocytes with oxygen uptake rate of $4.22 \times 10^{-18}\,\mathrm{mol\,cell^{-1}\,s^{-1}}$ and shear tolerance of $\Sigma_d = 0.05\,\mathrm{Pa}$; solid box marks optimal operating conditions for cells with uptake rate of $\sim 10^{-17}\,\mathrm{mol\,cell^{-1}\,s^{-1}}$ and shear tolerance of $\Sigma_d \sim 0.1\,\mathrm{Pa}$ (see main text).

$\Sigma_d = 0.05\,\mathrm{Pa}$, for example, the optimal operating conditions and aggregate seeding strategy (marked by the dashed box in Figure 3.12) are $Q_{in} = 2.75 \times 10^{-5}$–$3 \times 10^{-5}\,\mathrm{m^2 s^{-1}}$ and $P_{l,out} = 1.077 \times 10^5$–$1.083 \times 10^5\,\mathrm{Pa}$ ($P_{l,out} = 15.6$–$15.7\,\mathrm{psi}$) and an evenly-spaced distribution.

It is evident from Figure 3.12 that achieving the maximum cell yield for a specific cell type requires a careful balance of the inlet flow rate, outlet pressure and seeding distribution. For instance, the optimal seeding distribution of the aggregates changes from moving towards the outlet with increasing oxygen demand when $\Sigma_d > 0.2\,\mathrm{Pa}$ to moving towards the inlet when Σ_d drops below $0.05\,\mathrm{Pa}$. This is because, for $\Sigma_d < 0.05\,\mathrm{Pa}$, the low shear tolerance of the cells prevents aggregates from growing near the outlet despite the improved oxygen delivery that can be achieved by seeding them there. The extent to which the cell

seeding process in the HFB can be controlled is thus an important issue, as cells are more likely to be inadvertently seeded in regions with unfavourable growth conditions if the control over the seeding is limited. This motivates further experimental studies to improve control over the seeding distribution. In the meantime, for random seeding of cells with typical oxygen demands, the cell yield can be maximised by using a flow rate and outlet pressure that ensure the shear stress is in the elevated proliferation rate range over as much of the membrane as possible. For example, from Figure 3.12 (see solid box) we can see that for cells with an oxygen uptake rate of the order of $10^{-17}\,\mathrm{mol\,cell^{-1}\,s^{-1}}$ and a shear stress death threshold $\Sigma_d \sim 0.1\,\mathrm{Pa}$ in an initial aggregate distribution skewed slightly towards the outlet, a flow rate of approximately $3 \times 10^{-6}\,\mathrm{m^2 s^{-1}}$ and an outlet pressure of $1.103 \times 10^5\,\mathrm{Pa}$ (16 psi) will ensure that the region of shear-stress-enhanced proliferation is as large as possible.

Although experimental validation of the model is clearly necessary, the model has enabled us to predict optimal ranges for the lumen inlet flow rate and outlet pressure for maximising the growth of different cell types. Thus it should provide a useful tool for experimentalists looking to optimise cell expansion in the HFB in the laboratory.

Nevertheless, there are improvements that could be made to the modelling framework we have presented, including modelling the full length of the HFB section, with the outlet on the top of the ECS, and modelling the full 3D HFB set-up. Both of these would require more sophisticated and computationally expensive numerical simulation approaches. Modelling the 3D set-up would also require consideration of the azimuthal dependence of the aggregate distribution over the fibre surface and the solution of 2D free boundary problems for the evolution of the aggregate boundaries, but would allow us to make detailed predictions of the aggregate growth over the full fibre surface. Some of the proposed extensions to the cell layer growth model in Chapter 3 also apply to this model, such as adding the transport of other solutes and accounting for heterogeneity in the membrane permeability, and for a discussion of these we refer the reader to §2.10.2. A further extension to the model would be to describe the individual cells in each aggregate using a discrete model, so that processes such as cell interaction, growth and movement can be incorporated at the level of single cells. We explore the possibility of modelling aggregate growth in this way in Chapter 4—investigating how well such a model can be approximated by a continuum description and discussing how to incorporate it into the framework developed here.

For the model to be used to make accurate quantitative predictions of the yield or confluence time for a given initial aggregate distribution and cell type, experiments need to be performed to determine the unknown parameter values in the model (the membrane outer surface and aggregate permeabilities, K_{hi} and K_{lo}; the oxygen concentration and

shear stress thresholds, C_d, C_p, C_{max}, Σ_p, Σ_d; and the growth rate parameters A_1, A_2, B_0, B_1, B_2) for the cell type in question. The membrane outer surface and aggregate permeabilities can be determined by fitting the model to measurements of the retentate and permeate masses for a prescribed flow with no cells and a confluent monolayer. Values for the concentration and shear stress thresholds and growth rate parameters could be determined by fitting experimental data for the variation in the cell proliferation and death rate with oxygen concentration and shear stress to the proposed functional dependencies (equations (3.22a) and (3.22b)). Alternatively, the precise functional dependencies for a particular cell type could be determined from experimental data and used to run cell-type-specific growth simulations. It would also be informative to simulate the aggregate growth for ranges of values of A_1, A_2, B_0, B_1 and B_2 to determine its sensitivity to these parameters.

There are also various experiments that could be performed that would provide useful data for validating the model. The ideal data would be time course measurements of the cell distribution and density on the fibre surface over the culture period. These could be compared to the growth predicted in simulations with the measured initial distributions as the initial conditions, and used to test the assumption that the cell density remains constant within the aggregates as they grow. However, it is difficult to obtain such data, as measuring the cell distribution and density generally requires dismantling the bioreactor and sacrificing the cells. Measurements could nevertheless still be obtained at fixed time points from multiple experiments, via cell staining, imaging of the fibre surface, and DNA quantification. These could be used to confirm that the model predicts sensible levels of growth over the course of the cell culture. Acquiring real-time data on the cell distribution in a single experiment is possible by fluorescently labelling cells and imaging the HFB using a nuclear magnetic resonance spectrometer [27, 273], but is less straightforward and much more expensive.

Chapter 4

Discrete-to-continuum modelling of cell aggregate growth

4.1 Introduction

Thus far, the models of cell expansion in the HFB that we have developed have treated the cell population as a continuum. In Chapter 2 we represented the cell layer as a growing porous medium, with a constant porosity, and used volume-averaged equations to describe flow and solute transport through it. In Chapter 3 we treated the aggregates as continuous 1D permeable membranes growing along the outer surface of the fibre. Whilst these models have enabled us to investigate the effects of changes in culture conditions on cell population growth, they have not explicitly incorporated microscale detail of cell behaviour. Such detail can be incorporated with a cell-based model. Hence in this chapter we develop a hybrid discrete-continuum model of nutrient-dependent cell aggregate growth, with a cell-based model for the cell population, and investigate its suitability for modelling aggregate growth in the HFB.

One of the main facets missing from the continuum description of cell aggregate growth in Chapter 3 is an explicit description of the mechanics of individual cells—*i.e.* of their movement, interaction and growth—and how they are affected by the external chemical and mechanical environment. We address this deficiency in the model developed here by applying force-balances to the discrete cells and coupling cell growth to an extracellular nutrient field. Although the number of cells considered in the aggregate growth model was relatively small ($\sim$ 100–1000), moving to a fully 3D model and/or modelling a cell layer or a HFB with multiple fibres demands consideration of much larger numbers of cells ($\sim$ 10^4–10^6). Since simulating this many cells and their interactions using a cell-based model is computationally expensive, it is expedient to consider approximating the discrete model with a continuum description that captures the key microscale details but at a lower computational cost. The work of Murray *et al.* [181] and Fozard *et al.* [78] described in

§1.2.4, in which continuum approximations of discrete models of cell motion and growth were derived in the limit of a large number of cells, provides a framework with which to do this.

To test the suitability of this framework for modelling cell aggregate growth in the HFB, we consider a simple set-up, with a 1D aggregate growing along the base of a nutrient bath. The discrete cell model we use is based on those presented by Murray *et al.* [181] and Fozard *et al.* [78]. As in Fozard *et al.*'s model, we represent the cells as vertices connected by linear springs and model cell growth (without division) by prescribing the rate of change of the resting (or 'target') lengths of the cells. However, we extend Fozard *et al.*'s framework to consider different dependencies of the growth on the cell properties and the external environment of the cells. To derive the continuum approximation in the limit that the number of cells, N, is large, we assume that the cell parameters and variables vary slowly at the cell length scale, so that they may be approximated by continuous functions of the cell index. Nondimensionalising the governing equations for the cell motion and growth (with the cell variables scaled by appropriate powers of N) introduces the small parameter $1/N \ll 1$ into the system, and the continuum approximation can then be obtained by expanding all variables in terms of the small parameter $1/N$ and taking the limit as $N \to \infty$.

Firstly, we compare linear growth of the cell target lengths with time (the growth law considered by Fozard *et al.*) with mechanosensitive growth, in which cells grow at a rate proportional to the amount by which they are stretched. We verify, via analytical and numerical solutions, that the continuum model closely approximates the discrete model for both growth laws. Next we consider cell growth that is dependent on the local nutrient and mechanical environment, where the nutrient diffuses and is consumed by the cells. We test agreement between the discrete and continuum cell models by comparing numerical simulations of each model. We also consider the effect of varying key model parameters, such as the nutrient supply and uptake rate, on the growth of the cell aggregate, to explore the range of behaviour that can be generated with the chosen growth law.

The main aim of this chapter is thus to determine whether the discrete cell model and continuum approximation continue to agree when coupled to the nutrient transport model, as this is required if we are to be able to use the continuum approximation to model cell aggregate growth in the HFB. A further aim is to assess the validity of the continuum growth law used to describe the evolution of the aggregate lengths in Chapter 3 (equation (3.22)).

4.1.1 Chapter outline

The remainder of this chapter is organised as follows. We define the model set-up in §4.2 and introduce the governing equations for the discrete cell model and nutrient transport in §4.3. In §§4.4–4.6.1, we nondimensionalise the model, derive the continuum approximation of the discrete cell model and compare the resulting continuum growth law in the limit of incompressible cells with that used in Chapter 3. Following this, we compare our discrete model and its continuum limit with those of Murray *et al.* and Fozard *et al.*, discussing the inclusion of cell division in Murray *et al.*'s model and how the cell density equation derived in the continuum limit depends on the discrete cell interaction force law. We give typical values of the model parameters and justify our assumptions about their relative magnitudes in §4.7, and describe how we solve the discrete and continuum cell models and nutrient transport equations in §4.8. In §4.9, we present analytical solutions and the results of numerical simulations for the different growth laws considered, including the convergence of the solutions of the discrete and continuum cell models and the sensitivity of the nutrient-dependent growth to various model parameters. We discuss our findings in §4.10, and conclude by describing the further work needed to build the discrete-to-continuum framework into a model of cell growth and proliferation coupled to fluid and nutrient transport in the HFB.

4.2 Model set-up

A schematic of the coupled cell and nutrient transport model set-up is shown in Figure 4.1. We model the cell aggregate as a 1D line of discrete cells attached to a substrate at the base of a 2D nutrient bath. We describe position in the bath using Cartesian coordinates (x, y), where $x \in [-R^*, R^*]$ is the distance along the base from its centre at $x = 0$ and $y \in [0, S^*]$ is the height above the base. The corresponding unit vectors in the x- and y-directions are denoted by $\mathbf{e}_x$ and $\mathbf{e}_y$. The aggregate consists of N adjacent cells with $N+1$ vertices denoted by x_0, $x_1, \ldots, x_N$ (so that the nth cell occupies the interval (x_n, x_{n+1}), $n = 0, 1, \ldots, N-1$). Variables associated with the nth cell are denoted by subscript $n + 1/2$. The length of the nth cell is given by $l_{n+1/2} = x_{n+1} - x_n$, and we denote its target ('natural') length by $a_{n+1/2}$. The cell vertex velocities are denoted by $u_n = \frac{\mathrm{d}x_n}{\mathrm{d}\tau}$ $(n = 0, 1, \ldots, N)$, where τ denotes time, and the static force exerted by the nth cell on the $(n+1)$th cell, or the 'pressure' of the nth cell, is denoted by $p_{n+1/2}$. The nutrient concentration in the culture medium is denoted by $c(x, y, \tau)$.

The cells are assumed to be linearly elastic, to adhere to each other and to the substrate, and to be unable to exchange positions with their neighbours. The cell vertices move in

response to the balance of the elastic forces exerted on them by the adjoining cells and a drag force due to adhesion to the substrate. The target length of each cell increases at a rate which can depend on the local nutrient concentration and the forces acting on the cell. The nutrient concentration at the surface of the bath, $y = S^*$, is maintained at a fixed value, so that $c(x, S^*, \tau) = C^*$. The culture medium is static, so there is no nutrient advection, but nutrient diffuses through the culture medium to the cell aggregate, where it is absorbed by the cells. The walls and base of the bath (outside of the cell aggregate) are assumed to be impermeable to nutrient, so there is no nutrient flux across these boundaries.

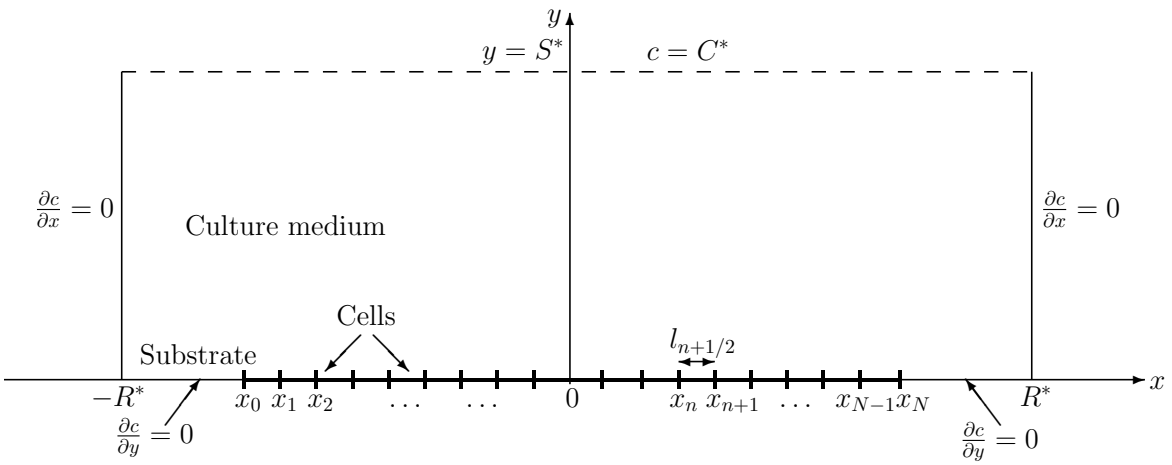

Figure 4.1: Model set-up for cells growing on substrate in nutrient bath. Notation and equations as defined and explained in main text. Not to scale.

4.3 Governing equations

The model consists of three components: a discrete cell model, a continuum nutrient model and constitutive relations for cell growth and nutrient uptake that couple the cell and nutrient models. We now introduce the governing equations for each component.

4.3.1 Cell motion

The rate of change of length of the nth cell is

$$\frac{\mathrm{d}l_{n+1/2}}{\mathrm{d}\tau} = u_{n+1} - u_n, \quad n = 0, \ldots, N-1. \tag{4.1}$$

Following Fozard *et al.* [78], we derive the equations of motion for the cell vertices by balancing the drag forces acting on them with the forces exerted on them by adjacent cells. We ignore inertial effects since they are typically negligible compared to the drag between

the cells and culture medium and the drag forces due to cell-cell and cell-substrate adhesion [225]. This yields

$$F_n + D_n = 0, \quad n = 0, \ldots, N, \tag{4.2}$$

where F_n is the force on the nth cell vertex due to interactions with neighbouring cells and D_n is the drag force on the nth cell vertex due to friction between the cells and the substrate. The interaction forces between cells are given by

$$F_n = p_{n-1/2} - p_{n+1/2}, \quad n = 0, \ldots, N, \tag{4.3}$$

where $p_{-1/2}$ and $p_{N+1/2}$ account for external forces acting on the aggregate ends. Since we model the cells as linear springs, the cell pressures are given by

$$p_{n+1/2} = \lambda_{n+1/2}(a_{n+1/2} - l_{n+1/2}), \quad n = 0, \ldots, N-1, \tag{4.4}$$

where $\lambda_{n+1/2}$ is the elasticity (spring constant) of the nth cell, and $\lambda_{n+1/2} > 0$, so $p_{n+1/2} > 0$ whenever a cell is compressed ($l_{n+1/2} < a_{n+1/2}$).

In many studies [37, 173, 184, 263] the cell-substrate drag is assumed to be proportional to the cell vertex velocities, such that

$$D_n = -\mu_n u_n, \tag{4.5}$$

where μ_n is the drag constant associated with the nth cell vertex. However, the drag force acts over the whole length of the cell not just on the vertices, and it is more natural to associate the drag constants with the cells rather than the vertices. Hence, following an approach similar to that used by Fozard *et al.*, we assume that the energy dissipation rate, G^s, due to the drag force is proportional to the square of the cell velocity (determined by linearly interpolating the cell vertex velocities over the length of the cell)

$$\begin{aligned} G^s(u_n, u_{n+1}, l_{n+1/2}; \mu_{n+1/2}) &= \frac{\mu_{n+1/2}}{l_{n+1/2}} \int_{x_n}^{x_{n+1}} u^2 \, \mathrm{d}x \\ &\simeq \frac{\mu_{n+1/2}}{l_{n+1/2}} \int_0^{l_{n+1/2}} \left(\frac{u_n(l_{n+1/2} - s) + u_{n+1}s}{l_{n+1/2}} \right)^2 \mathrm{d}s \\ &= \frac{1}{3}\mu_{n+1/2}(u_n^2 + u_n u_{n+1} + u_{n+1}^2), \end{aligned} \tag{4.6}$$

where $\mu_{n+1/2}$ is the drag constant associated with the nth cell. The corresponding drag force on the nth vertex is given by (see [78])

$$D_n = -\frac{1}{2}\frac{\partial}{\partial u_n} \left(\sum_{m=\max(n-1,0)}^{\min(n,N)} G^s(u_m, u_{m+1}, l_{m+1/2}; \mu_{m+1/2}) \right),$$

where $\mu_{-1/2} = \mu_{N+1/2} = 0$, so that the formula holds for $n = 0$ and $n = N$. Thus, summing contributions from neighbouring cells we have that

$$D_n = -\frac{1}{6}\left(\mu_{n-1/2}(u_{n-1} + 2u_n) + \mu_{n+1/2}(2u_n + u_{n+1})\right), \quad n = 0, \ldots, N. \tag{4.7}$$

Combining (4.3) and (4.7) gives the equation of motion of the nth cell vertex as

$$\frac{1}{6}\left(\mu_{n-1/2}(u_{n-1} + 2u_n) + \mu_{n+1/2}(2u_n + u_{n+1})\right) = p_{n-1/2} - p_{n+1/2}, \quad n = 0, \ldots, N. \tag{4.8}$$

With $n = 0$ and $n = N$, (4.8) gives the evolution equations for the ends of the aggregate. We assume that there are no external forces acting on the end vertices, *i.e.* $p_{-1/2} = p_{N+1/2} = 0$, so that (4.8) reduces to

$$\frac{1}{6}\mu_{1/2}(2u_0 + u_1) = -p_{1/2} \quad \text{and} \quad \frac{1}{6}\mu_{N-1/2}(2u_{N-1} + u_N) = p_{N-1/2} \tag{4.9}$$

in these cases. The initial positions of the cell vertices are prescribed by a discrete function x_{init} of the cell index n, *i.e.*

$$x_n(0) = x_{init}(n), \quad n = 0, \ldots, N. \tag{4.10}$$

4.3.2 Nutrient transport

The nutrient in the culture medium diffuses freely and is absorbed by the cell aggregate along the base of the nutrient bath. We focus on the timescale of cell growth ($\mathcal{O}$(hrs–days)), which is much longer than the timescales for diffusion over the length of the aggregate ($\mathcal{O}$(s–mins)) and cell relaxation ($\mathcal{O}$(mins)) (as we verify in §4.7.5), and on the cell length scale, over which the nutrient concentration can be assumed to vary smoothly, as it is much longer than the molecular length scale and there are large numbers of nutrient molecules per unit length. Hence, the nutrient transport is quasi-steady and we describe it by

$$D\nabla^2 c = 0, \quad x \in (-R^*, R^*), \; y \in (0, S^*), \tag{4.11}$$

where D is the nutrient diffusivity in the culture medium, which is assumed to be constant.

At the base of the bath outside of the aggregate, and on the walls of the bath, we impose no diffusive flux, so that

$$-D\boldsymbol{\nabla} c \cdot \mathbf{e}_y = -D\frac{\partial c}{\partial y} = 0 \quad \text{on} \;\; y = 0, \; x \notin [x_0(\tau), x_N(\tau)], \tag{4.12}$$

$$\pm D\boldsymbol{\nabla} c \cdot \mathbf{e}_x = \pm D\frac{\partial c}{\partial x} = 0 \quad \text{on} \;\; x = \pm R^*, \; y \in (0, S^*). \tag{4.13}$$

At the upper surface of the bath we impose a fixed nutrient concentration, to model rapid supply of the nutrient

$$c = C^* \quad \text{on} \;\; y = S^*, \; x \in [-R^*, R^*]. \tag{4.14}$$

Nutrient uptake by the cells in the aggregate is described in terms of the rate at which each cell consumes nutrient, *i.e.* by prescribing the diffusive flux through each section of the boundary corresponding to a cell via

$$-D\boldsymbol{\nabla}c\cdot\mathbf{e}_y = -D\frac{\partial c}{\partial y} = -M(l_{n+1/2}, a_{n+1/2}, p_{n+1/2}, c), \quad \text{on } x\in(x_n(\tau), x_{n+1}(\tau)),\ y=0,$$
$$n=0,\ldots,N-1, \tag{4.15}$$

where $M>0$ is a function of the cell variables and the local nutrient concentration. There are various possible choices for the functional form of $M(l_{n+1/2}, a_{n+1/2}, p_{n+1/2}, c)$ depending on how the cells consume nutrient. We assume that for a fixed nutrient concentration all cells consume nutrient at a rate which is independent of their length (so that the uptake flux at each point in each cell is inversely proportional to the cell's length) and that the uptake flux has a Michaelis-Menten dependence on the nutrient concentration. Hence, the uptake flux in each cell is given by

$$D\frac{\partial c}{\partial y} = M(l_{n+1/2}, a_{n+1/2}, p_{n+1/2}, c) = \frac{1}{l_{n+1/2}}\frac{M^* c}{C_{1/2}+c}, \quad \text{on } x\in(x_n(\tau), x_{n+1}(\tau)),\ y=0,$$
$$n=0,\ldots,N-1, \tag{4.16}$$

where M^* is the maximum uptake rate (in $\mathrm{mol\,m^{-1}\,s^{-1}}$) and $C_{1/2}$ is the half-maximal uptake concentration. We note that this definition of M gives discontinuities in the uptake flux at the ends of the cells due to the differences in the lengths of adjacent cells. However, in deriving the continuum limit of the cell model we assume that the cell lengths vary slowly with n (see §4.4), so the flux discontinuities will be small and the uptake can be approximated by a continuum description.

4.3.3 Cell growth

Cell growth (elongation) is modelled by prescribing the evolution of the cell target lengths

$$\frac{\mathrm{d}a_{n+1/2}}{\mathrm{d}\tau} = \Gamma(l_{n+1/2}, a_{n+1/2}, p_{n+1/2}, c_{n+1/2}; \gamma_{n+1/2}), \quad n=0,\ldots,N-1, \tag{4.17}$$

where the elongation rate Γ (in $\mu\mathrm{m\,hr^{-1}}$) depends on the cell variables and $c_{n+1/2}$, the average of the continuous nutrient concentration at the base of the bath over the length of the nth cell,

$$c_{n+1/2}(\tau) = \frac{1}{l_{n+1/2}}\int_{x_n}^{x_{n+1}} c(x,0,\tau)\,\mathrm{d}x. \tag{4.18}$$

In (4.17) $\gamma_{n+1/2}$ parameterises the growth rate of the nth cell. As for the initial cell vertex positions, the initial cell target lengths are prescribed by a discrete function of the cell index n,

$$a_{n+1/2}(0) = a_{init}(n+\tfrac{1}{2}), \quad n=0,\ldots,N-1. \tag{4.19}$$

The growth function $\Gamma = \Gamma(l, a, p, c; \gamma)$ can be prescribed in numerous different ways to reflect different constitutive assumptions about cell growth. We will investigate different growth laws by specifying different functional forms of Γ as follows.

- *Constant elongation rate*:

$$\Gamma = \gamma = \gamma^* = \text{const.} \tag{4.20}$$

  Fozard *et al.* [78] demonstrated that a constant elongation rate can successfully describe the superlinear growth in time of the free edge of an epithelial sheet observed in wound healing assays [211], suggesting that this may be an appropriate growth law for epithelial cells.

- *Pressure-dependent growth*, for which a cell's target length increases if the cell is stretched relative to its target length ($l_{n+1/2} > a_{n+1/2} \Rightarrow p_{n+1/2} < 0$) and decreases if it is compressed ($l_{n+1/2} < a_{n+1/2} \Rightarrow p_{n+1/2} > 0$), at a rate proportional to the amount it is stretched/compressed

$$\Gamma = -\gamma^* p. \tag{4.21}$$

  There are various cell types for which such a growth law may be applicable [265], including skeletal muscle cells [264], smooth muscle cells [198], cardiomyocytes [220], bone cells [101] and epithelial cells [23].

- *Target-length-, pressure- and nutrient-dependent growth*, for which the rate of increase of a cell's target length depends on its current target length, its pressure and the nutrient concentration over its length according to

$$\Gamma = \gamma^*(a^*_{max} - a)\mathrm{S}(p; p^*_s, p^*_c)\frac{c}{K_g + c}. \tag{4.22}$$

  In (4.22), a^*_{max} is the maximum target length; K_g is the concentration at which the growth rate is half-maximal for a given target length; and S is a smoothed step function of the pressure given by

$$\mathrm{S}(p, p^*_s, p^*_c) = \frac{1}{2}[\tanh(s_p(p - p^*_s)) + \tanh(s_p(p^*_c - p))],$$

  where $p_s < 0$ and $p_c > 0$ are thresholds for excess stretching and compression, and the smoothing factor s_p determines the steepness of the transition in the growth rate at $p = p_s$ and $p = p_c$. With this form of Γ, the elongation rate of $a_{n+1/2}$ increases with the nutrient concentration and decreases as $a_{n+1/2}$ approaches a^*_{max}, provided $p_s < p_{n+1/2} < p_c$, (*i.e.* the cell is neither too compressed nor too stretched to grow). To ensure the cell target lengths either stay constant or increase, a_{init} is chosen such that $a_{init}(n + \frac{1}{2}) < a^*_{max}$, $\forall n$. We adopt this dependence on $a_{n+1/2}$ so that the cell target

length does not grow indefinitely. We use Monod kinetics for the dependence of the growth rate on the nutrient concentration, for which the growth rate is an increasing saturating function of the concentration. Growth of this kind may be applicable to cells with high nutrient demands, such as hepatocytes [246], or cells with lower nutrient demands whose growth is stimulated by moderate mechanical strain, such as chondrocytes [277]. Although more complicated dependencies could be considered, we use this simple functional form as we are primarily interested in determining whether the discrete cell model coupled to the nutrient transport model can be accurately approximated via the continuum model without formal homogenisation.

For the forms of Γ in (4.20) and (4.21) the cell growth is independent of the nutrient concentration, so we solve the discrete cell model in isolation. For the form of Γ in (4.22), however, the cell model and nutrient transport are coupled so that the growth depends on the nutrient concentration and the nutrient uptake depends on the growth (as described in §4.3.2). We therefore solve the coupled system for the cells and nutrient for this form of Γ.

4.4 Nondimensionalisation

We assume that the cell parameters and variables vary slowly with the cell index n over $\mathcal{O}(N) \gg 1$ cells and nondimensionalise the discrete cell model and nutrient transport equations (4.1)–(4.14) as follows (where asterisks denote typical dimensional values of the parameters)

$$\begin{gathered} n = N\hat{n}, \quad \mu_{n+1/2} = \mu^*\hat{\mu}_{\hat{n}+\frac{1}{2N}}, \quad \lambda_{n+1/2} = \lambda^*\hat{\lambda}_{\hat{n}+\frac{1}{2N}}, \quad \gamma_{n+1/2} = \gamma^*\hat{\gamma}_{\hat{n}+\frac{1}{2N}}, \\ x_n = Na^*\hat{x}_{\hat{n}}, \quad x = L^*\hat{x}, \quad y = L^*\hat{y}, \quad \tau = \frac{a^*}{\Gamma^*}\hat{\tau}, \\ l_{n+1/2} = a^*\hat{l}_{\hat{n}+\frac{1}{2N}}, \quad a_{n+1/2} = a^*\hat{a}_{\hat{n}+\frac{1}{2N}}, \quad p_{n+1/2} = N^2\mu^*\Gamma^*\hat{p}_{\hat{n}+\frac{1}{2N}}, \quad u_n = N\Gamma^*\hat{u}_{\hat{n}}, \\ c_{n+1/2} = C^*\hat{c}_{\hat{n}+\frac{1}{2N}}, \quad c = C^*\hat{c}, \quad x_0(n) = Na^*\hat{x}_0(\hat{n}), \quad M = M^*m, \quad \Gamma = \Gamma^*\hat{\Gamma}, \\ x_{init}(n) = L\hat{x}_{init}(\hat{n}), \quad a_{init}\left(n+\tfrac{1}{2}\right) = a^*\hat{a}_{init}\left(\hat{n}+\tfrac{1}{2N}\right), \end{gathered} \tag{4.23}$$

where $\hat{c}_{\hat{n}+\frac{1}{2N}}$ is the dimensionless average nutrient concentration over the length of the nth cell

$$\hat{c}_{\hat{n}+\frac{1}{2N}}(\hat{\tau}) = \frac{N}{\hat{l}_{\hat{n}+\frac{1}{2N}}}\int_{\hat{x}_{\hat{n}}}^{\hat{x}_{\hat{n}+\frac{1}{N}}} \hat{c}(\hat{x},0,\hat{\tau})\,\mathrm{d}\hat{x}, \tag{4.24}$$

and L^* is chosen as the typical aggregate length scale, $L^* = Na^*$ (so that lengths in the x-direction are scaled consistently in the cell model and nutrient transport equations). With the discrete cell index n scaled by N, the cell vertices are no longer labelled by integers, but by numbers between 0 and 1. Whereas in Fozard *et al.*'s model the system is

nondimensionalised on the timescale for cell relaxation, μ^*/λ^*, here we nondimensionalise on the timescale for cell growth, a^*/Γ^*, as we are interested in how the system evolves on this timescale. Accordingly, we choose different scalings for the cell vertex velocities and pressures to balance the rate of change of cell length with the vertex velocities in (4.1) and the drag forces with the cell pressures in (4.8). Unless otherwise stated, for the remainder of this chapter we consider dimensionless quantities and omit hats on dimensionless variables for ease of notation.

4.4.1 Cell motion

From the definitions for the cell lengths and vertex velocities, we have that

$$l_{n+\frac{1}{2N}} = N\left(x_{n+\frac{1}{N}} - x_n\right), \quad u_n = \frac{\mathrm{d}x_n}{\mathrm{d}\tau}. \tag{4.25}$$

On nondimensionalisation, the discrete cell motion equations given by (4.1), (4.4) and (4.8) become

$$\frac{1}{N}\frac{\mathrm{d}l_{n+\frac{1}{2N}}}{\mathrm{d}\tau} = u_{n+\frac{1}{N}} - u_n, \quad n = 0, \ldots, 1 - \tfrac{1}{N}, \tag{4.26}$$

$$\alpha p_{n+\frac{1}{2N}} = \lambda_{n+\frac{1}{2N}}\left(a_{n+\frac{1}{2N}} - l_{n+\frac{1}{2N}}\right), \quad n = 0, \ldots, 1 - \tfrac{1}{N}, \tag{4.27}$$

$$\frac{1}{6N}\left(\mu_{n-\frac{1}{2N}}\left(u_{n-\frac{1}{N}} + 2u_n\right) + \mu_{n+\frac{1}{2N}}\left(2u_n + u_{n+\frac{1}{N}}\right)\right) = p_{n-\frac{1}{2N}} - p_{n+\frac{1}{2N}}, \quad n = \tfrac{1}{N}, \ldots, 1 - \tfrac{1}{N}, \tag{4.28}$$

where $\alpha = N^2\Gamma^*\mu^*/(a^*\lambda^*)$ is the ratio of the timescales for cell (spring) relaxation against the substrate drag, μ^*/λ^*, and cell elongation, a^*/Γ^*, multiplied by N^2. The equations of motion for the end vertices (4.9) become

$$\frac{1}{6N}\mu_{\frac{1}{2N}}\left(2u_0 + u_{\frac{1}{N}}\right) = -p_{\frac{1}{2N}}, \tag{4.29}$$

$$\frac{1}{6N}\mu_{1-\frac{1}{N}}\left(u_{1-\frac{1}{N}} + 2u_1\right) = p_{1-\frac{1}{2N}}. \tag{4.30}$$

From (4.10), the dimensionless initial cell vertex positions are given by

$$x_n(0) = x_{init}(n) \quad n = 0, \ldots, 1. \tag{4.31}$$

4.4.2 Nutrient transport

On nondimensionalisation, the diffusion equation for the nutrient in the cell region becomes

$$\nabla^2 c = 0, \quad x \in (-R, R),\ y \in (0, S), \tag{4.32}$$

where $R = R^*/L^*$ and $S = S^*/L^*$.

The nutrient uptake condition for each cell (4.16) becomes

$$\frac{\partial c}{\partial y} = \mathrm{Da}\,\frac{1}{l_{n+\frac{1}{2N}}}\,\frac{c}{c_{1/2}+c}, \quad \text{on } x \in \left(x_n(\tau), x_{n+\frac{1}{N}}(\tau)\right),\ y = 0, \quad n = 0, \ldots, 1-\tfrac{1}{N}, \tag{4.33}$$

where $\mathrm{Da} = M^* L^*/(a^* C^* D)$ is the second Damköhler number (the ratio of the rates of nutrient uptake and diffusive transport, $M^*/(a^* C^* L^*)$ and D/L^{*2} respectively), and $c_{1/2} = C_{1/2}/C^*$ is the dimensionless half-maximal nutrient uptake concentration.

The zero-diffusive-flux boundary conditions on the walls and base of the bath outside the aggregate, (4.12) and (4.13), become

$$\frac{\partial c}{\partial y} = 0 \quad \text{on } y = 0,\ x \notin [x_0(\tau), x_1(\tau)], \tag{4.34}$$

$$\frac{\partial c}{\partial x} = 0 \quad \text{on } x = \pm R,\ y \in (0, S). \tag{4.35}$$

The fixed nutrient concentration condition (4.14) becomes

$$c = 1 \quad \text{on } y = S,\ x \in [-R, R]. \tag{4.36}$$

4.4.3 Cell growth

Nondimensionalising the evolution equations for the cell target lengths (4.17) for constant-rate growth (4.20) and pressure-dependent growth (4.21) with $\Gamma^* = \gamma^*$ yields

$$\frac{\mathrm{d}a_{n+\frac{1}{2N}}}{\mathrm{d}\tau} = \Gamma = \begin{cases} 1 & \text{for constant-rate growth,} \\ -p_{n+\frac{1}{2N}} & \text{for pressure-dependent growth,} \end{cases} \quad n = 0, \ldots, 1-\tfrac{1}{N}. \tag{4.37a,b}$$

For the target-length-, pressure- and nutrient-dependent growth given by (4.22), choosing instead $\Gamma^* = \gamma^* a^*$ gives

$$\frac{\mathrm{d}a_{n+\frac{1}{2N}}}{\mathrm{d}\tau} = \left(a_{max} - a_{n+\frac{1}{2N}}\right) \mathrm{S}(p_{n+\frac{1}{2N}}, p_s, p_c)\,\frac{c_{n+\frac{1}{2N}}}{k_g + c_{n+\frac{1}{2N}}}, \quad n = 0, \ldots, 1-\tfrac{1}{N}, \tag{4.37c}$$

where $a_{max} := a^*_{max}/a^*$ is the dimensionless maximum target length, $p_i = p_i^*/(N^2 \mu^* \Gamma^*)$ $(i = s, c)$ are the dimensionless excess stretching and compression thresholds, and $k_g = K_g/C^*$ is the dimensionless half-maximal growth rate concentration.

The dimensionless initial cell target lengths are given by

$$a_{n+\frac{1}{2N}}(0) = a_{init}\left(n + \tfrac{1}{2N}\right), \quad n = 0, \ldots, 1-\tfrac{1}{N}. \tag{4.38}$$

4.5 Continuum approximation

Since the discrete cell variables in (4.26)–(4.38) are assumed to vary slowly with the cell index, we can approximate them by continuous functions of n and τ whose derivatives with respect to n are small. This allows us to derive a continuum approximation to the system in the limit $N \to \infty$ for which the approximation error is small. For the cell model ((4.26)–(4.31), (4.37)–(4.38)) we do this formally, by expanding the continuous cell variables as Taylor series for large N and neglecting higher order terms as $N \to \infty$. In equations (4.32)–(4.36), we have assumed that the nutrient concentration can be treated as a continuum at the cell length scale, so we do not formally homogenise these transport equations when we derive the continuum approximation. Instead, we assume that the discrete uptake boundary conditions (4.33) can be approximated by a single, continuous boundary condition which depends on the continuum cell density (see §4.5.3). We start by deriving the continuum limit of the cell model.

4.5.1 Continuum limit of discrete cell model

We assume that the physical quantities associated with each cell and their initial data can be extended (*e.g.* by band-limited interpolation, see [254]) to smooth functions of n and τ, *i.e.* that for a cell variable $\phi_n(\tau)$ $(n = 0, \dots, 1)$ there is a smooth function $\phi(n, \tau)$ such that

$$\phi_n(\tau) = \phi(n, \tau), \quad n \in [0, 1]. \tag{4.39}$$

Since $c_{n+\frac{1}{2N}}$ is derived by averaging the smooth nutrient concentration $c(x(n,\tau), 0, \tau)$, no interpolation is needed and we can simply replace $c_{n+\frac{1}{2N}}$ with $c(x(n,\tau), 0, \tau)$ (determined from (4.32)–(4.36)). The continuous versions of the cell length and vertex velocity are thus

$$l(n + \tfrac{1}{2N}, \tau) = N\left(x(n + \tfrac{1}{N}, \tau) - x(n, \tau)\right), \quad u(n, \tau) = \frac{\partial x}{\partial \tau}(n, \tau), \tag{4.40}$$

and we can rewrite the system (4.26)–(4.37) in terms of the continuous cell parameters and variables (dropping the τ-dependence of the variables in our notation for convenience) as

$$\frac{1}{N}\frac{\partial l}{\partial \tau}(n + \tfrac{1}{2N}) = u(n + \tfrac{1}{N}) - u(n), \quad n \in [0, 1 - \tfrac{1}{N}], \tag{4.41}$$

$$\alpha p(n + \tfrac{1}{2N}) = \lambda(n + \tfrac{1}{2N})\left[a(n + \tfrac{1}{2N}) - l(n + \tfrac{1}{2N})\right], \quad n \in [0, 1 - \tfrac{1}{N}], \tag{4.42}$$

$$\frac{1}{6N}\Big[\mu(n - \tfrac{1}{2N})\left[u(n - \tfrac{1}{N}) + 2u(n)\right] + \mu(n + \tfrac{1}{2N})\left[2u(n) + u(n + \tfrac{1}{N})\right]\Big] = p(n - \tfrac{1}{2N}) - p(n + \tfrac{1}{2N}), \quad n \in [\tfrac{1}{N}, 1 - \tfrac{1}{N}], \tag{4.43}$$

$$\frac{\partial a}{\partial \tau}(n + \tfrac{1}{2N}) = \Gamma\left(l(n + \tfrac{1}{2N}), a(n + \tfrac{1}{2N}), p(n + \tfrac{1}{2N}), c(x(n), 0); \gamma(n + \tfrac{1}{2N})\right), \quad n \in [0, 1 - \tfrac{1}{N}]. \tag{4.44}$$

Equations (4.29) and (4.30) for the aggregate endpoints become

$$\frac{1}{6N}\mu(\tfrac{1}{2N})\left[2u(0)+u(\tfrac{1}{N})\right]=-p(\tfrac{1}{2N}), \tag{4.45}$$

$$\frac{1}{6N}\mu(1-\tfrac{1}{2N})\left[u(1-\tfrac{1}{N})+2u(1)\right]=p(1-\tfrac{1}{2N}). \tag{4.46}$$

The initial conditions become

$$x(n,0)=x_{init}(n),\quad n\in[0,1], \tag{4.47}$$

$$a(n,0)=a_{init}(n),\quad n\in[0,1-\tfrac{1}{N}]. \tag{4.48}$$

Since variations in the cell parameters and variables have been assumed to occur over large numbers of cells, their derivatives with respect to n will be $\mathcal{O}(1/N)$ and we can Taylor expand (4.40)–(4.46) for $N\gg 1$. Expanding the parameters and variables in (4.43) about n as

$$\mu(n+\tfrac{1}{2N})=\mu(n)+\frac{1}{2N}\frac{\partial\mu}{\partial n}(n)+\mathcal{O}(\tfrac{1}{N^2}),$$

$$u(n-\tfrac{1}{N},\tau)=u(n,\tau)-\frac{1}{N}\frac{\partial u}{\partial n}(n,\tau)+\mathcal{O}(\tfrac{1}{N^2}),\quad etc.,$$

in (4.41), (4.42) and (4.44) about $n+\frac{1}{2N}$ as

$$u(n+\tfrac{1}{N},\tau)=u(n+\tfrac{1}{2N},\tau)+\frac{1}{2N}\frac{\partial u}{\partial n}(n+\tfrac{1}{2N},\tau)+\mathcal{O}(\tfrac{1}{N^2}),\quad etc.,$$

and in (4.45) and (4.46) about $n=0$ and $n=1$, respectively, and taking the limit as $N\to\infty$ (*i.e.* neglecting $\mathcal{O}(1/N^2)$ terms), (4.40)–(4.46) reduce to

$$l=\frac{\partial x}{\partial n},\quad u=\frac{\partial x}{\partial \tau}, \tag{4.49}$$

$$\frac{\partial l}{\partial \tau}=\frac{\partial u}{\partial n},\quad n\in(0,1), \tag{4.50}$$

$$\alpha p=\lambda(a-l),\quad n\in(0,1), \tag{4.51}$$

$$\mu u=-\frac{\partial p}{\partial n},\quad n\in(0,1), \tag{4.52}$$

$$\frac{\partial a}{\partial \tau}=\Gamma(l,p,a,c(x(n,\tau),0,\tau);\gamma),\quad n\in(0,1). \tag{4.53}$$

with the stress-free boundary conditions

$$p=0\quad \text{at } n=0,1. \tag{4.54}$$

The functional forms of the different choices for Γ are identical to those for the discrete cell model:

$$\Gamma=\begin{cases}1, & \text{for constant-rate growth,}\\ -p, & \text{for pressure-dependent growth,}\\ (a_{max}-a)\mathrm{S}(p,p_s,p_c)\frac{c}{k_g+c}, & \text{for target-length-, pressure- and nutrient-dependent growth.}\end{cases} \tag{4.55a–c}$$

In the continuum limit, (4.47) and (4.48) can be written as

$$l(n,0) = l_{init}(n) := \frac{\partial x_{init}}{\partial n}(n), \quad n \in [0,1], \tag{4.56}$$

$$a(n,0) = a_{init}(n), \quad n \in [0,1]. \tag{4.57}$$

As the terms omitted from the expansions in (4.50)–(4.54) are $\mathcal{O}(1/N^2)$, we expect the error in the continuum approximation to be of the same order and hence decrease rapidly as the number of cells increases.

4.5.2 Spatial form of continuum approximation

We now transform (4.50)–(4.57) from Lagrangian (cell-vertex-based) coordinates (n,τ) to Eulerian (spatial) coordinates (x,t), where $t=\tau$ and $x(n,\tau)$ is the Eulerian position of the vertex with index n (corresponding to $x_n(\tau)$ in the discrete model). This allows us to derive a nonlinear diffusion equation for the cell density, which facilitates physical interpretation of the model and comparison with the models of Murray *et al.* and Fozard *et al.*

Using the continuum limit of the definitions of l and u (4.49) and the chain rule we have that

$$\frac{\partial}{\partial n} = \frac{\partial x}{\partial n}\frac{\partial}{\partial x} + \frac{\partial t}{\partial n}\frac{\partial}{\partial t} = l\frac{\partial}{\partial x}, \tag{4.58}$$

$$\frac{\partial}{\partial \tau} = \frac{\partial x}{\partial \tau}\frac{\partial}{\partial x} + \frac{\partial t}{\partial \tau}\frac{\partial}{\partial t} = u\frac{\partial}{\partial x} + \frac{\partial}{\partial t} =: \frac{\mathrm{D}}{\mathrm{D}t}, \tag{4.59}$$

where $\frac{\mathrm{D}}{\mathrm{D}t}$ is the convective derivative in the Eulerian frame. Substituting these identities into (4.50)–(4.53) gives

$$\frac{\mathrm{D}l}{\mathrm{D}t} = l\frac{\partial u}{\partial x}, \tag{4.60}$$

$$\alpha p = \lambda(a-l), \tag{4.61}$$

$$\mu u = -l\frac{\partial p}{\partial x}, \tag{4.62}$$

$$\frac{\mathrm{D}a}{\mathrm{D}t} = \Gamma. \tag{4.63}$$

These equations hold for $x \in (x_L(t), x_R(t)) = (x(0,t), x(1,t))$, where the boundaries x_L and x_R move with the local cell velocity, *i.e.* $\frac{\mathrm{d}x_{L,R}}{\mathrm{d}t} = u(x_{L,R}(t),t)$. Using (4.51), the boundary conditions at $x = x_{L,R}$ from (4.54) are

$$l = a \quad \text{at } x = x_L(t), x_R(t). \tag{4.64}$$

Initial conditions for $l = l(x,t)$ and $a = a(x,t)$ are obtained by inverting (4.47) to give

$$n(x,0) = x_{init}^{-1}(x),$$

and substituting this into (4.56) and (4.57) to obtain

$$l(x,0) = l_{init,x}(x) := l_{init}(x_{init}^{-1}(x)) = \frac{\partial x_{init}}{\partial n}\left(x_{init}^{-1}(x)\right), \tag{4.65}$$

$$a(x,0) = a_{init,x}(x) := a_{init}(x_{init}^{-1}(x)). \tag{4.66}$$

Defining the cell density by $\rho := 1/l$, we observe that (4.60) corresponds to conservation of cell number,

$$\frac{\partial \rho}{\partial t} + \frac{\partial}{\partial x}(\rho u) = 0. \tag{4.67}$$

Combining (4.61), (4.62) and (4.67) to eliminate p and u and substituting $l = 1/\rho$ yields

$$\alpha \frac{\partial \rho}{\partial t} = \frac{\partial}{\partial x}\left(\frac{1}{\mu}\frac{\partial}{\partial x}\left(\lambda\left(a - \tfrac{1}{\rho}\right)\right)\right), \tag{4.68}$$

$$\frac{\mathrm{D}a}{\mathrm{D}t} = \Gamma\left(\tfrac{1}{\rho}, a, \lambda\left(a - \tfrac{1}{\rho}\right), c; \gamma\right), \tag{4.69}$$

$$\text{wherein} \quad u = -\frac{1}{\alpha\mu\rho}\frac{\partial}{\partial x}\left(\lambda\left(a - \tfrac{1}{\rho}\right)\right). \tag{4.70}$$

From here on we assume that $\lambda_{n+1/2}$, $\mu_{n+1/2}$ and $\gamma_{n+1/2}$ are all constant, so that $\lambda = \mu = \gamma = 1$ upon nondimensionalisation. With this assumption, (4.68)–(4.70) simplify to the following nonlinear diffusion equation for the cell density and evolution equation for the cell target length

$$\alpha \frac{\partial \rho}{\partial t} = \frac{\partial}{\partial x}\left(\frac{1}{\rho^2}\frac{\partial \rho}{\partial x}\right) + \frac{\partial^2 a}{\partial x^2}, \tag{4.71}$$

$$\frac{\mathrm{D}a}{\mathrm{D}t} = \Gamma\left(\tfrac{1}{\rho}, a, a - \tfrac{1}{\rho}, c\right), \tag{4.72}$$

$$\text{wherein} \quad u = -\frac{1}{\alpha\rho}\left(\frac{\partial a}{\partial x} + \frac{1}{\rho^2}\frac{\partial \rho}{\partial x}\right). \tag{4.73}$$

Equations (4.64) and (4.65) give the following boundary and initial conditions for ρ

$$\rho = \frac{1}{a} \quad \text{at } x = x_L(t), x_R(t), \tag{4.74}$$

$$\rho(x,0) = \rho_{init}(x) := \frac{1}{l_{init,x}(x)} = \left(\frac{\partial x_{init}}{\partial n}(x_{init}^{-1}(x))\right)^{-1}. \tag{4.75}$$

Interpretation of the nonlinear diffusion coefficient $D(\rho) = 1/\rho^2$ in (4.71) is aided by considering the limits of very low and very high cell density. As $\rho \to 0$, $D(\rho) \to \infty$. This corresponds to the springs between the vertices in the discrete model (the cells) being greatly stretched so that there is a large restoring force returning the cells to their target lengths (since the cells cannot separate), which gives a large diffusion coefficient in the continuum limit. As $\rho \to \infty$, however, $D(\rho) \to 0$. In the discrete model, this corresponds to the cells in the aggregate interior being very compressed and unable to relax to their target lengths until the cells at the ends of the aggregate have moved to create space and relieve

internal stress, which leads to a very small diffusion coefficient in the continuum limit. The $\frac{\partial^2 a}{\partial x^2}$ source term in (4.71) arises from the evolution of the cell target lengths. The physical interpretation of this term is that, due to cell growth, the cell density will increase most rapidly where the cells are locally most compressed (where the gradient in a is increasing fastest, *i.e.* $\frac{\partial^2 a}{\partial x^2} > 0$ is most positive), and decrease most rapidly where the cells are most stretched (where the gradient in a is decreasing fastest, *i.e.* $\frac{\partial^2 a}{\partial x^2} < 0$ is most negative).

4.5.3 Continuum approximation of nutrient uptake

As explained previously, we do not formally average the nutrient transport when deriving the continuum approximation of the discrete model. Instead, we use the diffusion equation (4.32) for the nutrient concentration

$$\nabla^2 c = 0, \quad x \in (-R, R),\, y \in (0, S),$$

with the boundary conditions (4.34)–(4.36), and modify the uptake boundary condition (4.33) so that it is continuous over the length of the aggregate. As the cell lengths are assumed to vary slowly with n, the discontinuities in uptake between neighbouring cells will be small, and we can approximate $l_{n+\frac{1}{2N}}$ in (4.33) by l without introducing large errors. Thus the continuous form of (4.33) that we use with the continuum cell model is

$$\frac{\partial c}{\partial y} = \mathrm{Da}\, m(l, c) = \mathrm{Da}\, \frac{1}{l} \frac{c}{c_{1/2} + c}, \quad \text{on } \; x \in [x_L(t), x_R(t)],\; y = 0. \tag{4.76}$$

As expected, this corresponds to the nutrient uptake flux being proportional to the cell density, $\rho = 1/l$,

$$\frac{\partial c}{\partial y} = \mathrm{Da}\, \rho \frac{c}{c_{1/2} + c}, \quad \text{on } \; x \in [x_L(t), x_R(t)],\; y = 0, \tag{4.77}$$

since (4.33) is based on all cells consuming nutrient at the same rate regardless of their length (for a given nutrient concentration).

4.5.4 Summary of the discrete and continuum models for nutrient-dependent aggregate growth

The governing equations for the coupled discrete cell model and nutrient transport are (4.25)–(4.38). As shown above, the spatial form of the continuum approximation of this system is given by (4.32), (4.34)–(4.36), (4.71)–(4.75) and (4.77), which is a coupled system of PDEs for ρ, a and c. In what follows, rather than using the spatial form of the continuum cell model to simulate aggregate growth, for which the cell model is formulated on an evolving domain, we will use the Lagrangian form given by (4.49)–(4.57), for which the domain size is fixed.

4.6 Comparison with existing models

In this section, we compare the spatial form of our continuum approximation with the cell aggregate growth law of Chapter 3 in the limit of incompressible cells, and with Murray *et al.*'s and Fozard *et al.*'s continuum approximations. We highlight the differences between our model and those of Murray *et al.* and Fozard *et al.*, discussing in particular the incorporation of cell division into Murray *et al.*'s model and the dependence of the diffusion coefficient in the cell density PDE (4.71) on the cell interaction force law in the discrete model.

4.6.1 Comparison with cell aggregate growth model in limit of incompressible cells

In the limit in which the cells are incompressible ($\lambda^* \gg N^2$) the cell relaxation timescale is very short and $\alpha = N^2 \frac{\Gamma^* \mu^*}{a^* \lambda^*} \ll 1$ (for fixed N). Hence, at leading order in α, (4.60)–(4.66) supply $l = a$ and

$$a \frac{\partial u}{\partial x} = \Gamma, \tag{4.78}$$

$$\mu u = -a \frac{\partial p}{\partial x}, \tag{4.79}$$

$$\frac{\mathrm{D}a}{\mathrm{D}t} = \Gamma, \tag{4.80}$$

$$p = 0 \quad \text{at } x = x_L,\, x_R, \tag{4.81}$$

$$a = a_{init,x} \quad \text{at } t = 0. \tag{4.82}$$

Since the ends of the aggregate move with the local cell velocity, the aggregate length, $L_{agg} := x_R - x_L$, evolves as follows

$$\frac{\mathrm{d}L_{agg}}{\mathrm{d}t} = \frac{\mathrm{d}}{\mathrm{d}t}(x_R - x_L) = u(x_R(t), t) - u(x_L(t), t) = \int_{x_L(t)}^{x_R(t)} \frac{\partial u}{\partial x}\, \mathrm{d}x = \int_{x_L(t)}^{x_R(t)} \frac{\Gamma}{a}\, \mathrm{d}x. \tag{4.83}$$

Equation (4.83) is of the same form as the continuum cell aggregate growth law (3.22) used in Chapter 3, if we identify Γ/a with $G_p - G_d$, where G_p is the local cell proliferation rate and G_d is the local cell death rate. Thus the growth law used previously gives a valid approximation to a discrete model of cell growth in the limit of incompressible cells. We therefore anticipate that our discrete model, embedded in a model for fluid flow and nutrient transport in the HFB, and with the target length evolution chosen to match the previous aggregate growth law, will reproduce the same growth behaviour. We postpone verification of this claim to future work.

4.6.2 Comparison with Murray *et al.*'s model

Murray *et al.* [181, 182] do not explicitly model cell growth in their discrete cell-centre model. Instead they assume that the resting lengths of the springs connecting the cell centres are constant, and derive the cell density diffusion equation (4.71) (with constant a) from their discrete model, *i.e.*

$$\alpha_M \frac{\partial \rho}{\partial t} = \frac{\partial}{\partial r}\left(\frac{1}{\rho^2}\frac{\partial \rho}{\partial r}\right), \tag{4.84}$$

where r is the dimensionless cell position coordinate, time has been scaled with the cell doubling time T_d, and $\alpha_M = N^2\mu^*/(\lambda^* T_d)$. In order to compare their model with our model and that of Fozard *et al.*, we provide a more detailed derivation of (4.84) in Appendix E.

4.6.2.1 Cell division

The key difference between our discrete model and that of Murray *et al.* is that the latter includes cell division. All cells are initially randomly assigned an age in the interval $[t_a, 1]$ and divide when their age reaches 1, where t_a determines whether the division is 'asynchronous' ($t_a = 0$) or 'synchronous' ($t_a = 1 - 1/T_d$). When a cell divides, the two daughter cells (cell centres) are placed 0.1 cell diameters on either side of the mother cell (centre), so that cell growth is modelled implicitly by the relaxation of the springs between the cell centres from compression following the division.

Murray *et al.* do not average this discrete model of cell division to derive corresponding terms in their continuum approximation, but instead add a source term, $f(\rho, t)$, to the cell density equation

$$\frac{\partial \rho}{\partial t} = \frac{1}{\alpha_M}\frac{\partial}{\partial r}\left(\frac{1}{\rho^2}\frac{\partial \rho}{\partial r}\right) + f(\rho, t),$$

and fix $f(\rho, t)$ to match the cell doubling times in the two models. This neglects the finer details of the discrete division process, such as how far apart the daughter cells are placed upon division and their symmetric placement about the mother cell, and it is not clear under what conditions this is valid. However, Murray *et al.* demonstrate via numerical simulations that there is close agreement between the solutions of the discrete and continuum models for sufficiently large cell numbers ($N = \mathcal{O}(100)$).

In Appendix E.4, we show that in the limit of incompressible cells, $\lambda^* \gg N^2$ (corresponding to $\alpha_M \ll 1$), Murray *et al.*'s continuum model with cell proliferation yields a cell aggregate growth law similar in form to that used in Chapter 3 (equation (3.22)). This demonstrates that (3.22) is a valid approximation of a discrete spring-based cell model with cell proliferation. Possible ways of including cell proliferation in our model are discussed in §4.11.

4.6.2.2 Classification of different cell interaction force laws

In [182], Murray *et al.* showed that different cell interaction force laws give rise to different density-dependent diffusion coefficients, $D(\rho)$, in the continuum PDE for the cell density

$$\alpha_M \frac{\partial \rho}{\partial t} = \frac{\partial}{\partial r}\left(D(\rho)\frac{\partial \rho}{\partial r}\right).$$

For an interaction force $F_{nj} = F(|r_n - r_j|)$ between the nth and jth cells with centres at r_n and r_j respectively, the diffusion coefficient is of the form

$$D(\rho) = -\frac{1}{\rho^2}F'(\tfrac{1}{\rho}), \tag{4.85}$$

where the prime denotes differentiation with respect to $|r_n - r_j|$. Equation (4.85) shows how to connect off-lattice discrete models and nonlinear diffusion models of cell motion via their force laws and diffusion coefficients.

As the interaction forces F_{nj} in Murray *et al.*'s cell-centre framework are equivalent to the cell pressures $p_{n+1/2}$ in our cell-vertex framework, we can repeat Murray *et al.*'s analysis to derive the general form of the diffusion coefficient in our model for $p_{n+\frac{1}{2N}} = p(l_{n+\frac{1}{2N}}, a_{n+\frac{1}{2N}})$. The diffusion equation for the cell density (4.71) (with varying a) becomes

$$\begin{aligned}\alpha\frac{\partial \rho}{\partial t} &= -\alpha\frac{\partial}{\partial x}(\rho u) = -\alpha\frac{\partial^2 p}{\partial x^2} \\ &= \frac{\partial}{\partial x}\left(D(\rho)\frac{\partial \rho}{\partial x}\right) + \frac{\partial}{\partial x}\left(\frac{\partial p}{\partial a}\frac{\partial a}{\partial x}\right),\end{aligned} \tag{4.86}$$

where the diffusion coefficient is given by

$$D(\rho) = -\frac{1}{\rho^2}\frac{\partial p}{\partial l}(l, a)\big|_{l=\frac{1}{\rho}}.$$

This confirms that, with equivalent definitions of the cell interaction force law and the cell pressure, the cell-centre and cell-vertex models give rise to the same continuum limit in 1D. We leave investigation of the behaviour arising from nonlinear dependence of the cell pressure on the cell length to future work.

4.6.3 Comparison with Fozard *et al.*'s model

Apart from the fact that it is not coupled to an external nutrient field, the main differences between Fozard *et al.*'s model and our model (and also Murray *et al.*'s model) are that it assumes the cell-substrate drag force *per unit length* (rather than the net substrate drag force) is proportional to the cell velocity, and it includes energy dissipation due to the internal viscosity of the cells. This means that the drag force on each cell vertex is given by the sum of the cell-substrate drag and a viscous drag, which is assumed to be linear in the

vertex velocities of the adjoining cells (corresponding to there being dashpots connecting the vertices in parallel with the springs). Taking the continuum limit of the discrete model for $N \gg 1$, Fozard *et al.* arrive at the system (4.50)–(4.53) but with the force balance equation (4.52) replaced by

$$\mu_F l u - V \frac{\partial}{\partial n}\left(\delta \frac{\partial u}{\partial n}\right) = -\frac{\partial p}{\partial n}, \quad n \in (0,1), \tag{4.87}$$

where μ_F $(= \mu/a^*)$ is the cell-substrate drag, δ parameterises the internal cell viscosity, and $V = \delta^*/(N^2 \mu_F^* a^*)$ is the ratio of the internal viscous drag to the cell-substrate drag (δ^* and μ_F^* being typical values of the internal viscosity and substrate drag respectively). Due to the inclusion of cell viscosity, the conditions on the end vertices (4.54) become

$$p = V\delta \frac{\partial u}{\partial n} \quad \text{at } n = 0, 1. \tag{4.88}$$

4.6.3.1 Spatial form of Fozard *et al.*'s continuum approximation

We now compare the spatial form of Fozard *et al.*'s continuum approximation with that of our continuum approximation ((4.60)–(4.64)) and with existing continuum cell models. Under the transformation to spatial coordinates $(n, \tau) \mapsto (x, t)$ in §4.5.2, Fozard *et al.*'s continuum approximation (given by (4.50), (4.51), (4.53), (4.87) and (4.88)) becomes

$$\frac{\mathrm{D}l}{\mathrm{D}t} = l \frac{\partial u}{\partial x}, \tag{4.89}$$

$$\alpha p = \lambda(a - l), \tag{4.90}$$

$$\mu_F u - V \frac{\partial}{\partial x}\left(\delta l \frac{\partial u}{\partial x}\right) = -\frac{\partial p}{\partial x}, \tag{4.91}$$

$$\frac{\mathrm{D}a}{\mathrm{D}t} = \Gamma(l, p, a; \gamma), \tag{4.92}$$

with

$$p = V\delta l \frac{\partial u}{\partial x} \quad \text{at } x = x_L, x_R. \tag{4.93}$$

In contrast to our equation for the cell velocity (4.62), (4.91) corresponds to Darcy's Law (*i.e.* cell movement being driven purely by gradient in the cell pressure) in the limit of no cell viscosity, $V = 0$. For $V > 0$, there is an additional Brinkman term in (4.91), which represents the viscous forces induced in the cells by their extension. Fozard *et al.*'s model is thus closer than our model to existing single- and two-phase models of tumour growth that use Darcy's law to describe cell motion [24, 26, 97, 137]. However, as shown below, Fozard *et al.*'s model leads to a more complicated system for the cell density and cell target length.

Fozard *et al.* assume that the cell parameters are uniform ($\lambda = \mu_F = \delta = 1$), so that combining equations (4.89)–(4.91) gives

$$\alpha\left(\frac{1}{\rho}\frac{\mathrm{D}\rho}{\mathrm{D}t} - V\frac{\partial^2}{\partial x^2}\left(\frac{1}{\rho^2}\frac{\mathrm{D}\rho}{\mathrm{D}t}\right)\right) = \frac{\partial}{\partial x}\left(\frac{1}{\rho^2}\frac{\partial \rho}{\partial x}\right) + \frac{\partial^2 a}{\partial x^2}. \tag{4.94}$$

Equations (4.91), (4.92), the boundary conditions (4.93), and the initial conditions for ρ and a,

$$u - V\frac{\partial}{\partial x}\left(\frac{1}{\rho}\frac{\partial u}{\partial x}\right) = -\frac{\partial a}{\partial x} - \frac{1}{\rho^2}\frac{\partial \rho}{\partial x}, \tag{4.95}$$

$$\frac{\mathrm{D}a}{\mathrm{D}t} = \Gamma\left(\tfrac{1}{\rho}, a, a - \tfrac{1}{\rho}; \gamma\right), \tag{4.96}$$

$$\rho = \frac{1}{a}\left(1 + V\frac{\partial u}{\partial x}\right) \quad \text{at } x = x_L, x_R, \tag{4.97}$$

$$\rho(x,0) = \rho_{init}(x), \quad a(x,0) = a_{init}(x), \tag{4.98}$$

close the model for ρ, u and a. Fozard *et al.*'s assumptions increase the complexity of the model in two ways. First, their assumption that the cell-substrate drag per unit length is proportional to the cell velocity leads to a convective derivative in the first term in (4.94) rather than just a partial derivative with respect to time. Second, their inclusion of cell viscosity means that u is defined by (4.95) implicitly rather than explicitly. We instead adopt the simplest form of dependence of the substrate drag on the cell velocity (in keeping with previous studies [173, 184, 263]), and neglect the viscous drag since for typical parameter values it is insignificant compared to the substrate drag (see §4.7.5).

4.7 Parameter values

We now discuss parameter values for the model. Complete sets of parameter values for individual cell types are not available, and some parameter values (such as the cell elasticity and drag constants) are not straightforward to measure experimentally. Hence, in our simulations we use a combination of parameter values taken from different experimental studies and consider ranges of values for parameters for which there is a lack of experimental data. First we state values for the dimensional cell model and nutrient transport parameters. We then use these to estimate the dimensionless parameters.

4.7.1 Cell motion

Literature-based estimates for the cell motion parameters for different cell types are presented in Table 4.1. The estimates of the cell elasticity constant, $\lambda^* = 0.4\,\mathrm{nN\,\mu m^{-2}}$, and cell-substrate drag constant, $\mu^* = 0.1\,\mathrm{nN\,hr\,\mu m^{-2}}$, were derived by Mi *et al.* [176] from measurements of enterocyte migration [32] and the traction forces required to stop migrating intestinal epithelial cells [212]. Since we are interested in determining the suitability of the model for describing bioreactor cell aggregate growth, for which the number of cells in an aggregate is typically $\mathcal{O}(100)$ (see §B.2.2), we consider cell numbers in the range $N = 10$–150 in our simulations.

Parameter	Description	Cell type	Value	References
N	number of cells	Epithelial cells	**10–150**	[78, 211]
		Mouse hepatocytes	26–94	[92]
a^*	cell target length	Epithelial cells	**10 μm**	[63, 65, 78, 88]
		Rat hepatocytes	**10 μm**	[122]
		Chondrocytes	8.5 μm, **10 μm**, 12 μm	[42], [85], [177]
		Rat myoblasts	12 μm	[229]
λ^*	cell elasticity constant	Epithelial cells	**0.4 nN μm^{-2}**, 1 nN μm^{-2}	[176], [88]
μ^*	cell-substrate drag constant	Epithelial cells	**0.1 nN hr μm^{-2}**, 0.28 nN hr μm^{-2}	[176], [88]

Table 4.1: Dimensional cell motion parameter values. Parameter values used in simulations are shown in bold.

4.7.2 Nutrient transport

Although equations (4.11)–(4.14) may be used to model the transport of a generic nutrient, we will focus on oxygen transport as in previous chapters. Associated parameter values are given in Table 4.2. We use an oxygen concentration at the surface of the bath (*i.e.* value for C^*) typical of that in culture medium, and also mimic limited supply by lowering this value. As in the previous chapter, we estimate the maximum uptake flux, $\tilde{M}$, by multiplying the cellular oxygen uptake rate, M_c, by the surface density of cells, ρ_s. This gives a large range of uptake fluxes for the different cell types we consider: $\tilde{M} \in [3.42 \times 10^{-9}, 2.67 \times 10^{-7}]\,\mathrm{mol\,m^{-2}\,s^{-1}}$. In our simulations we use values in the range $\tilde{M} \in [10^{-8}, 10^{-5}]\,\mathrm{mol\,m^{-2}\,s^{-1}}$ (which extends beyond the range reported in the literature) to investigate the sensitivity of the oxygen distribution, and therefore cell growth, to the uptake flux.

4.7.3 Cell growth

Parameter values associated with the cell growth are listed in Table 4.3. The cell elongation rate, Γ^*, is estimated by assuming that the cell target length doubles from a^* to $2a^*$ in the doubling time, T_d, *e.g.* for epithelial cells with a doubling time of $T_d = 72\,\mathrm{hrs}$ the elongation rate is

$$\Gamma^* \approx \frac{a^*}{T_d} \approx 0.14\,\mu\mathrm{m\,hr^{-1}}.$$

The maximum cell target length, a^*_{max}, is assumed to be twice the initial target length of the cell, since most cells roughly double in size during the cell cycle [199]. Data for

Parameter	Description	Cell type	Value	References
D	oxygen diffusivity in culture medium	N/A	$3\times10^{-9}\,\mathrm{m^2 s^{-1}}$	[55, 208, 280]
M_c	maximum cellular oxygen uptake rate	Human epithelial cells	$3.42\times10^{-16}\,\mathrm{mol\,cell^{-1}\,s^{-1}}$	[51]
		Hepatocytes	$3.07\times10^{-18}\,\mathrm{mol\,cell^{-1}\,s^{-1}}$ †, 4.8×10^{-17}–$8.9\times10^{-17}\,\mathrm{mol\,cell^{-1}\,s^{-1}}$	[246], [201]
		Bovine chondrocytes	$4.0\times10^{-18}\,\mathrm{mol\,cell^{-1}\,s^{-1}}$	[163, 188]
		Rat cardiomyocytes	$1.38\times10^{-18}\,\mathrm{mol\,cell^{-1}\,s^{-1}}$ †	[215]
ρ_s	surface cell density	Human epithelial cells	$1\times10^{7}\,\mathrm{cells\,m^{-2}}$	[51]
		Hepatocytes	$3\times10^{9}\,\mathrm{cells\,m^{-2}}$	[55]
		Chondrocytes	$2.5\times10^{9}\,\mathrm{cells\,m^{-2}}$	[159]
		Rat cardiomyocytes	$1.03\times10^{9}\,\mathrm{cells\,m^{-2}}$	[215]
$\tilde{M}=M^*/a^*$ $=M_c\rho_s$	maximum oxygen uptake flux	Human epithelial cells	$9.42\times10^{-12}\,\mathrm{mol\,m^{-2}\,s^{-1}}$, $3.42\times10^{-9}\,\mathrm{mol\,m^{-2}\,s^{-1}}$	[61], [51]
		Hepatocytes	$9.22\times10^{-9}\,\mathrm{mol\,m^{-2}\,s^{-1}}$, 1.44×10^{-7}–$2.67\times10^{-7}\,\mathrm{mol\,m^{-2}\,s^{-1}}$	[246], [201]
		Bovine chondrocytes	$1\times10^{-8}\,\mathrm{mol\,m^{-2}\,s^{-1}}$	[163, 188]
		Rat cardiomyocytes	$1.43\times10^{-9}\,\mathrm{mol\,m^{-2}\,s^{-1}}$	[215]
$C_{1/2}$	half-maximal oxygen uptake concentration	Human epithelial cells	$1.0\times10^{-3}\,\mathrm{mol\,m^{-3}}$	[61]
		Rat hepatocytes	$6.24\times10^{-3}\,\mathrm{mol\,m^{-3}}$	[246]
		Chondrocytes	$5\times10^{-3}\,\mathrm{mol\,m^{-3}}$	[102]
		Rat cardiomyocytes	$6.88\times10^{-3}\,\mathrm{mol\,m^{-3}}$	[215]
C^*	oxygen concentration at surface of nutrient bath	Human epithelial cells	$0.21\,\mathrm{mol\,m^{-3}}$	[61]
		Hepatocytes	0.19–$0.28\,\mathrm{mol\,m^{-3}}$	[47, 246]
		Chondrocytes	0.07–$0.14\,\mathrm{mol\,m^{-3}}$, $0.21\,\mathrm{mol\,m^{-3}}$	[76, 188], [42]
		Rat cardiomyocytes	$0.22\,\mathrm{mol\,m^{-3}}$	[215]

Table 4.2: Dimensional oxygen transport parameter values for different cell types.
† Estimated using $M_c \approx V_{max}V_c$, where V_{max} is maximal volumetric uptake rate and $V_c \approx \frac{4}{3}\pi(a^*/2)^3$ is estimated cell volume.

Parameter	Description	Cell type	Value	References
T_d	cell doubling time	Epithelial cells	**72 hrs**, 20 hrs, 19 hrs, 12 hrs	[48], [213], [65], [173]
		Rat hepatocytes	**20 hrs**	[187]
		Chondrocytes	56 hrs, **40 hrs**, 25 hrs, 12 hrs,	[272], [177], [85], [40]
		Rat myoblasts	12.6 hrs	[46]
$\Gamma^* = a^*/T_d$	cell elongation rate	Epithelial cells	$\mathbf{0.14\ \mu m\ hr^{-1}}$, $0.5\ \mu m\ hr^{-1}$, $0.52\ \mu m\ hr^{-1}$, $0.83\ \mu m\ hr^{-1}$	-
		Rat hepatocytes	$\mathbf{0.5\ \mu m\ hr^{-1}}$	-
		Chondrocytes	$0.18\ \mu m\ hr^{-1}$, $\mathbf{0.3\ \mu m\ hr^{-1}}$, $0.40\ \mu m\ hr^{-1}$, $0.83, \mu m\ hr^{-1}$,	-
		Rat myoblasts	$0.95\ \mu m\ hr^{-1}$	-
a^*_{max}	maximum cell target length	-	$\mathbf{2a^*}$	[199]
K_g	half-maximal growth rate concentration	Chondrocytes	$\mathbf{6.3 \times 10^{-2}\ mol\ m^{-3}}$	[42]
		Rat myoblasts	$6 \times 10^{-3}\ mol\ m^{-3}$	[46]
p^*_s	maximum stretch threshold for cell growth	-	$\mathbf{-2\ to\ -0.5\ nN\ \mu m^{-1}}$	†
p^*_c	maximum compression threshold for cell growth	-	$\mathbf{0.5\ to\ 2\ nN\ \mu m^{-1}}$	†

Table 4.3: Parameter values for cell growth laws. Parameter values used in simulations are shown in bold.
† Parameter values for which limited or no experimental data is available.

the other parameters is limited. For the oxygen concentration at which the growth rate is half maximal, K_g, we use a value of $0.01\ mol\ m^{-3}$ for epithelial cells and hepatocytes (based on K_g being $\sim 10^{-2}\ mol\ m^{-3}$ for chondrocytes and rat myoblasts). In the absence of experimental data for the thresholds for excess stretching and compression, p^*_s and p^*_c, we assume that cell growth can occur under equal amounts of stretching and compression, *i.e.* that $p^*_c = -p^*_s$, and vary p^*_s in the range $[-2, -0.5]\ nN\ \mu m^{-1}$.

4.7.4 Size of nutrient bath and culture time

As we consider cell numbers $N \in [10, 150]$, we take the length of the nutrient bath to be 4 mm ($R^* = 2$ mm), *i.e.* approximately 400 cells in length. We take the height of the bath, S^*, to be 2 mm.

Cell culture times vary considerably. Here we will use simulation times in the range 72 – 100 hrs depending on the cell type, initial conditions and growth law under consideration.

Parameter	Description	Cell type			
		Epithelial	Hepatocytes‡	Chondrocytes◇	Myocytes
$\alpha = \Gamma^*\mu^* N^2/(a^*\lambda^*)$	ratio of cell relaxation and elongation timescales	$3.5{\times}10^{-3}N^2$	$0.013N^2$	$7.5\times10^{-3}N^2$	$0.02N^2$
$a_{max} = a^*_{max}/a^*$	dimensionless maximum cell target length	2	2	2	2
$k_g = K_g/C^*$	half-maximal growth rate concentration	0.048†	0.043†	0.30	0.027
$p_s = p^*_s/(N^2\mu^*\Gamma^*)$	dimensionless maximum stretch threshold for cell growth	$-143/N^2$ to $-35.7/N^2$	$-40/N^2$ to $10/N^2$	$-66.7/N^2$ to $-16.7/N^2$	$-21.1/N^2$ to $-5.26/N^2$
$p_c = p^*_c/(N^2\mu^*\Gamma^*)$	dimensionless maximum compression threshold for cell growth	$35.7/N^2$ to $143/N^2$	$10/N^2$ to $40/N^2$	$16.7/N^2$ to $66.7/N^2$	$5.26/N^2$ to $21.1/N^2$
$\mathrm{Da} = \tilde{M}Na^*/(C^*D)$	ratio of nutrient diffusion and uptake timescales	$5.4\times10^{-5}N$	$1.3\times10^{-4}N$, $2.1{\times}10^{-3}N$–$3.9\times10^{-3}N$	$1.6\times10^{-4}N$	$7.8\times10^{-5}N$
$c_{1/2} = C_{1/2}/C^*$	dimensionless half-maximal uptake concentration	4.8×10^{-3}	0.027	0.024	0.031
s_p	smoothing factor in $S(p, p_s, p_c)$	50	50	50	50

Table 4.4: Dimensionless cell model and oxygen transport parameter values
† Limited data available, so estimate of $K_g = 10^{-2}\,\mathrm{mol\,m^{-3}}$ used, based on values for chondrocytes and rat myoblasts (see Table 4.3).
‡ Average value of $C^* = 0.23\,\mathrm{mol\,m^{-3}}$ from range in Table 4.2 used for surface concentration.
◇ Higher value of $C^* = 0.21\,\mathrm{mol\,m^{-3}}$ from Table 4.2 used, and elongation rate of $0.3\,\mu\mathrm{m\,hr^{-1}}$ from Table 4.3 used.

4.7.5 Dimensionless parameter values

Values for the dimensionless cell model and oxygen transport parameters, corresponding to the dimensional values in Tables 4.1–4.3, are listed in Table 4.4. The diffusion timescale (the time it takes for oxygen to diffuse over the length of the aggregate) is in the range 3 s (for $N = 10$ cells) to 12.5 min (for $N = 150$ cells). The range of the cell relaxation timescale μ^*/λ^* is $0.25-0.28$ hrs. Both of these timescales are much shorter than the cell growth timescale, T_d, which is in the range $12-72$ hrs for the cell types we consider (Table 4.3), which justifies our assumption that the oxygen transport is quasi-steady on the timescale of cell growth. Although the ratio of the cell relaxation and elongation timescales is small ($\Gamma^*\mu^*/(a^*\lambda^*) \ll 1$) for all the cell types, even for small cell numbers, α (which is proportional to N^2) is $\mathcal{O}(1)$, ranging from 0.35 to 2 for $N = 10$, and from 35 to 200 for $N = 100$. The Damköhler number also scales with the cell number (as it is proportional to the cell aggregate length, $L^* = Na^*$), and for $N = 10$ ranges from 5.4×10^{-4} for epithelial cells to 2.9 for the maximum uptake flux that we use for hepatocytes. Fozard *et al.* [78] estimate the cell viscosity constant, δ^*, to be 7×10^{-3} nN hr μm^{-2}, so that the ratio of the viscous and cell-substrate drag forces is $V = \delta^*/(N^2\mu^*) \approx 0.07/N^2$. Hence for $N = 10$–100, $V \approx 7 \times 10^{-6} - 7 \times 10^{-4} \ll 1/N^2$, so viscous effects can be neglected.

Since the dimensional domain is the same for all the cell growth simulations and the domain half-length R^* and height S^* are scaled with $L^* = Na^*$ in the nondimensionalisation, the dimensionless domain half-length, $R = R^*/L^* = R^*/(Na^*)$, and height, $S = S^*/L^*$, decrease as the cell number N is increased. This has consequences for the numerical scheme used to solve the oxygen transport equations, which are discussed in Appendix F.2.1. The dimensionless simulation time, T, is in the range 1–5 for the different cell types considered.

4.8 Solution of the discrete and continuum models

For constant-rate growth (4.37a) and pressure-dependent growth (4.37b), we solve the dimensionless discrete cell model, (4.26)–(4.31) and (4.37)–(4.38), and its continuum approximation, (4.50)–(4.57), analytically (see §4.9.1.1 and §4.9.2.1) and numerically. To solve the discrete model numerically we reduce (4.26)–(4.30) to a system of coupled ODEs for the cell vertex positions and target lengths and integrate them using the MATLAB stiff solver `ode15s` (see Appendix F.1.1). To solve the continuum model we write (4.50)–(4.53) as a coupled PDE system for the cell length and target length, which we solve using the finite difference method on a regular grid with a grid space of $\Delta n = 10^{-3}$ and a time step of $\Delta\tau = 10^{-4}$ (see Appendix F.1.2 for details).

For nutrient-dependent growth (4.37c), we solve the discrete and continuum models numerically using an iterative scheme. We solve the nutrient transport equations ((4.32)–(4.36) for the discrete model, and (4.32), (4.34)–(4.36) and (4.76) for the continuum model) for the current cell configuration, use this solution to update the cell variables, and then repeat this process for the rest of the simulation period (see Appendix F.2.1). The transport equations are solved using the Galerkin FEM with piecewise linear basis elements on a regular triangular mesh with 2.56×10^6 elements ($1,282,401$ nodes). The discrete and continuum cell model equations, with Γ given by (4.37c) and (4.55c) respectively, are solved using the same approach as when growth is independent of the nutrient distribution, with the average concentration in each cell, $c_{n+\frac{1}{2N}}$, in the discrete model calculated using (4.24) and the concentration interpolated from the FE mesh onto the cell model mesh in the continuum model (see Appendix F.2.2–F.2.3). The checks carried out to verify the accuracy of the numerical scheme are described in Appendix F.3.

4.9 Analytical solutions and numerical simulations

We now use the discrete cell model and its continuum approximation to simulate the growth of an aggregate of N cells for the different cell growth laws described above. First we consider the constant-rate and pressure-dependent growth laws (4.37a,b), verify for each that the continuum model closely approximates the discrete model for $N \gg 1$, and compare the growth dynamics predicted by each. We then test whether the continuum model provides a good approximation to the discrete model with the target-length-, pressure- and nutrient-dependent growth law (4.37c) for $N \gg 1$, and investigate the impact of the oxygen transport, pressure-sensitivity of the cells and initial cell conditions on the cell growth for this law. Finally, for the nutrient-dependent growth, we investigate whether the discrete and continuum solutions converge as the cell number increases and whether the continuum approximation breaks down for small N.

Rather than attempt to prescribe biophysically accurate initial conditions for the cell lengths and target lengths (*e.g.* with random variations between cells), we use simple illustrative initial conditions that satisfy the boundary conditions at the ends of the aggregate, $l = a$ at $n = 0, 1$. Unless otherwise stated, all simulation results are presented in dimensionless form.

As mentioned above, we assume that the elasticity and drag constants are identical for all cells, *i.e.* $\lambda_{n+\frac{1}{2N}} = \mu_{n+\frac{1}{2N}} = 1$ ($n = \frac{1}{N}, \ldots, 1 - \frac{1}{N}$) after nondimensionalisation. Under this assumption the equations for the cell pressures and velocities in the discrete model,

(4.27)–(4.30), simplify to

$$\alpha p_{n+\frac{1}{2N}} = a_{n+\frac{1}{2N}} - l_{n+\frac{1}{2N}}, \quad n = 0, \dots, 1 - \tfrac{1}{N}, \tag{4.99}$$

$$\frac{1}{6N}(u_{n-\frac{1}{N}} + 4u_n + u_{n+\frac{1}{N}}) = p_{n-\frac{1}{2N}} - p_{n+\frac{1}{2N}}, \quad n = \tfrac{1}{N}, \dots, 1 - \tfrac{1}{N} \tag{4.100}$$

$$\frac{1}{6N}(2u_0 + u_{\frac{1}{N}}) = -p_{\frac{1}{2N}}, \tag{4.101}$$

$$\frac{1}{6N}(u_{1-\frac{1}{N}} + 2u_1) = p_{1-\frac{1}{2N}}, \tag{4.102}$$

and those in the continuum approximation, (4.51) and (4.52), become

$$\alpha p = a - l, \tag{4.103}$$

$$u = -\frac{\partial p}{\partial n}; \tag{4.104}$$

all other model equations are unchanged.

4.9.1 Constant-rate growth, $\Gamma = 1$

4.9.1.1 Analytical solution

Discrete model

From the cell target length evolution equation (4.37a) we have that

$$a_{n+\frac{1}{2N}}(\tau) = a_{init}(n + \tfrac{1}{2N}) + \tau, \quad n = 0, \dots, 1 - \tfrac{1}{N}. \tag{4.105}$$

Subtracting equation (4.26) from (4.37a) and eliminating u, l and a using (4.99) and (4.100) we obtain

$$\frac{\alpha}{6N^2}\frac{\mathrm{d}}{\mathrm{d}\tau}\left(p_{n-\frac{1}{2N}} + 4p_{n+\frac{1}{2N}} + p_{n+\frac{3}{2N}}\right) = p_{n-\frac{1}{2N}} - 2p_{n+\frac{1}{2N}} + p_{n+\frac{3}{2N}} + \tfrac{1}{N^2}, \; n = 0, \dots, 1 - \tfrac{1}{N}, \tag{4.106}$$

$$\text{with} \quad p_{-\frac{1}{2N}} = p_{1+\frac{1}{2N}} = 0. \tag{4.107}$$

We solve (4.106)–(4.107) by seeking solutions of the form

$$p_{n+\frac{1}{2N}}(\tau) = p^{ss}_{n+\frac{1}{2N}} + q_{n+\frac{1}{2N}}(\tau),$$

where the steady state solution $p^{ss}_{n+\frac{1}{2N}}$ satisfies

$$0 = p^{ss}_{n-\frac{1}{2N}} - 2p^{ss}_{n+\frac{1}{2N}} + p^{ss}_{n+\frac{3}{2N}} + \tfrac{1}{N^2}, \tag{4.108}$$

$$\text{with} \quad p^{ss}_{-\frac{1}{2N}} = p^{ss}_{1+\frac{1}{2N}} = 0, \tag{4.109}$$

and $q_{n+\frac{1}{2N}}$ satisfies the homogeneous problem

$$\frac{\alpha}{6N^2}\frac{\mathrm{d}}{\mathrm{d}\tau}\left(q_{n-\frac{1}{2N}}+4q_{n+\frac{1}{2N}}+q_{n+\frac{3}{2N}}\right)=q_{n-\frac{1}{2N}}-2q_{n+\frac{1}{2N}}+q_{n+\frac{3}{2N}},\quad n=0,\dots,1-\tfrac{1}{N}, \tag{4.110}$$

$$\text{with}\quad q_{-\frac{1}{2N}}=0,\quad q_{1+\frac{1}{2N}}=0, \tag{4.111}$$

$$\text{and}\quad q_{n+\frac{1}{2N}}(0)=p_{init}(n+\tfrac{1}{2N})-p^{ss}_{n+\frac{1}{2N}}, \tag{4.112}$$

$$\text{where}\quad p_{init}(n+\tfrac{1}{2N})=\frac{1}{\alpha}\left[a_{init}(n+\tfrac{1}{2N})-N(x_{init}(n+\tfrac{1}{N})-x_{init}(n))\right].$$

Solving (4.108) subject to (4.109) gives

$$p^{ss}_{n+\frac{1}{2N}}=\frac{1}{2}\left(n+\tfrac{1}{2N}\right)\left(1-\left(n+\tfrac{1}{2N}\right)\right),$$

i.e. the steady state cell pressures are quadratic with respect to the cell index n.

If we seek a solution to (4.110) of the form $q_{n+\frac{1}{2N}}=\Re(A_k(\tau)e^{ik(n+\frac{1}{N})})$, where $0\le k\le 2N\pi$, and apply (4.111) we obtain

$$q_{n+\frac{1}{2N}}=\sum_{j=1}^{N}A_j e^{-\beta_j\tau/\alpha}\sin\left(\frac{j\pi(n+\frac{1}{N})}{1+\frac{1}{N}}\right),$$

where, by (4.112), the constants A_j $(j=1,\dots,N)$ satisfy

$$\sum_{j=1}^{N}A_j\sin\left(\frac{j\pi(n+\frac{1}{N})}{1+\frac{1}{N}}\right)=p_{init}(n+\tfrac{1}{2N})-\frac{1}{2}(n+\tfrac{1}{2N})(1-(n+\tfrac{1}{2N})),\quad n=0,\dots,1-\tfrac{1}{N}, \tag{4.113}$$

and the constants β_j are given by

$$\beta_j=\frac{6N^2(1-\cos\frac{j\pi}{N+1})}{2+\cos\frac{j\pi}{N+1}},\quad j=1,\dots,N. \tag{4.114}$$

Hence, the cell pressures are given by

$$p_{n+\frac{1}{2N}}=\frac{1}{2}(n+\tfrac{1}{2N})(1-(n+\tfrac{1}{2N}))+\sum_{j=1}^{N}A_j e^{-\beta_j\tau/\alpha}\sin\left(\frac{j\pi(n+\frac{1}{N})}{1+\frac{1}{N}}\right), \tag{4.115}$$

and the cell lengths by

$$l_{n+\frac{1}{2N}}=a_{init}(n+\tfrac{1}{2N})+\tau-\frac{\alpha}{2}(n+\tfrac{1}{2N})(1-(n+\tfrac{1}{2N}))+\sum_{j=1}^{N}A_j e^{-\beta_j\tau/\alpha}\sin\left(\frac{j\pi(n+\frac{1}{N})}{1+\frac{1}{N}}\right), \tag{4.116}$$

where $(A_j)_{j=1,\dots,N}=\left(\sin\left(\frac{ij\pi}{N+1}\right)\right)^{-1}_{i,j=1,\dots,N}\left(p_{init}(\frac{i}{N}-\frac{1}{2N})-\frac{1}{2}\frac{i}{N}(1-\frac{i}{N})\right)_{i=1,\dots,N}$. The terms in the sum in (4.115) decay to zero as $\tau\to\infty$, so the cell pressures approach the steady

state quadratic profile in the first term. The cell lengths and target lengths continue to grow linearly with time and for large τ the distribution of cell lengths behaves like

$$l_{n+\frac{1}{2N}} \sim a_{init}(n+\tfrac{1}{2N}) + \tau - \frac{\alpha}{2}(n+\tfrac{1}{2N})(1-(n+\tfrac{1}{2N})).$$

Continuum approximation

As for the discrete model, the cell target length increases linearly over time (see (4.53) and (4.55a)) so that

$$a(n,\tau) = a_{init}(n) + \tau. \tag{4.117}$$

Combining the equations for the continuum approximation in the same way as those for the discrete model (subtracting (4.50) from (4.53) and using (4.103) and (4.104) to eliminate u, l and a) we obtain an inhomogeneous diffusion equation for the cell pressure

$$\alpha\frac{\partial p}{\partial \tau} = \frac{\partial^2 p}{\partial n^2} + 1, \tag{4.118}$$

with boundary and initial conditions from (4.54), (4.56) and (4.57)

$$p = 0 \quad \text{at } n = 0, 1, \tag{4.119}$$

$$p(n,0) = p_{init}(n) := \frac{1}{\alpha}(a_{init}(n) - l_{init}(n)). \tag{4.120}$$

Seeking a solution as the sum of a steady state solution and the solution of the homogeneous problem yields

$$p = \tfrac{1}{2}n(1-n) + \sum_{j=1}^{\infty} A_j^{ctm} e^{-j^2\pi^2\tau/\alpha}\sin(j\pi n), \tag{4.121}$$

where the Fourier coefficients are given by

$$A_j^{ctm} = 2\int_0^1 \left(p_{init}(n) - \tfrac{1}{2}n(1-n)\right)\sin(j\pi n)\,\mathrm{d}n. \tag{4.122}$$

Then, (4.103) gives the continuum cell length as

$$l(n,\tau) = a_{init}(n) + \tau - \frac{\alpha}{2}n(1-n) - \alpha\sum_{j=1}^{\infty} A_j^{ctm} e^{-j^2\pi^2\tau/\alpha}\sin(j\pi n),$$

while (4.104) supplies the cell velocity as

$$u(n,\tau) = \left(n - \tfrac{1}{2}\right) - \sum_{j=1}^{\infty} A_j^{ctm} j\pi e^{-j^2\pi^2\tau/\alpha}\cos(j\pi n). \tag{4.123}$$

As for the discrete cell pressures, the terms in the Fourier series in (4.121) decay to zero at long times and the pressure approaches the quadratic steady state solution. Hence the cell velocity approaches a linear profile $u \sim n - \frac{1}{2}$ as $\tau \to \infty$. The behaviour of the cell length at long times is identical to that for the discrete model

$$l(n,\tau) \sim a_{init}(n) + \tau - \frac{\alpha}{2}n(1-n).$$

4.9.1.2 Comparison of discrete and continuum solutions

We simulate the growth of N cells subject to the following initial conditions

$$x_{init}(n) = n - \frac{1}{\pi}\cos(\pi n) - \frac{1}{2} \quad \Rightarrow \quad l_{init}(n+\tfrac{1}{2N}) = 1 + \sin(\pi(n+\tfrac{1}{2N})), \tag{4.124}$$

$$a_{init}(n+\tfrac{1}{2N}) = 1, \quad n = 0, \ldots, 1-\tfrac{1}{N}, \tag{4.125}$$

(so $l_{init} = 1 + \sin(\pi n)$, $a_{init} = 1$, $n \in (0,1)$ for the continuum approximation) for $N = 10$–150. With these initial conditions, all the cells have the same target lengths and are initially stretched relative to their target lengths—most in the centre of the aggregate (up to double their target length) and progressively less towards its ends (see Figure 4.3). We use this initial configuration to compare the dynamics for constant-rate and pressure-dependent growth and as a test case for our numerical code.

For the given initial cell lengths and target lengths, the initial cell pressure in the continuum case is given by $p_{init} = -\frac{1}{\alpha}\sin(\pi n)$ (corresponding to $p_{init}(n+\frac{1}{2N}) = -\frac{1}{\alpha}\sin(\pi(n+\frac{1}{2N}))$ in the discrete case), and we can find the Fourier coefficients in the continuum pressure solution exactly

$$\begin{aligned} A_j^{ctm} &= 2\int_0^1 (-\frac{1}{\alpha}\sin(\pi n) - \frac{1}{2}n(1-n))\sin(j\pi n)\,\mathrm{d}n \\ &= \begin{cases} -\frac{1}{\alpha} - \frac{4}{\pi^3} & \text{if } j = 1, \\ -\frac{4}{(2k+1)^3\pi^3} & \text{if } j = 2k+1,\ k \in \mathbb{N}, \\ 0 & \text{if } j = 2k,\ k \in \mathbb{N}, \end{cases} \end{aligned} \tag{4.126}$$

Hence, the continuum cell pressure, length, target length and velocity are given by

$$\begin{aligned} p &= \frac{1}{2}n(1-n) - \left(\tfrac{1}{\alpha} + \tfrac{4}{\pi^3}\right)e^{-\pi^2\tau/\alpha}\sin(\pi n) - \sum_{k=1}^{\infty} \tfrac{4}{(2k+1)^3\pi^3} e^{-(2k+1)^2\pi^2\tau/\alpha}\sin((2k+1)\pi n), \\ l &= 1 + \tau - \tfrac{\alpha}{2}n(1-n) + \left(1 + \tfrac{4\alpha}{\pi^3}\right)e^{-\pi^2\tau/\alpha}\sin(\pi n) \\ &\qquad + \sum_{k=1}^{\infty} \tfrac{4\alpha}{(2k+1)^3\pi^3} e^{-(2k+1)^2\pi^2\tau/\alpha}\sin((2k+1)\pi n), \\ a &= 1 + \tau, \\ u &= n - \frac{1}{2} + \left(\tfrac{\pi}{\alpha} + \tfrac{4}{\pi^2}\right)e^{-\pi^2\tau/\alpha}\cos(\pi n) + \sum_{k=1}^{\infty} \tfrac{4}{(2k+1)^3\pi^3} e^{-(2k+1)^2\pi^2\tau/\alpha}\cos((2k+1)\pi n). \end{aligned} \tag{4.127}$$

Figure 4.2 shows for $N = 20$ cells and the chosen initial conditions how the positions of the cell vertices, $x_n(\tau)$, change over the course of the simulation. Figure 4.3 shows the evolution of the discrete cell lengths, target lengths, pressures and vertex velocities (shown by crosses) in spatial coordinates (x,t) along with the numerical solutions of the continuum model (shown by solid lines) and the analytical solutions of the discrete and

continuum models (shown by circles and dashed lines respectively). The discrete and continuum solutions agree very closely throughout the course of the simulation, showing that the continuum model provides an excellent approximation to the discrete model for N as small as 20. In addition, the numerical and analytical solutions for the continuum model are indistinguishable at the scale shown, confirming the accuracy of our numerical scheme.

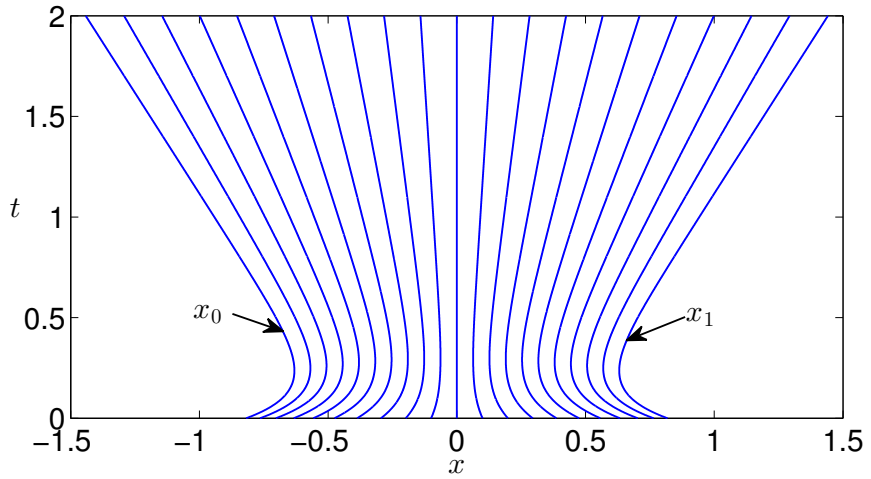

Figure 4.2: Evolution of the dimensionless cell vertex positions x_n $(n = 0, \ldots, 1)$ for constant growth, $\Gamma = 1$, of an aggregate of $N = 20$ cells. Initial conditions: $x_{init}(n) = n - \frac{1}{\pi}\cos(\pi n) - \frac{1}{2}$, $a_{init}(n + \frac{1}{2N}) = 1$ $(n = 0, \ldots, 1 - \frac{1}{N})$. Parameter values: $\alpha = 1.4$, $\Delta n = 10^{-3}$, $\Delta\tau = 10^{-4}$.

Initially the cell lengths decrease towards the target lengths, most rapidly in the middle of the aggregate where the cells are most stretched, and the cell pressures decrease towards zero, while the cell target lengths steadily increase. The relaxation of the cells happens on a faster time scale than the growth of the cell target lengths, but eventually the target lengths exceed the cell lengths, and the cells become compressed ($p > 0$). The cells then start to relax from compression (their lengths stop decreasing and start to increase). As time progresses, the cell lengths continue to increase due to the constant increase in the target lengths and the aggregate expands symmetrically about its centre. The cell pressures approach the non-uniform steady state values $p^{ss}_{n+\frac{1}{2N}} = \frac{1}{2}(n + \frac{1}{2N})(1 - (n + \frac{1}{2N}))$ in cell-index coordinates (n, τ) (so in spatial coordinates the pressure distribution approaches a fixed magnitude and then spreads as the cells grow as shown in Figure 4.3). Hence the cell vertex velocities approach an approximately linear profile in x (corresponding to the linear profile $u = n - \frac{1}{2}$ in cell index coordinates).

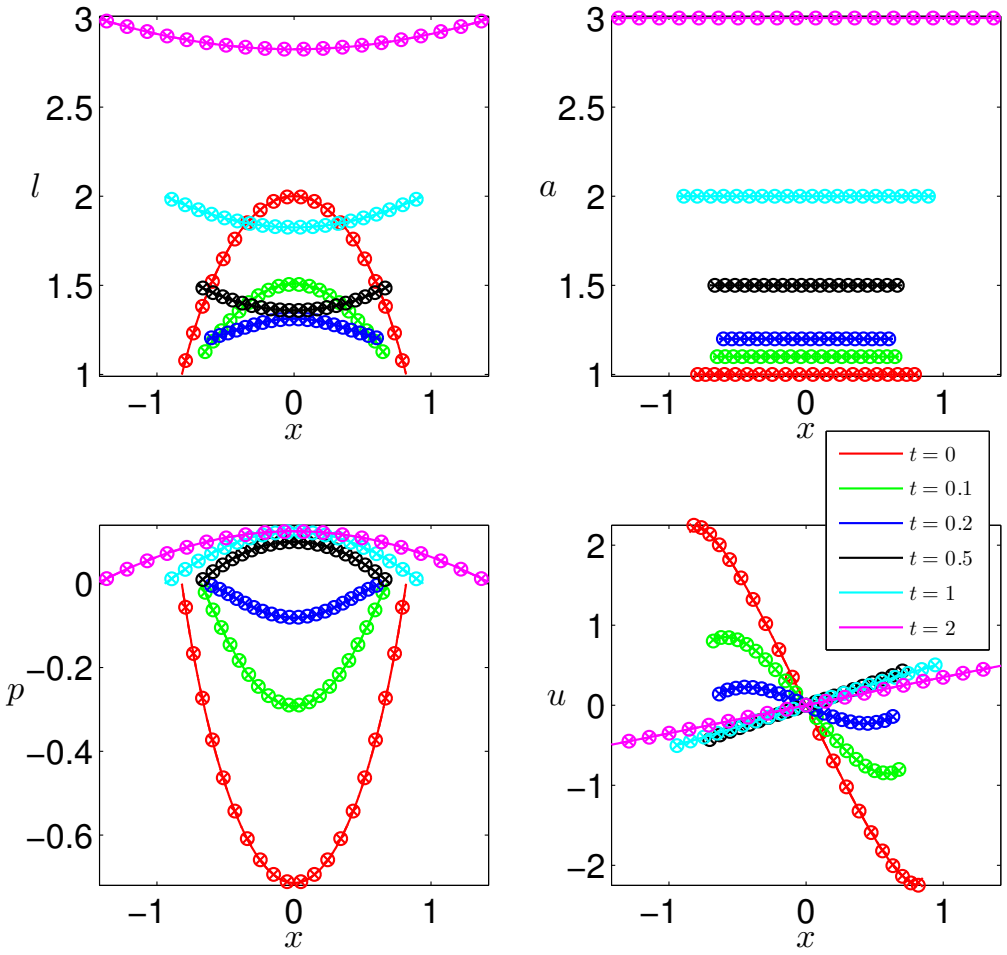

Figure 4.3: Evolution of the dimensionless cell lengths l, target lengths a, pressures p and vertex velocities u in spatial coordinates (x,t) for the constant growth in Figure 4.2. Crosses and circles show numerical and analytical solutions of the discrete model respectively, solid lines and dashed lines show numerical and analytical solutions of the continuum model respectively (indistinguishable from each other at scale shown).

4.9.1.3 Convergence of the discrete and continuum solutions

We define the error in the continuum approximation as the maximum absolute difference between the discrete cell lengths and continuum cell length at the cell centres over the course of the simulation,

$$E_l := \max_{n\in\{0,\dots,1-\frac{1}{N}\},\,\tau\in[0,T]} \left| l_{n+\frac{1}{2N}}(\tau) - l(n+\tfrac{1}{2N},\tau) \right|. \tag{4.128}$$

It is clear from Figure 4.4(a), which shows how E_l varies with the cell number N, that the discrete solution converges to the continuum solution as $N\to\infty$, the difference between the

solutions being $\mathcal{O}(1/N^2)$ as expected (since the gradient of the log-log plot of the analytical error is -2). Thus, the error in the continuum approximation is small, even for relatively small cell numbers; for $N > 20$ the error is less than 0.1%. Figure 4.4(a) also shows that the numerical solutions for the discrete and continuum models show the expected convergence behaviour.

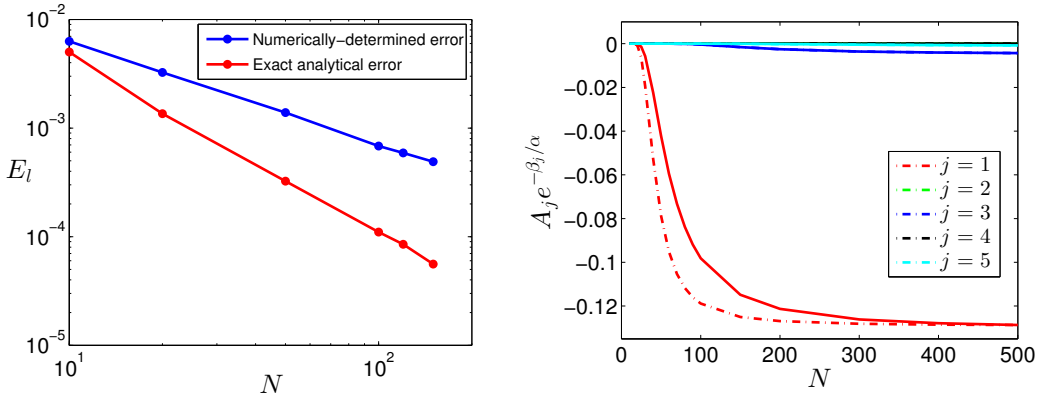

(a) **(b)**

Figure 4.4: Convergence of the discrete and continuum solutions for constant-rate growth as the cell number N increases. (a) Convergence of the discrete and continuum cell lengths in terms of E_l, their maximum absolute difference over the course of the simulation (see (4.128)). (b) Convergence of the terms in the discrete pressure solution, $A_j e^{-\beta_j \tau/\alpha}$ (dashed lines), to the Fourier terms in the continuum pressure solution, $A_j^{ctm} e^{-j^2\pi^2\tau/\alpha}$ (solid lines), at $\tau = 1$ ($j = 1, \ldots, 5$). Initial conditions and parameter values as in Figure 4.2 with $\alpha = 3.5 \times 10^{-3} N^2$.

We can examine the convergence of the discrete solution to the continuum solution in more detail using the analytical solutions for the cell pressure, (4.115) and (4.121), and the numerical solution from §4.9.1.2. The terms in the sum in the discrete pressure solution (4.115) decrease rapidly in magnitude as j increases and approach the terms in the Fourier series in the continuum pressure solution (4.121) as $N \to \infty$ (Figure 4.4(b)). Thus, we have that

$$p_{n+\frac{1}{2N}} = \frac{1}{2}(n+\tfrac{1}{2N})(1-(n+\tfrac{1}{2N})) + \sum_{j=1}^{N} A_j \exp\left(-\frac{6N^2(1-\cos\frac{j\pi}{N+1})}{\alpha(2+\cos\frac{j\pi}{N+1})}\tau\right)\sin\left(\frac{j\pi(n+\frac{1}{N})}{1+\frac{1}{N}}\right)$$

$$\to \frac{1}{2}n(1-n) + \sum_{j=1}^{\infty} A_j^{ctm} e^{-j^2\pi^2\tau/\alpha}\sin(j\pi n) = p \quad \text{as } N \to \infty.$$

4.9.2 Pressure-dependent growth, $\Gamma = -p$

4.9.2.1 Analytical solution

Discrete model

Combining the ODEs for the cell lengths and cell target lengths, (4.26) and (4.37b), as in §4.9.1 yields

$$\begin{aligned}&\frac{\alpha}{6N^2}\frac{\mathrm{d}}{\mathrm{d}\tau}\left(p_{n-\frac{1}{2N}} + 4p_{n+\frac{1}{2N}} + p_{n+\frac{3}{2N}}\right)\\ &\qquad = \left(1-\tfrac{1}{6N^2}\right)p_{n-\frac{1}{2N}} - 2\left(1+\tfrac{1}{3N^2}\right)p_{n+\frac{1}{2N}} + \left(1-\tfrac{1}{6N^2}\right)p_{n+\frac{3}{2N}}, \quad n = 0,\dots,1-\tfrac{1}{N},\\ &\text{with} \quad p_{-\frac{1}{2N}} = p_{1+\frac{1}{2N}} = 0.\end{aligned}$$

Seeking a solution of the form $p_{n+\frac{1}{2N}} = \Re(A_k(\tau)e^{ik(n+\frac{1}{N})})$, we obtain

$$p_{n+\frac{1}{2N}} = \sum_{j=1}^{N} B_j e^{-(1+\beta_j)\tau/\alpha}\sin\left(\frac{j\pi(n+\frac{1}{N})}{1+\frac{1}{N}}\right), \tag{4.129}$$

where the constants B_j $(j = 1,\dots,N)$ satisfy

$$\sum_{j=1}^{N} B_j \sin\left(\frac{j\pi(n+\frac{1}{N})}{1+\frac{1}{N}}\right) = p_{init}(n+\tfrac{1}{2N}), \quad n = 0,\dots,1-\tfrac{1}{N}, \tag{4.130}$$

so that $(B_j)_{j=1,\dots,N} = \left(\sin\left(\frac{ij\pi}{N+1}\right)\right)^{-1}_{i,j=1,\dots,N}(p_{init}(\frac{i}{N}-\frac{1}{2N}))_{i=1,\dots,N}$, and β_j are given by (4.114).

The cell target lengths are obtained by integrating the evolution equations

$$\begin{aligned}&\frac{\mathrm{d}a_{n+\frac{1}{2N}}}{\mathrm{d}\tau} = -p_{n+\frac{1}{2N}}, \quad n = 0,\dots,1-\tfrac{1}{N},\\ \Rightarrow\quad &a_{n+\frac{1}{2N}} = a^{ss}_{n+\frac{1}{2N}} + \sum_{j=1}^{N}\frac{\alpha}{1+\beta_j}B_j e^{-(1+\beta_j)\tau/\alpha}\sin\left(\frac{j\pi(n+\frac{1}{N})}{1+\frac{1}{N}}\right),\end{aligned} \tag{4.131}$$

where the steady state cell target lengths, $a^{ss}_{n+\frac{1}{2N}}$, are given by

$$a^{ss}_{n+\frac{1}{2N}} = a_{init}(n+\tfrac{1}{2N}) - \sum_{j=1}^{N}\frac{\alpha}{1+\beta_j}B_j\sin\left(\frac{j\pi(n+\frac{1}{N})}{1+\frac{1}{N}}\right). \tag{4.132}$$

From (4.99), the cell lengths are given by

$$l_{n+\frac{1}{2N}} = a^{ss}_{n+\frac{1}{2N}} - \sum_{j=1}^{N}\frac{\alpha\beta_j}{1+\beta_j}B_j e^{-(1+\beta_j)\tau/\alpha}\sin\left(\frac{j\pi(n+\frac{1}{N})}{1+\frac{1}{N}}\right). \tag{4.133}$$

As $\tau\to\infty$, the terms in the sums in (4.129), (4.131) and (4.133) decay to zero, so that the cell pressures approach zero and the cell lengths and target lengths converge to the

non-uniform steady state $a^{ss}_{n+\frac{1}{2N}}$ given by (4.132) (which depends on the initial cell target lengths $a_{init}(n+\frac{1}{2N})$).

Continuum approximation

By combining the continuum equations in the same way as for the constant-rate growth, we find that p satisfies the following reaction-diffusion equation

$$\alpha\frac{\partial p}{\partial \tau} = \frac{\partial^2 p}{\partial n^2} - p,$$

with the boundary and initial conditions (4.119) and (4.120). This has the Fourier series solution

$$p = \sum_{j=1}^{\infty} B_j^{ctm} e^{-(1+j^2\pi^2)\tau/\alpha}\sin(j\pi n), \tag{4.134}$$

where

$$B_j^{ctm} = 2\int_0^1 p_{init}(n)\sin(j\pi n)\,\mathrm{d}n.$$

Substituting this into the evolution equation for a and integrating gives

$$a(n,\tau) = a^{ss}(n) + \sum_{j=1}^{\infty}\frac{\alpha}{1+j^2\pi^2}B_j^{ctm}e^{-(1+j^2\pi^2)\tau/\alpha}\sin(j\pi n),$$

where the steady state solution, a^{ss}, is given by

$$a^{ss}(n) = a_{init}(n) - \sum_{j=1}^{\infty}\frac{\alpha}{1+j^2\pi^2}B_j^{ctm}\sin(j\pi n);$$

and (4.103) gives

$$l(n,\tau) = a^{ss}(n) - \sum_{j=1}^{\infty}\frac{\alpha j^2\pi^2}{1+j^2\pi^2}B_j^{ctm}e^{-(1+j^2\pi^2)\tau/\alpha}\sin(j\pi n).$$

The long time behaviour of the continuum solution is thus identical to that of the discrete solution:

$$l, a \to a^{ss}(n), \quad p \to 0 \quad \text{as } \tau\to\infty.$$

4.9.2.2 Comparison of discrete and continuum solutions

We simulate the growth of N cells for $N = 10$–150 using the same initial conditions as for the constant-rate growth (equations (4.124)–(4.125)), so $p_{init} = -\frac{1}{\alpha}\sin(\pi n)$ and the Fourier coefficients for the continuum solution (4.134) are

$$B_j^{ctm} = -2\int_0^1 \frac{1}{\alpha}\sin(\pi n)\sin(j\pi n)\,\mathrm{d}n = \begin{cases} -\frac{1}{\alpha} & \text{if } j=1,\\ 0 & \text{otherwise.}\end{cases}$$

Thus the continuum cell pressure, target length and length are given by

$$\begin{aligned} p &= -\frac{1}{\alpha} e^{-(1+\pi^2)\tau/\alpha} \sin(\pi n), \\ a &= a^{ss}(n) - \frac{1}{1+\pi^2} e^{-(1+\pi^2)\tau/\alpha} \sin(\pi n), \\ l &= a^{ss}(n) + \frac{\pi^2}{1+\pi^2} e^{-(1+\pi^2)\tau/\alpha} \sin(\pi n), \\ \text{where} \quad a^{ss}(n) &= 1 + \frac{1}{1+\pi^2} \sin(\pi n). \end{aligned}$$

Figures 4.5 and 4.6 show that for these initial conditions the cells shorten towards their target lengths—fastest in the middle of the aggregate where they are initially most stretched, and less rapidly towards its ends—so that the aggregate contracts symmetrically about its centre. As the cells shorten, their target lengths increase, since the cells are under tension ($p < 0$). As the cell and target lengths converge, the cell pressures approach zero and the growth of the target lengths slows, so that the system approaches the equilibrium

$$l = a = a^{ss}(n), \quad p = 0.$$

As for the case of constant growth, the discrete and continuum solutions are in good agreement.

4.9.2.3 Convergence of the discrete and continuum solutions

As for the constant-elongation-rate case, the solution of the discrete model converges to that of the continuum model as $N \to \infty$, and the difference between the two solutions for the

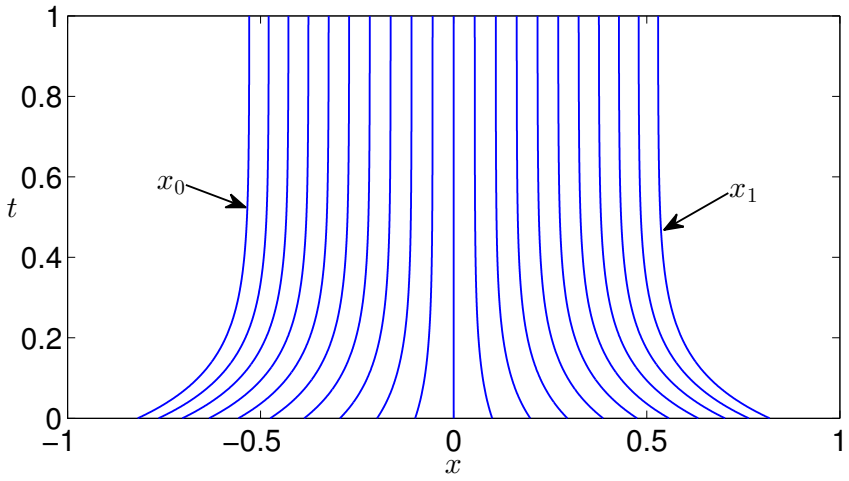

Figure 4.5: Evolution of the cell vertex positions x_n ($n = 0, \ldots, 1$) for pressure-dependent growth, $\Gamma = -p_{n+\frac{1}{2N}}$, of an aggregate of $N = 20$ cells. Initial conditions and parameter values as in Figure 4.2.

cell length scales like $1/N^2$ (Figure 4.7). The convergence of the discrete to the continuum solution can also be shown via the analytical and numerical solutions as in §4.9.1.3.

4.9.3 Comparison of constant-rate growth and pressure-dependent growth

A major issue with assuming that the cell target lengths increase at a constant rate, as in Fozard *et al.*'s model, is that the cells grow without bound regardless of their initial and target lengths. Without a model for cell division this is unrealistic (unless we focus on the continuum model and take the continued growth to represent the macroscopic volume increase generated by cell growth and division combined). With a constant rate of growth, the cells never reach equilibrium, because the continual increase in their target lengths

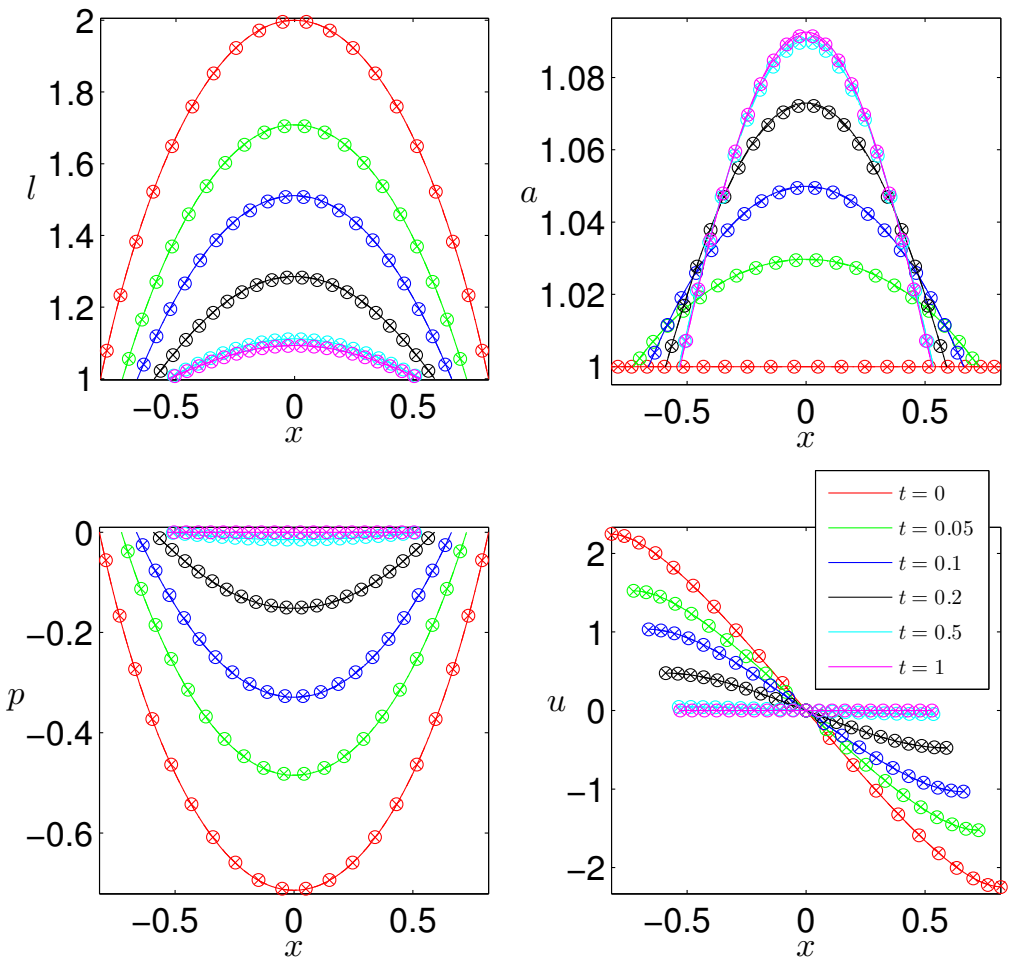

Figure 4.6: Evolution of the cell lengths l, target lengths a, pressures p and vertex velocities u for the pressure-dependent growth in Figure 4.5. Markers and lines show discrete and continuum solutions respectively, as in Figure 4.3.

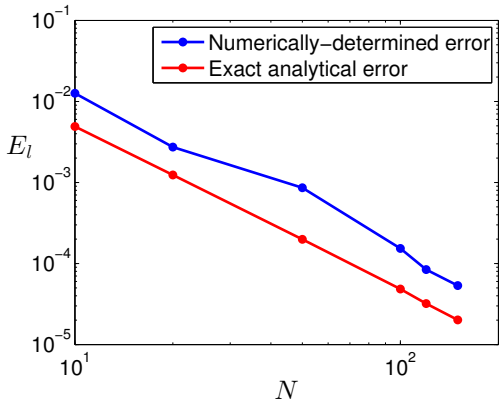

Figure 4.7: Convergence of the discrete and continuum solutions for the cell lengths for pressure-dependent growth as N increases. E_l as defined in (4.128). Initial conditions and other parameter values as in Figure 4.4.

means that they are always compressed ($l_{n+\frac{1}{2N}} < a_{n+\frac{1}{2N}}$). With pressure-dependent growth, however, the relaxation of cells towards their target lengths is accompanied by a slow increase (if the cells are under tension, $p < 0$), or decrease (if the cells are compressed, $p > 0$), in the target lengths. The system evolves towards a steady state that depends on the initial conditions, where the cell pressures are all zero and the cell lengths and target lengths are equal for each cell but vary between cells. This history-dependence and growth toward equilibrium mean that a pressure-dependent growth law such as (4.37b) is more suitable for modelling growth that does not continue indefinitely.

4.9.4 Target-length-, pressure- and nutrient-dependent growth

Having considered growth laws that depend only on the cell variables, we now suppose that growth depends on the local oxygen concentration according to (4.37c). In this case it is not possible to construct exact analytical solutions for the cell model equations, but in certain limits approximate solutions may be derived (see §4.9.4.6). Hence we now investigate how the oxygen requirements and mechanosensitivity of the cells affects their growth via numerical simulations. For this purpose we use parameter values from §4.7 corresponding to different cell types, such as fast-growing cells with high oxygen uptake rates like hepatocytes and slower growing cells with lower uptake rates like epithelial cells.

4.9.4.1 Sensitivity of growth to oxygen uptake

We simulate the growth of $N = 20$ cells using the initial conditions from §§4.9.1–4.9.2 (for which all the cells are stretched) and the parameter values for hepatocytes stated in Table 4.4 for oxygen uptake fluxes in the range $\tilde{M} \in [10^{-8}, 10^{-5}]\,\mathrm{mol\,m^{-2}\,s^{-1}}$ (Da $\in [2.9 \times 10^{-3}, 2.9]$).

Figure 4.8(a) shows how the length of the aggregate, L_{agg}, evolves for different values of the uptake flux for the discrete and continuum models, and Figure 4.8(b) shows how the total change in the aggregate length over the course of the simulation (100 hrs), ΔL_{agg}, varies with the uptake flux. Both figures reveal that the discrepancy between the discrete and continuum models is small for the uptake flux range considered. In all cases, the aggregate initially shortens as the cells relax from being stretched, and then grows as the cells elongate towards their maximum target length (Figure 4.8(a)). For uptake values in the reported range for hepatocytes, $\tilde{M} \in [9.22 \times 10^{-9}, 2.67 \times 10^{-7}]\text{mol}\,\text{m}^{-2}\,\text{s}^{-1}$ (Da $\in [2.7 \times 10^{-3}, 0.077]$), there is little change in the growth of the aggregate as the uptake increases (Figure 4.8(b)), since the oxygen concentration remains much higher than the half-maximal uptake concentration, $k_g = 0.043$, (so $c/(k_g + c) \sim 1$ on $y = 0$, $x \in [x_0, x_1]$). However, for larger uptake fluxes (Da > 1), the rate of uptake exceeds that at which oxygen is supplied through diffusion, so the concentration around the aggregate is much lower and the aggregate grows more slowly. Indeed for Da > 1, the aggregate growth decreases more quickly as the uptake flux increases than for Da < 1, and for Da > 2.4 the aggregate does not regain its original length after 100 hrs in culture (Figure 4.8(b)).

We can examine the differences in the cell growth for low and high uptake and the agreement between the discrete and continuum models in more detail by looking at the

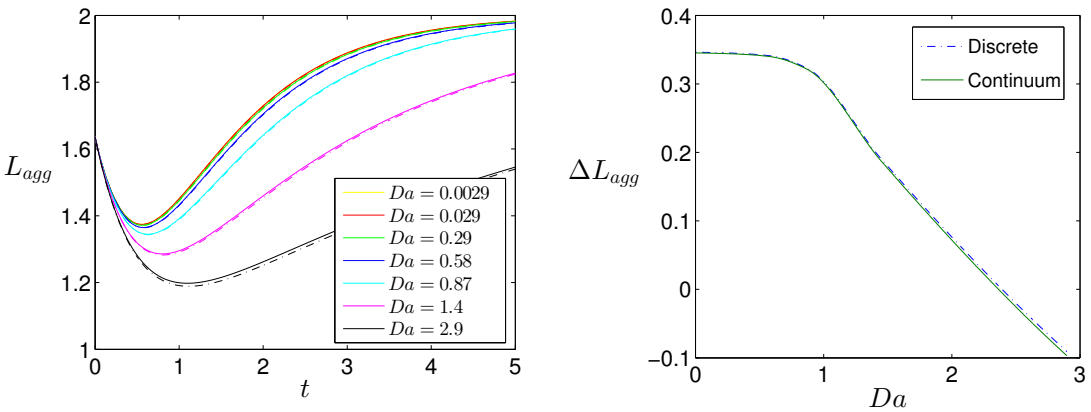

Figure 4.8: Variation in aggregate growth with oxygen uptake for target-length-, pressure- and oxygen-dependent growth. (a) Evolution of the aggregate length, $L_{agg}(t) := x_1(t) - x_0(t)$, for different uptake fluxes, Da $= 2.9 \times 10^{-3} - 2.9$ ($\tilde{M} = 1.0 \times 10^{-8} - 1.0 \times 10^{-5}\,\text{mol}\,\text{m}^{-2}\,\text{s}^{-1}$). Dotted lines correspond to discrete solutions, solid lines correspond to continuum solutions. (b) Variation in the overall aggregate growth, $\Delta L_{agg} = L_{agg}(T) - L_{agg}(0)$, with the uptake flux. Initial conditions as in Figure 4.2. Parameter values (corresponding to hepatocytes): $N = 20$, $T = 5$, $c_{1/2} = 0.027$, $\alpha = 5$, $a_{max} = 2$, $k_g = 0.043$, $p_s = -0.1$, $p_c = 0.1$.

evolution of the cell variables and oxygen concentration along the aggregate over the course of the simulation. From Figures 4.9 and 4.10, which show the evolution for low oxygen uptake (Da $= 8 \times 10^{-3}$) and very high uptake (Da $= 2.9$) respectively, we can see that the differences in the growth are considerable. For both uptake levels, the cells initially relax towards their target lengths and the target lengths grow only at the ends of the aggregate where the cell pressures are between $p_s = -0.1$ and $p_c = 0.1$ ($p_s^* = -2\,\mathrm{nN\,\mu m^{-1}}$, $p_c^* = 2\,\mathrm{nN\,\mu m^{-1}}$) (see Figures 4.9(a)–(c) and 4.10(a)–(c)). Once the cells have relaxed sufficiently for the cell pressures to fall within the range $[p_s, p_c]$ over the whole of the aggregate (by $t = 0.4$), the cell target lengths in the middle of the aggregate also increase. For the low uptake rate, $c \approx 1$ over the whole of the aggregate (Figure 4.9(e)) throughout the simulation, so the uptake has little effect on the target length growth. All the target lengths grow towards $a_{max} = 2$, and the target lengths and cell lengths in the middle of the aggregate approach those at the ends as time progresses. For the high uptake rate, however, the concentration over the aggregate is very low and constant except at its ends, where it increases sharply (Figure 4.10(e)), and it remains this way as the cells grow. Hence, the cells in the middle of the aggregate grow very slowly even after their pressures fall within $[p_s, p_c]$, while those at the end of the aggregate grow almost as quickly as with the low uptake rate (Figure 4.10(b)).

The solutions of the discrete and continuum models agree closely for the low and high oxygen uptake simulations, the maximum absolute difference in any of the cell variables in either simulation being approximately 5×10^{-3} (in the cell velocity for the low uptake) and that in the concentration being 1×10^{-3} (for the high uptake). The continuum approximation starts to break down for $N < 10$, when the maximum difference between the continuum and discrete cell velocities in the low uptake simulation exceeds 4%.

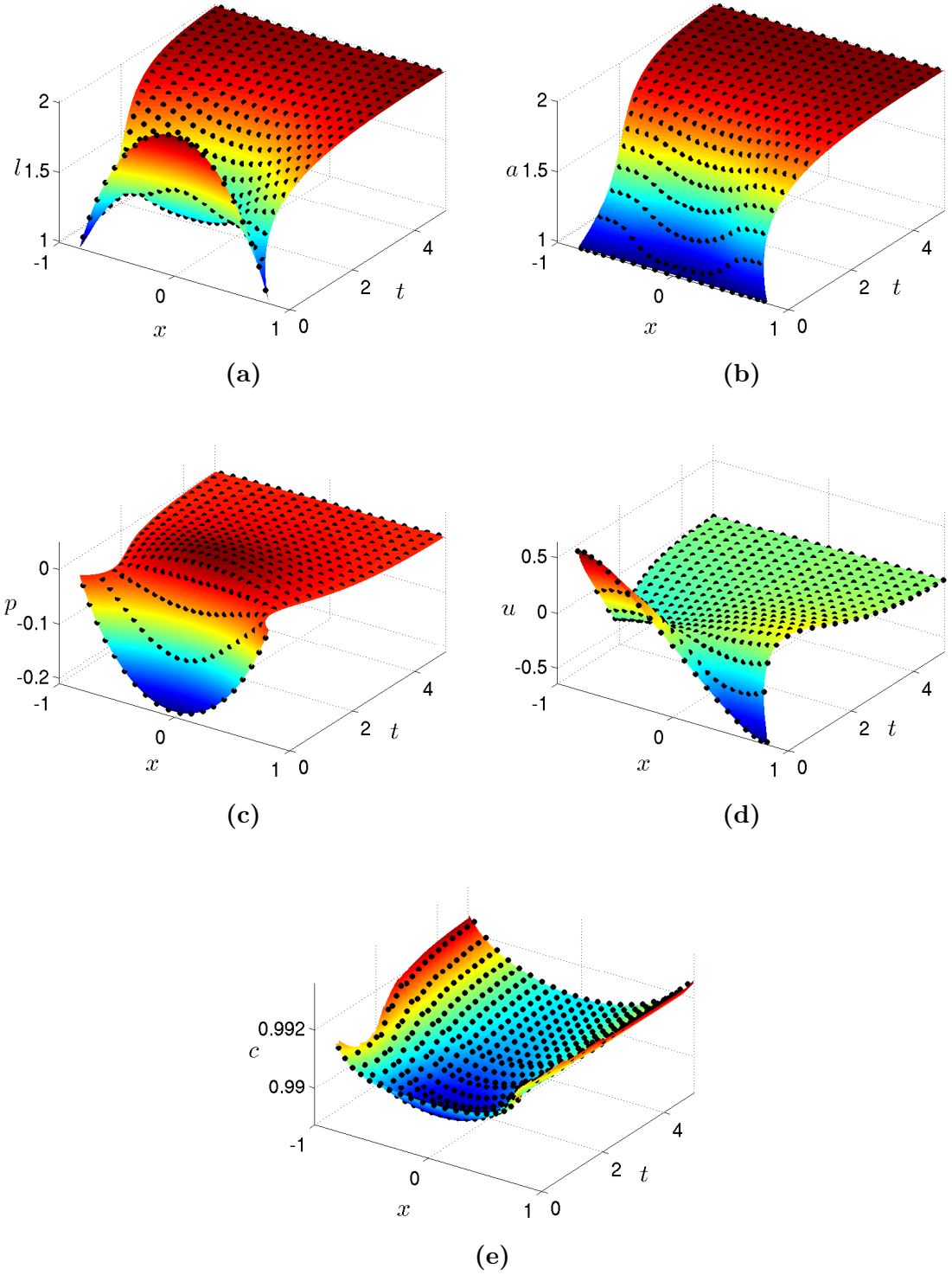

Figure 4.9: Evolution of (a) the cell lengths, (b) the cell target lengths, (c) the cell pressures, (d) the cell velocities, and (e) the oxygen concentration over the aggregate for the discrete and continuum models for the aggregate growth in Figure 4.8 with low oxygen uptake. Black dots show the solutions of the discrete model, coloured surfaces the solutions of the continuum model. Oxygen uptake, $\mathrm{Da} = 8 \times 10^{-3}$ ($\tilde{M} = 2.77 \times 10^{-8}\,\mathrm{mol\,m^{-2}\,s^{-1}}$).

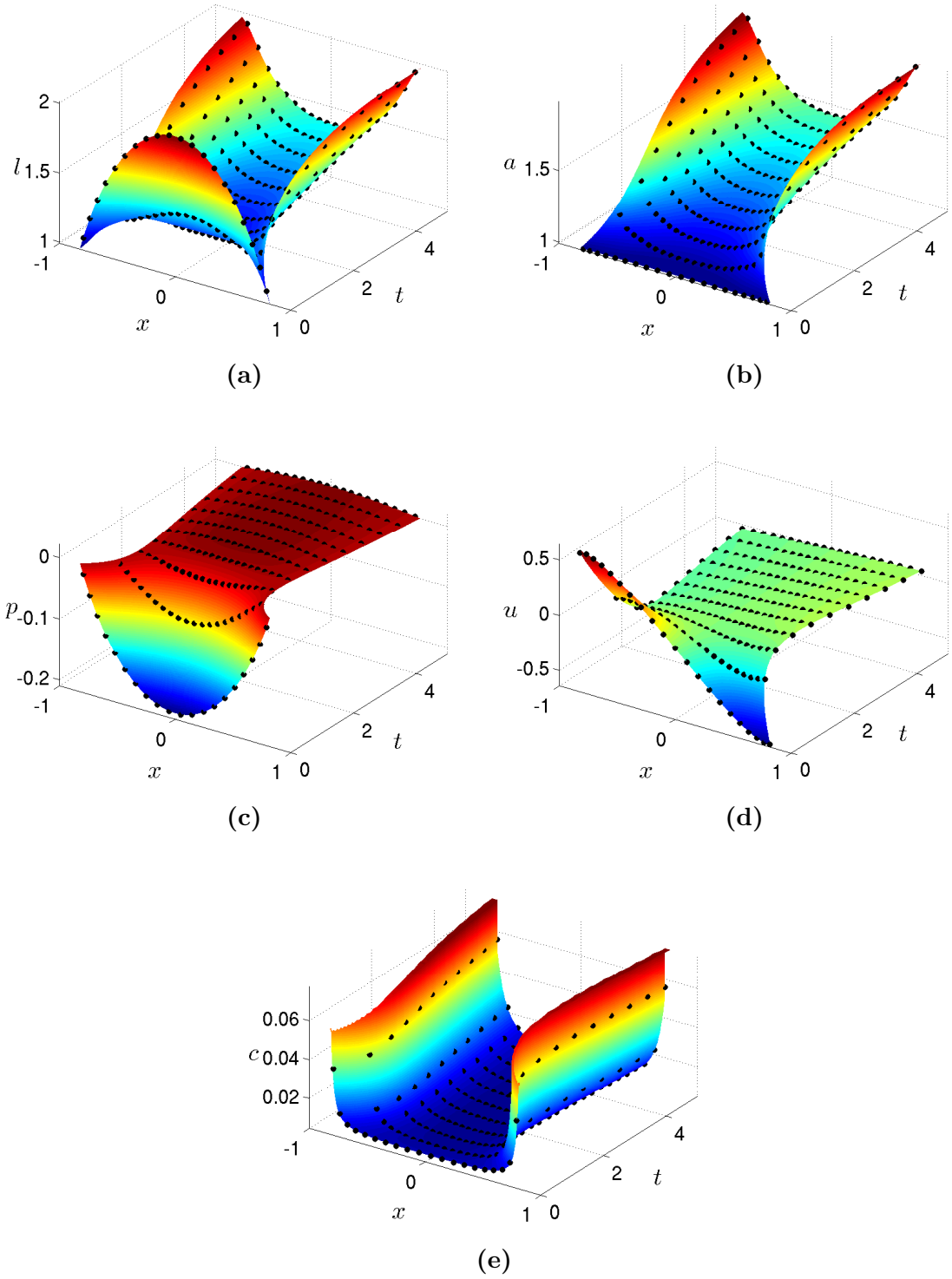

Figure 4.10: Evolution of the cell variables ((a)–(d)) and the oxygen concentration over the aggregate ((e)) for the discrete and continuum models for the aggregate growth in Figure 4.8 with high oxygen uptake. Oxygen uptake, Da $= 2.9$ ($\tilde{M} = 1.0 \times 10^{-5}\,\mathrm{mol\,m^{-2}\,s^{-1}}$).

4.9.4.2 Impact of limited oxygen supply on growth

As shown in Figure 4.11, the oxygen concentration at the surface of the bath, C^* (dimensionally), can have a major effect on the cell growth if the cells have high oxygen demands. For cells with an uptake flux of $\tilde{M} = 2.0 \times 10^{-6}\,\mathrm{mol\,m^{-2}\,s^{-1}}$ that are initially all stretched (as in Figure 4.2), the overall aggregate growth ΔL_{agg} decreases as the surface concentration falls. For $C^* < 0.06\,\mathrm{mol\,m^{-3}}$, after the cells initially relax, the aggregate fails to grow back to its original length 100 hrs after the start of the simulation (Figure 4.11(b)). The rate of aggregate growth continues to decrease as the surface concentration decreases, so that with a 50-fold decrease from $C^* = 0.23\,\mathrm{mol\,m^{-3}}$ to $C^* = 4.6 \times 10^{-3}\,\mathrm{mol\,m^{-3}}$ there is very little growth (Figure 4.11(a)). As for changes in the oxygen uptake in §4.9.4.1, the solutions of the discrete and continuum models show excellent agreement over the whole range of surface concentrations.

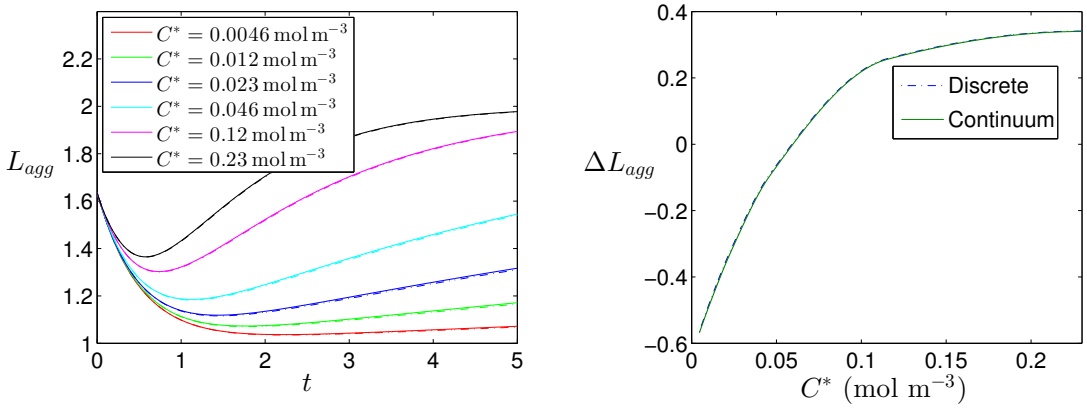

Figure 4.11: Variation in the aggregate growth with the oxygen concentration at the surface of the nutrient bath. (a) Evolution of the aggregate length $L_{agg}(t)$ for different surface concentrations, $C^* = 4.6 \times 10^{-3} - 0.23\,\mathrm{mol\,m^{-3}}$. Dotted lines show discrete solutions, solid lines show continuum solutions. (b) Variation in the overall aggregate growth ΔL_{agg} with the surface concentration. Initial conditions as in Figure 4.2. Parameter values (corresponding to hepatocytes): $N = 20$, $\mathrm{Da} = 0.13/C^*$ ($M^* = 2.0 \times 10^{-6}\,\mathrm{mol\,m^{-2}\,s^{-1}}$), $c_{1/2} = 6.4 \times 10^{-3}/C^*$, $\alpha = 5$, $a_{max} = 2$, $k_g = 0.043$, $p_s = -0.1$, $p_c = 0.1$.

4.9.4.3 Sensitivity of growth to half-maximal growth rate concentration k_g

In the absence of estimates for the half-maximal growth rate concentration k_g, we determine the sensitivity of the aggregate growth to k_g via simulation. The variation in aggregate growth for 20 hepatocytes with a high uptake rate ($\mathrm{Da} = 0.58$) for $k_g \in [4.3 \times 10^{-3}, 0.43]$ ($K_g \in [0.001, 0.1]\,\mathrm{mol\,m^{-3}}$) is shown in Figure 4.12. Although the aggregate growth appears qualitatively similar across the range of k_g values (Figure 4.12(a)), there is a significant

decrease in the net growth as k_g increases (Figure 4.12(b)). This is because $c(x,0,t) \sim k_g$ ($x \in [x_0, x_1]$) at higher values of k_g for a high uptake rate, so there is a discernible decrease in the Monod growth rate $c/(k_g + c)$ as k_g increases. We note, however, that k_g has a much smaller effect on the growth for lower uptake rates.

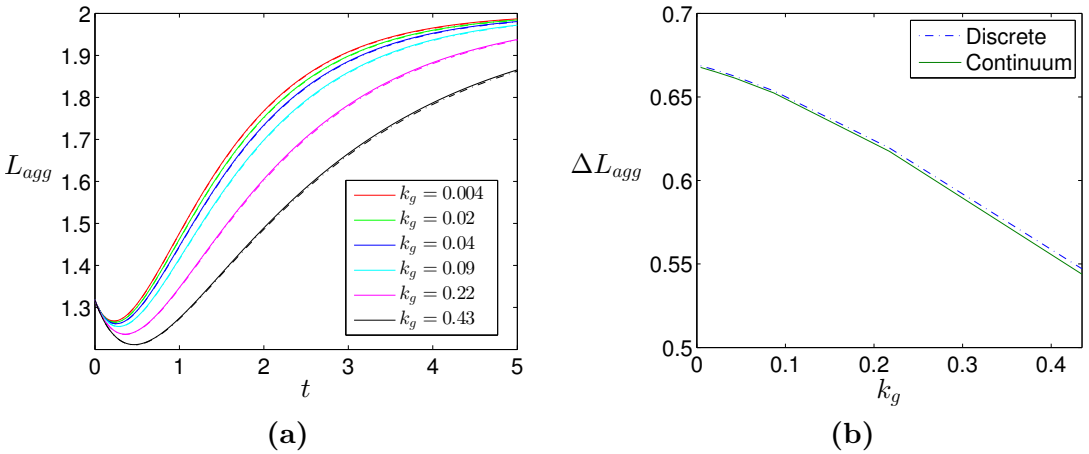

Figure 4.12: Variation in the aggregate growth with the half-maximal growth rate concentration k_g for high oxygen uptake flux. (a) Evolution of the aggregate length L_{agg} for different values of k_g. (b) Variation in the overall aggregate growth ΔL_{agg} with k_g. Initial conditions: $l_{n+\frac{1}{2N}} = 1 + \frac{1}{2}\sin(\pi(n+\frac{1}{2N}))$, $a_{n+\frac{1}{2N}} = 1$ $(n = 0, \ldots, 1 - \frac{1}{N})$. Oxygen uptake, Da $= 0.58$. Other parameter values as in Figure 4.8.

4.9.4.4 Impact of initial conditions on growth

To investigate the effect that the initial conditions have on the cell growth we simulate the growth of 20 cells for two choices of the initial set of cell lengths: one in which all the cells are stretched,

$$l_{init}(n+\tfrac{1}{2N}) = 1 + \frac{1}{2}\sin(\pi(n+\tfrac{1}{2N})), \quad a_{init}(n+\tfrac{1}{2N}) = 1, \quad n = 0, \ldots, 1-\tfrac{1}{N}, \tag{4.135}$$

and one in which the cells in the left half of the aggregate ($0 < n < 1/2$) are stretched and those in the right half ($1/2 < n < 1$) are compressed,

$$l_{init}(n+\tfrac{1}{2N}) = 1 + \frac{1}{2}\sin(2\pi(n+\tfrac{1}{2N})), \quad a_{init}(n+\tfrac{1}{2N}) = 1, \quad n = 0, \ldots, 1-\tfrac{1}{N}. \tag{4.136}$$

We use the parameter values for epithelial cells from Table 4.4, for which Da $= 1.1 \times 10^{-3}$ ($\tilde{M} = 3.42 \times 10^{-9}\,\mathrm{mol\,m^{-2}\,s^{-1}}$). With these parameters, there is very little drop in the oxygen concentration from the surface of the bath to the aggregate since the uptake flux is small, so the effect of the oxygen distribution on the cell growth is negligible irrespective

of the initial conditions. This allows us to isolate the effect of the initial conditions on the growth.

Figure 4.13 shows the evolution of the cells when all the cells are initially stretched, while Figure 4.14 shows the evolution when half of the cells are initially stretched and half are compressed. With the former distribution, all the cell lengths initially decrease towards the target lengths (Figure 4.13(a)), but with the latter the lengths of the compressed cells initially increase while those of the stretched cells decrease (Figure 4.14(a)). In both cases the target lengths of all the cells increase, since all the cell pressures are within the thresholds for growth, $p_s = -0.36$ and $p_s = 0.36$ ($p_s^* = -2\,\text{nN}\,\mu\text{m}^{-1}$, $p_c^* = 2\,\text{nN}\,\mu\text{m}^{-1}$) (Figures 4.13(b)–(c) and 4.14(b)–(c)). For both distributions, the cell pressures eventually become positive due to the continual increase in the target lengths.

When all the cells are initially stretched, the cell positions, all the cell variables except the vertex velocities, and the oxygen concentration are initially symmetric about $x = 0$ and remain so throughout the simulation. For the half-stretched half-compressed case, the cell variables and oxygen distribution are initially asymmetric, but evolve to symmetric distributions over time.

4.9.4.5 Impact of pressure-sensitivity of cells on growth

By varying the maximum stretch and compression thresholds, p_s and p_c, we can examine the impact of pressure-sensitivity on the cell growth. Figures 4.15 and 4.16 show simulation results for the same initial distributions as in §4.9.4.4 but with a much narrower range of pressures over which cells can grow, $p \in [p_s, p_c] = [-0.089, 0.089]$ ($[p_s^*, p_c^*] = [-0.5, 0.5]\,\text{nN}\,\mu\text{m}^{-1}$), *i.e.* more mechanosensitive cells.

For both cases the initial cell pressures exceed the stretch and compression thresholds in parts of the aggregate. When all the cells are initially stretched the cell pressures are below p_s in the middle of the aggregate, so the cells do not initially grow there (Figure 4.15(a)–(c)). Only after the cells have relaxed sufficiently towards their target lengths do the cell pressures fall between p_s and p_c, and the target lengths in the middle of the aggregate start to increase. With the half-stretched half-compressed initial conditions, the cell pressures are initially in the range $[p_s, p_c]$ at the ends of the aggregate and in a narrow strip in the middle of the aggregate, where the cells transition from being stretched to compressed, so increases in the cell target lengths are initially restricted to these regions (Figure 4.16(b)–(c)). Once the cells relax from their initial states of extension and compression, the cell pressures fall into the range $[p_s, p_c]$ across the whole aggregate and so all the target lengths increase.

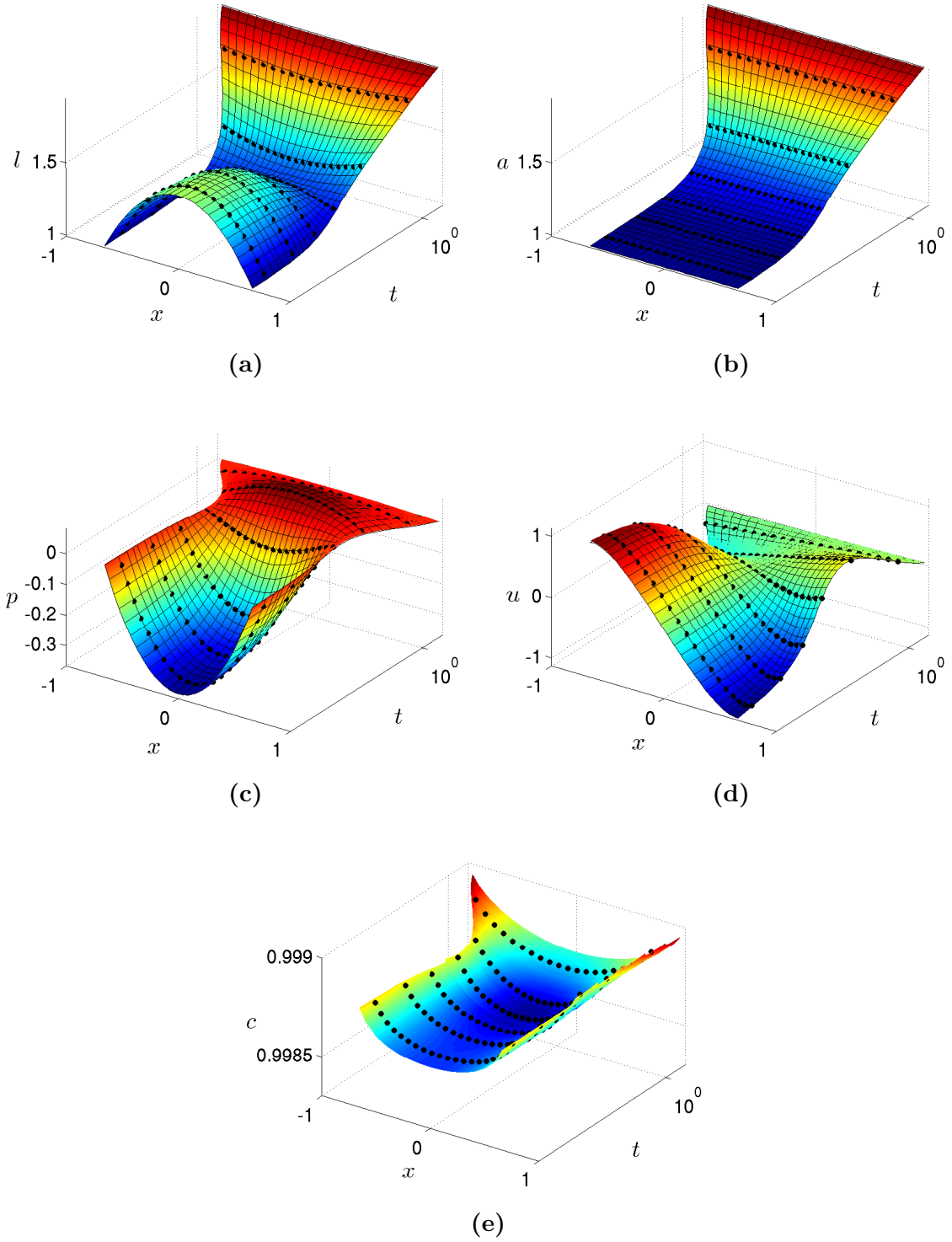

Figure 4.13: Evolution of the cell variables ((a)–(d)) and the oxygen concentration ((e)) when all cells are initially stretched. Grid lines in (a)–(d) show approximate analytical solutions (see §4.9.4.6). Note that scale on t-axis is logarithmic. Initial conditions: $l_{n+\frac{1}{2N}} = 1 + \frac{1}{2}\sin(\pi(n + \frac{1}{2N}))$, $a_{n+\frac{1}{2N}} = 1$ $(n = 0, \ldots, 1 - \frac{1}{N})$. Parameter values (corresponding to epithelial cells): $N = 20$, $\mathrm{Da} = 1.1 \times 10^{-3}$, $c_{1/2} = 4.8 \times 10^{-3}$, $\alpha = 1.4$, $a_{max} = 2$, $k_g = 0.048$, $p_s = -0.36$, $p_c = 0.36$.

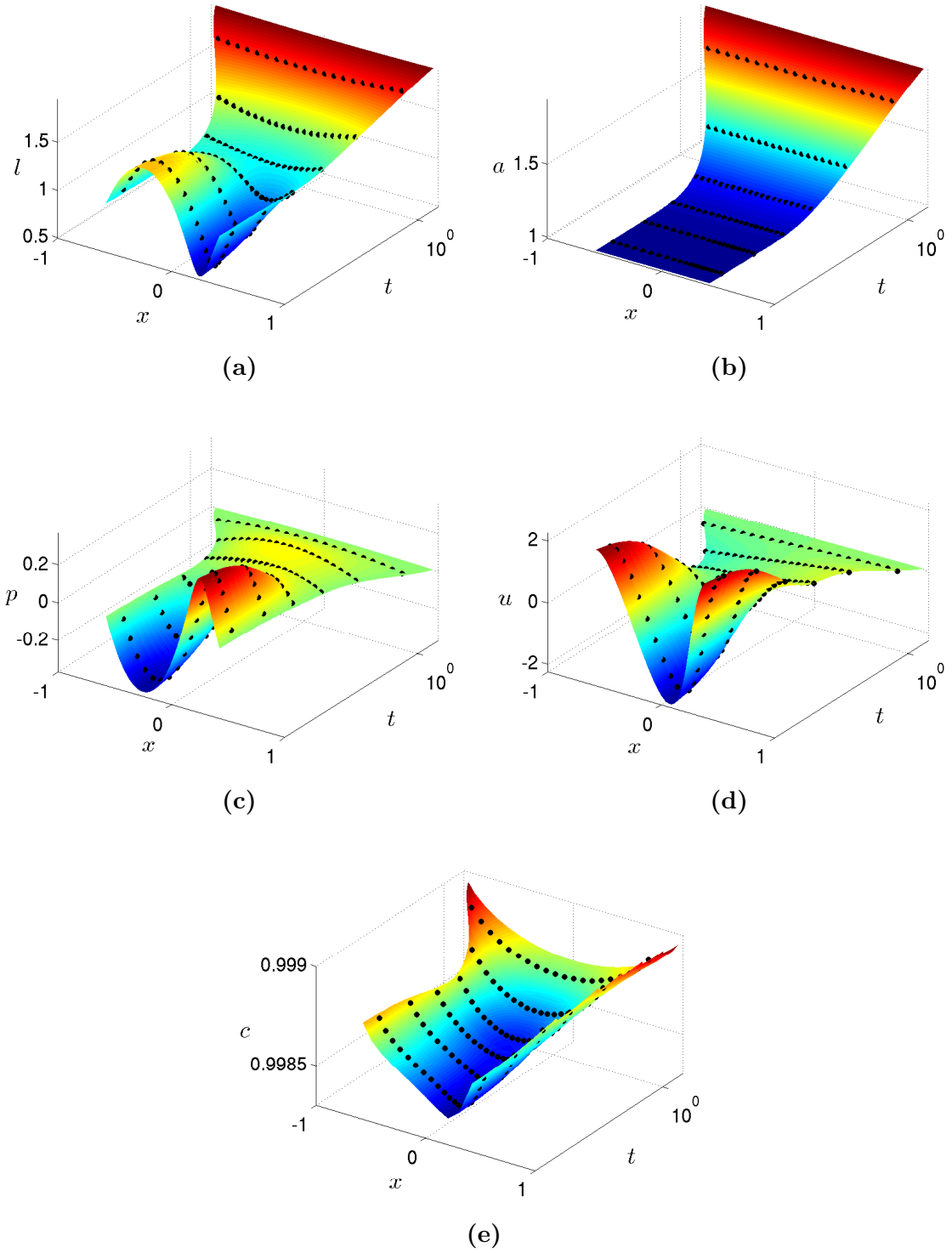

Figure 4.14: Evolution of the cell variables ((a)–(d)) and the oxygen concentration ((e)) when half of the cells are stretched and half are compressed initially. Logarithmic scale on t-axis. Initial conditions: $l_{n+\frac{1}{2N}} = 1 + \frac{1}{2}\sin(2\pi(n+\frac{1}{2N}))$, $a_{n+\frac{1}{2N}} = 1$, $n = 0, \ldots, 1 - \frac{1}{N}$. All parameter values as in Figure 4.13.

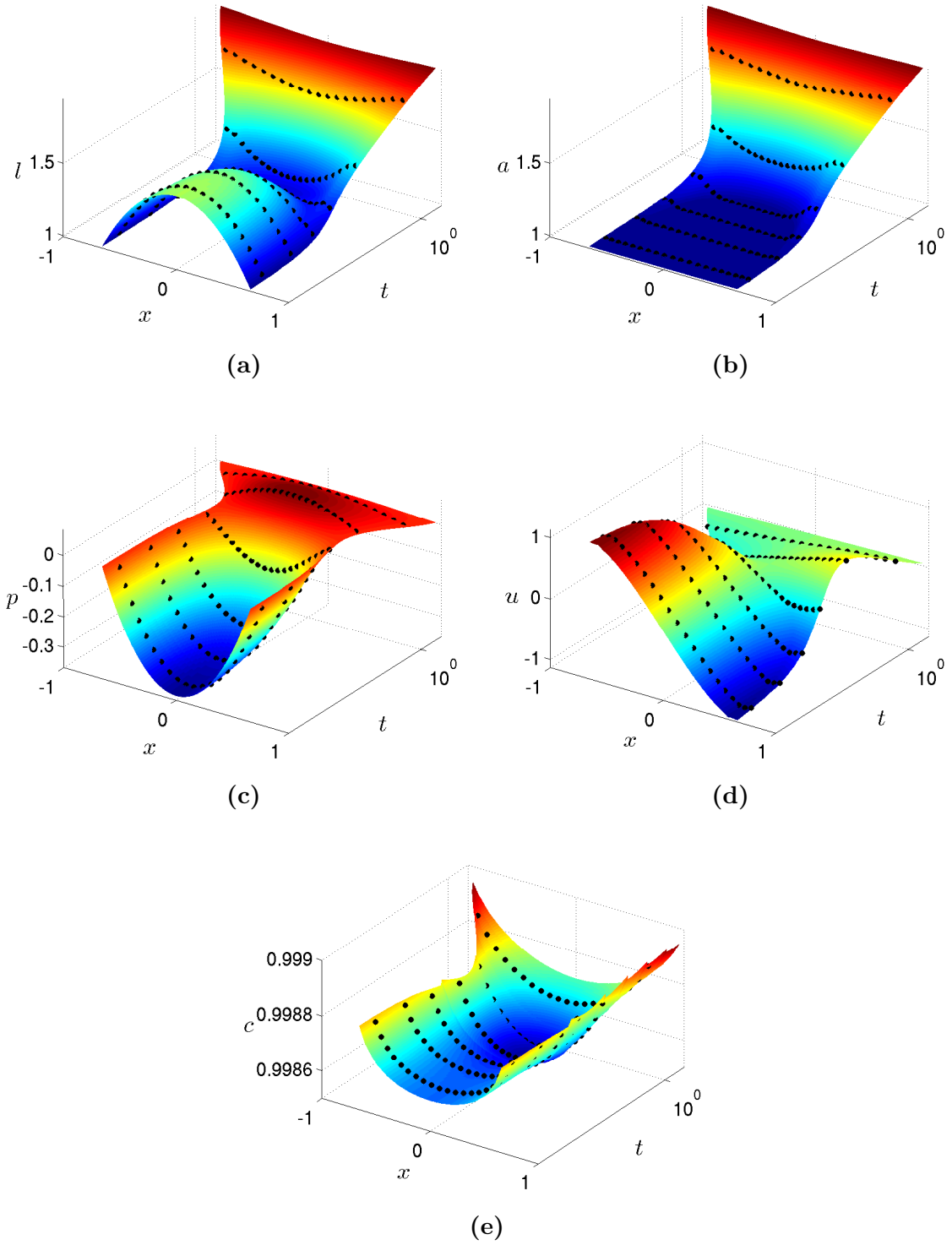

Figure 4.15: Evolution of the cell variables ((a)–(d)) and the oxygen concentration ((e)) for highly pressure-sensitive cells that are all initially stretched. Logarithmic scale on t-axis. Initial conditions as in Figure 4.13. Parameter values: $p_s = -0.089$, $p_c = 0.089$. All other parameter values as in Figure 4.13.

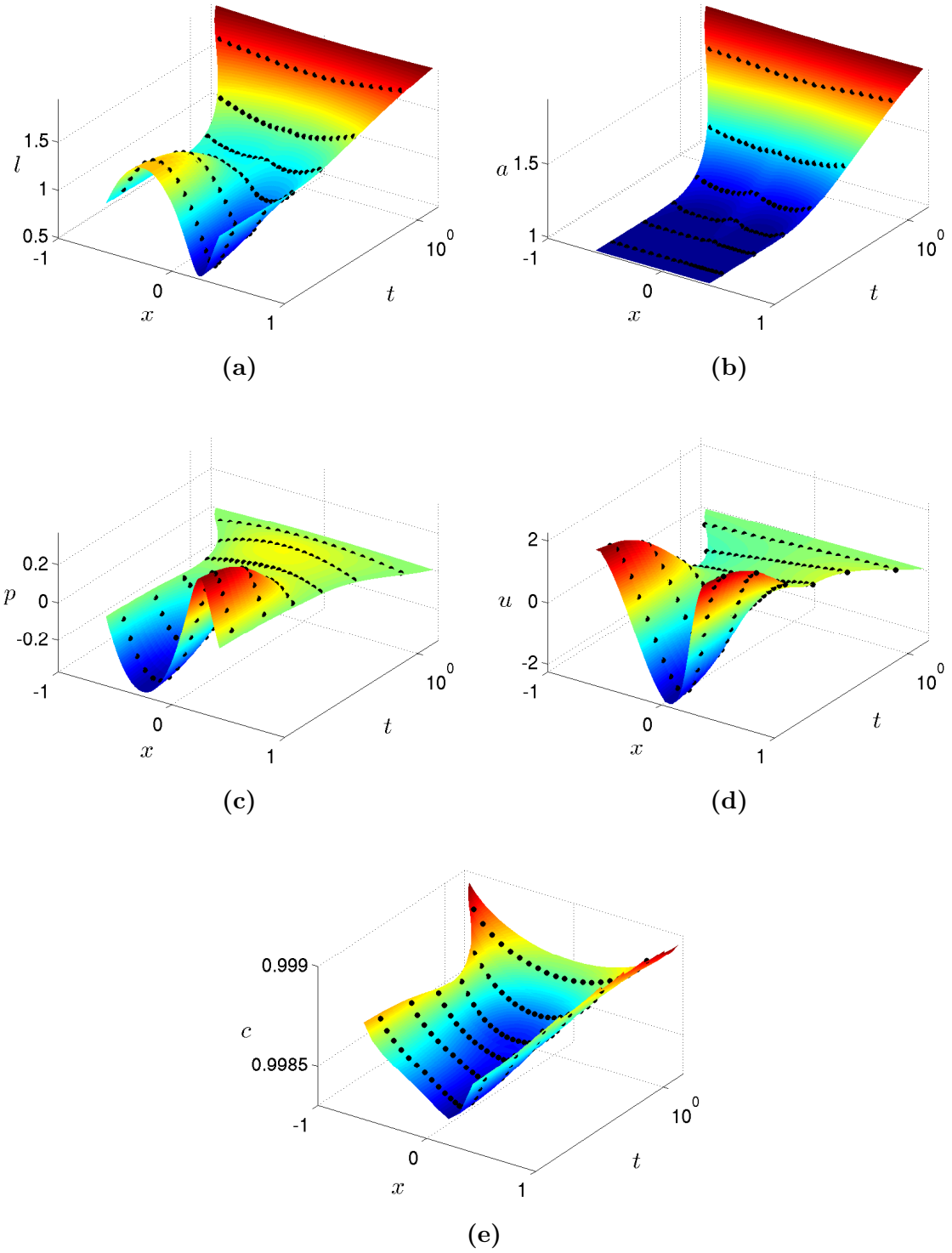

Figure 4.16: Evolution of the cell variables ((a)–(d)) and the oxygen concentration ((e)) for highly pressure-sensitive cells half of which are stretched and half of which are compressed initially. Logarithmic scale on t-axis. Initial conditions as in Figure 4.14. All parameter values as in Figure 4.15.

Delayed growth of cells in the interior of the aggregate leads to less uniform distributions of cell lengths and target lengths at later times than for less pressure-sensitive cells (*cf.* Figures 4.15(a),(b) and 4.16(a),(b) with Figures 4.13(a),(b) and 4.14(a),(b)), but does not significantly retard net aggregate growth.

The sensitivity of the growth of an aggregate of 20 initially stretched cells to variation in the excess stretching threshold p_s is shown in Figure 4.17. The net change in the aggregate length over 100 hrs of culture is virtually constant for $p_s < -0.1$ ($p_s^* < -0.56\,\mathrm{nN\,\mu m^{-1}}$) (Figure 4.17(b)), but decreases rapidly for $p_s > -0.1$ ($p_s^* > -0.56\,\mathrm{nN\,\mu m^{-1}}$), such that for $p_s > -6 \times 10^{-3}$ the aggregate fails to regain its initial length following the initial cell relaxation. The rapid decrease in net growth arises because as $p_s \uparrow 0$ the proportion of the aggregate over which the cell pressures are initially below p_s increases, and therefore it takes longer for the system to relax to the state where all the cell pressures exceed p_s. For $p_s < -0.1$, however, the cell pressures are within the thresholds for growth over the whole aggregate, so further reductions in p_s have no effect on the growth. Our simulations suggest that p_s can have a large effect on growth; however, experimental data is needed to determine whether the pressure-dependent growth law used here is physically realistic, and to estimate the threshold pressures p_s and p_c.

Although we have only investigated the dependence of the growth on p_s for cells that are initially stretched, varying p_c would have a similar effect for cells that are initially compressed. However, it would be interesting to investigate the effect of asymmetry in the sensitivity to stretching versus compression ($p_s \neq -p_c$) for a mixture of stretched and

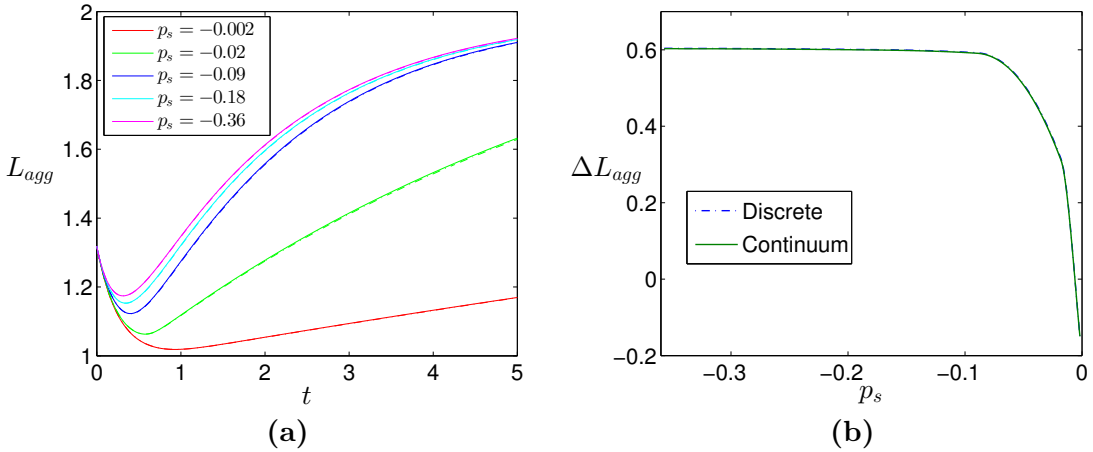

Figure 4.17: Dependence of aggregate growth on excess stretching threshold, p_s. (a) Evolution of aggregate length, L_{agg}, for different values of p_s. (b) Variation in the overall aggregate growth, ΔL_{agg}, with p_s. Initial conditions and parameter values, other than p_s, as per Figure 4.13.

compressed cells as part of future work, as some cell types will be more sensitive to stretching than compression or vice versa.

4.9.4.6 Analytical solution for $c \gg k_g$, $p_s < p < p_c$

If the oxygen concentration over the aggregate is much larger than the half-maximal uptake concentration, $c \gg k_g$, and the cell pressure is within the threshold values for growth ($p_s < p < p_c$), we can derive an approximate analytical solution of the continuum cell model. (It is also possible to derive the corresponding analytical solution of the discrete cell model, but we omit this here for the sake of brevity.) In this limit, $c/(k_g + c) \sim 1$ and $\mathrm{S}(p, p_s, p_c) = 1$, so from (4.55c) the target length evolves via

$$\frac{\partial a}{\partial \tau} \approx a_{max} - a \quad \Rightarrow \quad a(n,\tau) \approx a_{max} - (a_{max} - a_{init}(n))e^{-\tau}. \tag{4.137}$$

Combining equations (4.50), (4.53), (4.103), (4.104) and (4.137) to eliminate u, l and a, we obtain

$$\alpha \frac{\partial p}{\partial \tau} = \frac{\partial^2 p}{\partial n^2} + (a_{max} - a_{init}(n))e^{-\tau}, \tag{4.138}$$

with the initial and boundary conditions

$$p = 0 \quad \text{at } n = 0, 1, \tag{4.139}$$

$$p = p_{init}(n) \quad \text{at } \tau = 0. \tag{4.140}$$

It is straightforward to show that (4.138)–(4.140) admit a separable solution of the form

$$p = \sum_{j=1}^{\infty} \left(\int_0^{\tau} C_j(s) e^{j^2\pi^2 s/\alpha} \, \mathrm{d}s + D_j \right) e^{-j^2\pi^2\tau/\alpha} \sin(j\pi n),$$

where

$$C_j(\tau) = \frac{2}{\alpha} \int_0^1 (a_{max} - a_{init}(n)) e^{-\tau} \sin(j\pi n) \, \mathrm{d}n, \quad D_j = 2 \int_0^1 p_{init}(n) \sin(j\pi n) \, \mathrm{d}n.$$

With the initial conditions and parameter values in Figure 4.13 (for which $c \gg k_g$ and $p_s < p < p_c$), the approximate analytical solution is

$$a(n,\tau) \approx 2 - e^{-\tau}, \tag{4.141}$$

$$p(n,\tau) \approx -\frac{1}{2\alpha} e^{-\pi^2\tau/\alpha} \sin(\pi n) + \sum_{k=0}^{\infty} \frac{4}{(2k+1)\pi((2k+1)^2\pi^2 - \alpha)} (e^{-\tau} - e^{-(2k+1)^2\pi^2\tau/\alpha}) \sin((2k+1)\pi n), \tag{4.142}$$

$$l(n,\tau) \approx 2 - e^{-\tau} - \alpha p. \tag{4.143}$$

Figure 4.13 shows that this approximate solution is in close agreement with the numerical solutions for the discrete and continuum cell models.

4.9.4.7 Convergence of the discrete and continuum solutions

We now turn to the question of whether the solutions of the discrete and continuum cell models converge as the cell number increases when the cell growth and nutrient transport are coupled. For the discrete cell variables $\phi_{n+\frac{1}{2N}} = l_{n+\frac{1}{2N}}$, $a_{n+\frac{1}{2N}}$, $p_{n+\frac{1}{2N}}$ $c_{n+\frac{1}{2N}}$, we define the error in the continuum solution, as previously, to be

$$E_\phi := \max_{n\in\{0,\dots,1-\frac{1}{N}\},\,\tau\in[0,T]} \left|\phi_{n+\frac{1}{2N}}(\tau) - \phi(n+\tfrac{1}{2N},\tau)\right|.$$

For the cell vertex velocities we define the error in the continuum solution to be

$$E_u := \max_{n\in\{0,\dots,1\},\,\tau\in[0,T]} \left|u_n(\tau) - u(n,\tau)\right|.$$

Figure 4.18 shows how the errors in the continuum solutions vary with the cell number N for simulations in which all the cells are initially stretched as in §4.9.1. For all the variables, the discrete and continuum solutions converge as N increases, the error decreasing like $1/N^2$ for the cell length and cell velocity, like $1/N^4$ for the cell pressure, and approximately exponentially for the cell target length. For a given cell number $N \in [10, 150]$, the relative error is largest in the cell velocity. The error in the oxygen concentration is $\mathcal{O}(10^{-4})$, but decreases slowly as N increases. This is to be expected, since we do not formally average the oxygen transport equations.

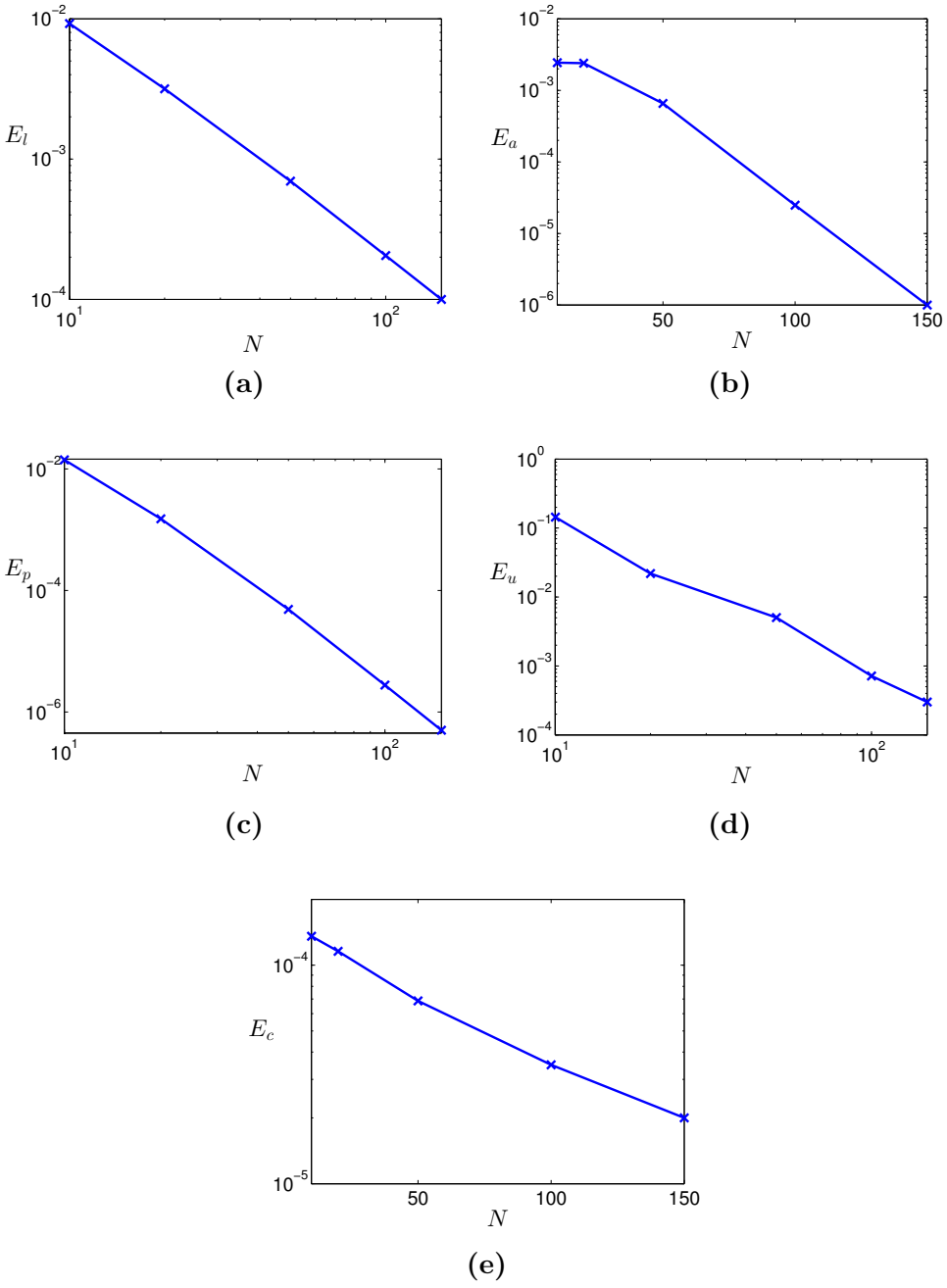

Figure 4.18: Convergence of the discrete and continuum solutions for the cell variables and oxygen concentration as N increases for target-length-, pressure- and oxygen-dependent growth. E_ϕ ($\phi = l, a, p, u, c$) is the maximum absolute difference between the discrete and continuum solutions over the course of the simulation. Convergence of (a) cell lengths, $l_{n+\frac{1}{2N}} \to l$, (b) cell target lengths, $a_{n+\frac{1}{2N}} \to a$, (c) cell pressures, $p_{n+\frac{1}{2N}} \to p$, (d) vertex velocities, $u_n \to u$, and (e) average oxygen concentration over each cell, $c_{n+\frac{1}{2N}} \to c$. Initial conditions as in Figure 4.2. Parameter values (corresponding to chondrocytes): $T = 3$, $\alpha = 7.5 \times 10^{-3} N^2$, $a_{max} = 2$, $k_g = 0.30$, $p_s = -33.3/N^2$, $p_c = 33.3/N^2$, $\mathrm{Da} = 1.6 \times 10^{-4} N$, $c_{1/2} = 0.024$.

4.10 Conclusions

Our main goal in this chapter was to assess the suitability of the discrete-to-continuum cell modelling framework of Fozard *et al.* [78] for describing bioreactor cell aggregate growth. To do this we needed to determine whether the framework could be coupled to a continuum model for a growth-rate-limiting nutrient while maintaining good agreement between the discrete and continuum cell models. As a simple trial model, we used a linear-spring cell-vertex model of a 1D cell aggregate growing along the base of a nutrient bath coupled to equations for the diffusion and uptake of oxygen in the bath, and derived a continuum approximation of this model following [78]. We discuss the results obtained with this model below, but first summarise our findings from comparing the models of Murray *et al.* and Fozard *et al.*, and comparing constant-rate and pressure-dependent growth laws that are independent of the nutrient concentration.

4.10.1 Comparison of Murray *et al.*'s and Fozard *et al.*'s models

By deriving the continuum limit of our discrete cell model, we have confirmed that treating the cells as linear springs with constant target lengths in Fozard *et al.*'s cell-vertex model gives rise to the same nonlinear diffusion equation for the cell density as that derived by Murray *et al.* [181], from their cell-centre model with a linear spring law for the cell interaction forces. Further we have shown that Fozard *et al.*'s and Murray *et al.*'s derivations of the continuum limit yield the same diffusion equation for the cell density whenever the same cell interaction force law is used. Hence we may conclude that cell-vertex and cell-centre models such as those of Fozard *et al.* and Murray *et al.* can be approximated for large cell numbers by the same continuum limit in 1D. We have also shown that modelling cell growth by prescribing the evolution of the cell target lengths leads to a source term $\left(\frac{\partial^2 a}{\partial x^2}\right)$ in the diffusion equation for the cell density with an analogous role to the source term added by Murray *et al.* [181] to model cell proliferation.

4.10.2 Comparison of constant and pressure-dependent cell growth

Fozard *et al.* only considered a constant rate of growth of the cell target lengths and assumed that all of the target lengths were initially the same. As a result, the cells continued to grow indefinitely without the system ever reaching equilibrium, and there was no spatial variation in the target lengths during the growth. Since such behaviour is not physically realistic, we considered an alternative growth law for which the target lengths grow/shrink at rates proportional to the extension/compression (*i.e.* pressure) of the cells. We showed that under such pressure-dependent growth the system evolves to a steady state that depends on the

initial conditions. At this steady state all the cell pressures are zero, and the cell lengths and target lengths are equal for each cell but may be non-uniform in space. This may be a more realistic model for cells whose growth and ultimate size depends on their initial size and extension/compression, and that grow more rapidly when stretched (either cyclically or under a sustained load), such as various types of muscle cells [198, 220, 264].

While Fozard *et al.* were only able to derive analytical solutions for their continuum model in the limits of slow growth and long times, representing the cells as linear springs and neglecting cell viscosity in our work has allowed us to derive analytical solutions for the discrete and continuum models for the cases of constant and pressure-dependent growth of the target lengths. Using these solutions and simulations of the cell growth for given initial conditions, we have also shown that the solutions of the discrete and continuum models converge in the limit $N \to \infty$ for both growth laws.

4.10.3 Coupled cell growth and oxygen transport

The coupling between the cells and the oxygen distribution in our model is two-way: the growth of the cell target lengths depends on the cells' local oxygen concentration, and the oxygen uptake rate is assumed to be proportional to the cell density. Importantly, however, we have not carried out a formal homogenisation in deriving the continuum approximation of the discrete cell model coupled to the oxygen transport, and have assumed that we can use the continuous analogue of the oxygen uptake condition for the discrete model in the continuum approximation.

The simulation results in §4.9.4 show that excellent agreement between the discrete and continuum models is maintained when each of them is coupled to the oxygen transport. Indeed, the discrepancy between the two models decreases as the cell number increases, being $\mathcal{O}(1/N^2)$ for the continuum cell length (§4.9.4.7) as for the non-nutrient-dependent growth (*cf.* §4.9.1.3 and §4.9.2.3). We therefore conclude that with appropriate coupling conditions it is possible for the discrete and continuum cell models to be coupled to an external continuum field without losing agreement between the two approaches.

The cell growth is also assumed to depend on the cell target lengths and pressures. The growth rate is taken to be proportional to the difference between the current and maximum target lengths provided the cells are neither too compressed nor too stretched (otherwise there is no growth). The range of growth behaviours possible with this growth law has been explored through numerical simulations across a range of parameter values corresponding to cell types with different oxygen demands and pressure-sensitivity. For typical values of the half-maximal uptake concentration and oxygen concentration at the surface

of the bath, variation in the oxygen uptake rate over a typical physiological range (10^{-18}–$10^{-17}\,\mathrm{mol\,cell^{-1}\,s^{-1}}$) has little effect on the cell growth. This is due to the Monod growth rate being approximately constant for concentrations much larger than the half-maximal uptake rate concentration. However, for uptake rates one or two orders of magnitude larger the growth rate is significantly slower, due to the reduced oxygen concentration at the aggregate (see §4.9.4.1). The cell growth rate also decreases when the oxygen supply at the surface of the bath is reduced (§4.9.4.2) and as the half-maximal uptake concentration is increased (§4.9.4.3), as these lead to a lower oxygen concentration at the aggregate and a lower Monod growth rate, respectively.

For the chosen growth law (equation (4.22)), the initial distribution of cell lengths and target lengths affects the initial growth of the cells, *e.g.* some cells will not grow at first if they are too stretched or compressed. However, all the target lengths and cell lengths eventually evolve towards the maximum target length since the system for the cell pressures is dissipative. This behaviour can be seen in the simulations in §4.9.4.4, where the cells relax quickly towards their target lengths and then grow more slowly towards the maximum target length. The same behaviour is observed in §4.9.4.5, except that greater sensitivity to the cell pressure prevents the most stretched and most compressed cells from growing initially, so that the non-uniformity in the cell lengths takes longer to dissipate.

The sensitivity of the cells to stretching and compression can also have a significant effect on the growth rate of an aggregate. If the cells can only tolerate small amounts of stretching or compression, the aggregate will grow more slowly if all cells are initially stretched or compressed (see §4.9.4.5). This is because as the range of pressures over which the cells grow ($[p_s, p_c]$) narrows, it takes longer for the pressures to fall within this range during the initial cell relaxation (unless they relax more rapidly to equilibrium).

In summary, we have shown that it is possible to couple Fozard *et al.*'s discrete cell model framework to a continuum model for an external field and still derive a continuum limit that closely approximates the behaviour of the discrete model, even for moderate numbers of cells ($N = 10$). This is the first step toward developing a discrete cell model of cell aggregate growth in the HFB coupled to continuum models for the fluid flow and nutrient transport that can be approximated by a fully continuum model. In the next section, we discuss how the work here can be extended and the steps that are needed to incorporate the discrete-to-continuum framework into a model of cell growth in the HFB.

4.11 Further work

Several aspects of the modelling framework presented in this chapter merit further investigation. There are also many ways in which the framework could be extended prior to its

incorporation into a model of fluid flow and advective nutrient transport in the HFB.

The effect of the initial conditions on the cell growth warrants further investigation, since we have only considered relatively simple initial cell length and cell target length distributions. It would be interesting to consider more non-uniform initial length distributions (*e.g.* corresponding to a greater initial mix of cell ages) and varying initial cell target lengths (*e.g.* corresponding to co-culture of different cell types). If the variations in the lengths and target lengths were large and occurred over short length scales it would be necessary to use the continuum approximation for heterogeneous cell properties given below.

Another factor that we have not investigated is how the boundary conditions at the ends of the cell aggregate affect the cell growth. For all simulations we have assumed stress-free boundary conditions, with no external forces on the ends of the aggregate. This means that the end cells can move outwards freely as they, and the cells in the aggregate interior, grow. If a force were applied to one end of the aggregate opposing or preventing this outward movement, we would expect the cells there first to become compressed and then to move in the opposite direction as they relaxed from compression. We would test this in future work and consider other forms of boundary conditions, *e.g.* time-dependent external forces representing cyclic mechanical stimulation of the cells.

Constitutive aspects of the model that would benefit greatly from experimental parameterisation and validation are the cell interaction force law, the target length growth law, and the nutrient uptake kinetics. If experimental data were available to fit functional forms for these three terms in the discrete model for a given cell type and nutrient, we could derive the corresponding continuum limit and validate the results of the discrete and continuum models against the experimental data. If there was insufficient data to do this, we could simulate cell aggregate growth for alternative forms of the interaction force law (*i.e.* different functional forms for $p = p(l, a)$), target length growth (*i.e.* different forms for $\Gamma = \Gamma(l, a, p, c; \gamma)$), and uptake kinetics and examine which gave the best qualitative comparison to the data available.

In order to incorporate the discrete-to-continuum framework into a model of cell aggregate growth in the HFB, the framework needs to be extended to include cell proliferation, fluid flow and shear stress dependence in the growth, and to account for heterogeneous cell properties and multiple cell aggregates. In the following sections we discuss each of these extensions in more detail.

4.11.1 Heterogeneous cell properties

A clear limitation of the modelling framework we have presented is that the continuum approximation to the discrete model in (4.49)–(4.53) is only valid if the cell variables and

parameters vary slowly with respect to the cell index n. In practice cell parameters may vary substantially between adjacent cells. Experiments with epithelial sheets, for example, have shown that the drag forces between the cells and the substrate can vary significantly over short length scales [221]. Cell division is also likely to cause significant local variation in cell sizes and mechanical properties. Periodic variation in the cell properties is also of interest for applications involving patterning of different cell types or cell properties on the substrate (such as liver zonation [56, 246], cell printing [243], and cell patterning via juxtacrine signalling [190, 191]).

In cases for which the cell parameters and variables are spatially periodic it is possible to derive the continuum limit of our discrete model following the multiple scales approach used by Fozard *et al.* [78] (assuming for the time being that the cell growth does not depend on the oxygen concentration). We assume that the cell properties are periodic with period $M \ll N$ and that the cell pressure and vertex velocities vary over $\mathcal{O}(N)$ cells, and use the scalings from §4.4 to nondimensionalise the discrete system. We denote the continuous cell label by ν ($\nu \in [0,1]$), take the cell variables to be functions of the discrete cell index $n \in \{0, \frac{1}{N}, \dots, 1\}$ and ν (treating n and ν as independent variables), and expand equations (4.26)–(4.30) and (4.37) with respect to ν for $N \gg 1$. We then seek solutions as asymptotic expansions in powers of $1/N$ of the form

$$l = \sum_{i=1}^{\infty} (\tfrac{1}{N})^i l^{(i)}, \quad a = \sum_{i=1}^{\infty} (\tfrac{1}{N})^i a^{(i)}, \quad p = \sum_{i=1}^{\infty} (\tfrac{1}{N})^i p^{(i)}, \quad u = \sum_{i=1}^{\infty} (\tfrac{1}{N})^i u^{(i)},$$

and impose the periodicity conditions. This gives that the cell pressures and velocities are independent of n at leading order and the governing equations for the leading order mean cell length, pressure and velocity are the same as (4.50)–(4.54), but with the parameters replaced by their average values over a period (except λ which is replaced by its harmonic mean) (see Appendix G), *i.e.*

$$\frac{\partial \overline{l^{(0)}}}{\partial \tau}(\nu,\tau) = \frac{\partial u^{(0)}}{\partial \nu}(\nu,\tau), \tag{4.144}$$

$$\alpha p^{(0)}(\nu,\tau) = \frac{1}{\overline{1/\lambda}}(\overline{a^{(0)}}(\nu,\tau) - \overline{l^{(0)}}(\nu,\tau)), \tag{4.145}$$

$$\bar{\mu} u^{(0)}(\nu,\tau) = -\frac{\partial p^{(0)}}{\partial \nu}(\nu,\tau), \tag{4.146}$$

$$\frac{\partial \overline{a^{(0)}}}{\partial \tau}(\nu,\tau) = \overline{\Gamma^{(0)}}(\nu,\tau), \tag{4.147}$$

$$p^{(0)}(0,\tau) = p^{(0)}(1,\tau) = 0, \tag{4.148}$$

where the overline denotes the average value with respect to n over a period of M cells

(which is independent of n via the periodicity condition) and

$$\overline{\Gamma^{(0)}} = \frac{1}{M}\sum_{i=0}^{M-1}\Gamma(l^{(0)}(n+\tfrac{1}{2N}+\tfrac{i}{N},\nu,\tau),a^{(0)}(n+\tfrac{1}{2N}+\tfrac{i}{N},\nu,\tau),p^{(0)}(\nu,\tau);\gamma_{n+\frac{1}{2N}}). \quad (4.149)$$

To extend our current work and that of Fozard *et al.*, we would first test whether solutions of equations (4.144)–(4.149) agree with those of the discrete model with periodic values of the cell parameters for choices of Γ that depend on the cell variables (*e.g.* $\Gamma = -\gamma p$, $\Gamma = \gamma a$). We would then couple the discrete and continuum cell models to the nutrient transport model as we have in the present work, and test via simulation whether there is still good agreement between the two.

4.11.2 Cell division

The most obvious process which is missing from the current model is cell division. Adding cell division significantly increases the complexity of the model, since when a cell divides the number of cells (and therefore the number of variables) in the discrete model increases, and the cells must be relabelled in both the discrete model and the continuum approximation [78]. Modelling cell division also requires us to prescribe the conditions under which division occurs and how the daughter cells are placed, and their mechanical state, following division. As described in §4.6.2.1, Murray *et al.* chose to make cells divide once they reached a dimensionless age of 1, having randomly assigned their initial ages in $[t_a, 1]$ to introduce asynchrony into the cell division, and to place the centres of the daughter cells a short distance on either side of the centre of the dividing mother cell so that the springs connecting the cells were initially compressed following division. Murray *et al.* added the appropriate source term to the cell density diffusion equation to match the net cell proliferation in the discrete model, so that

$$\frac{\partial\rho}{\partial t} = \frac{1}{\alpha_M}\frac{\partial}{\partial r}\left(\frac{1}{\rho^2}\frac{\partial\rho}{\partial r}\right) + f(\rho,t),$$

where

$$f(\rho,t) = \mathrm{H}(t \bmod 1 - t_a)\frac{\ln 2}{1-t_a}\rho.$$

To gain insight into modelling cell proliferation in this way, we reverse the process of taking the continuum limit to find the equivalent discrete formulation of our equation for the cell density with a source term

$$\frac{\partial\rho}{\partial t} = \frac{1}{\alpha}\left(\frac{\partial}{\partial x}\left(\frac{1}{\rho^2}\frac{\partial\rho}{\partial x}\right) + \frac{\partial^2 a}{\partial x^2}\right) + f(\rho,t). \quad (4.150)$$

If we assume the relationship between the cell pressures and the cell lengths is the same and the force balance on the vertices is the same, so that

$$p = a - l \quad \text{and} \quad u = -l\frac{\partial p}{\partial x},$$

then (4.150) can be rewritten as

$$\frac{\mathrm{D}l}{\mathrm{D}t} = l\frac{\partial u}{\partial x} - l^2 f(\tfrac{1}{l}, t).$$

Reversing the transformation to spatial coordinates yields

$$\frac{\partial l}{\partial \tau} = \frac{\partial u}{\partial n} - l^2 f(\tfrac{1}{l}, \tau),$$

a discrete form of which is

$$\frac{1}{N^*}\frac{\mathrm{d}l_{n+\frac{1}{2N}}}{\mathrm{d}\tau} = u_{n+\frac{1}{N}} - u_n - \frac{1}{N^*} l^2_{n+\frac{1}{2N}} f\left(\frac{1}{l_{n+\frac{1}{2N}}}, \tau\right), \tag{4.151}$$

where N^* is the initial number of cells. Here the vertex velocities u_n are functions of the cell lengths and target lengths through

$$\frac{1}{6N^*}\left(u_{n-\frac{1}{N}} + 4u_n + u_{n+\frac{1}{2N}}\right) = p_{n-\frac{1}{2N}} - p_{n+\frac{1}{2N}},$$
$$\alpha p_{n+\frac{1}{2N}} = a_{n+\frac{1}{2N}} - l_{n+\frac{1}{2N}},$$

and the cell target lengths grow according to

$$\frac{\partial a_{n+\frac{1}{2N}}}{\partial \tau} = \Gamma\left(l_{n+\frac{1}{2N}}, a_{n+\frac{1}{2N}}, p_{n+\frac{1}{2N}}, c_{n+\frac{1}{2N}}\right).$$

Modelling cell division in the continuum limit through a source term in the cell density equation is therefore equivalent to treating cell division as a smooth process at the discrete level through which the cell's density continually increases if the cell is static (as $-\frac{1}{N^*} l^2_{n+\frac{1}{2N}} f(\frac{1}{l_{n+\frac{1}{2N}}}, \tau) < 0$ since $f > 0$). Tlili *et al.* [252] derived essentially the same equation as (4.151) (equation (34), page 9 in [252]) for the elongation of a cell of length l_{cell} in a growing 1D cell aggregate

$$\frac{\mathrm{d}l_{cell}}{\mathrm{d}\tau} = \left(\frac{1}{L_{agg}}\frac{\mathrm{d}L_{agg}}{\mathrm{d}\tau} - \frac{1}{\hat{N}}\frac{\mathrm{d}\hat{N}}{\mathrm{d}\tau}\right) l_{cell} = \left(\frac{u_1 - u_0}{L_{agg}} - 1\right) l_{cell}, \tag{4.152}$$

where $\hat{N}(\tau)$ is the total cell number at time τ normalised with respect to N^* (and the other variables are as previously defined), except that they assumed all the cells were the same length, $l_{cell} = L_{agg}/\hat{N}$, and that the cell number grew exponentially, $\frac{\mathrm{d}\hat{N}}{\mathrm{d}\tau} = \hat{N}$. The latter assumption is equivalent to assuming $f(\rho, \tau) = \rho$, so that (4.151) reduces to

$$\frac{1}{N^*}\frac{\mathrm{d}l_{n+\frac{1}{2N}}}{\mathrm{d}\tau} = u_{n+\frac{1}{N}} - u_n - \frac{1}{N^*} l_{n+\frac{1}{2N}}.$$

Although (4.151) allows for variations between cells, both (4.151) and (4.152) imply that the growth rate of the length of each cell is the difference between the aggregate growth

rate (due to the increase in the cell target lengths) and the cell shortening rate representing cell division.

Clearly, this is not a suitable representation of cell division in the discrete model. However, it motivates attempting to include cell division in the following way. As before, we would prescribe the growth of the cell target lengths, but once a cell's length doubled, we would split the cell into two daughter cells of equal length and with target lengths half that of their mother cell. Initially we would try giving the daughter cells the same spring constants and drag constants as the mother cell, but if the resulting jumps in the cell pressures and vertex velocities at cell division caused difficulty in deriving the continuum approximation, we would pick the spring constants and drag constants to maintain continuity of either the cell pressures or vertex velocities or both at division. We would attempt to obtain the continuum approximation by a formal homogenisation of the discrete system accounting for the different length and time scales of the various processes involved and any spatial heterogeneity in the cell parameters. We anticipate that this would yield a similar diffusion equation for the cell density to (4.150) with a cell-density-dependent source term. However if our homogenisation attempts proved unsuccessful, we would try adding an appropriate source term to the cell density equation as in (4.150) to match the overall increase in the cell number in the discrete model. Having successfully matched the proliferation in the discrete and continuum models, we would investigate the effect of specifying more complicated conditions for cell division, such as cells not being able to divide if their pressure exceeded certain thresholds, and determine whether the discrete and continuum models still agreed under these conditions.

4.11.3 Fluid flow and shear dependence

Following the introduction of cell division into the model, the next step would be to add flow of the culture medium and shear-stress dependence into the growth and division. Initially we would consider a simple set-up with an aggregate of cells attached to the base of a narrow channel through which the culture medium was flowing. The flow through the channel would be modelled as Stokes flow and the nutrient transport with an advection-diffusion equation. It is likely that the flow would affect the movement of the cells, and we would incorporate this by adding a drag force proportional to the relative velocity between the fluid and cells to the force balance on the cells. The effect of the shear stress on cell division would be incorporated by making the growth rate (and therefore the time to division) depend on the shear stress on the cell. As before, the agreement between the discrete and continuum cell models would be tested via numerical simulation.

4.11.4 Multiple aggregates and cell death

Using the same set-up, we would extend the model to deal with multiple aggregates by describing the growth of each aggregate with the continuum approximation if it contained a sufficiently large number of cells, or the discrete model if it contained a very small number of cells ($N = \mathcal{O}(1)$). One advantage of the discrete-to-continuum framework in this respect is that the continuum model closely approximates the discrete model for relatively small cell numbers ($N = \mathcal{O}(10)$), due to the approximation error being $\mathcal{O}(1/N^2)$. With multiple aggregates it would be necessary to give a description for adjacent aggregates moving or growing to touch other. We would assume that the aggregates moved or grew until the vertices of the end cells touched each other, at which point the vertices would be replaced by a single vertex and the external forces on the cell vertices replaced by the new cell pressures of the end cells. It is likely that the cell pressures would increase locally due to the end cells becoming compressed as the aggregates collided. The two aggregates would thereafter be treated as one larger aggregate. Simulations of this hybrid discrete-continuum cell model would be compared with simulations of the fully discrete cell model to check that the approximation was accurate.

Modelling multiple aggregates in this way would allow us to introduce cell death into the model. Cells would be assumed to die and become detached from the membrane in response to insufficient nutrient levels or high shear stresses. This would be described by the removal of the cell and the forces exerted on its end vertices, so that the aggregate containing the cell would be split into two smaller aggregates. The discrete model or continuum approximation would subsequently be used for the smaller aggregates according to the number of cells they contained. Simulations of the hybrid cell model would again be compared against those of the fully discrete model to verify accuracy.

Modelling multiple aggregates and cell death as described would constitute an adaptive hybrid discrete-continuum model of the set-up, since there would be switches between using the discrete and continuum descriptions at different times depending on the number of cells in an aggregate and the splitting and merging of aggregates.

4.11.5 Modelling cell growth in the HFB set-up

The final step needed to use the discrete-to-continuum framework to describe cell growth in the HFB would be to incorporate the hybrid cell model into the 2D HFB set-up of Chapter 3. This would require careful consideration of how the cells and the flow interact, since there would be flow incident on the cells through the membrane as well as over the top of them in the ECS. We would need to consider how the forces on the cells from the flow through the membrane affected their lateral movement and growth. We would model the

feedback effect of the cell growth on the flow and the nutrient transport in the same way as in Chapter 3, through decreases/increases in the permeability of the membrane surface and nutrient uptake as the cell aggregates grew/shrunk.

Simulating cell growth and proliferation in the HFB using this model with similar dependence on the nutrient concentration and shear stress as in the aggregate growth model in Chapter 3 would allow us to further assess the validity of that model as an approximation of a cell-based model.

4.11.6 Extension to higher dimensions

To use the discrete-to-continuum framework to model growth in higher dimensions, *e.g.* the growth of cell aggregates over the fibre surface in the HFB in 3D, it is necessary to extend the existing analysis to 2D and 3D. A significant challenge in doing this is that in 2D and 3D the neighbours of a cell are not fixed, but can change over time due to cell movement, growth and division.

Murray [180] showed that it is possible to derive the continuum limit of the 2D analogue of his linear-spring cell-centre model but only by making various simplifying assumptions, such as the neighbours of a cell being distributed at approximately equal angles about the cell and the cell connectivity tensor being locally constant. Murray obtained good agreement between the continuum limit and the cell-based model for the relaxation of cells to equilibrium in periodic rectangular and radially symmetric geometries and demonstrated that the framework was robust to the inclusion of cell division via a source term in the cell density equation as in the 1D case.

Deriving the continuum limit of the 2D analogue of our cell-vertex model is considerably more complicated, however, not least because it is necessary to account for changes in cell connectivity. Fozard *et al.* [78] reported that in a preliminary investigation of a 2D version of their model, cells adopted significantly different shapes in the interior and at the exterior of an aggregate, and suggested that it may be necessary to develop a hybrid model with a discrete model at the exterior matched to a continuum approximation in the interior to capture this effect (such as in the work of Kim *et al.* [127]). This provides further motivation for first developing a 1D hybrid discrete-continuum cell model as we have described.

Chapter 5

Discussion

Mathematical modelling can aid significant improvements in bioreactor design and operation by providing insight into the effects of changes in design and operating parameters on tissue growth. In this thesis, we have focussed on modelling cell expansion in the single-fibre hollow fibre bioreactor (HFB) shown in Figure 5.1. As discussed in Chapter 1, HFBs show great promise for efficient and controlled cell expansion and scaling-up laboratory tissue engineering experiments for clinical application. However, most existing models of cell culture in HFBs either completely neglect cell proliferation or consider shorter timescales than those associated with cell proliferation (*e.g.* those of transport processes), over which the cell population can be assumed to be in quasi-steady state (see §1.2.5). Consequently, there is a lack of knowledge about the feedback effects of cell proliferation, *i.e.* how it affects fluid and solute transport in the bioreactor, and how this in turn affects proliferation. The effects of mechanotransduction, for example due to fluid shear stress exerted on cells, in the HFB, which can be both positive and negative for cell proliferation, and the impact of the cell seeding distribution on proliferation have also generally been ignored in most previous studies. Thus, the first aim of this thesis has been to develop models of cell expansion in HFBs that account for the influence of fluid shear stress and cell seeding on cell proliferation, and the feedback effects of cell proliferation on fluid and nutrient transport.

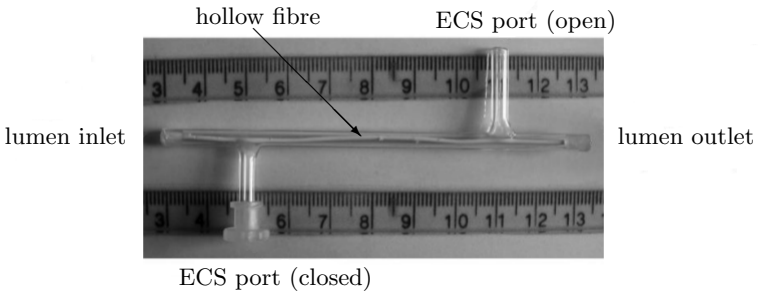

Figure 5.1: The single-fibre hollow fibre bioreactor modelled in this thesis. Adapted from [231].

As described in §1.2, the approaches taken to model cell culture in HFBs and other bioreactors have for the most part been based around standard continuum models of fluid and nutrient transport and tissue growth, and have not attempted to derive macroscale descriptions of cell dynamics from discrete representations of cells. During the initial stages of cell culture, it may be more appropriate to use a discrete description of the cell population rather than a continuum description, especially if the cell density is low. However, once the cell population becomes large it may be necessary to use a continuum description to ensure that the computational cost of simulations remains reasonable. It is also desirable to be able to couple discrete and continuum cell models to continuum models of nutrient transport and uptake in a consistent way. The second aim of this thesis has therefore been to consider an alternative framework for modelling coupled cell population growth and nutrient transport that enables individual cell dynamics to be incorporated into a continuum description.

5.1 Summary of key results

In this thesis we have developed continuum models of different stages of cell population expansion in the single-fibre HFB, and investigated the suitability of a hybrid discrete-continuum framework for modelling cell aggregate growth in the HFB. We have used the models to explore the range of growth behaviours possible for each system with changes in operating conditions, initial cell distribution and cell type. We have predicted how the growth of the cell population varies in response to changes in key operating parameters, such as the lumen inlet flow rate and outlet pressure, and the cell seeding distribution. In addition, we have been able to predict optimal conditions for maximising the yield of cell types with different oxygen requirements and shear stress tolerances. For instance, cell types with high oxygen demands but relatively low shear tolerance, such as hepatocytes and cardiomyocytes, require high rates of oxygen delivery with controlled levels of shear stress, so high inlet flow rates and intermediate outlet pressures are predicted to be optimal. Other cell types, such as chondrocytes, benefit from exposure to higher levels of shear stress, and our models suggest they are better suited by high inlet flow rates and high outlet pressures. To predict the growth of different cell types it has been necessary to make various constitutive assumptions about how cells grow and proliferate in response to chemical and physical stimuli, but the models we have developed are flexible and readily allow different assumptions to be incorporated. Below we summarise each of the models and the key results they have generated.

5.1.1 Cell layer growth model

In Chapter 2, we presented a 3D axisymmetric continuum model for the growth of a cell layer on the surface of the fibre in the HFB. This work significantly extended Shipley and Waters' description of fluid and solute transport in the HFB [231] to include cell proliferation and death, which were represented by the evolution of the cell layer free boundary in response to the local oxygen and lactate concentrations and fluid shear stress. The model was shown to be equivalent to a two-phase free boundary model of tissue growth (of the sort commonly used to describe tumour growth [25]), in which the cells and culture medium are treated as separate fluid phases with constant volume fractions. Via numerical simulations of the model we investigated the impact of opening the ECS ports and varying the lumen inlet flow rate and outlet pressure on the cell layer growth.

The simulations indicated that opening the ECS ports and increasing the flow rate and outlet pressure increased oxygen delivery to, and lactate clearance from, the cell layer, by increasing the radial flow through the membrane. This promoted growth—more so for cells with high oxygen demands—provided the cells could tolerate the increased shear stress due to the greater radial flow. Using the model we were able to identify lumen inlet flow rates and outlet pressures that maximised the yield of specific cell types over a culture period of 60 days, and found that a lower outlet pressure was required to optimise the growth of shear-sensitive cells. We also observed that variation in the cell layer depth along the fibre (which could arise, for example, from a non-uniform initial seeding distribution) could lead to significant reductions in growth for shear-sensitive cells when the ECS ports were open. Thus, while the simulation results suggested that it is better to culture cells with high oxygen demands, such as cardiomyocytes and hepatocytes, with the ECS ports open, it may be safer to culture highly shear-sensitive cells with lower oxygen demands, such as human foreskin fibroblasts, with the ECS ports closed, to avoid the risk of damaging the cells.

5.1.2 Cell aggregate growth model

In Chapter 3, we considered a different set-up, applicable to the initial stages of cell culture, with the upstream ECS port closed, the downstream port open and cells attached to the fibre surface in monolayer aggregates. One of the motivations for considering this set-up is that cells on the membrane surface are less likely to be damaged by high shear stresses than if both ECS ports are open, due to the weaker radial flow through the membrane, but oxygen delivery is still enhanced over both ports being closed. Rather than considering both axial and radial growth of the cell population as in Chapter 2, we focussed on axial expansion of the cell aggregates. The model was used to investigate the influence on the cell

aggregate growth of the inlet flow rate, outlet pressure and initial aggregate distribution, through their effects on the oxygen levels and shear stress experienced by the cells.

As well as assuming that the cell proliferation rate increases with oxygen concentration and cell death occurs at high shear stresses, as in Chapter 2, we modelled an increase in proliferation rate at intermediate shear stresses due to shear stimulation and cell death at low oxygen concentrations due to hypoxia. Initially we considered a simple distribution of evenly-spaced aggregates, to help isolate the effects of oxygen and shear stress on the aggregate growth. We observed that while the advective oxygen flux through the membrane and shear stress on the aggregates increased as either the flow rate or outlet pressure were increased, they were much more sensitive to changes in the outlet pressure than in the flow rate over typical ranges used in experiments. Accordingly, the time taken for aggregates of shear-tolerant cells to reach confluence was found to decrease significantly as the outlet pressure was increased, but only marginally as the flow rate was increased, for growth that depended either solely on the oxygen concentration or solely on the shear stress (due to improved oxygen delivery and shear stimulation respectively).

Model simulations revealed that shear-sensitive cells, however, did not grow to confluence at high outlet pressures. By performing additional simulations we were able to identify operating conditions and initial aggregate distributions for which oxygen delivery to the cells was enhanced without them being exposed to damaging levels of shear stress. In the alternative distributions we considered, the aggregates were concentrated towards the inlet end of the membrane, spaced evenly along the membrane, or concentrated towards the outlet end. The optimal conditions for growth were found to depend strongly on the oxygen requirements and shear tolerance of the cell type being cultured. For example, using high flow rates and high outlet pressures, and seeding aggregates towards the outlet end of the membrane, gave the greatest cell yields for cell types with high oxygen demands and high shear tolerance; while low flow rates, intermediate outlet pressures, and uniform cell distributions gave the greatest yields for cells with low oxygen demands and low shear tolerance. The differences observed with different cell types highlight the importance of measuring the oxygen requirements and shear tolerance of the cells prior to culture, and having control over the initial cell distribution, for maximising the cell yield.

5.1.3 Discrete-to-continuum modelling of aggregate growth

Finally, in Chapter 4, we assessed the suitability of an alternative framework for modelling cell aggregate growth in the HFB based on the discrete-to-continuum cell modelling frameworks of Fozard *et al.* [78] and Murray *et al.* [181]. These frameworks are potentially very useful for describing cell aggregate growth in the HFB, as they provide consistent discrete

and continuum representations of cell aggregate growth that can be used for low and high cell density regions respectively. However, they lack a description of how the extracellular environment affects the behaviour of the cells, in particular, of how external nutrient supply affects their growth. We therefore extended Fozard *et al.*'s cell-vertex framework by coupling it to a continuum model of nutrient transport and uptake. We considered a simple static culture set-up, with a 1D aggregate of discrete cells absorbing nutrient and growing along the base of a 2D nutrient bath. The cells were represented as linear springs whose resting lengths grew in response to the local nutrient concentration and extension/compression of the cells. Following Fozard *et al.*'s approach, we derived a continuum approximation of the model in the limit of large cell number.

The main objective of this work was to determine if the discrete cell model and continuum approximation still agreed closely when coupled to the nutrient transport model. This was not necessarily guaranteed as the nutrient transport equations were not formally homogenised in deriving the continuum limit. We confirmed via numerical simulations that the discrete and continuum models did continue to agree closely (and to converge as the cell number increased) with coupling to the nutrient transport. We also investigated the possible model behaviours associated with different growth laws, and observed that the oxygen demands, oxygen supply and mechanosensitivity of the cells could all significantly impact the overall growth of the aggregate.

In deriving the continuum limit of the discrete cell model, we showed that the continuum limits of Murray *et al.*'s cell-centre model and Fozard *et al.*'s cell-vertex model are the same in 1D (*i.e.* they give the same nonlinear diffusion equation for the cell density), provided the cell interaction force (or cell 'pressure') in each model is the same. This is unlikely to be the case in higher dimensions, however, due to the differences in the way cells rearrange through movement, growth and division in 2D and 3D cell-centre and cell-vertex models. In 2D and 3D cell-centre models, contacts between cells change as the distances between their centres change, but in 2D and 3D cell-vertex models, cell contacts change with the formation of new cell edges and removal of existing cell edges. This can result in significant differences in model behaviour [196, 267], and could plausibly, therefore, lead to quite different continuum limits. Deriving continuum limits of 2D and 3D cell-centre and cell-vertex models corresponding to the 1D models of Murray *et al.* and Fozard *et al.*, and investigating how they differ, would be an interesting subject for future research.

In Chapter 4 we also showed that the cell aggregate growth law used in Chapter 3 is equivalent to the continuum limit of our cell-vertex model with incompressible cells. This was true either with cell growth included in the cell-vertex model via a suitable growth law for the cell resting lengths, or with cell proliferation included in the continuum limit

via a source term in the diffusion equation for the cell density. In the latter case this was as expected, since the growth law in Chapter 3 treated the cells in the aggregates as incompressible, by assuming that they instantaneously push each other outwards along the membrane upon division.

5.2 Further work

In developing each of the models in this thesis, we have stated the assumptions made regarding parameter values and constitutive laws for which there is a lack of experimental data. We have also discussed experiments that could be performed to determine unknown parameter values and validate our model predictions. In addition to the further work already discussed (see §§2.10, 3.8 and 4.11), we now consider other extensions and improvements to the models we have presented.

In the HFB models in Chapters 2 and 3, we assumed that the fibre membrane could be treated as a homogeneous porous medium with a constant permeability. We used a value for the permeability determined from experimental measurements of the retentate and permeate masses as described in Appendix A. However, the membrane permeability does in fact vary to some degree between different fibres and within each fibre due to the nature of the fabrication process. Given that the membrane permeability is a key determinant of the flow through the bioreactor, it would therefore be useful to determine the sensitivity of the cell layer and cell aggregate growth to this variation. This could be achieved by simulating the growth with different values of the averaged membrane permeability and with different functions of space for the permeability. If the predicted growth was found to be sensitive to these parameters, experiments similar to those in Appendix A could be performed to quantify the variation in the permeability between different fibres and within individual fibres, to determine if it was likely to significantly affect the growth.

Other information that would aid the parameterisation and validation of the cell aggregate growth model includes better characterisation of the cells being cultured (*i.e.* their oxygen requirements, shear tolerances and proliferation rates); measurements of the seeding efficiency and typical cell distributions following seeding; and measurements of the cell density and distribution through time for different cell types. This data would provide us with more realistic inputs for the model and measurements against which to test the growth rates predicted.

A key assumption in the cell layer and aggregate growth models is that the cell density remains constant as the layer and aggregates grow. This could be tested by measuring the cell density at various stages of the cell culture process by staining the cell nuclei in the layer/aggregates. Significant variation in the cell density in the cell layer could be

incorporated into the model by treating the layer as a three-phase mixture of cells, fluid and ECM, with mass transfer between the phases to account for cell proliferation and ECM deposition (as in [204, 205] but with a varying ECM fraction). Variation in the cell density in the aggregates could be accounted for by allowing the indicator function for the aggregates to vary continuously with position in each aggregate, rather than just being constant inside each aggregate.

The accuracy of the cell layer model could be improved by relaxing the assumptions that the cell layer, fluid flow and solute distributions are symmetric about the lumen axis, since azimuthal variation in the cell layer depth and the asymmetric positions of the ECS ports will introduce some asymmetry into the flow and solute transport. However, solving the coupled flow, solute transport and cell layer growth equations for the full bioreactor geometry (with the ECS ports at opposite ends of the ECS on either side of the bioreactor) and azimuthal variation in the cell layer depth would require computationally expensive numerical methods. This is also true of extending the cell aggregate growth model to three dimensions to account for flow asymmetry and variation in the aggregate distribution over the full fibre surface. Nevertheless, this would provide useful information on the validity of the simplified 2D model we have presented and allow a more detailed investigation of the relationships between the aggregate distribution, flow and growth. It would also enable the cell aggregate growth and cell layer growth to be modelled with the same flow regime (*e.g.* with both ECS ports open or only the downstream port open), to compare how the optimal conditions for growth differ between the two.

There are a number of other extensions to the HFB growth models that could be investigated. We have focussed on the effects of changes in the inlet flow rate and outlet pressure on cell population expansion, but we could also consider the impact of varying the inlet nutrient concentration or the flow configuration. For instance, we could consider the effect of imposing a flow through the ECS in the same or the opposite direction to the lumen flow (as in [204, 205]), and compare the resulting growth behaviour with that for the flow configurations we have considered. We have also restricted our attention to the transport of oxygen, since it is considered to be the rate-limiting nutrient for cell proliferation. However, it would be straightforward to include the transport of other key nutrients, such as glucose and proteins, in the models via the addition of extra reaction-advection-diffusion equations (as in [235]).

Another simple extension would be to consider variation in the operating conditions with time. Given the non-uniformity of the oxygen and shear stress distributions in the bioreactor observed in the models in Chapters 2 and 3, and the changes in these distributions as the cell population grows, greater cell yields could potentially be obtained by varying the operating

conditions over the course of the culture period. Indeed, much higher outlet pressures were required to achieve the same shear stresses on cells at the surface of the cell layer (Chapter 2) as on cell aggregates on the fibre surface (Chapter 3), due to the decrease in the shear stress with distance from the fibre surface. Proliferation of cells over the fibre surface and then outwards into the ECS will in general lead to increased resistance to fluid flow through the ECS and greater oxygen uptake, and hence reductions in the oxygen concentration and shear stress experienced by the cells. Therefore, to sustain the cell proliferation rate it may be necessary to increase one or all of the outlet pressure, flow rate and inlet concentration with time to maintain oxygen and shear stress levels. We could test this straightforwardly in the cell layer and cell aggregate growth models by simulating the growth with operating conditions as prescribed functions of time (*e.g.* the outlet pressure increasing linearly with time).

It would be useful to compare our results with those obtained for different HFB set-ups (such as those in [2, 55, 177, 204, 205, 231, 280]) and other similar perfusion systems [41, 46, 272, 288] to determine whether they differ and whether alternative set-ups could yield further improvements in growth for specific cell types. As our primary interest has been in the use of HFBs to expand cell populations, we have concentrated on predicting the conditions that maximise the growth of monocultures, and not considered co-culturing multiple cell types or cell differentiation. Alternative goals, such as achieving non-uniform cell distributions (appropriate to liver zonation [56]) or specific proportions of different cell types in the culture of multiple cell populations [203], could nonetheless be investigated with our models.

The further work necessary to incorporate the discrete-to-continuum modelling framework of Chapter 4 into a model of cell aggregate growth in the HFB was discussed in detail in §4.11. Here, therefore, we simply note that the most important step needed to apply this framework to cell growth and proliferation in the HFB would be to parameterise and validate the laws used to describe cell-cell interactions, growth and proliferation. In addition to the discrete-to-continuum approach we have considered, it would be instructive to investigate other modelling approaches, such as hybrid cellular automata [39, 42, 180] with stochastic rules for cell movement and proliferation, to compare their suitability for modelling cell population growth in the HFB.

In conclusion, there are numerous avenues for further research based on the work presented in this thesis. However, the models we have developed have already provided insight into the effects of operating conditions and seeding strategies on cell population growth in HFBs. In addition, the models have been used to predict optimal conditions for growth

that can be tested experimentally, and will aid future improvements in the protocols used to expand cell lines in HFBs.

Appendix A

Determination of membrane permeability

To determine the flow through the HFB in the cell layer and cell aggregate growth models in Chapters 2 and 3 an estimate of the membrane permeability k_m is required. Here we describe how this is determined.

A.1 Theory

The membrane permeability may be estimated using the model of fluid transport in the HFB with the ECS port open presented in §2.4.1 and §2.6.1 combined with experimental data for $Q_{l,out}$, $Q_{e,out}$ and $P_{l,out}$ for the set-up without any cells. Equations (2.64), (2.93) and (2.102) give the dimensional lumen outlet flow rate as

$$Q_{l,out} = 2\pi R_l^2 U \hat{Q}_{l,out} = \frac{1}{\cosh\lambda}\left(Q_{l,in} - \frac{\pi R_l^2 U}{8}\hat{P}_{l,out}\lambda\sinh\lambda\right). \tag{A.1}$$

If we know $Q_{l,out}$ and $Q_{e,out}$, then the lumen inlet flow rate is given by $Q_{l,in} = Q_{l,out} + Q_{e,out}$ and the lumen flow velocity scale is given by $U = Q_{l,in}/(2\pi R_l^2)$. Hence, rearranging (A.1) and substituting for $Q_{l,in}$ and U gives an implicit equation for λ in terms of $Q_{l,out}$, $Q_{e,out}$ and $\hat{P}_{l,out}$

$$16Q_{l,out}\cosh\lambda + (Q_{l,out} + Q_{e,out})(\hat{P}_{l,out}\lambda\sinh\lambda - 16) = 0. \tag{A.2}$$

Solving (A.2) numerically by the Newton-Raphson method (with an initial guess for λ of 0.2) yields a unique positive value for λ, and from (2.90) with $\hat{R}_c(z,t) = \hat{R}_m$ (since there is no cell layer) we have

$$\lambda^2 = \frac{16}{\kappa_m \ln\hat{R}_m}, \tag{A.3}$$

so we can estimate the permeability by

$$k_m = \frac{d^2\epsilon^2}{\kappa_m} = \frac{d^2\epsilon^2\lambda^2\ln\hat{R}_m}{16}. \tag{A.4}$$

A.2 Experiment

PLGA-PVA hollow fibres were fabricated from a dope of 1:3:16 PVA:PLGA:NMP (N-Methyl-2-pyrrolidone) by electrospinning, as described in [70] and [268]. This process essentially involves pumping the dope solution through the outer bore of a spinneret vertically downwards into a water bath, with a fast jet of deionised water (the non-solvent) flowing down the middle from an inner needle to form the lumen. The water in the tank and jet causes the PLGA-PVA to polymerise to form a long hollow cylindrical fibre with a porous membrane. The diameter of the lumen and membrane depth can be altered by changing the width of the needle and the flow rates of the polymer solution and jet, while other properties of the membrane such as the pore size and its hydrophilicity change with the proportion of PVA in the dope [174], the size of the air gap above the water bath and temperature [70]. The fibres used here had a mean pore diameter of 1.1 µm, a porosity of 0.77 [174], a lumen diameter of 400 µm and a membrane depth of 200 µm [233]. After fabrication the fibres were left in distilled water for 2 days to ensure that any remaining solvent diffused out of the membrane, and then left to dry.

To set up the single-fibre module, a length of dried fibre was inserted into the glass module and glued in place using Araldite epoxy resin. The ends of the fibre protruding from the glass module were then carefully cut off with a scalpel (without crushing the membrane). The membrane was wetted by pumping 70% ethanol through the lumen and gradually increasing the pressure at the lumen outlet (by screwing up the clamp on the rubber outflow tube a bit at a time) until ethanol beads appeared on the membrane surface from the ethanol permeating the membrane. After 15 minutes, the feed was switched to phosphate buffered saline (PBS) and left for a further 15 minutes to wash out the ethanol. Readings of the lumen outlet pressure were then taken with a pressure gauge accurate to ± 0.1 psi, and the retentate and permeate mass measured with scales accurate to ± 0.005 g, every 5 minutes for 30 minutes.

A.3 Results

Table A.1 shows the readings obtained for the lumen outlet pressure and retentate and permeate masses from the experimental procedure described above. These values have been converted into the dimensionless lumen outlet pressure and lumen and ECS outlet

flow rates using the following formulae

$$\hat{P}_{l,out} = \frac{\epsilon^2 L}{\mu U} f_c (P_{l,out} - P_{atm}), \tag{A.5}$$

$$Q_{l,out} = \frac{m_{Ret}}{\rho T_{int}}, \tag{A.6}$$

$$Q_{e,out} = \frac{m_{Perm}}{\rho T_{int}}, \tag{A.7}$$

where the values of the parameters are as given in Table 2.1, $f_c = 6894.76$ is the conversion factor for pressure from psi to Pa [68], m_{Ret} and m_{Perm} are the retentate and permeate masses collected in each time interval $T_{int} = 300\,\text{s}$. The membrane permeability has been calculated for each set of readings in the final column by the method outlined above. Taking the mean of these values as the membrane permeability gives $k_m = 2.39 \times 10^{-16}\,\text{m}^2$. This estimate is used in both Chapter 2 and Chapter 3.

t (mins)	Gauge pressure, $P_{l,out} - P_{atm}$ (psi)	$\hat{P}_{l,out}$	Retentate mass, m_{Ret} (g)	Permeate mass, m_{Perm} (g)	$Q_{l,out}$ ($10^{-8}\,\text{m}^3\,\text{s}^{-1}$)	$Q_{e,out}$ ($10^{-8}\,\text{m}^3\,\text{s}^{-1}$)	k_m ($10^{-16}\,\text{m}^2$)
0	4.2	-	-	-	-	-	-
5	4.1	104.5	6.219	1.936	2.073	0.645	2.366
10	4.1	102.6	6.343	1.963	2.114	0.654	2.396
15	4.0	101.5	6.258	1.934	2.086	0.645	2.419
20	4.1	102.6	6.278	2.033	2.093	0.678	2.483
25	4.2	106.2	6.204	2.023	2.068	0.674	2.417
30	4.6	116.1	6.180	2.061	2.060	0.687	2.260

Table A.1: Readings for the lumen outlet pressure $\hat{P}_{l,out}$ and lumen and ECS outlet flow rates, $Q_{l,out}$ and $Q_{e,out}$, used to estimate the membrane permeability k_m.

Appendix B

Estimation of parameter values

In this appendix we explain how we estimate the growth and seeding parameters for the cell layer and cell aggregate growth models in Chapters 2 and 3.

B.1 Cell layer growth model

B.1.1 Growth rate

We estimate the growth rate of the cell layer per unit concentration, A_p, for different cell types from their cell doubling times (see Table B.1). As we have assumed that only the outermost layer of cells in the cell region proliferates, we can assume that in the absence of cell death the depth of the cell region will increase by approximately one cell diameter d_{cell} in the cell doubling time T_d, so that

$$A_p \approx \frac{d_{cell}}{C_{in} T_d}.$$

Estimates for A_p for different cell types are given in Table B.1. For simplicity we assume that the baseline recession rate of the cell layer due to cell death and detachment from excess lactate or shear stress, B_d, is the same as the rate at which the cell layer grows due to cell proliferation, $A_p C_{in}$, and the dimensionless weights for the excess lactate and shear stress recession rates, B_L and B_s, are both 1, so that $\beta_L = B_L B_d/(A_p C_{in}) = 1$, $\beta_s = B_s B_d/(A_p C_{in}) = 1$, and $\beta_{L,s} = B_L B_s B_d/(A_p C_{in}) = 1$.

B.1.2 Concentration thresholds

For the minimum oxygen concentration required for cell proliferation, C_{min}, we use data for minimum culture requirements for different cell types from [231] (see Table B.2). Experimental data for the concentration at which lactate becomes toxic to the cells, L_{max}, is more limited. It has been estimated that a lactic acid concentration of around $0.4\,\mathrm{mol\,m^{-3}}$ is harmful to growing cells in a buffered cultured medium, assuming that growing cells can

Cell type	d_{cell} (µm)	T_d (hrs)	$A_p = d_{cell}/(C_{in}T_d)$ $(\mu m\,hr^{-1}\,(mol\,m^{-3})^{-1})$	Reference
Neonatal rat cardiomyocytes	10	20	2.3	[250]
Primary rat hepatocytes	10	20	2.3	[55, 187]
Bovine chondrocytes	10	56	1.8	[85, 272]
HFFs	40	17	12.1	[129]

Table B.1: Cell doubling time T_d and estimated cell layer growth rate per unit oxygen concentration A_p for different cell types.

tolerate a pH change of up to ±0.5 [272]. Lactate is produced by the dissociation of lactic acid in equimolar ratios, which suggests $L_{max} \approx 0.4\,mol\,m^{-3}$. We use this value for L_{max} for all cell types in our simulations, but also separately investigate the sensitivity of the cell layer growth to L_{max}.

Cell type	C_{min} $(mol\,m^{-3})$	$c_{min} = C_{min}/C_{in}$	Reference
Neonatal rat cardiomyocytes	6×10^{-3}–8×10^{-2}	0.027–0.36	[29, 215]
Primary rat hepatocytes	2.1×10^{-2}	0.095	[47, 246]
Pancreatic βTC3 cells	1.46×10^{-2}	0.066	[241, 260]
Bovine chondrocytes	2.2×10^{-3}–1.32×10^{-2}	0.01–0.06	[76]
Human foreskin fibroblasts (HFFs)	2.1×10^{-2}	0.095	[129]

Table B.2: Dimensional and dimensionless minimum oxygen concentration required for cell proliferation, C_{min} and c_{min}, for various cell types. (Adapted from [231].)

B.1.3 Shear stress parameters

To estimate the dimensionless shear stress constant, $\kappa_s = 8k_c/(R_l d)$, we need to estimate the size of the interstitial spaces in the cell layer d. Using equation (2.82) and our estimate for k_c from §2.5.1 ($7.5 \times 10^{-13}\,m^2$) gives $d \approx \sqrt{k_c/C} = 3.4 \times 10^{-5}\,m$, so $\kappa_s \approx 8.9 \times 10^{-4}$. The maximum shear stress that the cells can withstand without dying or detaching from the surface of the cell layer, Σ_d, depends to a large extent on the cell type. Table B.3 lists the effects of different shear stress regimes on the growth of various cell types. While bovine chondrocytes grow well under shear stresses of up to 2 Pa [240], rat cardimyocytes can be

damaged or killed by shear stresses higher than 0.16 Pa. The data also suggests that the shear stress that cells can withstand decreases (from order 1 Pa to order 0.1 Pa and smaller) as the length of time that they are exposed to it increases. Studies with human foreskin fibroblasts (HFFs) and mouse osteoblasts in micro-channel bioreactors have shown that cell detachment can occur at shear stresses as low as 0.03 Pa [129, 142]. To incorporate the possibility of thinning of the cell layer due to cell detachment, we use values of Σ_d in the range 0.03–2 Pa that are appropriate to the cell types we consider. The corresponding range of the dimensionless shear stress σ_d is 4×10^{-4}–3×10^{-2}. The smoothing factors s_L and s_s for the lactate and shear-stress dependence in the growth function $\hat{G}$ (equation (2.80)), *i.e.* in $\mathrm{F}(c_L - l_{max}) = \frac{1}{2}[1 + \tanh(s_L(c_L - l_{max}))]$ and $\mathrm{F}(\sigma_d - \sigma) = \frac{1}{2}[1 + \tanh(s_s(\sigma_d - \sigma))]$, are chosen as 10 and 10^5 respectively.

Cell type	Bioreactor type	Shear stress threshold	Effect	Reference
Neonatal rat cardiomyocytes	parallel micro-channel array	> 0.16 Pa	cell damage and death	[215]
Rat hepatocytes	micro-channel flat plate	0.1–1 Pa for 12 hrs	no adverse effect	[285]
Pancreatic β-cells	dammed micro-channel	0.1–1.4 Pa for 24–48 hrs	impaired metabolic function at highest shear stresses	[223]
Bovine chondrocytes	cone viscometer	1.6–2.2 Pa for 72 hrs	increased glycosaminoglycan (GAG) synthesis	[240]
Endothelial cells	2D parallel plate laminar flow chamber	2.3 Pa for 1 hr	no adverse effect	[285]
Leukocytes	stirred-flask	0.5–10 Pa for 12 hrs	adherent cells detached from surfaces	[285]
Human hepatocytes	rotating HFB	0.5–2 Pa for 12 days	specific functions of liver cells compromised leading to toxicity	[47]
		> 2 Pa	cell death	
HFFs	micro-channel flat plate	> 0.03 Pa for 2 days	cell detachment	[129]
Mouse calvarial osteoblasts MC3T3-E1	3D micro-channel array	0.035 Pa for 2 days	cell detachment	[142]

Table B.3: Effects of different shear stress regimes on different cell types in perfusion bioreactors.

B.2 Cell aggregate growth model

B.2.1 Oxygen uptake flux

Table B.4 gives the maximal oxygen uptake rates of different cell types. It is clear from the data that the maximal volumetric uptake rate V_{max} varies considerably with cell type and cell density. We assume that for a given cell type the cell density in the aggregates is initially constant, and remains so as they grow, so that the maximal uptake flux M is constant. For the cell types in Table B.4, the cellular oxygen uptake rate M_c (the number of moles of oxygen taken up by one cell per second) lies in the range 1.86×10^{-18}–$8.9 \times 10^{-17}\,\mathrm{mol\,cell^{-1}\,s^{-1}}$. We estimate M by multiplying M_c by the cell surface density ρ_s. For ρ_s we use the range of cell surface densities observed for Chinese hamster lung fibroblasts cultured for 12 days in a HFB in [251]: 5×10^8–$7.3 \times 10^{10}\,\mathrm{cells\,m^{-2}}$. This gives values for M in the range 9.3×10^{-10}–$6.5 \times 10^{-6}\,\mathrm{mol\,m^{-2}\,s^{-1}}$ (Table B.4), which agrees well with the estimate of $M = 1.5 \times 10^{-8}\,\mathrm{mol\,m^{-2}\,s^{-1}}$ for human foreskin fibroblasts used by Korin *et al.* [129]. The corresponding range for $\mathrm{Da} = R_l M / D_e C_{in}$ is 2.8×10^{-4}–2.0. The reduced model is valid for $4 \times 10^{-6} = \epsilon^2 \ll \mathrm{Da} \ll 1/\epsilon^2 = 2.5 \times 10^5$, so it is valid for all the cell types given in Table B.4.

B.2.2 Seeding and growth parameters

Using experimental data we obtain estimates of a typical initial cell density and aggregate elongation rate for the model set-up.

B.2.2.1 Initial cell density

Ellis and Chaudhuri [70] seeded an 8 ml inoculum of 500,000 cells (equating to a cell concentration of $6.25 \times 10^{10}\,\mathrm{cells\,m^{-3}}$) onto 10 PLGA fibres of similar dimensions to those in Table 2.1. For a dynamic seeding protocol on a rotating mixer, they found that on average 65% of the cells in the seeding mixture attached to the fibres. This gives an estimate of the initial cell density via

$$\begin{aligned}
\text{no. of cells attached to each fibre} &= \text{no. of cells in inoculum/no. of fibres} \times \text{seeding efficiency} \\
&= 500,000/10 \times 0.65 = 32,500, \\
\text{surface area of fibre} &= 2\pi R_m L = 2\pi(4 \times 10^{-4}) \times 0.1 = 2.51\,\mathrm{cm^2}, \\
\text{initial cell density} &= \text{no. of cells/fibre surface area} \\
&= 32,500/2.51 \approx 13,000\,\mathrm{cells/cm^2}.
\end{aligned}$$

When attached to the membrane in a monolayer, cells have a flatter morphology and a typical cell diameter of 40 µm [129], so, if we approximate the cells as being circular in

Cell type	Cell density (cells m^{-3})	V_{max} (mol m^{-3} s^{-1})	M_c (mol $cell^{-1}$ s^{-1})	$M = M_c\rho_s$ (mol m^{-2} s^{-1})†	Reference
Neonatal rat cardiomyocytes	10^{12}	2.64×10^{-3}	4.22×10^{-18} *	2.11×10^{-9} – 3.08×10^{-7}	[215]
Primary rat hepatocytes	1.25×10^{13}	1.76×10^{-3}	2.82×10^{-18} *	1.41×10^{-9} – 2.06×10^{-7}	[246]
Pancreatic βTC3 cells	2.8×10^{14}	6.37×10^{-3}	1.02×10^{-17} *	5.1×10^{-9} – 7.45×10^{-7}	[260]
Chinese hamster lung H1 fibroblasts	10^{12}	3.9×10^{-5}	3.9×10^{-17}	1.95×10^{-8} – 2.85×10^{-7}	[251]
Mouse hybridoma CR1606 cells	2×10^{14}	2.8×10^{-5}	2.8×10^{-17}	1.4×10^{-8} – 2.04×10^{-6}	[207, 208]
Bovine chondrocytes	2×10^{14}	1.17×10^{-3}	1.86×10^{-18}	9.3×10^{-10} – 1.36×10^{-7}	[189]
Human mesenchymal stem cells (hMSCs)	10^{12}	3.3×10^{-6}	3.3×10^{-18}	1.65×10^{-9} – 2.41×10^{-7}	[288]
Rat hepatocytes	5×10^{12}	4.45×10^{-4}	8.9×10^{-17}	4.45×10^{-8} – 6.5×10^{-6}	[230]
HepG2 hepatocytes	10^{13}	2.4×10^{-4}	2.4×10^{-17}	1.2×10^{-8} – 1.75×10^{-6}	[187]
Porcine hepatocytes	2.5×10^{13}	8.25×10^{-4}	3.3×10^{-17}	1.65×10^{-8} – 2.41×10^{-6}	[53]
HFFs	3.8×10^{12}	1.15×10^{-4}	3×10^{-17}	1.5×10^{-8}	[129]

Table B.4: Oxygen uptake rates for different cell types grown in the ECSs of HFBs. Maximal volumetric oxygen uptake rate V_{max} and cellular oxygen uptake rate M_c. For more data on oxygen uptake rates for hepatocytes see Table 1 in [201].
* Estimated using $M_c \approx V_{max}V_{cell}$, where $V_{cell} \approx 1.6 \times 10^{-15}\,m^3$ is the cell volume, approximated by treating cells as spherical with an average diameter of 14.5 µm (average of cell diameters in Table B.5)
† Range for $\rho_s = 5 \times 10^8$–7.3×10^{10} cells m^{-2} taken from [251], apart from for HFFs for which $\rho_s = 5 \times 10^8$ cells m^{-2} [129].

cross-section in the plane of the surface, the fraction of the membrane surface covered by the cells is

$$\begin{aligned}\text{fraction of membrane surface covered} &= \text{total area covered by cells/membrane surface area}\\ &= \text{no. of cells} \times \text{cell area/membrane surface area}\\ &= \text{cell density} \times \text{cell area}\\ &= (1.3 \times 10^8) \times \pi(20 \times 10^{-6})^2 = 0.16.\end{aligned}$$

Cell type	Cell diameter (μm)	Reference
Chinese hamster ovary (CHO) cells	12.8	[227]
Mouse hybridoma	13.7	[107]
Human embryonic kidney cells	14.5	[119]
CHO cells	13.9	[108]
CHO cells	17.1	[45]

Table B.5: Average cell diameters for different cell types cultured in 3D perfusion bioreactors.

Assuming that the percentage coverage is the same in 1D as in 2D, *i.e.* 16% of the line along the outer surface of the membrane in our model is covered by cells, the initial number of cells on the line is approximately

$$\begin{aligned}\text{number of cells on membrane line segment} &= \text{length covered by cells/cell diameter}\\ &= 0.016/(40\times10^{-6}) = 400.\end{aligned}$$

This number corresponds to the cell concentration in the inoculum and seeding efficiency in [70]. For our simulations, we assume that 25% of the membrane is initially covered by cells (*i.e.* that the initial total aggregate length is 2.5 cm, equivalent to ∼625 cells), corresponding to a higher concentration of cells in the inoculum or higher seeding efficiency or both.

B.2.2.2 Aggregate growth rate

We estimate the baseline aggregate growth rate, A_1, for the case in which the concentration and shear stress at the aggregates are constant and $c_e|_{y=R_m} > C_{max}$, $\sigma_{e,xy}|_{y=R_m} < \Sigma_p$. For this case there is no cell death and the aggregate growth rate is proportional to the aggregate length, with $A_1(C_{max} - C_p)$ as the constant of proportionality, *i.e.* the length of the jth aggregate, L_j, satisfies

$$\frac{\mathrm{d}L_j}{\mathrm{d}t} = A_1(C_{max} - C_p)L_j, \quad i = 1,\ldots,N, \quad \Rightarrow \quad L_j(t) = L_j(0)e^{A_1(C_{max}-C_p)t}.$$

Hence, if we assume that the aggregate length doubles when the population doubles and there are approximately 1.5 population doublings in 7 days [70], we can use the fact that $C_{max} - C_p < C_{in}$ to calculate a lower bound for A_1

$$A_1 = \frac{\ln\frac{L_j}{L_j(0)}}{(C_{max}-C_p)t} > \frac{1.5\ln 2}{0.22\times 7} = 0.68\,\mathrm{day}^{-1}\,(\mathrm{mol\,m}^{-3})^{-1} = 7.8\times10^{-6}\,\mathrm{s}^{-1}\,(\mathrm{mol\,m}^{-3})^{-1}.$$

The rates at which cells in the aggregates die due to insufficient oxygen and excess shear stress, B_1B_0 and B_2B_0, will vary according to cell type, but in the absence of experimental

data we assume that they are both slower than the cell proliferation rate and take them to be $B_1B_0 = B_2B_0 = A_1C_{in}/2$.

B.2.2.3 Oxygen and shear stress thresholds

As described above, the functional form we adopt for the dependence of the growth on the oxygen concentration is an approximation of a sigmoidal relationship. For the minimum concentration needed for cells to survive, C_d, we use the values for C_{min} from Table B.2 (noting that here we have assumed cells are quiescent for $C_d < c_e|_{y=R_m} < C_p$). Experimental data with which we can estimate the cell proliferation and the maximal growth rate concentration thresholds, C_p and C_{max}, is not readily available. We therefore pick different values of the concentration thresholds in the ranges $C_p = 0.05$–$0.1\,\mathrm{mol\,m^{-3}}$ and $C_{max} = 0.18$–$0.21\,\mathrm{mol\,m^{-3}}$, such that the range over which the growth rate is not constant in c_e ($c_e \in (C_p, C_{max})$) is large.

Various shear stress regimes used to culture different cell types in perfusion bioreactors are listed in Table B.6. It is evident that the shear stresses used vary hugely depending on the cell type, bioreactor and culture period. However, the shear stress regimes tend to fall into two broad categories: short-term, often cyclical, exposure (24–72 hrs) of 2D cell cultures to high shear stresses (0.01–2 Pa); and long-term steady exposure (7–21 days) of 3D cultures to much lower shear stresses (1×10^{-5}–0.2 Pa). The latter category is more appropriate to the set-up considered in Chapter 3 and the shear stresses on the aggregates fall in the same range (see §3.7). In their respective reviews of the influence of shear stress on osteogenic cell lines, Yeatts and Fisher [282] and McCoy and O'Brien [169] identified the optimum shear stress ranges for 3D culture to be 0.005–0.1 Pa and 0.01–0.05 Pa. We use these ranges as a rough guide for the shear stress threshold for increased proliferation, Σ_p, considering values in the range $\Sigma_p = 0.01$–0.05 Pa. Further examples of increased proliferation in response to shear stress stimulation are given in Table B.7.

The data in Table B.3 suggests that, while endothelial cells and osteoblasts may be tolerant to short-term exposure to shear stresses in excess of 2 Pa in parallel plate flow chambers, cells cultured for longer periods in microfluidic devices can be damaged by much lower shear stresses (0.03–0.16 Pa). Therefore, for the shear stress threshold for cell death, Σ_d, we use values in the range 0.05–0.16 Pa that are appropriate to the cell types considered.

Cell type	Bioreactor type	Shear stress range (Pa)	Duration	Reference
hMSCs	3D steady perfusion	1×10^{-5}–1.2×10^{-4}	20 days	[289]
Bone marrow stromal cells (BMSCs)	2D parallel plate flow chamber	0.16	5–120 mins every other day 20 days	[132]
Rat BMSCs	2D radial flow device	0.036–0.27	30 mins every other day for 13 days	[131]
Rat BMSCs	3D steady perfusion	0.1–0.2	16 days	[14]
Human BMSCs	3D perfusion	0.005–0.015	28 days	[151]
Fetal calf endothelial cells	2D rotating dish	0.03–0.17	24 hrs	[11]
Fibroblasts	3D perfusion	0.1–2	72 hrs	[147]
Bovine aortic endothelial cells	2D parallel plate flow chamber	1.2	5 mins–16 hrs	[261]
Rat calvarial osteoblasts, human umbilical vein endothelial cells, baby hamster kidney fibroblasts	2D parallel flow chamber	0.01–3.5	15 mins	[217]
Rat BMSCs	3D steady perfusion	0.005	4–16 days	[237]
Mouse osteosarcoma K8	3D steady perfusion	1.57×10^{-4}	21 days	[172]
Mouse MGZ5 embryonic stem cells	2D parallel plate flow chamber	0.15–1	24–72 hrs	[279]
Human hepatocytes	rotating HFB	0.05	12 days	[47]
Rat cardiomyocytes	parallel micro-channel array	0.1	3 days	[215]
HFFs	micro-channel flat plate	0.02	14 days	[129]
Mouse calvarial osteoblasts MC3T3-E1	3D micro-channel array	0.005	7 days	[142]

Table B.6: Shear stress ranges used to culture different cell types in different perfusion bioreactors.

Cell type	Bioreactor type	Shear stress regime	Effect	Reference
Human osteoblasts	2D parallel plate flow chamber	2 Pa for 30 mins	increased proliferation	[121]
Bovine chondrocytes	2D parallel plate flow chamber	3.5 Pa for 96 hrs	1.5 × higher proliferation rate	[162]
Mouse MGZ5 embryonic stem cells	2D parallel plate flow chamber	0.15–1 Pa for 24–72 hrs	increased proliferation	[279]
hMSCs	3D steady perfusion	1.2×10^{-4} Pa for 20 days	increased proliferation	[289]

Table B.7: Examples of increased cell proliferation in perfusion bioreactors due to shear stimulation.

Appendix C

Reduced model for cell layer growth with ECS port closed

C.1 Mass transport

For the cell layer growth model in Chapter 2, the reduced system for the solute transport in the HFB with the ECS port closed (from (2.68)–(2.78)) is, at leading order in ϵ,

$$4\epsilon^2 \mathrm{Pe}_l \hat{Q}_{l,in}(1-r^2)\frac{\partial c_l}{\partial z} = \frac{1}{r}\frac{\partial}{\partial r}\left(r\frac{\partial c_l}{\partial r}\right), \tag{C.1}$$

$$0 = \frac{1}{r}\frac{\partial}{\partial r}\left(r\frac{\partial c_i}{\partial r}\right), \quad i = m, e, \tag{C.2}$$

$$0 = \frac{1}{r}\frac{\partial}{\partial r}\left(r\frac{\partial c_c}{\partial r}\right) + m\mathcal{M}, \tag{C.3}$$

where we have substituted for $u_{l,z}$ in (C.1) with (2.122) and used the fact that $u_{i,r}, u_{i,z} = \mathcal{O}(\epsilon^2)$ $(i = m, c, e)$ in (C.2) and (C.3). Integrating (C.2) and (C.3) and applying boundary conditions (2.73)–(2.75) we obtain

$$c_m(r,z,t) = \frac{\phi_c D_c}{\phi_m D_m}\frac{m\mathcal{M}}{2}(\hat{R}_c(z,t)^2 - \hat{R}_m^2)\ln r + C_m(z,t), \tag{C.4}$$

$$c_c(r,z,t) = \frac{m\mathcal{M}}{4}(2\hat{R}_c(z,t)^2 \ln r - r^2) + C_c(z,t), \tag{C.5}$$

$$c_e(r,z,t) = \frac{m\mathcal{M}}{4}\hat{R}_c(z,t)^2(2\ln \hat{R}_c(z,t) - 1) + C_c(z,t), \tag{C.6}$$

where

$$C_c(z,t) = \frac{m\mathcal{M}}{4}\left(2\left(\frac{\phi_c D_c}{\phi_m D_m}(\hat{R}_c(z,t)^2 - \hat{R}_m^2) - \hat{R}_c(z,t)^2\right)\ln \hat{R}_m + \hat{R}_m^2\right) + C_m(z,t), \tag{C.7}$$

and $C_m(z,t)$ is determined from the concentration continuity condition on the lumen-membrane interface in (2.72)

$$C_m(z,t) = c_l(1,z,t).$$

To close the system we need to solve the equation for the lumen concentration (C.1) subject to the boundary conditions (from (2.72) and (2.77))

$$\frac{\partial c_l}{\partial r}(0,z,t)=0, \quad \frac{\partial c_l}{\partial r}(1,z,t)=\gamma(z,t), \quad c_l(r,0,t)=\begin{cases}1 & \text{for oxygen}\\ 0 & \text{for lactate}\end{cases}, \quad \frac{\partial c_l}{\partial z}(r,1,t)=0, \tag{C.8}$$

where

$$\gamma(z,t)=\frac{\phi_c D_c}{D_l}\frac{m\mathcal{M}}{2}(\hat{R}_c(z,t)^2-\hat{R}_m^2). \tag{C.9}$$

In [231], Shipley and Waters solved this problem analytically for constant γ to express the lumen concentration in terms of an infinite sum of the eigenfunctions of the corresponding Sturm-Liouville problem. However, since we assume that γ varies with z, we must solve (C.1), (C.8)–(C.9) numerically as described below.

C.2 Numerical solution of the leading order system

The leading order system for the fluid flow, oxygen and lactate transport and cell layer growth when the ECS port is closed is given by equations (2.79)–(2.81), (2.122)–(2.123), (C.1) and (C.4)–(C.9). The algorithm for solving this system is essentially the same as that used when the ECS port is open (see §2.6.3). At each time step the steady flow and solute transport problems are solved for the current position of the outer surface of the cell layer, $r=\hat{R}_c(z,t)$, and the solutions used to update $\hat{R}_c$. However, in step 2 of the algorithm (page 60) the advection-diffusion equation for the lumen concentration (C.1) is solved subject to (C.8)–(C.9), and (2.122)–(2.123) and (C.4)–(C.7) are used to determine the lumen pressure, lumen axial velocity and solute concentrations throughout the bioreactor. We solve (C.1) using the finite difference method with a grid of 501 by 201 nodes in the z- and r-directions respectively ($\Delta z=2\times10^{-3}$, $\Delta r=5\times10^{-3}$) and central difference approximations of the derivatives.

Appendix D

Verification of numerical scheme for cell aggregate growth model

The numerical scheme for solving the leading order system for the fluid flow, oxygen transport and cell aggregate growth (equations (3.30), (3.56)–(3.57), (3.52)–(3.54), and (3.43)–(3.49)) in Chapter 3 is described in §3.6.3. In this appendix we describe the steps taken to verify its accuracy. To start with, the following checks were performed:

- The finite element code was used to solve the following PDE on the model domain, $\{(x,y) \in [0,1] \times [0,\hat{R}_e]\}$, with a combination of Dirichlet and Neumann boundary conditions on the external and internal boundaries:

$$\frac{\partial^2 c_i}{\partial y^2} = 0, \quad i = l, m, e, \tag{D.1}$$

$$c_i = 0, \quad \text{on } x = 0, \quad \frac{\partial c_i}{\partial x} = y, \quad \text{on } x = 1, \quad i = l, m, e,$$

$$c_l = 0, \quad \text{on } y = 0,\ 0 < x < 1, \quad \frac{\partial c_e}{\partial y} = x, \quad \text{on } y = \hat{R}_e,\ 0 < x < 1,$$

$$c_l = c_m, \quad \frac{\partial c_l}{\partial y} = \frac{\partial c_m}{\partial y}, \quad \text{on } y = 1,\ 0 < x < 1,$$

$$c_m = c_e, \quad \frac{\partial c_m}{\partial y} = \frac{\partial c_e}{\partial y}, \quad \text{on } y = \hat{R}_m,\ 0 < x < 1,$$

  with $\hat{R}_m = 2$ and $\hat{R}_e = 5$. This problem has the exact analytical solution

$$c_i = xy, \quad i = l, m, e.$$

  Convergence of the numerical solution to the analytical solution with mesh refinement was checked. This process was repeated with the following inhomogeneous form of (D.1) with an added advection term, $(y, 0)^T \boldsymbol{\nabla} c_i$ $(i = l, m, e)$,

$$\frac{\partial^2 c_i}{\partial y^2} = y\frac{\partial c_i}{\partial x} - y^2, \quad i = l, m, e,$$

and the same boundary conditions, which has the same analytical solution, $c_i = xy$ $(i = l, m, e)$.

- The code was then used to solve the dimensionless oxygen transport system with constant uptake but no flow or aggregate growth

$$\epsilon^2 \frac{\partial^2 c_i}{\partial x^2} + \frac{\partial^2 c_i}{\partial y^2} = 0, \quad i = l, m, e,$$

$$c_l = 1 \quad \text{on } x = 0, \quad \frac{\partial c_l}{\partial x} = 0 \quad \text{on } x = 1, \quad \frac{\partial c_l}{\partial y} = 0 \quad \text{on } y = 0,$$

$$\frac{\partial c_m}{\partial x} = 0 \quad \text{on } x = 0, 1, \ 1 < y < \hat{R}_m,$$

$$\frac{\partial c_e}{\partial x} = 0 \quad \text{on } x = 0, 1, \ \hat{R}_m < y < \hat{R}_e, \quad \frac{\partial c_e}{\partial y} = 0 \quad \text{on } y = \hat{R}_e, \ 0 < x < 1,$$

$$c_l = c_m, \quad \frac{D_l}{\phi_m D_m} \frac{\partial c_l}{\partial y} = \frac{\partial c_m}{\partial y} \quad \text{on } y = 1, \ 0 < x < 1,$$

$$c_m = c_e, \quad \frac{\partial c_e}{\partial y} - \frac{\phi_m D_m}{D_e} \frac{\partial c_m}{\partial y} = \mathrm{Da} \quad \text{on } y = \hat{R}_m, \ 0 < x < 1,$$

with $\mathrm{Da} = 0.1$. It was verified that the numerical solution was correct, *i.e.* was zero everywhere except in an $\mathcal{O}(\epsilon)$ boundary layer at the inlet ($x = 0$, $0 < y < 1$), where the concentration changed sharply to satisfy $c_l = 1$ on $x = 0$, $0 < y < 1$.

- Finally aggregate growth was added to the model and the outlet oxygen flux and total uptake flux checked to ensure it balanced with the inlet oxygen flux.

Following these checks, we verified the accuracy of the solutions to the reduced model for the fluid and oxygen transport by solving the full (dimensional) flow and oxygen transport problem (equations (3.2)–(3.21) with steady incompressible Navier-Stokes equations for the lumen and ECS flow) for a fixed aggregate distribution using the FE package COMSOL Multiphysics 4.3. The Navier-Stokes equations in the lumen and ECS,

$$\boldsymbol{\nabla} \cdot \mathbf{u}_i = 0, \quad \mathbf{u}_i \cdot \boldsymbol{\nabla} \mathbf{u}_i = -\boldsymbol{\nabla} p_i + \nabla^2 \mathbf{u}_i, \quad i = l, e, \tag{D.2}$$

were solved using the inbuilt 'Laminar Flow' solver, the Laplace problem for the membrane pressure using the 'Laplace Equation' solver, and the oxygen transport equations using the 'Convection-Diffusion Equation' solver. The FE mesh consisted of 147,714 elements (75,000 nodes), which were a mixture of triangular elements and quadrilateral elements (on boundaries with boundary layers). We used the smooth dimensional form of the aggregate indicator function in the fluid flux and uptake conditions at the outer surface of the membrane (in (3.4) and (3.15) respectively), *i.e.*

$$I_a(x, t) = \sum_{j=1}^{N} \tfrac{1}{2} \left[\tanh(\tfrac{s}{L}(x - x_{2j-1}(t))) + \tanh(\tfrac{s}{L}(x_{2j}(t) - x)) \right]. \tag{D.3}$$

Since the full Navier-Stokes equations were solved in the lumen it was necessary to specify the flow profile at the lumen inlet, $\mathbf{u}_l|_{x=0}$. We assumed that the flow had a half-Poiseuille profile, *i.e.*

$$u_l|_{x=0} = -\frac{3Q_{in}}{2R_l^3}(R_l^2 - y^2), \quad v_l|_{x=0} = 0. \tag{D.4}$$

Refining the mesh to 300,000 elements did not change the solutions to within a relative error of 10^{-5}.

Figures D.1 and D.2 show the numerical solutions for the fluid pressure, x- and y- flow velocity components, and oxygen concentration obtained using the code for the reduced model and COMSOL respectively with the static distribution of five 0.5 cm aggregates evenly distributed along the membrane from Chapter 3. The solutions show very close agreement.

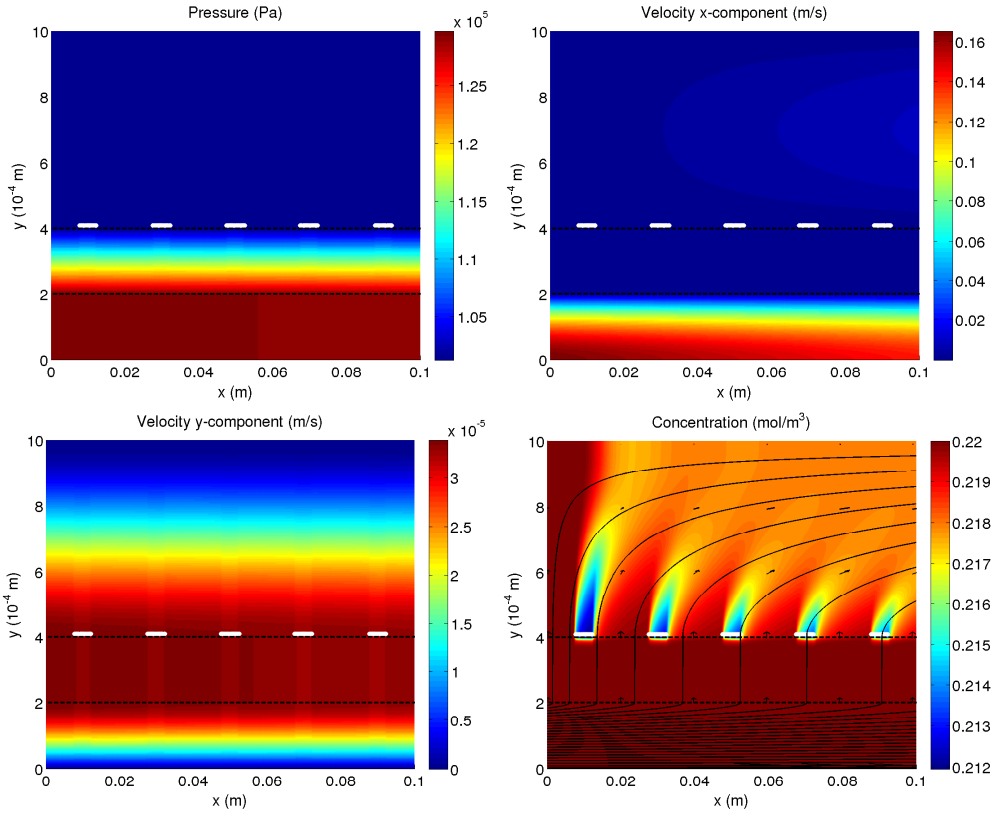

Figure D.1: Fluid pressure, flow velocity components, and oxygen distribution given by the reduced model (MATLAB code) with five 0.5 cm aggregates evenly distributed along the membrane. Parameter values: $Q_{in} = 2.2 \times 10^{-5}\,\mathrm{m^2 s^{-1}}$, $P_{l,out} = 1.289 \times 10^5\,\mathrm{Pa}$, $M = 3.3 \times 10^{-7}\,\mathrm{mol\,m^{-2}\,s^{-1}}$, $C_{in} = 0.22\,\mathrm{mol\,m^{-3}}$, $C_{1/2} = 0.05\,\mathrm{mol\,m^{-3}}$. All other parameter values as in Tables 2.1 and 3.1.

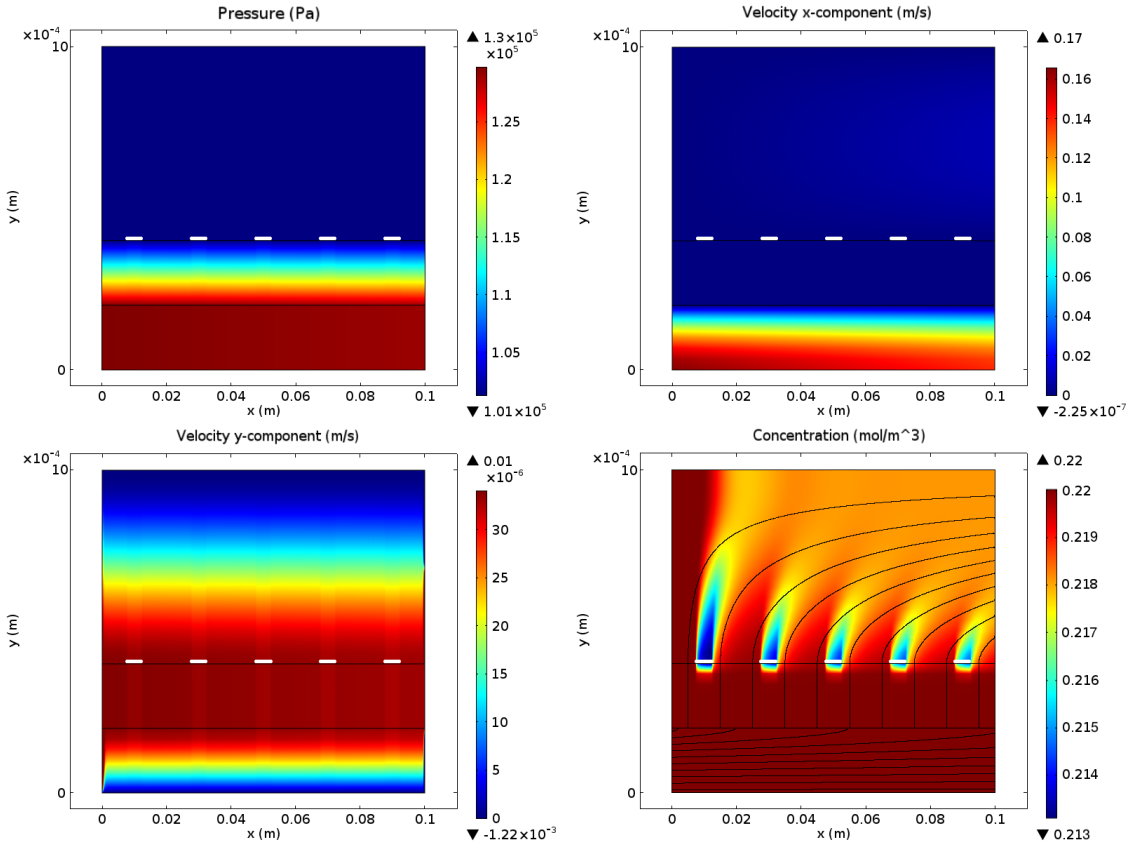

Figure D.2: Fluid pressure, flow velocity components, and oxygen distribution given by the full flow and oxygen transport model (solved in COMSOL) for the same aggregate distribution and parameter values as in Figure D.1.

Defining the error in the dimensionless concentration given by the reduced model, c, as

$$\text{Error} = c_f - c,$$

where c_f is the dimensionless concentration given by the full transport model, gives that the error is $\mathcal{O}(\epsilon)$ at its largest near the aggregate, but is $\mathcal{O}(\epsilon^2)$ or smaller over most of the domain (Figure D.3). This is consistent with the size of the terms neglected in reduced model. The error is larger nearer the aggregates since the assumption that the x length scale over which changes in the concentration occur is much longer than the y length scale is not strictly valid here. Close inspection of the plot for the y-component of the fluid velocity in Figure D.2 (bottom left) reveals that there are narrow boundary layers near the inlets and outlets. However, these do not affect the flow in the bulk of the domain, so we neglect them in the reduced model for the flow and oxygen transport.

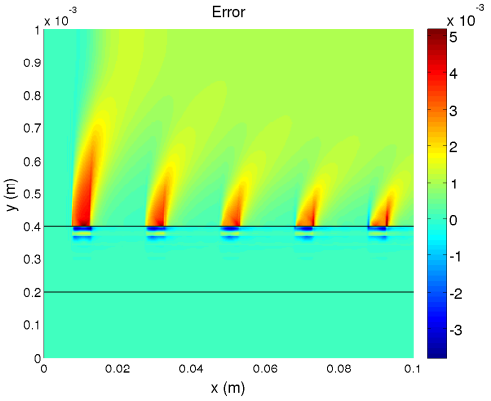

Figure D.3: Error in the dimensionless concentration given by the reduced model (with respect to the dimensionless concentration for the full model) for the set-up and parameter values in Figure D.1.

Appendix E

Derivation of cell density diffusion equation for Murray model

Murray *et al.* [181, 182] do not provide a detailed derivation of the nonlinear diffusion equation for the cell density (equation (4.84)) that they obtain as the continuum limit of their cell-based model. To aid comparison of Murray *et al.*'s model with our model and Fozard *et al.*'s model and the corresponding derivation approaches, we give a more detailed version of the derivation here. We also show that the equation for the evolution of the cell aggregate length given by Murray *et al.*'s continuum approximation has the same form as the cell aggregate growth law in Chapter 3 in the limit of incompressible cells.

E.1 Governing equations

The derivation starts from a force balance on each cell centre. The position of the nth cell centre is denoted by $\mathbf{r}_n$ and the cell motion is approximated as overdamped (*i.e.* cell acceleration is neglected since drag forces dominate inertial forces), as in §4.3.1. Therefore, conservation of momentum gives

$$\sum_{j \neq n} \mathbf{F}_{nj} + \mathbf{D}_n = 0,$$

where $\mathbf{F}_{nj}$ is the interaction force between the nth cell and its neighbours, and $\mathbf{D}_n$ is the drag force on the nth cell. The interaction force, $\mathbf{F}_{nj}$, is a linear spring force as in our model

$$\mathbf{F}_{nj} = \lambda^*(a^* - |\mathbf{r}_n - \mathbf{r}_j|)\frac{\mathbf{r}_n - \mathbf{r}_j}{|\mathbf{r}_n - \mathbf{r}_j|},$$

where λ^* is the spring constant and a^* is the resting spring length (assumed constant). The drag force on each cell is assumed to be proportional to its velocity

$$\mathbf{D}_n = -\mu^* \frac{\mathrm{d}\mathbf{r}_n}{\mathrm{d}\tau},$$

where μ^* is the cell drag coefficient. For a 1D line of N cells with the first cell (centre) pinned at the origin, the equations of motion for the cell centres reduce to

$$r_1(\tau) = 0, \ \forall \tau \geq 0, \tag{E.1}$$

$$-D_n = F_{n,n-1} - F_{n,n+1} \ \Rightarrow \ \mu^* \frac{\mathrm{d}r_n}{\mathrm{d}\tau} = \lambda^*(r_{n-1}(\tau) - 2r_n(\tau) + r_{n+1}(\tau)), \quad n = 2, \ldots, N-1, \tag{E.2}$$

$$-D_N = F_{N,N-1} \quad \Rightarrow \quad \mu^* \frac{\mathrm{d}r_N}{\mathrm{d}\tau} = \lambda^*(a^* - (r_N(\tau) - r_{N-1}(\tau))), \tag{E.3}$$

where $F_{nj} := \lambda^*(a^* - |r_n - r_j|)$. The initial positions of the cells are prescribed as a function of the cell index

$$r_n(0) = r_{init}(n). \tag{E.4}$$

E.2 Nondimensionalisation and continuum approximation

We nondimensionalise the cell motion equations (E.1)–(E.3) for $N \gg 1$, by scaling the variables as follows

$$n = N\hat{n}, \quad r = Na^*\hat{r}, \quad \tau = T_d\hat{\tau}.$$

where T_d is the cell doubling time, and henceforth drop hats on dimensionless variables. We assume that the discrete cell positions $r_n(\tau)$ sample from a smooth function $r(n, \tau)$ such that

$$r(n, \tau) = r_n(\tau) \quad \text{for} \ \ n = \tfrac{1}{N}, \ldots, 1.$$

With this assumption, the dimensionless cell motion equations are

$$r(\tfrac{1}{N}, \tau) = 0, \tag{E.5}$$

$$\frac{\alpha_M}{N^2}\frac{\partial r}{\partial \tau}(n, \tau) = r(n - \tfrac{1}{N}, \tau) - 2r(n, \tau) + r(n + \tfrac{1}{N}, \tau), \quad n \in (\tfrac{1}{N}, 1 - \tfrac{1}{N}), \tag{E.6}$$

$$\frac{\alpha_M}{N^2}\frac{\partial r}{\partial \tau}(1, \tau) = \frac{1}{N} - (r(1, \tau) - r(1 - \tfrac{1}{N})). \tag{E.7}$$

where $\alpha_M = N^2\mu^*/(\lambda^* T_d)$. Taylor expanding the terms in (E.5)–(E.7) about $n = 0$, n and $n = 1$ respectively for $N \gg 1$ gives

$$\begin{aligned}
&r(0, \tau) + \mathcal{O}(\tfrac{1}{N}) = 0, \\
&\alpha_M \frac{\partial r}{\partial \tau} = \frac{\partial^2 r}{\partial n^2} + \mathcal{O}(\tfrac{1}{N}), \quad n \in (0, 1), \\
&\frac{\alpha_M}{N}\frac{\partial r}{\partial \tau}(1, \tau) = 1 - \frac{\partial r}{\partial n}(1, \tau) + \mathcal{O}(\tfrac{1}{N}).
\end{aligned}$$

Assuming that $\alpha_M = \mathcal{O}(1)$ and retaining only leading order terms in $1/N$, the system reduces to

$$r(0,\tau) = 0, \tag{E.8}$$
$$\alpha_M \frac{\partial r}{\partial \tau} = \frac{\partial^2 r}{\partial n^2}, \quad n \in (0,1), \tag{E.9}$$
$$\frac{\partial r}{\partial n}(1,\tau) = 1, \tag{E.10}$$

with the initial condition

$$r(n,0) = r_{init}(n). \tag{E.11}$$

E.3 Transformation to spatial coordinates

Since $r(n,\tau)$ is a monotonically increasing function of n it has a well-defined inverse $n(r,\tau)$. Murray *et al.* define the cell density (the number of cells per unit length) by

$$\rho(r,\tau) := \frac{\partial n}{\partial r}(r,\tau), \tag{E.12}$$

or equivalently,

$$n(r,\tau) = \int_0^r \rho(r',\tau)\,\mathrm{d}r'. \tag{E.13}$$

We note that this is equivalent to our definition of the cell density as

$$\rho := \frac{1}{l} = \frac{1}{\frac{\partial x}{\partial n}}$$

with $r \mapsto x$, assuming that $\frac{1}{\frac{\partial x}{\partial n}} = \frac{\partial n}{\partial x}$.

Changing coordinates from the cell-index coordinates to spatial coordinates, *i.e.* $(n,\tau) \mapsto (r,t)$, with (E.13) and $\tau(r,t) = t$, the chain rule gives

$$\frac{\partial}{\partial r} = \frac{\partial n}{\partial r}\frac{\partial}{\partial n} + \frac{\partial \tau}{\partial r}\frac{\partial}{\partial \tau} = \rho(r,\tau)\frac{\partial}{\partial n},$$
$$\frac{\partial}{\partial t} = \frac{\partial n}{\partial t}\frac{\partial}{\partial n} + \frac{\partial \tau}{\partial t}\frac{\partial}{\partial \tau} = \frac{\partial n}{\partial t}\frac{\partial}{\partial n} + \frac{\partial}{\partial \tau}.$$

Writing this in matrix form and inverting gives

$$\begin{pmatrix} \frac{\partial}{\partial r} \\ \frac{\partial}{\partial t} \end{pmatrix} = \begin{pmatrix} \rho & 0 \\ \frac{\partial n}{\partial t} & 1 \end{pmatrix} \begin{pmatrix} \frac{\partial}{\partial n} \\ \frac{\partial}{\partial \tau} \end{pmatrix} \quad \Rightarrow \quad \frac{\partial}{\partial n} = \frac{1}{\rho}\frac{\partial}{\partial r}, \quad \frac{\partial}{\partial \tau} = -\frac{1}{\rho}\frac{\partial n}{\partial t}\frac{\partial}{\partial r} + \frac{\partial}{\partial t}. \tag{E.14}$$

Again, we note that this is the same as the transformation to spatial coordinates used in §4.5.2 with $r \mapsto x$, $-\frac{1}{\rho}\frac{\partial n}{\partial t} = u$ and $u\frac{\partial}{\partial r} + \frac{\partial}{\partial t} = \frac{\mathrm{D}}{\mathrm{D}t}$ as the convective derivative. Substituting (E.14) into (E.9) and rearranging, we obtain

$$\alpha_M \rho u = -\alpha_M \frac{\partial n}{\partial t} = -\frac{\partial}{\partial r}\left(\frac{1}{\rho}\right) = -\frac{1}{\rho^2}\frac{\partial \rho}{\partial r}. \tag{E.15}$$

Differentiation of (E.15) with respect to r and substitution for $\frac{\partial n}{\partial r}$ on the left-hand side using (E.12) yields

$$\alpha_M \frac{\partial \rho}{\partial t} = \frac{\partial}{\partial r}\left(\frac{1}{\rho^2}\frac{\partial \rho}{\partial r}\right). \tag{E.16}$$

With $r \mapsto x$ and $\alpha_M \mapsto \alpha$ this is the same as the diffusion equation we derived for the cell density from our cell-vertex model, equation (4.68), for $a = \text{const}$. This shows that the spatial discrepancy between the cell-centre and cell-vertex models disappears in the continuum limit for $N \gg 1$.

Murray *et al.* capture the condition at the left end of the cell line, $r(0,\tau) = 0$, by introducing an image cell in the discrete model at $n = 0$ such that $r(0,\tau) = -r(2/N,\tau)$, *i.e.* such that the image cell and the $n = 2/N$ cell are always equidistant from the $n = 1/N$ cell and the $n = 1/N$ cell remains stationary as there is no net force on acting on it. This condition then implies that r increases linearly with n at $n = 1/N$, so that

$$\frac{\partial^2 r}{\partial n^2}(\tfrac{1}{N},\tau) = 0.$$

Taking the limit as $N \to \infty$ and transforming to spatial coordinates yields

$$-\frac{1}{\rho^2}\frac{\partial \rho}{\partial r}\bigg|_{r=0} = 0, \tag{E.17}$$

which is a no-flux condition for the cell density at the origin. In cell-index coordinates (n,τ) the cell domain is fixed ($n \in (0,1)$), but in spatial coordinates (r,t) the right-hand end of the cell line, $r = r_R(t)$, is free to move and moves with the local cell velocity. From (E.15), this means that

$$\frac{\mathrm{d}r_R}{\mathrm{d}t} = u|_{r=r_R(t)} = -\frac{1}{\alpha_M}\frac{1}{\rho^3}\frac{\partial \rho}{\partial r}\bigg|_{r=r_R(t)}. \tag{E.18}$$

The boundary condition (E.10) at $n = 1$ becomes

$$\rho(r_R(t),t) = 1. \tag{E.19}$$

The initial cell density $\rho(r,0)$ is determined from $r_{init}(n)$ by

$$\rho(r,0) = \frac{\partial n}{\partial r}(r,0) = \frac{\partial r_{init}^{-1}}{\partial r}(r). \tag{E.20}$$

E.4 Comparison with cell aggregate growth law in limit of incompressible cells

As described in §4.6.2.1, Murray *et al.* incorporate cell division into their continuum model by adding a density-dependent source term, $f(\rho,t)$, to (E.16),

$$\frac{\partial \rho}{\partial t} = \frac{1}{\alpha_M}\frac{\partial}{\partial r}\left(\frac{1}{\rho^2}\frac{\partial \rho}{\partial r}\right) + f(\rho,t).$$

In the limit of incompressible cells $\lambda^* \gg N^2$, which corresponds to $\alpha_M \ll 1$, the leading order equation for the cell density is

$$\frac{\partial}{\partial r}\left(\frac{1}{\rho^2}\frac{\partial \rho}{\partial r}\right) = 0.$$

Solving this subject to (E.17) and (E.19) gives

$$\rho(r,t) = 1,$$

which corresponds to the system being in equilibrium with all the springs at their resting lengths. If $\hat{N}(t)$ is the total number of cells at time t normalised with respect to the initial number of cells, *i.e.*

$$\hat{N}(t) = \int_0^{r_R(t)} \rho(r,t)\,\mathrm{d}r,$$

then by conservation of cell number we have that

$$\frac{\partial \hat{N}}{\partial t} = \frac{\partial}{\partial t}\int_0^{r_R(t)} \rho\,\mathrm{d}r = \int_0^{r_R(t)} f(\rho,t)\,\mathrm{d}r.$$

Substituting the equilibrium solution $\rho = 1$ into this equation gives

$$\frac{\mathrm{d}\hat{N}}{\mathrm{d}t} = \frac{\mathrm{d}}{\mathrm{d}t}\int_0^{r_R(t)} \mathrm{d}r = \frac{\mathrm{d}r_R}{\mathrm{d}t} = \int_0^{r_R(t)} f(\rho,t)\,\mathrm{d}r,$$

so that the rate at which the aggregate grows is equal to the net proliferation rate over its length. This has the same form as the cell aggregate growth law (3.22) in Chapter 3 (with $G_p - G_d$, the difference between the local cell proliferation and death rates, replaced by $f(\rho,t)$ and the left end of the aggregate fixed), and shows that it is a valid approximation to Murray *et al.*'s discrete model with cell proliferation in the limit of incompressible cells.

Appendix F

Numerical methods for discrete-to-continuum modelling

In this appendix we describe the numerical methods used to solve the discrete and continuum cell growth models in Chapter 4. First we describe the methods used to solve the discrete and continuum cell models when they are independent of the oxygen transport (§F.1), then those used to solve the coupled cell and oxygen transport models (§F.2). In §F.3, we list the steps taken to verify the accuracy of the numerical schemes for the coupled cell and oxygen transport models.

We solve the dimensionless discrete cell model equations (4.26)–(4.31), (4.37)–(4.38) and continuum cell model equations (4.50)–(4.57) in cell-vertex-based coordinates (n, τ), since in these coordinates the cell aggregate domain is fixed ($n \in [0, 1]$) (not evolving as in spatial coordinates (x, t)). The solutions are then transformed to spatial coordinates using the solution for the cell vertex positions $x_n(\tau)$ in the discrete case (which is determined directly), and the continuum cell position $x(n, \tau)$ in the continuum case, which is found by solving

$$\frac{\partial x}{\partial \tau} = u,$$

subject to the initial condition $x(n, 0) = x_{init}(n)$.

F.1 Cell models without oxygen transport, $\Gamma \neq \Gamma(c)$

F.1.1 Discrete cell model

In the absence of coupling to the oxygen transport, we solve the cell motion and growth equations by reducing (4.26)–(4.28) and (4.37) to a system of coupled ODEs for the cell vertex positions x_n and the cell target lengths $a_{n+\frac{1}{2N}}$ (using the definition of the cell vertex

velocities in (4.25))

$$\frac{1}{6N}\frac{\mathrm{d}}{\mathrm{d}\tau}\left(x_{n-\frac{1}{N}} + 4x_n + x_{n+\frac{1}{N}}\right) = p_{n-\frac{1}{2N}} - p_{n+\frac{1}{2N}}, \quad n = \tfrac{1}{N}, \tfrac{2}{N}, \ldots, 1 - \tfrac{1}{N}, \tag{F.1}$$

$$\frac{\mathrm{d}a_{n+\frac{1}{2N}}}{\mathrm{d}\tau} = \Gamma\left(l_{n+\frac{1}{2N}}, a_{n+\frac{1}{2N}}, p_{n+\frac{1}{2N}}; \gamma_{n+\frac{1}{2N}}\right), \quad n = 0, \tfrac{1}{N}, \ldots, 1 - \tfrac{1}{N}, \tag{F.2}$$

where the equations for the end vertices are provided by the boundary conditions (4.29)–(4.30)

$$\frac{1}{6N}\frac{\mathrm{d}}{\mathrm{d}\tau}\left(2x_0 + x_{\frac{1}{N}}\right) = -p_{\frac{1}{2N}}, \qquad \frac{1}{6N}\frac{\mathrm{d}}{\mathrm{d}\tau}\left(x_{1-\frac{1}{N}} + 2x_1\right) = p_{1-\frac{1}{2N}}, \tag{F.3}$$

and the cell lengths and pressures are given by the algebraic equations

$$l_{n+\frac{1}{2N}} = N\left(x_{n+\frac{1}{N}} - x_n\right), \quad p_{n+\frac{1}{2N}} = \frac{1}{\alpha}\left(a_{n+\frac{1}{2N}} - l_{n+\frac{1}{2N}}\right), \quad n = 0, \tfrac{1}{N}, \ldots, 1 - \tfrac{1}{N}.$$

We solve (F.1)–(F.3) subject to prescribed initial conditions

$$x_n(0) = x_{init}(n), \;\; n = 0, \tfrac{1}{N}, \ldots, 1, \qquad a_{n+\frac{1}{2N}}(0) = a_{init}(n + \tfrac{1}{2N}), \;\; n = 0, \tfrac{1}{N}, \ldots, 1 - \tfrac{1}{N},$$

using the MATLAB stiff ODE solver `ode15s` with a fixed time step of $\Delta\tau = 10^{-4}$.

F.1.2 Continuum approximation

For the continuum approximation of the cell model without oxygen transport, we combine equations (4.50)–(4.52) to obtain the following coupled equations for the continuum cell length l and target length a

$$\alpha\frac{\partial l}{\partial \tau} = \frac{\partial^2 l}{\partial n^2} - \frac{\partial^2 a}{\partial n^2}, \quad n \in (0,1), \tag{F.4}$$

$$\frac{\partial a}{\partial \tau} = \Gamma(l, a, \tfrac{1}{\alpha}(a - l); \gamma), \quad n \in (0,1), \tag{F.5}$$

$$\text{with} \quad l = a \quad \text{at } n = 0, 1, \tag{F.6}$$

$$\text{and} \quad l(n,0) = l_{init}(n), \quad a(n,0) = a_{init}(n), \quad n \in [0,1]. \tag{F.7}$$

We solve these equations by the finite difference method, with central difference approximations to the second order derivatives in n and a semi-implicit discretisation in time (implicit with respect to the $\frac{\partial^2 l}{\partial n^2}$ term and explicit with respect to the $\frac{\partial^2 a}{\partial n^2}$ term) for (F.4), and an explicit time discretisation of (F.5). We checked that the numerical solution of (F.4)–(F.7) for l and a with

$$\Gamma = 1, \quad l_{init}(n) = 1 + \sin(\pi n), \quad a_{init}(n) = 1,$$

converged to the analytical solution for these initial conditions given by (4.127) as the grid space Δn and time step $\Delta\tau$ were reduced. We found that $\Delta n = 10^{-3}$ and $\Delta\tau = 10^{-4}$ were sufficient to reduce the relative error in the solution to less than 10^{-4}.

F.2 Cell models coupled to oxygen transport, $\Gamma = \Gamma(c)$

Due to the coupling of the cell growth to the oxygen concentration in equation (4.37c) and the oxygen uptake to the cell lengths in equation (4.33) (and the corresponding coupling in equations (4.53) and (4.76) for the continuum cell model), the cell models and oxygen transport must be solved together. We do this iteratively, *i.e.* by solving the transport equations to find the oxygen concentration for given initial cell vertex positions, then solving the cell model to update the cell vertex positions using the concentration solution, and repeating until the simulation time has elapsed.

F.2.1 Oxygen transport

F.2.1.1 Smoothing of oxygen uptake boundary conditions

With the uptake boundary conditions for the discrete and continuum cell models as prescribed in (4.33) and (4.76), there are large jumps in the diffusive flux through $y = 0$ ($\frac{\partial c}{\partial y}|_{y=0}$) at the ends of the aggregate. To avoid the difficulties that this causes in accurately solving the oxygen diffusion equation (4.32) near the ends of the aggregate, we smooth the uptake boundary conditions (4.33) and (4.76) using tanh functions as in §3.6.2. Hence, the boundary conditions at the base of the nutrient bath for the discrete cell model (equations (4.33) and (4.34)) become

$$\frac{\partial c}{\partial y} = \mathrm{Da}\, I_a(x, x_0(\tau), x_1(\tau)) \frac{1}{l_{n+\frac{1}{2N}}} \frac{c}{c_{1/2}+c}, \quad x \in [x_n(\tau), x_{n+\frac{1}{N}}(\tau)],\ y = 0, \\ n = 0, \ldots, 1 - \tfrac{1}{N}, \tag{F.8}$$

and those for the continuum model (equations (4.34) and (4.76)) become

$$\frac{\partial c}{\partial y} = \mathrm{Da}\, I_a(x, x_L(\tau), x_R(\tau)) \frac{1}{l} \frac{c}{c_{1/2}+c}, \quad x \in [x_L(\tau), x_R(\tau)],\ y = 0, \tag{F.9}$$

where the smoothing function I_a is given by

$$I_a(x, x_a(\tau), x_b(\tau)) = \frac{1}{2}\left[\tanh(s(x - x_a(\tau))) - \tanh(s(x_b(\tau) - x))\right],$$

and the constant s determines how sharp the transition to zero uptake is at the ends of the aggregate. Testing different values of s confirmed that taking $s = 50$ provides a sufficiently sharp transition in the uptake flux without causing resolution issues in the numerics, so we use this value in all the simulations.

We note that although I_a will initially have the same value for the discrete and continuum cell models, as the systems evolve it will take different values for each due to the error in the continuum approximation for the cell motion and growth.

F.2.1.2 Finite element solution

At each time step in the simulation, we solve the steady oxygen transport problem (given by equations (4.32), (4.35)–(4.36) and (F.8) for the discrete model and (4.32), (4.35)–(4.36) and (F.9) for the continuum model) for the current cell configuration. We do this using the Galerkin FEM with piecewise linear basis elements on a regular triangular mesh with $N_x + 1$ and $N_y + 1$ nodes in the x- and y-directions respectively.

As we have assumed that the nutrient concentration is continuous at the cell length scale, we require that the FE mesh for the concentration is much finer than the cell vertex grid. This imposes a lower bound on N_x, since the mesh space, $\Delta x = 2R/N_x$, must be much smaller than the shortest cell length. Assuming that the minimum dimensionless aggregate length is 1 and the shortest length any cell reaches is half of the average cell length $1/N$, we require that

$$\Delta x = \frac{2R}{N_x} = \frac{2R^*}{Na^*N_x} = \frac{4\times10^{-3}}{10\times10^{-5}NN_x} = \frac{400}{NN_x} \ll \min_n(l_{n+\frac{1}{2N}}) = \frac{1}{2N} \quad \Rightarrow \quad N_x \gg 800.$$

We determine the values of $N_x \gg 800$ and N_y needed to give a sufficiently accurate solution for c via convergence tests in §F.3.

F.2.1.3 Implementation of oxygen uptake

We implement the Michaelis-Menten term in (F.8) and (F.9) in the same way as the oxygen uptake condition in Chapter 3. At time $\tau = \tau_k = k\Delta\tau$, we evaluate the denominator using the concentration at the previous time step, $c^{(k-1)}|_{y=0}$, so that the FE problem can be solved as a linear system. This only introduces an $\mathcal{O}(\Delta\tau)$ error in the solution, which is the same order as the error from the time discretisation of the continuum cell model. At time $\tau = \tau_k$, the discretised forms of (F.8) and (F.9) are

$$\frac{\partial c^{(k)}}{\partial y} = \mathrm{Da}\, I_a(x, x_0^{(k)}, x_1^{(k)}) \frac{1}{l^{(k)}_{n+\frac{1}{2N}}} \frac{c^{(k)}}{c_{1/2} + c^{(k-1)}}, \quad x \in [x_n^{(k)}, x^{(k)}_{n+\frac{1}{N}}],\ y = 0, \tag{F.10}$$

and

$$\frac{\partial c^{(k)}}{\partial y} = \mathrm{Da}\, I_a(x, x_L^{(k)}, x_R^{(k)}) \frac{1}{l^{(k)}} \frac{c^{(k)}}{c_{1/2} + c^{(k-1)}}, \quad x \in [x_L^{(k)}, x_R^{(k)}],\ y = 0. \tag{F.11}$$

At the first time step ($k = 1$), an estimate is required for $c^{(0)}_{y=0}$. This is found in the same way as for the uptake condition in Chapter 3, *i.e.* by solving the oxygen transport equations for the discrete and continuum cell models iteratively with the cell distribution fixed, starting with $c|_{y=0} \equiv 1$, until a fixed point is reached (which we take to be when the maximum difference between successive solutions is less than 10^{-5}).

F.2.2 Discrete cell model

We solve the same equations as in §F.1.1, except with (F.2) replaced by (4.37c). Evaluating Γ at the kth time step requires us to calculate the average concentration over the length of each cell

$$c^{(k)}_{n+\frac{1}{2N}} = \frac{N}{l^{(k)}_{n+\frac{1}{2N}}} \int_{x^{(k)}_n}^{x^{(k)}_{n+\frac{1}{N}}} c^{(k)}(x,0)\,\mathrm{d}x, \quad n = 0, \tfrac{1}{N} \ldots, 1 - \tfrac{1}{N}.$$

For each cell this is done by linearly interpolating the concentration solution for the discrete cell model, $c^{(k)}$, onto a combined grid of the FE nodes within the cell and the cell vertex positions, $x^{(k)}_n$ and $x^{(k)}_{n+\frac{1}{N}}$, and approximating the integral using the trapezium rule. The cell motion and growth equations are then solved up to the next time step using the inbuilt MATLAB ODE solver `ode45`, as this was found to be the quickest and most accurate method for solving the discrete system.

F.2.3 Continuum cell model

We solve the same equations as in §F.1.2, but with the concentration-dependent form of Γ (4.55c) in (F.5). Since the cell model is solved in cell-vertex-based coordinates (n, τ) and the oxygen transport equations are solved in spatial coordinates (x, y, τ), it is necessary to determine the values of the concentration at the cell model grid points, $n_i = i\Delta n$ ($i = 0, \ldots, N_n$), to evaluate the Monod growth term $c/(k_g + c)$ in (4.55c). To do this we linearly interpolate the concentration values at the nodes in the FE mesh onto the Eulerian cell position points corresponding to the n_i points, x_i ($i = 0, \ldots, N_n$), given by solving $\frac{\partial x_i}{\partial \tau} = u_i$ subject to $x(n_i, 0) = x_{init}(n_i)$.

F.2.4 Choice of time step and grid space for continuum cell model

For the central differences discretisation of the cell length diffusion equation (F.1) and the explicit discretisation of the cell target length evolution equation (F.2), the error in the numerical scheme for the continuum cell model is $\mathcal{O}(\Delta n^2, \Delta\tau)$. The error from the discretisation of the uptake boundary conditions (F.10) and (F.11) is $\mathcal{O}(\Delta\tau)$. Assuming that we use a sufficiently fine mesh for the FE scheme for the concentration (see §F.3), the overall numerical error in the coupled cell model and nutrient transport should therefore be $\mathcal{O}(\Delta n^2, \Delta\tau)$. Hence, so that we can resolve the error in the continuum cell model, which we expect to be $\mathcal{O}(1/N^2)$, up to at least $N = 100$, we use a grid space of $\Delta n = 10^{-3}$ and a time step of $\Delta\tau = 10^{-4}$.

F.3 Verification of numerical schemes for cell models coupled to oxygen transport

Before using the numerical scheme described in §F.2 to simulate target-length-, pressure- and nutrient-dependent cell growth, several checks and tests were performed to ensure the scheme would produce accurate solutions:

- We checked that the FE code for the oxygen transport problem for the continuum model (equations (4.32), (4.35)–(4.36) and (F.9)) gives the solution $c = 1$ throughout the domain when there is no oxygen uptake ($\mathrm{Da} = 0$ in (F.9)).

- We checked that the total concentration flux across the boundaries (the flux in across $y = 1$ minus the flux out across $y = 0$) for the oxygen transport problem for the continuum model (with $\mathrm{Da} = 0.2$ in (F.9)) is zero, *i.e.*

$$0 = \int_\Omega \nabla^2 c \, \mathrm{d}x \, \mathrm{d}y = \int_{\partial\Omega} \boldsymbol{\nabla} c \cdot \mathbf{n} \, \mathrm{d}s = \int_{y=1} \frac{\partial c}{\partial y} \, \mathrm{d}x - \int_{y=0} \frac{\partial c}{\partial y} \, \mathrm{d}x,$$

  where $\Omega = \{(x, y) \in [-R, R] \times [0, S]\}$ and $\partial\Omega$ is the boundary of Ω.

- We checked that the numerical solutions of the oxygen transport problems for the discrete and continuum cell models both converge as the FE mesh is refined. Figures F.1(a) and F.1(b) show that, for a fixed distribution of $N = 20$ cells

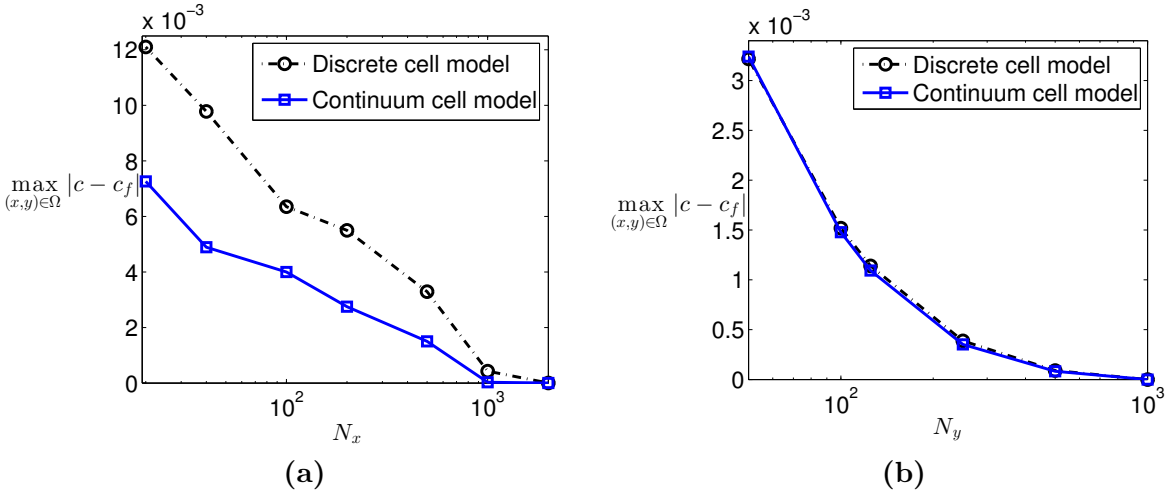

Figure F.1: Convergence of the FE solution for the oxygen concentration with mesh refinement for the discrete and continuum cell models. (a) Error in concentration vs. number of mesh spaces in x-direction N_x. (b) Error in concentration vs. number of mesh spaces in y-direction N_y. Error estimated as the maximum absolute difference from c_f, the solution for $N_x = 2000$ and $N_y = 1000$, over the domain, *i.e.* $\max_{(x,y)\in\Omega} |c - c_f|$, $\Omega = [-R, R] \times [0, S]$. Fixed cell vertex positions: $x_n = n - \frac{1}{\pi}\cos(\pi n) - \frac{1}{2}$ $(n = 0, \frac{1}{N}, \ldots, 1)$. Parameter values: $N = 20$, $R = 10$, $S = 10$, $\mathrm{Da} = 0.2$, $c_{1/2} = 0.05$.

$(x_n = n - \frac{1}{\pi}\cos(\pi n) - \frac{1}{2},\ (n = 0, \frac{1}{N}, \ldots, 1))$, the maximum absolute difference between the solution c and the solution c_f for $N_x = 2000$ and $N_y = 1000$ ($\Delta x = 0.01$ and $\Delta y = 0.01$) decreases monotonically as N_x and N_y are increased, for both the discrete and continuum cell models. From the graphs we can see that for $N_x = 1600$ and $N_y = 800$ the mesh is sufficiently fine for the relative error in the solutions for both models to be $\mathcal{O}(10^{-5})$. The concentration solutions on $y = 0$ for the discrete and continuum cell models are sufficiently smooth with this number of nodes. Hence we use these values for all the nutrient-dependent growth simulations.

Appendix G

Continuum approximation of discrete cell model with heterogeneous cell properties

Here we give the derivation of equations (4.144)–(4.149), the continuum approximation of the discrete cell-vertex model in Chapter 4 (equations (4.1), (4.4), (4.8)–(4.10), (4.17), (4.19)) with heterogeneous cell parameters, *i.e.* parameters that vary rapidly with respect to the cell index n.

We start by assuming that the cell properties are periodic with period $M/N \ll 1$, where $M = \mathcal{O}(1)$ and $N \gg 1$, and that the pressures and vertex velocities vary over $\mathcal{O}(N)$ cells. We also assume that the nutrient supply is sufficient that the growth of the cell target lengths can be treated as independent of the nutrient concentration ($\Gamma \neq \Gamma(c)$). We nondimensionalise the discrete model using the same scalings as in (4.23), and so obtain the same dimensionless discrete system as in §4.4,

$$\frac{1}{N}\frac{\mathrm{d}l_{n+\frac{1}{2N}}}{\mathrm{d}\tau} = u_{n+\frac{1}{N}} - u_n, \quad n = 0, \dots, 1 - \tfrac{1}{N}, \tag{G.1}$$

$$\alpha p_{n+\frac{1}{2N}} = \lambda_{n+\frac{1}{2N}}(a_{n+\frac{1}{2N}} - l_{n+\frac{1}{2N}}), \quad n = 0, \dots, 1 - \tfrac{1}{N}, \tag{G.2}$$

$$\frac{1}{6N}\left(\mu_{n-\frac{1}{2N}}\left(u_{n-\frac{1}{N}} + 2u_n\right) + \mu_{n+\frac{1}{2N}}\left(2u_n + u_{n+\frac{1}{N}}\right)\right) = p_{n-\frac{1}{2N}} - p_{n+\frac{1}{2N}}, \quad n = \tfrac{1}{N}, \dots, 1 - \tfrac{1}{N}, \tag{G.3}$$

$$\frac{\mathrm{d}a_{n+\frac{1}{2N}}}{\mathrm{d}\tau} = \Gamma(l_{n+\frac{1}{2N}}, a_{n+\frac{1}{2N}}, p_{n+\frac{1}{2N}}; \gamma_{n+\frac{1}{2N}}), \quad n = 0, \dots, 1 - \tfrac{1}{N}, \tag{G.4}$$

with $\frac{1}{6N}\mu_{\frac{1}{2N}}(2u_0 + u_{\frac{1}{N}}) = -p_{\frac{1}{2N}}, \quad \frac{1}{6N}\mu_{1-\frac{1}{2N}}(u_{1-\frac{1}{N}} + 2u_1) = p_{1-\frac{1}{2N}},$ (G.5)

and $x_n(0) = x_{init}(n), \quad n = 0, \dots, 1, \quad a_{n+\frac{1}{2N}}(0) = a_{init}\left(n + \frac{1}{2N}\right), \quad n = 0, \dots, 1 - \frac{1}{N}.$ (G.6)

We follow a multiscale approach and treat the cell variables as functions of n (here taken

to be the scaled discrete cell index), ν (the scaled continuous cell-index variable) and τ,

$$\begin{aligned} l_{n+\frac{1}{2N}} &= l(n+\tfrac{1}{2N},\nu+\tfrac{1}{2N},\tau), \quad a_{n+\frac{1}{2N}} = a(n+\tfrac{1}{2N},\nu+\tfrac{1}{2N},\tau), \\ p_{n+\frac{1}{2N}} &= p(n+\tfrac{1}{2N},\nu+\tfrac{1}{2N},\tau), \quad u_n = u(n,\nu,\tau), \end{aligned} \tag{G.7}$$

where l, a, p and u are periodic in n (with period M/N) for each value of ν. We expand the finite differences in (G.1) and (G.3) about $\nu+\frac{1}{2N}$ and ν respectively as

$$\begin{aligned} u_{n+\frac{1}{N}} - u_n =& u(n+\tfrac{1}{N},\nu+\tfrac{1}{N},\tau) - u(n,\nu,\tau) \\ =& u(n+\tfrac{1}{N},\nu+\tfrac{1}{2N},\tau) - u(n,\nu+\tfrac{1}{2N},\tau) \\ &+ \frac{1}{2N}\left(\frac{\partial u}{\partial \nu}(n+\tfrac{1}{N},\nu+\tfrac{1}{2N},\tau) + \frac{\partial u}{\partial \nu}(n,\nu+\tfrac{1}{2N},\tau)\right) + \mathcal{O}\left(\tfrac{1}{N^2}\right), \\ p_{n-\frac{1}{2N}} - p_{n+\frac{1}{2N}} =& p(n-\tfrac{1}{2N},\nu-\tfrac{1}{2N},\tau) - p(n+\tfrac{1}{2N},\nu+\tfrac{1}{2N},\tau) \\ =& p(n-\tfrac{1}{2N},\nu,\tau) - p(n+\tfrac{1}{2N},\nu,\tau) \\ &- \frac{1}{2N}\left(\frac{\partial p}{\partial \nu}(n-\tfrac{1}{2N},\nu,\tau) + \frac{\partial p}{\partial \nu}(n+\tfrac{1}{2N},\nu,\tau)\right) + \mathcal{O}\left(\tfrac{1}{N^2}\right), \end{aligned}$$

and the vertex velocities in (G.3) about ν as

$$\begin{aligned} u_{n+\frac{1}{N}} &= u(n+\tfrac{1}{N},\nu+\tfrac{1}{N},\tau) = u(n+\tfrac{1}{N},\nu,\tau) + \frac{1}{N}\frac{\partial u}{\partial \nu}(n+\tfrac{1}{N},\nu,\tau) + \mathcal{O}\left(\tfrac{1}{N^2}\right), \\ u_{n-\frac{1}{N}} &= u(n-\tfrac{1}{N},\nu-\tfrac{1}{N},\tau) = u(n-\tfrac{1}{N},\nu,\tau) - \frac{1}{N}\frac{\partial u}{\partial \nu}(n-\tfrac{1}{N},\nu,\tau) + \mathcal{O}\left(\tfrac{1}{N^2}\right). \end{aligned}$$

Thus, (G.1) and (G.3) become

$$\begin{aligned} \frac{1}{N}\frac{\partial l}{\partial \tau}(n+\tfrac{1}{2N},\nu+\tfrac{1}{2N},\tau) =& u(n+\tfrac{1}{N},\nu+\tfrac{1}{2N},\tau) - u(n,\nu+\tfrac{1}{2N},\tau) \\ &+ \frac{1}{2N}\left(\frac{\partial u}{\partial \nu}(n+\tfrac{1}{N},\nu+\tfrac{1}{2N},\tau) + \frac{\partial u}{\partial \nu}(n,\nu+\tfrac{1}{2N},\tau)\right) + \mathcal{O}\left(\tfrac{1}{N^2}\right), \end{aligned} \tag{G.8}$$

$$\begin{aligned} &\frac{1}{6N}\left(\mu_{n-\frac{1}{2N}}\left[u(n-\tfrac{1}{N},\nu,\tau)+2u(n,\nu,\tau)\right] + \mu_{n+\frac{1}{2N}}\left[2u(n,\nu,\tau)+u(n+\tfrac{1}{N},\nu,\tau)\right]\right) \\ &= p(n-\tfrac{1}{2N},\nu,\tau) - p(n+\tfrac{1}{2N},\nu,\tau) - \frac{1}{2N}\left(\frac{\partial p}{\partial \nu}(n-\tfrac{1}{2N},\nu,\tau) + \frac{\partial p}{\partial \nu}(n+\tfrac{1}{2N},\nu,\tau)\right) + \mathcal{O}\left(\tfrac{1}{N^2}\right). \end{aligned} \tag{G.9}$$

We look for solutions as asymptotic expansions

$$l = \sum_{i=0}^{\infty}\left(\tfrac{1}{N}\right)^i l^{(i)}, \quad a = \sum_{i=0}^{\infty}\left(\tfrac{1}{N}\right)^i a^{(i)}, \quad p = \sum_{i=0}^{\infty}\left(\tfrac{1}{N}\right)^i p^{(i)}, \quad u = \sum_{i=0}^{\infty}\left(\tfrac{1}{N}\right)^i u^{(i)}. \tag{G.10}$$

At leading order ($\mathcal{O}(1)$), (G.8) and (G.9) give

$$\begin{aligned} u^{(0)}(n+\tfrac{1}{N},\nu+\tfrac{1}{2N},\tau) - u^{(0)}(n,\nu+\tfrac{1}{2N},\tau) = 0, \quad \nu \in [0, 1-\tfrac{1}{2N}], \\ p^{(0)}(n-\tfrac{1}{2N},\nu,\tau) - p^{(0)}(n+\tfrac{1}{2N},\nu,\tau) = 0, \quad \nu \in [0,1], \end{aligned}$$

so $u^{(0)}$ and $p^{(0)}$ are periodic in n with period $1/N$. Since n is discrete, this means that $u^{(0)}$ and $p^{(0)}$ are independent of n, *i.e.* $u^{(0)} \equiv u^{(0)}(\nu,\tau)$ and $p^{(0)} \equiv p^{(0)}(\nu,\tau)$. Therefore, at $\mathcal{O}(1/N)$, (G.8) gives

$$u^{(1)}(n+\tfrac{1}{N},\nu+\tfrac{1}{2N},\tau) = u^{(1)}(n,\nu+\tfrac{1}{2N},\tau) + \frac{\partial l^{(0)}}{\partial\tau}(n+\tfrac{1}{2N},\nu+\tfrac{1}{2N},\tau) - \frac{\partial u^{(0)}}{\partial\nu}(\nu+\tfrac{1}{2N},\tau).$$

By induction on n, we obtain

$$u^{(1)}(n+\tfrac{M}{N},\nu+\tfrac{1}{2N},\tau) = u^{(1)}(n,\nu+\tfrac{1}{2N},\tau) + M\frac{\partial\overline{l^{(0)}}}{\partial\tau}(\nu+\tfrac{1}{2N},\tau) - M\frac{\partial u^{(0)}}{\partial\nu}(\nu+\tfrac{1}{2N},\tau),$$

where $\overline{l^{(0)}}$ is the average value of $l^{(0)}$ with respect to n over a period of M cells given by

$$\overline{l^{(0)}}(\nu,\tau) = \frac{1}{M}\sum_{i=0}^{M-1} l^{(0)}(n+\tfrac{1}{2N}+\tfrac{i}{N},\nu,\tau), \tag{G.11}$$

which is independent of n by the periodicity of l. Since $u^{(1)}$ is periodic in n with period M/N,

$$u^{(1)}(n+\tfrac{M}{N},\nu+\tfrac{1}{2N},\tau) = u^{(1)}(n,\nu+\tfrac{1}{2N},\tau),$$

and so

$$\frac{\partial\overline{l^{(0)}}}{\partial\tau}(\nu+\tfrac{1}{2N},\tau) = \frac{\partial u^{(0)}}{\partial\nu}(\nu+\tfrac{1}{2N},\tau).$$

At $\mathcal{O}(1/N)$, (G.9) gives

$$\tfrac{1}{2}(\mu_{n-\frac{1}{2N}}+\mu_{n+\frac{1}{2N}})u^{(0)}(\nu,\tau) = p^{(1)}(n+\tfrac{1}{2N},\nu,\tau) - p^{(1)}(n-\tfrac{1}{2N},\nu,\tau) - \frac{\partial p^{(0)}}{\partial\nu}(\nu,\tau).$$

As before, by induction on n and periodicity of $p^{(1)}$, we have that

$$\overline{\mu}u^{(0)}(\nu,\tau) = \frac{1}{M}\left(p^{(1)}(n+\tfrac{M}{N}-\tfrac{1}{2N},\nu,\tau) - p^{(1)}(n-\tfrac{1}{2N},\nu,\tau)\right) - \frac{\partial p^{(0)}}{\partial\nu}(\nu,\tau) = -\frac{\partial p^{(0)}}{\partial\nu}(\nu,\tau),$$

where $\overline{\mu}$ is the average value of $\mu_{n+\frac{1}{2N}}$ over a period of M cells given by

$$\overline{\mu} = \frac{1}{M}\left(\tfrac{1}{2}\mu_{n-\frac{1}{2N}} + \sum_{i=1}^{M-1}\mu_{n-\frac{1}{2N}+\frac{i}{N}} + \tfrac{1}{2}\mu_{n-\frac{1}{2N}+\frac{M}{N}}\right). \tag{G.12}$$

From (G.2), we have that at leading order

$$l^{(0)}(n+\tfrac{1}{2N},\nu,\tau) = a^{(0)}(n+\tfrac{1}{2N},\nu,\tau) - \alpha\frac{1}{\lambda_{n+\frac{1}{2N}}}p^{(0)}(\nu,\tau).$$

Taking the average of this equation over M cells gives

$$\overline{l^{(0)}}(\nu,\tau) = \overline{a^{(0)}}(\nu,\tau) - \alpha\overline{(1/\lambda)}p^{(0)}(\nu,\tau),$$

where

$$\overline{a^{(0)}}(\nu,\tau) = \frac{1}{M}\sum_{i=0}^{M-1} a^{(0)}(n+\tfrac{1}{2N}+\tfrac{i}{N},\nu,\tau), \quad \overline{1/\lambda} = \frac{1}{M}\sum_{i=0}^{M-1}\frac{1}{\lambda_{n+\frac{1}{2N}+\frac{i}{N}}}. \tag{G.13}$$

Substituting (G.7) and the asymptotic expansions in (G.10) into the evolution equation for the cell target lengths (G.4) and expanding Γ in powers of $1/N$ for $N \gg 1$, we obtain at leading order

$$\begin{aligned}\frac{\partial a^{(0)}}{\partial\tau}(n+\tfrac{1}{2N},&\nu+\tfrac{1}{2N},\tau)\\ &= \Gamma(l^{(0)}(n+\tfrac{1}{2N},\nu+\tfrac{1}{2N},\tau), a^{(0)}(n+\tfrac{1}{2N},\nu+\tfrac{1}{2N},\tau), p^{(0)}(\nu+\tfrac{1}{2N},\tau);\gamma_{n+\frac{1}{2N}})\\ &=: \Gamma^{(0)}(n+\tfrac{1}{2N},\nu+\tfrac{1}{2N},\tau).\end{aligned}$$

Averaging this equation over a period yields

$$\frac{\partial\overline{a^{(0)}}}{\partial\tau}(\nu+\tfrac{1}{2N},\tau) = \overline{\Gamma^{(0)}}(\nu+\tfrac{1}{2N},\tau),$$

where

$$\overline{\Gamma^{(0)}}(\nu,\tau) = \sum_{i=0}^{M-1}\Gamma^{(0)}(n+\tfrac{1}{2N}+\tfrac{i}{N},\nu,\tau). \tag{G.14}$$

With (G.7), the boundary conditions (G.5) become

$$\begin{aligned}\frac{1}{6N}\mu_{1/2N}\left(2u(0,0,\tau)+u(\tfrac{1}{N},\tfrac{1}{N},\tau)\right) &= -p(\tfrac{1}{2N},\tfrac{1}{2N},\tau)\\ &= -\left(p(\tfrac{1}{2N},0,\tau)+\frac{1}{2N}\frac{\partial p}{\partial\nu}(\tfrac{1}{2N},0,\tau)\right)+\mathcal{O}(\tfrac{1}{N^2}),\\ \frac{1}{6N}\mu_{1-1/2N}\left(u(1-\tfrac{1}{N},1-\tfrac{1}{N},\tau)+2u(1,1,\tau)\right) &= -p(1-\tfrac{1}{2N},1-\tfrac{1}{2N},\tau)\\ &= p(1-\tfrac{1}{2N},1,\tau)-\frac{1}{2N}\frac{\partial p}{\partial\nu}(1-\tfrac{1}{2N},1,\tau)+\mathcal{O}(\tfrac{1}{N^2}),\end{aligned}$$

where we have expanded about $\nu=0$ and $\nu=1$ respectively. Substituting in the asymptotic expansions (G.10) yields at $\mathcal{O}(1)$

$$p^{(0)}(0,\tau)=0, \quad p^{(0)}(1,\tau)=0.$$

In summary, the leading order system for the cell variables is given by

$$\frac{\partial\overline{l^{(0)}}}{\partial\tau}(\nu,\tau) = \frac{\partial u^{(0)}}{\partial\nu}(\nu,\tau), \tag{G.15}$$

$$\alpha p^{(0)}(\nu,\tau) = \frac{1}{\overline{1/\lambda}}(\overline{a^{(0)}}(\nu,\tau)-\overline{l^{(0)}}(\nu,\tau)), \tag{G.16}$$

$$\overline{\mu}u^{(0)}(\nu,\tau) = -\frac{\partial p^{(0)}}{\partial\nu}(\nu,\tau), \tag{G.17}$$

$$\frac{\partial\overline{a^{(0)}}}{\partial\tau}(\nu,\tau) = \overline{\Gamma^{(0)}}(\nu,\tau), \tag{G.18}$$

$$p^{(0)}(0,\tau) = p^{(0)}(1,\tau) = 0, \tag{G.19}$$

with averaged quantities as defined in (G.11)–(G.14). The leading order cell pressure and velocity are dependent on the cell index only through the continuous variable ν, and the leading order system (G.15)–(G.19) is the same as that for slowly-varying cell properties (4.50)–(4.54), with all parameters replaced by their average values over a period (except λ, which is replaced by its harmonic mean, $1/\overline{(1/\lambda)}$).

Bibliography

[1] Basic principles of tissue engineering. http://textile.iitd.ac.in/highlights/fol8/01.htm.

[2] N.S. Abdullah and D.B. Das. Modelling nutrient transport in hollow fibre membrane bioreactor for growing bone tissue with consideration of multi-component interactions. *Chemical Engineering Science*, 62(21):5821–5839, 2007.

[3] N.S. Abdullah, D.R. Jones, and D.B. Das. Nutrient transport in bioreactors for bone tissue growth: Why do hollow fibre membrane bioreactors work? *Chemical Engineering Science*, 64 (1):109–125, 2009.

[4] T. Alarcón, H.M. Byrne, and P.K. Maini. A cellular automaton model for tumour growth in inhomogeneous environment. *Journal of Theoretical Biology*, 225(2):257–274, 2003.

[5] T. Alarcón, H.M. Byrne, and P.K. Maini. Towards whole-organ modelling of tumour growth. *Progress in Biophysics and Molecular Biology*, 85(2):451–472, 2004.

[6] M. Alber, N. Chen, P.M. Lushnikov, and S.A. Newman. Continuous macroscopic limit of a discrete stochastic model for interaction of living cells. *Physical Review Letters*, 99(16):168102, 2007.

[7] J.W. Allen, T. Hassanein, and S.N. Bhatia. Advances in bioartificial liver devices. *Hepatology*, 34(3):447–455, 2001.

[8] A.R. Amini, C.T. Laurencin, and S.P. Nukavarapu. Bone tissue engineering: recent advances and challenges. *Critical Reviews in Biomedical Engineering*, 40(5):363–408, 2012.

[9] A.R.A. Anderson and V. Quaranta. Integrative mathematical oncology. *Nature Reviews Cancer*, 8(3):227–234, 2008.

[10] A.R.A. Anderson, K.A. Rejniak, P. Gerlee, and V. Quaranta. Microenvironment driven invasion: a multiscale multimodel investigation. *Journal of Mathematical Biology*, 58(4):579–624, 2009.

[11] J. Ando, H. Nomura, and A. Kamiya. The effect of fluid shear stress on the migration and proliferation of cultured endothelial cells. *Microvascular Research*, 33(1):62–70, 1987.

[12] A. Atala, S.B. Bauer, S. Soker, J.J. Yoo, and A.B. Retik. Tissue-engineered autologous bladders for patients needing cystoplasty. *The Lancet*, 367(9518):1241–1246, 2006.

[13] B. Azimi, P. Nourpanah, M. Rabiee, and S. Arbab. Poly (lactide-co-glycolide) fiber: An overview. *Journal of Engineered Fabrics & Fibers*, 9(1):47–66, 2014.

[14] G.N. Bancroft, V.I. Sikavitsas, J. van den Dolder, T.L. Sheffield, C.G. Ambrose, J.A. Jansen, and A.G. Mikos. Fluid flow increases mineralized matrix deposition in 3D perfusion culture of marrow stromal osteoblasts in a dose-dependent manner. *Proceedings of the National Academy of Sciences*, 99(20):12600–12605, 2002.

[15] D. Basanta, D.W. Strand, R.B. Lukner, O.E. Franco, D.E. Cliffel, G.E. Ayala, S.W. Hayward, and A.R.A. Anderson. The role of transforming growth factor-β–mediated tumor-stroma interactions in prostate cancer progression: An integrative approach. *Cancer Research*, 69 (17):7111–7120, 2009.

[16] J. Bear. *Dynamics of fluids in porous media*. Dover publications, 1988.

[17] G. Beavers and D. Joseph. Boundary conditions at a naturally permeable wall. *Journal of Fluid Mechanics*, 30(1):197–207, 1967.

[18] M. Bodnar and J.J.L. Velazquez. Derivation of macroscopic equations for individual cell-based models: a formal approach. *Mathematical Methods in the Applied Sciences*, 28(15):1757–1779, 2005.

[19] F. Boschetti, M.T. Raimondi, F. Migliavacca, and G. Dubini. Prediction of the micro-fluid dynamic environment imposed to three-dimensional engineered cell systems in bioreactors. *Journal of Biomechanics*, 39(3):418–425, 2006.

[20] T.R. Bradley, G.S. Hodgson, and M. Rosendaal. The effect of oxygen tension on haemopoietic and fibroblast cell proliferation in vitro. *Journal of Cellular Physiology*, 97(3):517–522, 1978.

[21] M. Brittberg, A. Lindahl, A. Nilsson, C. Ohlsson, O. Isaksson, and L. Peterson. Treatment of deep cartilage defects in the knee with autologous chondrocyte transplantation. *New England Journal of Medicine*, 331(14):889–895, 1994.

[22] J.D. Brotherton and P.C. Chau. Modeling of axial-flow hollow fiber cell culture bioreactors. *Biotechnology Progress*, 12(5):575–590, 1996.

[23] D.M. Brunette. Mechanical stretching increases the number of epithelial cells synthesizing DNA in culture. *Journal of Cell Science*, 69(1):35–45, 1984.

[24] H. Byrne and D. Drasdo. Individual-based and continuum models of growing cell populations: a comparison. *Journal of Mathematical Biology*, 58(4):657–687, 2009.

[25] H.M. Byrne and M.A.J. Chaplain. Free boundary value problems associated with the growth and development of multicellular spheroids. *European Journal of Applied Mathematics*, 8(06): 639–658, 1997.

[26] H.M. Byrne, J.R. King, D.S. McElwain, and L. Preziosi. A two-phase model of solid tumour growth. *Applied Mathematics Letters*, 16(4):567–573, 2003.

[27] R. Callies, M.E. Jackson, and K.M. Brindle. Measurements of the growth and distribution of mammalian cells in a hollow–fiber bioreactor using nuclear magnetic resonance imaging. *Nature Biotechnology*, 12(1):75–78, 1994.

[28] P.C. Carman. Fluid flow through granular beds. *Transactions–Institution of Chemical Engineers*, 15:150–166, 1937.

[29] R.L. Carrier, M. Papadaki, M. Rupnick, F.J. Schoen, N. Bursac, R. Langer, L.E. Freed, and G. Vunjak-Novakovic. Cardiac tissue engineering: cell seeding, cultivation parameters, and tissue construct characterization. *Biotechnology and Bioengineering*, 64(5):580–589, 1999.

[30] J.J. Casciari, S.V. Sotirchos, and R.M. Sutherland. Mathematical modelling of microenvironment and growth in EMT6/Ro multicellular tumour spheroids. *Cell Proliferation*, 25(1):1–22, 1992.

[31] P. Causin and R. Sacco. A computational model for biomass growth simulation in tissue engineering. *Communications in Applied and Industrial Mathematics*, 2(1), 2011.

[32] S. Cetin, C.L. Leaphart, J. Li, I. Ischenko, M. Hayman, J. Upperman, R. Zamora, S. Watkins, H.R. Ford, J. Wang, *et al.* Nitric oxide inhibits enterocyte migration through activation of RhoA-GTPase in a SHP-2-dependent manner. *American Journal of Physiology - Gastrointestinal and Liver Physiology*, 292(5):G1347–G1358, 2007.

[33] C. Chang, D.A. Lauffenburger, and T.I. Morales. Motile chondrocytes from newborn calf: migration properties and synthesis of collagen II. *Osteoarthritis and Cartilage*, 11(8):603–612, 2003.

[34] L.A.C. Chapman, R.J. Shipley, J.P. Whiteley, M.J. Ellis, H.M. Byrne, and S.L. Waters. Optimising cell aggregate expansion in a perfused hollow fibre bioreactor via mathematical modelling. *PLoS ONE*, 9(8):e105813, 2014.

[35] C.Y. Chen, H.M. Byrne, and J.R. King. The influence of growth-induced stress from the surrounding medium on the development of multicell spheroids. *Journal of Mathematical Biology*, 43(3):191–220, 2001.

[36] G. Chen and A. Palmer. Hemoglobin-based oxygen carrier and convection enhanced oxygen transport in a hollow fiber bioreactor. *Biotechnology and Bioengineering*, 102:1603–1612, 2009.

[37] H.H. Chen and G.W. Brodland. Cell-level finite element studies of viscous cells in planar aggregates. *Journal of Biomechanical Engineering*, 122(4):394–401, 2000.

[38] G. Cheng, B.B. Youssef, P. Markenscoff, and K. Zygourakis. Cell population dynamics modulate the rates of tissue growth processes. *Biophysical Journal*, 90(3):713–724, 2006.

[39] G. Cheng, P. Markenscoff, and K. Zygourakis. A 3D Hybrid Model for Tissue Growth: The Interplay between Cell Population and Mass Transport Dynamics. *Biophysical Journal*, 97(2): 401–414, 2009.

[40] C.A. Chung, C.W. Yang, and C.W. Chen. Analysis of cell growth and diffusion in a scaffold for cartilage tissue engineering. *Biotechnology and Bioengineering*, 94(6):1138–1146, 2006.

[41] C.A. Chung, C.W. Chen, C.P. Chen, and C.S. Tseng. Enhancement of cell growth in tissue-engineering constructs under direct perfusion: Modeling and simulation. *Biotechnology and Bioengineering*, 97(6):1603–1616, 2007.

[42] C.A. Chung, T.H. Lin, S.D. Chen, and H.I. Huang. Hybrid cellular automaton modeling of nutrient modulated cell growth in tissue engineering constructs. *Journal of Theoretical Biology*, 262(2):267–278, 2010.

[43] M. Cioffi, F. Boschetti, M.T. Raimondi, and G. Dubini. Modeling evaulation of the fluid-dynamic microenvironment in tissue-engineered constructs: a micro-CT based model. *Biotechnology and Bioengineering*, 93(3):500–510, 2006.

[44] M. Cioffi, J. Küffer, S. Ströbel, G. Dubini, I. Martin, and D. Wendt. Computational evaluation of oxygen and shear stress distributions in 3D perfusion culture systems: macro-scale and micro-structured models. *Journal of Biomechanics*, 41(14):2918–2925, 2008.

[45] M.F. Clincke, Carinmölleryd, Y. Zhang, E. Lindskog, K. Walsh, and V. Chotteau. Very high density of CHO cells in perfusionby ATF or TFF in WAVE bioreactor - Part I. effect of the cell density on the process. *Biotechnology Progress*, 29:768–777, 2013.

[46] F. Coletti, S. Macchietto, and N. Elvassore. Mathematical modeling of three-dimensional cell cultures in perfusion bioreactors. *Industrial & Engineering Chemistry Research*, 45(24): 8158–8169, 2006.

[47] F. Consolo, G.B. Fiore, S. Truscello, M. Caronna, U. Morbiducci, F.M. Montevecchi, and A. Redaelli. A computational model for the optimization of transport phenomena in a rotating hollow-fiber bioreactor for artificial liver. *Tissue Engineering Part C: Methods*, 15(1):41–55, 2008.

[48] M.R. Corkins, J.H.Y. Park, D.V. Davis, D.H. Slentz, and R.G. MacDonald. Regulation of the insulin-like growth factor axis by increasing cell number in intestinal epithelial (IEC-6) cells. *Growth Hormone & IGF Research*, 9(6):414–424, 1999.

[49] L.J. Cummings and S.L. Waters. Tissue growth in a rotating bioreactor. Part II: fluid flow and nutrient transport problems. *Mathematical Medicine and Biology*, 24:169–208, 2006.

[50] L.J. Cummings, N.B.E. Sawyer, S.P. Morgan, F. Rose, and S.L. Waters. Tracking large solid constructs suspended in a rotating bioreactor: a combined experimental and theoretical study. *Biotechnology and Bioengineering*, 104(6):1224–1234, 2009.

[51] E. Curcio, A. Piscioneri, S. Morelli, S. Salerno, P. Macchiarini, and L. De Bartolo. Kinetics of oxygen uptake by cells potentially used in a tissue engineered trachea. *Biomaterials*, 35(25): 6829–6837, 2014.

[52] A. Curtis and M. Riehle. Tissue engineering: the biophysical background. *Physics in Medicine and Biology*, 46(4):R47–R65, 2001.

[53] L. Custer and C.J.P. Mullon. Oxygen delivery to and use by primary porcine hepatocytes in the hepatassist 2000 system for extracorporeal treatment of patients in end-stage liver failure. In *Oxygen Transport to Tissue XX*, volume 454 of *Advances in Experimental Medicine and Biology*, pages 261–271. Springer, 1998.

[54] D.B. Das. Multiscale simulation of nutrient transport in hollow fibre membrane bioreactor for growing bone tissue: Sub-cellular scale and beyond. *Chemical Engineering Science*, 62(13): 3627–3639, 2007.

[55] A.J. Davidson, M.J. Ellis, and J.B. Chaudhuri. A theoretical method to improve and optimize the design of bioartificial livers. *Biotechnology and Bioengineering*, 106(6):980–988, 2010.

[56] A.J. Davidson, M.J. Ellis, and J.B. Chaudhuri. A theoretical approach to zonation in a bioartificial liver. *Biotechnology and Bioengineering*, 109(1):234–243, 2012.

[57] T. Davisson, R.L. Sah, and A. Ratcliffe. Perfusion increases cell content and matrix synthesis in chondrocyte three-dimensional cultures. *Tissue Engineering*, 8(5):807–816, 2002.

[58] I.E. De Napoli, E.M. Zanetti, G. Fragomeni, E. Giuzio, A.L. Audenino, and G. Catapano. Transport modeling of convection-enhanced hollow fiber membrane bioreactors for therapeutic applications. *Journal of Membrane Science*, 471:347–361, 2014.

[59] I.E. De Napoli, S. Scaglione, P. Giannoni, R. Quarto, and G. Catapano. Mesenchymal stem cell culture in convection-enhanced hollow fibre membrane bioreactors for bone tissue engineering. *Journal of Membrane Science*, 379(1):341–352, 2011.

[60] T.S. Deisboeck, Z. Wang, P. Macklin, and V. Cristini. Multiscale cancer modeling. *Annual Review of Biomedical Engineering*, 13(1):127–155, 2011.

[61] R.L. DiMarco, J. Su, K.S. Yan, R. Dewi, C.J. Kuo, and S.C. Heilshorn. Engineering of three-dimensional microenvironments to promote contractile behavior in primary intestinal organoids. *Integrative Biology*, 6(2):127–142, 2014.

[62] S. Dormann and A. Deutsch. Modeling of self-organized avascular tumor growth with a hybrid cellular automaton. *In Silico Biology*, 2(3):393–406, 2002.

[63] D. Drasdo and M. Loeffler. Individual-based models to growth and folding in one-layered tissues: intestinal crypts and early development. *Nonlinear Analysis - Theory Methods and Applications*, 47(1):245–256, 2001.

[64] D. Drasdo. Coarse Graining in Simulated Cell Populations. *Advances in Complex Systems*, 08 (02n03):319–363, 2005.

[65] D. Drasdo and S. Höhme. A single-cell-based model of tumor growth in vitro: monolayers and spheroids. *Physical Biology*, 2(3):133–147, 2005.

[66] J.C.Y. Dunn, W.Y. Chan, V. Cristini, J.S. Kim, J. Lowengrub, S. Singh, and B.M. Wu. Analysis of cell growth in three-dimensional scaffolds. *Tissue Engineering*, 12(4):705–716, 2006.

[67] G.P. Eggleton, P. Eggleton, and A.V. Hill. The coefficient of diffusion of lactic acid through muscle. *Proceedings of the Royal Society of London B*, 103(727):620–628, 1928.

[68] G. Elert. *The Physics Hypertextbook*. 2015. http://physics.info/.

[69] M. Ellis, M. Jarman-Smith, and J. Chaudhuri. Bioreactor systems for tissue engineering: a four-dimensional challenge. In *Bioreactors for Tissue Engineering*, pages 1–18. Springer, 2005.

[70] M.J. Ellis and J.B. Chaudhuri. Poly (lactic-co-glycolic acid) hollow fibre membranes for use as a tissue engineering scaffold. *Biotechnology and Bioengineering*, 96(1):177–187, 2007.

[71] M.J. Ellis and J.B. Chaudhuri. Human bone derived cell culture on PLGA flat sheet membranes of different lactide:glycolide ratio. *Biotechnology and Bioengineering*, 101(2):369–377, 2008.

[72] H. Enderling, N.R. Alexander, E.S. Clark, K.M. Branch, L. Estrada, C. Crooke, J. Jourquin, N. Lobdell, M.H. Zaman, S.A. Guelcher, A.R. Anderson, and A.M. Weaver. Dependence of invadopodia function on collagen fiber spacing and cross-linking: computational modeling and experimental evidence. *Biophysical Journal*, 95(5):2203–2218, 2008.

[73] H. Enderling, A.R.A. Anderson, M.A.J. Chaplain, A. Beheshti, L. Hlatky, and P. Hahnfeldt. Paradoxical dependencies of tumor dormancy and progression on basic cell kinetics. *Cancer Research*, 69(22):8814–8821, 2009.

[74] F.B. Engel, M. Schebesta, M.T. Duong, G. Lu, S. Ren, J.B. Madwed, H. Jiang, Y. Wang, and M.T. Keating. p38 MAP kinase inhibition enables proliferation of adult mammalian cardiomyocytes. *Genes & Development*, 19(10):1175–1187, 2005.

[75] S. Eshghi and D.V. Schaffer. Engineering microenvironments to control stem cell fate and function. In *Stem Book*. Harvard Stem Cell Institute, 2008.

[76] B. Fermor, S.E. Christensen, I. Youn, J.M. Cernanec, C.M. Davies, and J.B. Weinberg. Oxygen, nitric oxide and articular cartilage. *European Cell Materials*, 13:56–65, 2007.

[77] A.G. Fletcher, M. Osterfield, R.E. Baker, and S.Y. Shvartsman. Vertex models of epithelial morphogenesis. *Biophysical Journal*, 106(11):2291–2304, 2014.

[78] J.A. Fozard, H.M. Byrne, O.E. Jensen, and J.R. King. Continuum approximations of individual-based models for epithelial monolayers. *Mathematical Medicine and Biology*, 27 (1):39–74, 2010.

[79] R.E. Fraser, W.L. Halseth, B. Johnson, and B.C. Paton. Experimental replacement of the superior vena cava: Autologous veins, free inverted jejunal grafts, and dacron grafts treated with graphite-benzalkonium-heparin. *Archives of Surgery*, 96(3):378–385, 1968.

[80] L.E. Freed, G. Vunjak-Novakovic, and R. Langer. Cultivation of cell-polymer cartilage implants in bioreactors. *Journal of Cellular Biochemistry*, 51(3):257–264, 1993.

[81] L.E. Freed, J.C. Marquis, R. Langer, and G. Vunjak-Novakovic. Kinetics of chondrocyte growth in cell-polymer implants. *Biotechnology and Bioengineering*, 43(7):597–604, 1994.

[82] L.E. Freed, J.C. Marquis, R. Langer, G. Vunjak-Novakovic, and J. Emmanual. Composition of cell-polymer cartilage implants. *Biotechnology and Bioengineering*, 43(7):605–614, 1994.

[83] L.E. Freed, R. Langer, I. Martin, N.R. Pellis, and G. Vunjak-Novakovic. Tissue engineering of cartilage in space. *Proceedings of the National Academy of Sciences*, 94(25):13885–13890, 1997.

[84] H.B. Frieboes, F. Jin, Y.L. Chuang, S.M. Wise, J.S. Lowengrub, and V. Cristini. Three-dimensional multispecies nonlinear tumor growth II: Tumor invasion and angiogenesis. *Journal of Theoretical Biology*, 264(4):1254–1278, 2010.

[85] C.J. Galban and B.R. Locke. Analysis of cell growth in a polymer scaffold using a moving boundary approach. *Biotechnology and Bioengineering*, 56(4):422–432, 1997.

[86] C.J. Galban and B.R. Locke. Analysis of cell growth kinetics and substrate diffusion in a polymer scaffold. *Biotechnology and Bioengineering*, 65(2):121–132, 1999.

[87] C.J. Galban and B.R. Locke. Effects of spatial variation of cells and nutrient and product concentrations coupled with product inhibition on cell growth in a polymer scaffold. *Biotechnology and Bioengineering*, 64(6):633–643, 1999.

[88] J. Galle, M. Loeffler, and D. Drasdo. Modeling the effect of deregulated proliferation and apoptosis on the growth dynamics of epithelial cell populations in vitro. *Biophysical Journal*, 88(1):62–75, 2005.

[89] R.A. Gatenby, K. Smallbone, P.K. Maini, F. Rose, J. Averill, R.B. Nagle, L. Worrall, and R.J. Gillies. Cellular adaptations to hypoxia and acidosis during somatic evolution of breast cancer. *British Journal of Cancer*, 97(5):646–653, 2007.

[90] L. Geris, P. Van Liedekerke, B. Smeets, E. Tijskens, and H. Ramon. A cell based modelling framework for skeletal tissue engineering applications. *Journal of Biomechanics*, 43(5):887–892, 2010.

[91] P. Gerlee and A.R.A. Anderson. An evolutionary hybrid cellular automaton model of solid tumour growth. *Journal of Theoretical Biology*, 246(4):583–603, 2007.

[92] E. Gevaert, L. Dolle, T. Billiet, P. Dubruel, L. van Grunsven, A. van Apeldoorn, and R. Cornelissen. High throughput micro-well generation of hepatocyte micro-aggregates for tissue engineering. *PLoS ONE*, 9(8):e105171, 2014.

[93] H. Gloeckner and H.D. Lemke. New miniaturized hollow-fiber bioreactor for in vivo like cell culture, cell expansion, and production of cell-derived products. *Biotechnology Progress*, 17 (5):828–831, 2001.

[94] M.J. Gramer and D.M. Poeschl. Comparison of cell growth in T-flasks, in micro hollow fiber bioreactors, and in an industrial scale hollow fiber bioreactor system. *Cytotechnology*, 34(1): 111–119, 2000.

[95] F. Graner and J.A. Glazier. Simulation of biological cell sorting using a two-dimensional extended Potts model. *Physical Review Letters*, 69(13):2013–2016, 1992.

[96] W.G. Gray. A derivation of the equations for multi-phase transport. *Chemical Engineering Science*, 30(2):229–233, 1975.

[97] H.P. Greenspan. On the growth and stability of cell cultures and solid tumors. *Journal of Theoretical Biology*, 56(1):229–242, 1976.

[98] L.G. Griffith and G. Naughton. Tissue engineering–current challenges and expanding opportunities. *Science*, 295(5557):1009–1014, 2002.

[99] J. Guo, G.W. Jourdian, and D.K. Maccallum. Culture and growth characteristics of chondrocytes encapsulated in alginate beads. *Connective Tissue Research*, 19(2-4):277–297, 1989.

[100] D.W. Hamilton, M.O. Riehle, W. Monaghan, and A.S.G. Curtis. Articular chondrocyte passage number: influence on adhesion, migration, cytoskeletal organisation and phenotype in response to nano- and micro-metric topography. *Cell Biology International*, 29(6):408–421, 2005.

[101] S. Hasegawa, S. Sato, S. Saito, Y. Suzuki, and D. Brunette. Mechanical stretching increases the number of cultured bone cells synthesizing DNA and alters their pattern of protein synthesis. *Calcified Tissue International*, 37(4):431–436, 1985.

[102] J.C. Haselgrove, I.M. Shapiro, and S.F. Silverton. Computer modeling of the oxygen supply and demand of cells of the avian growth cartilage. *American Journal of Physiology - Cell Physiology*, 265(2):C497–C506, 1993.

[103] R. Hass, C. Kasper, S. Bohm, R. Jacobs, *et al.* Different populations and sources of human mesenchymal stem cells (MSC): a comparison of adult and neonatal tissue-derived MSC. *Cell Communication and Signaling*, 9(1):12, 2011.

[104] P.D. Hay, A.R. Veitch, and J.D.S. Gaylor. Oxygen transfer in a convection-enhanced hollow fiber bioartificial liver. *Artificial Organs*, 25(2):119–130, 2001.

[105] C.A. Heath, G. Belfort, B.E. Hammer, S.D. Mirer, and J.M. Pimbley. Magnetic resonance imaging and modeling of flow in hollow-fiber bioreactors. *AIChE Journal*, 36(4):547–558, 1990.

[106] A. Hilal-Alnaqbi, A.H.I. Mourad, B.F. Yousef, and J.D. Gaylor. Experimental evaluation and theoretical modeling of oxygen transfer rate for the newly developed hollow fiber bioreactor with three compartments. *Bio-medical Materials and Engineering*, 23(5):387–403, 2013.

[107] G.W. Hiller, D.S. Clark, and H.W. Blanch. Cell retention–chemostat studies of hybridoma cells–analysis of hybridoma growth and metabolism in continuous suspension culture in serum-free medium. *Biotechnology and Bioengineering*, 42(2):185–195, 1993.

[108] C.A. Hoesli, M. Luu, and J.M. Piret. A novel alginate hollow fiber bioreactor process for cellular therapy applications. *Biotechnology Progress*, 25(6):1740–1751, 2009.

[109] S. Holm, A. Maroudas, J.P.G. Urban, G. Selstam, and A. Nachemson. Nutrition of the intervertebral disc: solute transport and metabolism. *Connective Tissue Research*, 8(2):101–119, 1981.

[110] C.E. Holy, M.S. Shoichet, and J.E. Davies. Engineering three-dimensional bone tissue in vitro using biodegradable scaffolds: investigating initial cell-seeding density and culture period. *Journal of Biomedical Materials Research*, 51(3):376–382, 2000.

[111] M.E. Hoque, Y.L. Chuan, and I. Pashby. Mathematical modelling on degradation of 3D tissue engineering scaffold materials. *Regenerative Research*, 1(1):58–61, 2012.

[112] G.T.J. Huang, S. Gronthos, and S. Shi. Mesenchymal stem cells derived from dental tissues vs. those from other sources: their biology and role in regenerative medicine. *Journal of Dental Research*, 88(9):792–806, 2009.

[113] H. Huang, R.D. Kamm, and R.T. Lee. Cell mechanics and mechanotransduction: pathways, probes, and physiology. *American Journal of Physiology - Cell Physiology*, 287(1):C1–C11, 2004.

[114] D.W. Hutmacher and H. Singh. Computational fluid dynamics for improved bioreactor design and 3D culture. *Trends in Biotechnology*, 26(4):166–172, 2008.

[115] W. Jäger and A. Mikelic. On the interface boundary condition of Beavers, Joseph, and Saffman. *SIAM Journal on Applied Mathematics*, 60(4):1111–1127, 2000.

[116] V.K. Jayaraman. The solution of hollow-fiber bioreactor design equations. *Biotechnology Progress*, 8(5):462–464, 1992.

[117] A.F. Jones, H.M. Byrne, J.S. Gibson, and J.W. Dold. A mathematical model of the stress induced during avascular tumour growth. *Journal of Mathematical Biology*, 40(6):473–499, 2000.

[118] S.C. Junior, M.L. Martins, and M.J. Vilela. A growth model for primary cancer. *Physica A: Statistical Mechanics and its Applications*, 261(3):569–580, 1998.

[119] A. Kamen and O. Henry. Development and optimization of an adenovirus production process. *The Journal of Gene Medicine*, 6(S1):S184–S192, 2004.

[120] A.R. Kansal, S. Torquato, E.A. Chiocca, and T.S. Deisboeck. Emergence of a subpopulation in a computational model of tumor growth. *Journal of Theoretical Biology*, 207(3):431–441, 2000.

[121] S. Kapur, D.J. Baylink, K. Lau, and K.H. William Lau. Fluid flow shear stress stimulates human osteoblast proliferation and differentiation through multiple interacting and competing signal transduction pathways. *Bone*, 32(3):241–251, 2003.

[122] S. Katayama, C. Tateno, T. Asahara, and K. Yoshizato. Size-dependent in vivo growth potential of adult rat hepatocytes. *The American Journal of Pathology*, 158(1):97–105, 2001.

[123] A. Khademhosseini, J.P. Vacanti, and R. Langer. Progress in tissue engineering. *Scientific American*, 300(5):64–71, 2009.

[124] B.S. Kim, A.J. Putnam, T.J. Kulik, and D.J. Mooney. Optimizing seeding and culture methods to engineer smooth muscle tissue on biodegradable polymer matrices. *Biotechnology and Bioengineering*, 57:46–54, 1998.

[125] B.Y. Kim, M.J. Han, and A.S. Chung. Effects of reactive oxygen species on proliferation of Chinese hamster lung fibroblast (V79) cells. *Free Radical Biology and Medicine*, 30(6):686–698, 2001.

[126] S.S. Kim and D.O. Cooney. An improved theoretical model for hollow-fiber enzyme reactors. *Chemical Engineering Science*, 31(4):289–294, 1976.

[127] Y. Kim, M.A. Stolarska, H.G. Othmer, N. Bellomo, and P.K. Maini. A hybrid model for tumor spheroid growth in vitro i: theoretical development and early results. *Mathematical Models and Methods in Applied Sciences*, 17:1773–1798, 2007.

[128] B.C. Knight and W.F. Tait. Dacron patch infection following carotid endarterectomy: a systematic review of the literature. *European Journal of Vascular and Endovascular Surgery*, 37(2):140–148, 2009.

[129] N. Korin, A. Bransky, U. Dinnar, and S. Levenberg. A parametric study of human fibroblasts culture in a microchannel bioreactor. *Lab on a Chip*, 7(5):611–617, 2007.

[130] J. Kozeny. Über kapillare leitung des wassers im boden. *Sitzungsber. Akad. Wiss. Wien*, 136: 271–306, 1927.

[131] M.R. Kreke and A.S. Goldstein. Hydrodynamic shear stimulates osteocalcin expression but not proliferation of bone marrow stromal cells. *Tissue Engineering*, 10(5-6):780–788, 2004.

[132] M.R. Kreke, W.R. Huckle, and A.S. Goldstein. Fluid flow stimulates expression of osteopontin and bone sialoprotein by bone marrow stromal cells in a temporally dependent manner. *Bone*, 36(6):1047–1055, 2005.

[133] M. Labecki, B.D. Bowen, and J.M. Piret. Two-dimensional analysis of protein transport in the extracapillary space of hollow-fibre bioreactors. *Chemical Engineering Science*, 51(17): 4197–4213, 1996.

[134] M. Labecki, J. Piret, and B. Bowen. Effects of free convection on three-dimensional protein transport in hollow-fiber bioreactors. *AIChE Journal*, 50(8):1974–1990, 2004.

[135] B. Ladoux. Biophysics: cells guided on their journey. *Nature Physics*, 5(6):377–378, 2009.

[136] K.A. Landman and A.Q. Cai. Cell proliferation and oxygen diffusion in a vascularising scaffold. *Bulletin of Mathematical Biology*, 69(7):2405–2428, 2007.

[137] K.A. Landman and C.P. Please. Tumour dynamics and necrosis: surface tension and stability. *Mathematical Medicine and Biology*, 18(2):131–158, 2001.

[138] R. Lanza, R. Langer, and J.P. Vacanti. *Principles of tissue engineering.* Academic Press, 2011.

[139] M. Lappa. Organic tissues in rotating bioreactors: fluid-mechanical aspects, dynamic growth models, and morphological evolution. *Biotechnology and Bioengineering*, 84(5):518–532, 2003.

[140] B.J. Lawrence, M. Devarapalli, and S.V. Madihally. Flow dynamics in bioreactors containing tissue engineering scaffolds. *Biotechnology and Bioengineering*, 102(3):935–947, 2009.

[141] M. Le Bars and M. Worster. Interfacial conditions between a pure fluid and a porous medium: implications for binary alloy solidification. *Journal of Fluid Mechanics*, 550:149–173, 2006.

[142] E. Leclerc, B. David, L. Griscom, B. Lepioufle, T. Fujii, P. Layrolle, and C. Legallaisa. Study of osteoblastic cells in a microfluidic environment. *Biomaterials*, 27(4):586–595, 2006.

[143] D.A. Lee, T. Reisler, and D.L. Bader. Expansion of chondrocytes for tissue engineering in alginate beads enhances chondrocytic phenotype compared to conventional monolayer techniques. *Acta Orthopaedica*, 74(1):6–15, 2003.

[144] G. Lemon and J.R. King. Multiphase modelling of cell behaviour on artificial scaffolds: effects of nutrient depletion and spatially nonuniform porosity. *Mathematical Medicine and Biology*, 24(1):57–83, 2007.

[145] G. Lemon, J.R. King, H.M. Byrne, O.E. Jensen, and K.M. Shakesheff. Mathematical modelling of engineered tissue growth using a multiphase porous flow mixture theory. *Journal of Mathematical Biology*, 52(5):571–594, 2006.

[146] D.P. Lennon, J.M. Edmison, and A.I. Caplan. Cultivation of rat marrow-derived mesenchymal stem cells in reduced oxygen tension: Effects on in vitro and in vivo osteochondrogenesis. *Journal of Cellular Physiology*, 187(3):345–355, 2001.

[147] A. Lesman, Y. Blinder, and S. Levenberg. Modeling of flow-induced shear stress applied on 3D cellular scaffolds: Implications for vascular tissue engineering. *Biotechnology and Bioengineering*, 105(3):645–654, 2010.

[148] S. Levenberg, N.F. Huang, E. Lavik, A.B. Rogers, J. Itskovitz-Eldor, and R. Langer. Differentiation of human embryonic stem cells on three-dimensional polymer scaffolds. *Proceedings of the National Academy of Sciences*, 100(22):12741–12746, 2003.

[149] T. Levy and E. Sanchez-Palencia. On boundary conditions for fluid flow in porous media. *International Journal of Engineering Science*, 13(11):923–940, 1975.

[150] M.C. Lewis, B.D. MacArthur, J. Malda, G. Pettet, and C.P. Please. Heterogeneous proliferation within engineered cartilaginous tissue: the role of oxygen tension. *Biotechnology and Bioengineering*, 91(5):607–615, 2005.

[151] D. Li, T. Tang, J. Lu, and K. Dai. Effects of flow shear stress and mass transport on the construction of a large-scale tissue-engineered bone in a perfusion bioreactor. *Tissue Engineering Part A*, 15(10):2773–2783, 2009.

[152] Y. Li, T. Ma, D.A. Kniss, L.C. Lasky, and S.T. Yang. Effects of filtration seeding on cell density, spatial distribution, and proliferation in nonwoven fibrous matrices. *Biotechnology Progress*, 17(5):935–944, 2001.

[153] J.Y. Lim and H.J. Donahue. Cell sensing and response to micro- and nanostructured surfaces produced by chemical and topographic patterning. *Tissue Engineering*, 13(8):1879–1891, 2007.

[154] J.S. Lowengrub, H.B. Frieboes, F. Jin, Y.L. Chuang, X. Li, P. Macklin, S.M. Wise, and V. Cristini. Nonlinear modelling of cancer: bridging the gap between cells and tumours. *Nonlinearity*, 23(1):R1–R91, 2009.

[155] H. Lu, W.S. Lim, P. Zhang, S.M. Chia, H. Yu, H. Mao, and K.W. Leong. Galactosylated poly (vinylidene difluoride) hollow fiber bioreactor for hepatocyte culture. *Tissue Engineering*, 11 (11-12):1667–1677, 2005.

[156] K. Lund-Olesen. Oxygen tension in synovial fluids. *Arthritis & Rheumatism*, 13(6):769–776, 1970.

[157] S.Y. Lunt and M.G. Vander Heiden. Aerobic glycolysis: meeting the metabolic requirements of cell proliferation. *Annual Review of Cell and Developmental Biology*, 27:441–464, 2011.

[158] P.M. Lushnikov, N. Chen, and M. Alber. Macroscopic dynamics of biological cells interacting via chemotaxis and direct contact. *Physical Review E*, 78(6):061904, 2008.

[159] M. Lutianov, S. Naire, S. Roberts, and J.H. Kuiper. A mathematical model of cartilage regeneration after cell therapy. *Journal of Theoretical Biology*, 289:136–150, 2011.

[160] P. Macchiarini, P. Jungebluth, T. Go, M.A. Asnaghi, L.E. Rees, T.A. Cogan, A. Dodson, J. Martorell, S. Bellini, P.P. Parnigotto, S.C. Dickinson, A.P. Hollander, S. Mantero, M.T. Conconi, and M.A. Birchall. Clinical transplantation of a tissue-engineered airway. *The Lancet*, 372(9655):2023–2030, 2008.

[161] M. Machide, A. Hashigasako, K. Matsumoto, and T. Nakamura. Contact inhibition of hepatocyte growth regulated by functional association of the c-Met/hepatocyte growth factor receptor and LAR protein-tyrosine phosphatase. *Journal of Biological Chemistry*, 281(13): 8765–8772, 2006.

[162] P. Malaviya and R.M. Nerem. Fluid-induced shear stress stimulates chondrocyte proliferation partially mediated via TGF-β 1. *Tissue Engineering*, 8(4):581–590, 2002.

[163] J. Malda, J. Rouwkema, D.E. Martens, E.P. Le Comte, F.K. Kooy, J. Tramper, C.A. Van Blitterswijk, and J. Riesle. Oxygen gradients in tissue-engineered Pegt/Pbt cartilaginous constructs: Measurement and modeling. *Biotechnology and Bioengineering*, 86(1):9–18, 2004.

[164] A. Marciniak-Czochra and A. Mikelic. Effective pressure interface law for transport phenomena between an unconfined fluid and a porous medium using homogenization. *Multiscale Modeling & Simulation*, 10(2):285–305, 2012.

[165] I. Martin, D. Wendt, and M. Heberer. The role of bioreactors in tissue engineering. *Trends in Biotechnology*, 22(2):80–86, 2004.

[166] Y. Martin and P. Vermette. Bioreactors for tissue mass culture: design, characterization, and recent advances. *Biomaterials*, 26(35):7481–7503, 2005.

[167] M. Massoudi. Constitutive relations for the interaction force in multicomponent particulate flows. *International Journal of Non-Linear Mechanics*, 38(3):313–336, 2003.

[168] G.V. Mazariegos, J.F. Patzer, R.C. Lopez, M. Giraldo, M.E. DeVera, T.A. Grogan, Y. Zhu, M.L. Fulmer, B.P. Amiot, and D.J. Kramer. First clinical use of a novel bioartificial liver support system. *American Journal of Transplantation*, 2(3):260–266, 2002.

[169] R.J. McCoy and F.J. O'Brien. Influence of shear stress in perfusion bioreactor cultures for the development of three-dimensional bone tissue constructs: a review. *Tissue Engineering Part B: Reviews*, 16(6):587–601, 2010.

[170] S.R. McDougall, A.R.A. Anderson, M.A.J. Chaplain, and J.A. Sherratt. Mathematical modelling of flow through vascular networks: implications for tumour-induced angiogenesis and chemotherapy strategies. *Bulletin of Mathematical Biology*, 64(4):673–702, 2002.

[171] D.L.S. McElwain and P.J. Ponzo. A model for the growth of a solid tumor with non-uniform oxygen consumption. *Mathematical Biosciences*, 35(3):267–279, 1977.

[172] J.G. McGarry, J. Klein-Nulend, M.G. Mullender, and P.J. Prendergast. A comparison of strain and fluid shear stress in stimulating bone cell responses–a computational and experimental study. *Journal of the Federation of American Societies for Experimental Biology*, 19(3):482–484, 2005.

[173] F.A. Meineke, C.S. Potten, and M. Loeffler. Cell migration and organization in the intestinal crypt using a lattice-free model. *Cell Proliferation*, 34(4):253–266, 2001.

[174] G. Meneghello, D.J. Parker, B.J. Ainsworth, S.P. Perera, J.B. Chaudhuri, M.J. Ellis, and P.A. De Bank. Fabrication and characterization of poly (lactic-co-glycolic acid)/polyvinyl alcohol blended hollow fibre membranes for tissue engineering applications. *Journal of Membrane Science*, 344(1-2):55–61, 2009.

[175] G. Meneghello. *Development of a Novel PVA-PLGA Hollow Fibre Bioreactor for Tissue Engineering*. PhD thesis, University of Bath, 2010.

[176] Q. Mi, D. Swigon, B. Riviere, S. Cetin, Y. Vodovotz, and D.J. Hackam. One-dimensional elastic continuum model of enterocyte layer migration. *Biophysical Journal*, 93(11):3745–3752, 2007.

[177] D. Mohebbi-Kalhori, A. Behzadmehr, C.J. Doillon, and A. Hadjizadeh. Computational modeling of adherent cell growth in a hollow-fiber membrane bioreactor for large-scale 3-D bone tissue engineering. *Journal of Artificial Organs*, 15(3):250–265, 2012.

[178] S.M. Morgan, S. Tilley, S. Perera, M.J. Ellis, J. Kanczler, J.B. Chaudhuri, and R.O.C. Oreffo. Expansion of human bone marrow stromal cells on poly-(DL-lactide-co-glycolide)(PDLLGA) hollow fibres designed for use in skeletal tissue engineering. *Biomaterials*, 28(35):5332–5343, 2007.

[179] M. Mullender, A.J. El-Haj, Y. Yang, M.A. van Duin, E.H. Burger, and J. Klein-Nulend. Mechanotransduction of bone cells *in vitro*: mechanobiology of bone tissue. *Medical and Biological Engineering and Computing*, 42:14–21, 2004.

[180] P. Murray. *From discrete to continuum models of tumour growth.* PhD thesis, University of Oxford, 2008.

[181] P.J. Murray, C.M. Edwards, M.J. Tindall, and P.K. Maini. From a discrete to a continuum model of cell dynamics in one dimension. *Physical Review E*, 80(3):031912, 2009.

[182] P.J. Murray, C.M. Edwards, M.J. Tindall, and P.K. Maini. Classifying general nonlinear force laws in cell-based models via the continuum limit. *Physical Review E*, 85(2):021921, 2012.

[183] G.A. Murrell, M. Francis, and L. Bromley. Modulation of fibroblast proliferation by oxygen free radicals. *Biochemical Journal*, 265:659–665, 1990.

[184] T. Nagai and H. Honda. A dynamic cell model for the formation of epithelial tissues. *Philosophical Magazine B*, 81(7):699–719, 2001.

[185] NHS Blood and Transplant, Statistics and Clinical Studies. Organ Donation and Transplantation: Activity Report 2013/14, 2014.

[186] S.L. Nyberg, R.A. Shatford, M.V. Peshwa, J.G. White, F.B. Cerra, and W.S. Hu. Evaluation of a hepatocyte-entrapment hollow fiber bioreactor: a potential bioartificial liver. *Biotechnology and Bioengineering*, 41(2):194–203, 1993.

[187] S.L. Nyberg, R.P. Remmel, H.J. Mann, M.V. Peshwa, W.S. Hu, and F.B. Cerra. Primary hepatocytes outperform Hep G2 cells as the source of biotransformation functions in a bioartificial liver. *Annals of Surgery*, 220(1):59–67, 1994.

[188] B. Obradovic, R.L. Carrier, G. Vunjak-Novakovic, and L.E. Freed. Gas exchange is essential for bioreactor cultivation of tissue engineered cartilage. *Biotechnology and Bioengineering*, 63 (2):197–205, 1999.

[189] B. Obradovic, J.H. Meldon, L.E. Freed, and G. Vunjak-Novakovic. Glycosaminoglycan deposition in engineered cartilage: experiments and mathematical model. *AIChE Journal*, 46(9): 1860–1871, 2000.

[190] R.D. O'Dea and J.R. King. Multiscale analysis of pattern formation via intercellular signalling. *Mathematical Biosciences*, 231(2):172–185, 2011.

[191] R.D. O'Dea and J.R. King. Continuum limits of pattern formation in hexagonal-cell monolayers. *Journal of Mathematical Biology*, 64(3):579–610, 2012.

[192] R.D. O'Dea, S.L. Waters, and H.M. Byrne. A multiphase model for tissue construct growth in a perfusion bioreactor. *Mathematical Medicine and Biology*, 27(2):95–127, 2010.

[193] R.D. O'Dea, H.M. Byrne, and S.L. Waters. Continuum modelling of in vitro tissue engineering: A review. In *Computational Modeling in Tissue Engineering*, pages 229–266. Springer, 2013.

[194] R.D. O'Dea, J.M. Osborne, A.J. El Haj, H.M. Byrne, and S.L. Waters. The interplay between tissue growth and scaffold degradation in engineered tissue constructs. *Journal of Mathematical Biology*, 67(5):1199–1225, 2013.

[195] R.D. O'Dea, S.L. Waters, and H.M. Byrne. A two-fluid model for tissue growth within a dynamic flow environment. *European Journal of Applied Mathematics*, 19(06):607–634, 2008.

[196] J.M. Osborne, A. Walter, S.K. Kershaw, G.R. Mirams, A.G. Fletcher, P. Pathmanathan, D. Gavaghan, O.E. Jensen, P.K. Maini, and H.M. Byrne. A hybrid approach to multi-scale modelling of cancer. *Philosophical Transactions of the Royal Society A*, 368(1930):5013–5028, 2010.

[197] M.R. Owen, T. Alarcón, P.K. Maini, and H.M. Byrne. Angiogenesis and vascular remodelling in normal and cancerous tissues. *Journal of Mathematical Biology*, 58(4):689–721, 2009.

[198] G.K. Owens. Control of hypertrophic versus hyperplastic growth of vascular smooth muscle cells. *American Journal of Physiology - Heart and Circulatory Physiology*, 257(6):H1755–H1765, 1989.

[199] D. Papachristodoulou, A. Snape, W.H. Elliott, and D.C. Elliott. *Biochemistry and Molecular Biology*. Oxford University Press, 2014.

[200] P. Pathmanathan, J. Cooper, A. Fletcher, G. Mirams, P. Murray, J. Osborne, J. Pitt-Francis, A. Walter, and S. Chapman. A computational study of discrete mechanical tissue models. *Physical Biology*, 6(3):036001, 2009.

[201] J.F. Patzer II. Oxygen consumption in a hollow fiber bioartificial liver-revisited. *Artificial Organs*, 28(1):83–98, 2004.

[202] N.C. Pearson, R.J. Shipley, S.L. Waters, and J.M. Oliver. Dispersion-enhanced solute transport in a cell-seeded hollow fibre membrane bioreactor. *Journal of Engineering Mathematics* (Accepted), 2014.

[203] N.C. Pearson. *Mathematical modelling of flow and transport phenomena in tissue engineering*. PhD thesis, University of Oxford, 2014.

[204] N.C. Pearson, R.J. Shipley, S.L. Waters, and J.M. Oliver. Multiphase modelling of the influence of fluid flow and chemical concentration on tissue growth in a hollow fibre membrane bioreactor. *Mathematical Medicine and Biology*, 31(4):393–430, 2014.

[205] N.C. Pearson, S.L. Waters, J.M. Oliver, and R.J. Shipley. Multiphase modelling of the effect of fluid shear stress on cell yield and distribution in a hollow fibre membrane bioreactor. *Biomechanics and Modeling in Mechanobiology*, 14(2):387–402, 2015.

[206] M.R. Pillarella and A.L. Zydney. Theoretical analysis of the effect of convective flow on solute transport and insulin release in a hollow fiber bioartificial pancreas. *Journal of Biomechanical Engineering*, 112:220–228, 1990.

[207] J.M. Piret and C.L. Cooney. Mammalian cell and protein distributions in ultrafiltration hollow fiber bioreactors. *Biotechnology and Bioengineering*, 36(9):902–910, 1990.

[208] J.M. Piret and C.L. Cooney. Model of oxygen transport limitations in hollow fiber bioreactors. *Biotechnology and Bioengineering*, 37(1):80–92, 1991.

[209] C.P. Please, G. Pettet, and D.L.S. McElwain. A new approach to modelling the formation of necrotic regions in tumours. *Applied Mathematics Letters*, 11(3):89–94, 1998.

[210] R. Pörtner, S. Nagel-Heyer, C. Goepfert, P. Adamietz, and N.M. Meenen. Bioreactor design for tissue engineering. *Journal of Bioscience and Bioengineering*, 100(3):235–245, 2005.

[211] M. Poujade, E. Grasland-Mongrain, A. Hertzog, J. Jouanneau, P. Chavrier, B. Ladoux, A. Buguin, and P. Silberzan. Collective migration of an epithelial monolayer in response to a model wound. *Proceedings of the National Academy of Sciences*, 104(41):15988–15993, 2007.

[212] M. Prass, K. Jacobson, A. Mogilner, and M. Radmacher. Direct measurement of the lamellipodial protrusive force in a migrating cell. *The Journal of Cell Biology*, 174(6):767–772, 2006.

[213] A. Quaroni, J. Wands, R.L. Trelstad, and K.J. Isselbacher. Epithelioid cell cultures from rat small intestine. Characterization by morphologic and immunologic criteria. *The Journal of Cell Biology*, 80(2):248–265, 1979.

[214] M. Quintard and S. Whitaker. Convection, dispersion, and interfacial transport of contaminants: Homogeneous porous media. *Advances in Water Resources*, 17(4):221–239, 1994.

[215] M. Radisic, W. Deen, R. Langer, and G. Vunjak-Novakovic. Mathematical model of oxygen distribution in engineered cardiac tissue with parallel channel array perfused with culture medium containing oxygen carriers. *American Journal of Physiology - Heart and Circulatory Physiology*, 288(3):H1278–H1289, 2005.

[216] M.T. Raimondi, F. Boschetti, L. Falcone, F. Migliavacca, A. Remuzzi, and G. Dubini. The effect of media perfusion on three-dimensional cultures of human chondrocytes: integration of experimental and computational approaches. *Biorheology*, 41(3-4):401–410, 2004.

[217] K.M. Reich, C.V. Gay, and J.A. Frangos. Fluid shear stress as a mediator of osteoblast cyclic adenosine monophosphate production. *Journal of Cellular Physiology*, 143(1):100–104, 1990.

[218] B.M. Rubenstein and L.J. Kaufman. The role of extracellular matrix in glioma invasion: a cellular potts model approach. *Biophysical Journal*, 95(12):5661–5680, 2008.

[219] J.A. Ruiz-Gines, S. Lopez-Ongil, M. Gonzalez-Rubio, L. Gonzalez-Santiago, M. Rodriguez-Puyol, and D. Rodriguez-Puyol. Reactive oxygen species induce proliferation of bovine aortic endothelial cells. *Journal of Cardiovascular Pharmacology*, 35(1):109–113, 2000.

[220] J. Sadoshima and S. Izumo. The cellular and molecular response of cardiac myocytes to mechanical stress. *Annual Review of Physiology*, 59(1):551–571, 1997.

[221] A. Saez, E. Anon, M. Ghibaudo, O. Du Roure, J.M. Di Meglio, P. Hersen, P. Silberzan, A. Buguin, and B. Ladoux. Traction forces exerted by epithelial cell sheets. *Journal of Physics: Condensed Matter*, 22(19):194119, 2010.

[222] P.G. Saffman. On the boundary condition at the interface of a porous medium. *Studies in Applied Mathematics*, 1(2):93–101, 1971.

[223] K.S. Sankar, B.J. Green, A.R. Crocker, J.E. Verity, S.M. Altamentova, and J.V. Rocheleau. Culturing pancreatic islets in microfluidic flow enhances morphology of the associated endothelial cells. *PLoS ONE*, 6(9):e24904, 2011.

[224] L. Saxby, E. Rosen, and M. Boulton. Lens epithelial cell proliferation, migration, and metaplasia following capsulorhexis. *British Journal of Ophthalmology*, 82(8):945–952, 1998.

[225] G. Schaller and M. Meyer-Hermann. Multicellular tumor spheroid in an off-lattice Voronoi-Delaunay cell model. *Physical Review E*, 71(5):051910, 2005.

[226] J.A. Schonberg and G. Belfort. Enhanced nutrient transport in hollow fiber perfusion bioreactors: a theoretical analysis. *Biotechnology Progress*, 3(2):80–89, 1987.

[227] T. Seewöster and J. Lehmann. Cell size distribution as a parameter for the predetermination of exponential growth during repeated batch cultivation of CHO cells. *Biotechnology and Bioengineering*, 55(5):793–797, 1997.

[228] B.G. Sengers, M. Taylor, C.P. Please, and R.O.C. Oreffo. Computational modelling of cell spreading and tissue regeneration in porous scaffolds. *Biomaterials*, 28(10):1926–1940, 2007.

[229] M. Shakeel, P.C. Matthews, R.S. Graham, and S.L. Waters. A continuum model of cell proliferation and nutrient transport in a perfusion bioreactor. *Mathematical Medicine and Biology*, 30(1):21–44, 2013.

[230] R.A. Shatford, S.L. Nyberg, S.J. Meier, J.G. White, W.D. Payne, W. Hu, and F.B. Cerra. Hepatocyte function in a hollow fiber bioreactor: a potential bioartificial liver. *Journal of Surgical Research*, 53(6):549–557, 1992.

[231] R.J. Shipley and S.L. Waters. Fluid and mass transport modelling to drive the design of cell-packed hollow fibre bioreactors for tissue engineering applications. *Mathematical Medicine and Biology*, 29(4):329–359, 2012.

[232] R.J. Shipley, G.W. Jones, R.J. Dyson, B.G. Sengers, C.L. Bailey, C.J. Catt, C.P. Please, and J. Malda. Design criteria for a printed tissue engineering construct: A mathematical homogenization approach. *Journal of Theoretical Biology*, 259(3):489–502, 2009.

[233] R.J. Shipley, S.L. Waters, and M.J. Ellis. Definition and validation of operating equations for poly (vinyl alcohol)-poly (lactide-co-glycolide) microfiltration membrane-scaffold bioreactors. *Biotechnology and Bioengineering*, 107(2):382–392, 2010.

[234] R.J. Shipley, A.J. Davidson, K. Chan, J.B. Chaudhuri, S.L. Waters, and M.J. Ellis. A strategy to determine operating parameters in tissue engineering hollow fiber bioreactors. *Biotechnology and Bioengineering*, 108(6):1450–1461, 2011.

[235] R.J. Shipley, M.J. Ellis, and S.L. Waters. Combining mathematical modelling with experimental data to characterize fluid and protein transport properties in hollow fibre scaffolds. In *Proceedings of ITP-09 (Interdisciplinary Transport Phenomena VI)*, 2009.

[236] A. Shirinifard, J.S. Gens, B.L. Zaitlen, N.J. Popławski, M. Swat, and J.A. Glazier. 3D multi-cell simulation of tumor growth and angiogenesis. *PLoS ONE*, 4(10):e7190, 2009.

[237] V.I. Sikavitsas, G.N. Bancroft, J.J. Lemoine, M.A.K. Liebschner, M. Dauner, and A.G. Mikos. Flow perfusion enhances the calcified matrix deposition of marrow stromal cells in biodegradable nonwoven fiber mesh scaffolds. *Annals of Biomedical Engineering*, 33(1):63–70, 2005.

[238] M.J. Simpson, K.A. Landman, B.D. Hughes, and A.E. Fernando. A model for mesoscale patterns in motile populations. *Physica A: Statistical Mechanics and its Applications*, 389(7): 1412–1424, 2010.

[239] K. Smallbone, R. Gatenby, R. Gillies, P. Maini, and D. Gavaghan. Metabolic changes during carcinogenesis: potential impact on invasiveness. *Journal of Theoretical Biology*, 244(4):703–713, 2007.

[240] R.L. Smith, B. Donlon, M. Gupta, M. Mohtai, P. Das, D. Carter, J. Cooke, G. Gibbons, N. Hutchinson, and D. Schurman. Effects of fluid-induced shear on articular chondrocyte morphology and metabolism in vitro. *Journal of Orthopaedic Research*, 13(6):824–831, 1995.

[241] C.L. Stabler, C. Fraker, E. Pedraza, I. Constantinidis, and A. Sambanis. Modeling and in vitro and in vivo characterization of a tissue engineered pancreatic substitute. *Journal of Combinatorial Optimization*, 17(1):54–73, 2009.

[242] A. Stephanou, S.R. McDougall, A.R.A. Anderson, and M.A.J. Chaplain. Mathematical modelling of flow in 2D and 3D vascular networks: applications to anti-angiogenic and chemotherapeutic drug strategies. *Mathematical and Computer Modelling*, 41(10):1137–1156, 2005.

[243] M.M. Stevens, M. Mayer, D.G. Anderson, D.B. Weibel, G.M. Whitesides, and R. Langer. Direct patterning of mammalian cells onto porous tissue engineering substrates using agarose stamps. *Biomaterials*, 26(36):7636–7641, 2005.

[244] U.A. Stock and J.P. Vacanti. Tissue engineering: current state and prospects. *Annual Review of Medicine*, 52(1):443–451, 2001.

[245] M.A. Stolarska, Y. Kim, and H.G. Othmer. Multi-scale models of cell and tissue dynamics. *Philosophical transactions of the Royal Society A*, 367(1902):3525–3553, 2009.

[246] J.P. Sullivan, J.E. Gordon, T. Bou-Akl, H.W.T. Matthew, and A.F. Palmer. Enhanced oxygen delivery to primary hepatocytes within a hollow fiber bioreactor facilitated via hemoglobin-based oxygen carriers. *Artificial Cells, Blood Substitutes and Biotechnology*, 35(6):585–606, 2007.

[247] J.P. Sullivan and A.F. Palmer. Targeted oxygen delivery within hepatic hollow fiber bioreactors via supplementation of hemoglobin-based oxygen carriers. *Biotechnology Progress*, 22(5):1374–1387, 2006.

[248] J.P. Sullivan, J.E. Gordon, and A.F. Palmer. Simulation of oxygen carrier mediated oxygen transport to C3A hepatoma cells housed within a hollow fiber bioreactor. *Biotechnology and Bioengineering*, 93(2):306–317, 2006.

[249] I. Swenne. The role of glucose in the in vitro regulation of cell cycle kinetics and proliferation of fetal pancreatic B-cells. *Diabetes*, 31(9):754–760, 1982.

[250] M. Takamiya, K.H. Haider, and M. Ashraf. Identification and characterization of a novel multipotent sub-population of Sca-1+ cardiac progenitor cells for myocardial regeneration. *PLoS ONE*, 6(9):e25265, 2011.

[251] J.P. Tharakan and P.C. Chau. A radial flow hollow fiber bioreactor for the large-scale culture of mammalian cells. *Biotechnology and Bioengineering*, 28(3):329–342, 1986.

[252] S. Tlili, C. Gay, F. Graner, P. Marcq, F. Molino, and P. Saramito. Mechanical formalism for tissue dynamics. *arXiv*, 2013. (Preprint) arXiv:1309.7432.

[253] M. Tomita, E.F. Sato, M. Nishikawa, Y. Yamano, and M. Inoue. Nitric oxide regulates mitochondrial respiration and functions of articular chondrocytes. *Arthritis & Rheumatism*, 44(1):96–104, 2001.

[254] L.N. Trefethen. *Spectral methods in MATLAB*, volume 10. SIAM, 2000.

[255] K.K. Treloar, M.J. Simpson, D.L.S. McElwain, and R.E. Baker. Are *in vitro* estimates of cell diffusivity and cell proliferation rate sensitive to assay geometry? *Journal of Theoretical Biology*, 356:71–84, 2014.

[256] P.S. Treuhaft and D.J. McCarty. Synovial fluid pH, lactate, oxygen and carbon dioxide partial pressure in various joint diseases. *Arthritis & Rheumatism*, 14(4):475–484, 1971.

[257] R.S. Tuan, G. Boland, and R. Tuli. Adult mesenchymal stem cells and cell-based tissue engineering. *Arthritis Research and Therapy*, 5(1):32–45, 2003.

[258] S. Turner, J. A Sherratt, and D. Cameron. Tamoxifen treatment failure in cancer and the nonlinear dynamics of TGF-β. *Journal of Theoretical Biology*, 229(1):101–111, 2004.

[259] S. Turner, J.A. Sherratt, K.J. Painter, and N.J. Savill. From a discrete to a continuous model of biological cell movement. *Physical Review E*, 69(2):021910, 2004.

[260] E. Tziampazis and A. Sambanis. Tissue engineering of a bioartificial pancreas: modeling the cell environment and device function. *Biotechnology Progress*, 11(2):115–126, 1995.

[261] E. Tzima, M. Irani-Tehrani, W.B. Kiosses, E. Dejana, D.A. Schultz, B. Engelhardt, G. Cao, H. DeLisser, and M.A. Schwartz. A mechanosensory complex that mediates the endothelial cell response to fluid shear stress. *Nature*, 437(7057):426–431, 2005.

[262] U.S. Department of Health and Human Services, Health Resouces and Services Administration. Organ Procurement and Transplantation Network/Scientific Registry of Transplant Recipients 2012 Annual Data Report, 2014.

[263] I.M.M. Van Leeuwen, G.R. Mirams, A. Walter, A. Fletcher, P. Murray, J. Osborne, S. Varma, S.J. Young, J. Cooper, B. Doyle, J. Pitt-Francis, L. Momtahan, P. Pathmanathan, J.P. Whiteley, S.J. Chapman, D.J. Gavaghan, O.E. Jensen, J.R. King, P.K. Maini, S.L. Waters, and H.M. Byrne. An integrative computational model for intestinal tissue renewal. *Cell Proliferation*, 42(5):617–636, 2009.

[264] H.H. Vandenburgh, S. Hatfaludy, P. Karlisch, and J. Shansky. Mechanically induced alterations in cultured skeletal muscle growth. *Journal of Biomechanics*, 24:91–99, 1991.

[265] H.H. Vandenburgh. Mechanical forces and their second messengers in stimulating cell growth in vitro. *American Journal of Physiology - Regulatory, Integrative and Comparative Physiology*, 262(3):R350–R355, 1992.

[266] M.G. Vander Heiden, L.C. Cantley, and C.B. Thompson. Understanding the Warburg effect: the metabolic requirements of cell proliferation. *Science*, 324(5930):1029–1033, 2009.

[267] A. Walter. *A comparison of continuum and cell-based models of colorectal cancer*. PhD thesis, University of Nottingham, 2009.

[268] D. Wang, K. Li, and W.K. Teo. Polyethersulfone hollow fiber gas separation membranes prepared from NMP/alcohol solvent systems. *Journal of Membrane Science*, 115(1):85–108, 1996.

[269] D.W. Wang, B. Fermor, J.M. Gimble, H.A. Awad, and F. Guilak. Influence of oxygen on the proliferation and metabolism of adipose derived adult stem cells. *Journal of Cellular Physiology*, 204(1):184–191, 2005.

[270] Z. Wang and T.S. Deisboeck. Computational modeling of brain tumors: discrete, continuum or hybrid? *Scientific Modeling and Simulations*, 15:381–393, 2009.

[271] S.L. Waters, L.J. Cummings, K.M. Shakesheff, and F. Rose. Tissue growth in a rotating bioreactor. Part I: mechanical stability. *Mathematical Medicine and Biology*, 23:311–337, 2006.

[272] R.J. Whittaker, R. Booth, R. Dyson, C. Bailey, L. Parsons Chini, S. Naire, S. Payvandi, Z. Rong, H. Woollard, L.J. Cummings, S.L. Waters, L. Mawasse, J.B. Chaudhuri, M.J. Ellis, V. Michael, N.J. Kuiperk, and S. Cartmell. Mathematical modelling of fibre-enhanced perfusion inside a tissue-engineering bioreactor. *Journal of Theoretical Biology*, 256(4):533–546, 2009.

[273] S.N.O. Williams, R.M. Callies, and K.M. Brindle. Mapping of oxygen tension and cell distribution in a hollow-fiber bioreactor using magnetic resonance imaging. *Biotechnology and Bioengineering*, 56(1):56–61, 1997.

[274] S.M. Wise, J.S. Lowengrub, H.B. Frieboes, and V. Cristini. Three-dimensional multispecies nonlinear tumor growth I: Model and numerical method. *Journal of Theoretical Biology*, 253 (3):524–543, 2008.

[275] G. Wolf, K. Sharma, Y. Chen, M. Ericksen, and F.N. Ziyadeh. High glucose-induced proliferation in mesangial cells is reversed by autocrine TGF-β. *Kidney International*, 42:647–656, 1992.

[276] D.Y. Wong, J.C. Leveque, H. Brumblay, P.H. Krebsbach, S.J. Hollister, and F. LaMarca. Macro-architectures in spinal cord scaffold implants influence regeneration. *Journal of Neurotrauma*, 25(8):1027–1037, 2008.

[277] Q. Wu and Q. Chen. Mechanoregulation of chondrocyte proliferation, maturation, and hypertrophy: ion-channel dependent transduction of matrix deformation signals. *Experimental Cell Research*, 256(2):383–391, 2000.

[278] N. Wung, S.M. Acott, D. Tosh, and M.J. Ellis. Hollow fibre membrane bioreactors for tissue engineering applications. *Biotechnology Letters*, 36(12):2357–2366, 2014.

[279] K. Yamamoto, T. Sokabe, T. Watabe, K. Miyazono, J.K. Yamashita, S. Obi, N. Ohura, A. Matsushita, A. Kamiya, and J. Ando. Fluid shear stress induces differentiation of Flk-1-positive embryonic stem cells into vascular endothelial cells in vitro. *American Journal of Physiology - Heart and Circulatory Physiology*, 288(4):H1915–H1924, 2005.

[280] H. Ye, D.B. Das, J.T. Triffitt, and Z. Cui. Modelling nutrient transport in hollow fibre membrane bioreactors for growing three-dimensional bone tissue. *Journal of Membrane Science*, 272(1-2):169–178, 2006.

[281] H. Ye, Z. Xia, D.J.P. Ferguson, J.T. Triffitt, and Z. Cui. Studies on the use of hollow fibre membrane bioreactors for tissue generation by using rat bone marrow fibroblastic cells and a composite scaffold. *Journal of Materials Science: Materials in Medicine*, 18(4):641–648, 2007.

[282] A.B. Yeatts and J.P. Fisher. Bone tissue engineering bioreactors: dynamic culture and the influence of shear stress. *Bone*, 48(2):171–181, 2011.

[283] H. Zahedmanesh and C. Lally. A multiscale mechanobiological modelling framework using agent-based models and finite element analysis: application to vascular tissue engineering. *Biomechanics and Modeling in Mechanobiology*, 11(3):363–377, 2012.

[284] J.M. Zahm, H. Kaplan, A.L. Hérard, F. Doriot, D. Pierrot, P. Somelette, and E. Puchelle. Cell migration and proliferation during the in vitro wound repair of the respiratory epithelium. *Cell Motility and Cytoskeleton*, 37(1):33–43, 1997.

[285] Y. Zeng, T.S. Lee, P. Yu, P. Roy, and H.T. Low. Mass transport and shear stress in a microchannel bioreactor: numerical simulation and dynamic similarity. *Journal of Biomechanical Engineering*, 128(2):185–193, 2006.

[286] L. Zhang, C.G. Strouthos, Z. Wang, and T.S. Deisboeck. Simulating brain tumor heterogeneity with a multiscale agent-based model: Linking molecular signatures, phenotypes and expansion rate. *Mathematical and Computer Modelling*, 49(1):307–319, 2009.

[287] L. Zhang, Z. Wang, J.A. Sagotsky, and T.S. Deisboeck. Multiscale agent-based cancer modeling. *Journal of Mathematical Biology*, 58(4):545–559, 2009.

[288] F. Zhao, P. Pathi, W. Grayson, Q. Xing, B.R. Locke, and T. Ma. Effects of oxygen transport on 3-D human mesenchymal stem cell metabolic activity in perfusion and static cultures: Experiments and mathematical model. *Biotechnology Progress*, 21(4):1269–1280, 2005.

[289] F. Zhao, R. Chella, and T. Ma. Effects of shear stress on 3-D human mesenchymal stem cell construct development in a perfusion bioreactor system: Experiments and hydrodynamic modeling. *Biotechnology and Bioengineering*, 96(3):584–595, 2007.